Chapter 3

Characterization of Nanomaterials

3.1 Analysis

3.1.1 ICP-AES Analysis of Nanoparticles[1]

3.1.1.1 What is ICP-AES?

Inductively coupled plasma atomic emission spectroscopy (ICP-AES) is a spectral method used to determine very precisely the elemental composition of samples; it can also be used to quantify the elemental concentration with the sample. ICP-AES uses high-energy plasma from an inert gas like argon to burn analytes very rapidly. The color that is emitted from the analyte is indicative of the elements present, and the intensity of the spectral signal is indicative of the concentration of the elements that is present. A schematic view of a typical experimental set-up is shown in Figure 3.1.

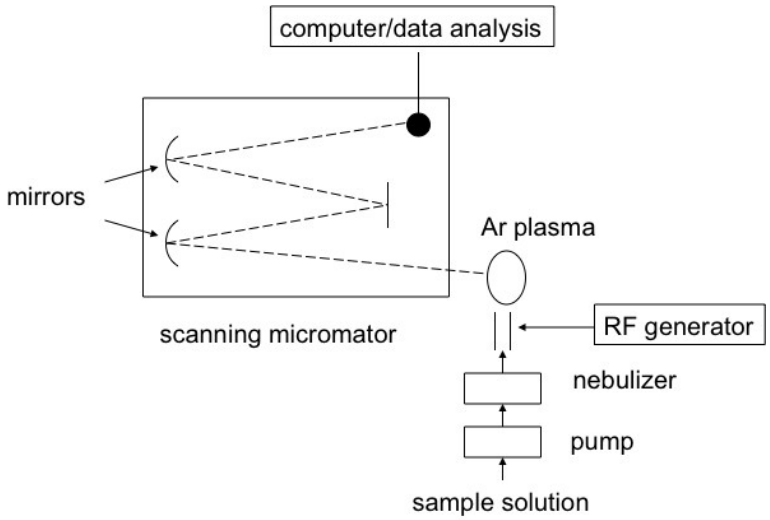

Figure 3.1: Schematic representation of an ICP-AES set-up.

[1] This content is available online at <http://cnx.org/content/m22058/1.19/>.

3.1.1.2 How does ICP-AES work?

ICP-AES works by the emission of photons from analytes that are brought to an excited state by the use of high-energy plasma. The plasma source is induced when passing argon gas through an alternating electric field that is created by an inductively couple coil. When the analyte is excited the electrons try to dissipate the induced energy moving to a ground state of lower energy, in doing this they emit the excess energy in the form of light. The wavelength of light emitted depends on the energy gap between the excited energy level and the ground state. This is specific to the element based on the number of electrons the element has and electron orbital's are filled. In this way the wavelength of light can be used to determine what elements are present by detection of the light at specific wavelengths.

As a simple example consider the situation when placing a piece of copper wire into the flame of a candle. The flame turns green due to the emission of excited electrons within the copper metal, as the electrons try to dissipate the energy incurred from the flame, they move to a more stable state emitting energy in the form of light. The energy gap between the excited state to the ground state (ΔE) dictates the color of the light or wavelength of the light, (3.1), where h is Plank's constant (6.626×10^{-34} m^2kg/s), and ν is the frequency of the emitted light.

$$E = h\nu \tag{3.1}$$

The wavelength of light is indicative of the element present. If another metal is placed in the flame such as iron a different color flame will be emitted because the electronic structure of iron is different from that of copper. This is a very simple analogy for what is happening in ICP-AES and how it is used to determine what elements are present. By detecting the wavelength of light that is emitted from the analyte one can deduce what elements are be present.

Naturally if there is a lot of the material present then there will be an accumulative effect making the intensity of the signal large. However, if there were very little materials present the signal would be low. By this rationale one can create a calibration curve from analyte solutions of known concentrations, whereby the intensity of the signal changes as a function of the concentration of the material that is present. When measuring the intensity from a sample of unknown concentration the intensity from this sample can be compared to that from the calibration curve, so this can be used to determine the concentration of the analytes within the sample.

3.1.1.3 ICP-AES of nanoparticles to determine elemental composition

As with any sample being studied by ICP-AES nanoparticles need to be digested so that all the atoms can be vaporized in the plasma equally. If a metal containing nanoparticle were not digested using a strong acid to bring the metals atoms into solution, the form of the particle could hinder some of the material being vaporized. The analyte would not be detected even though it is present in the sample and this would give an erroneous result. Nanoparticles are often covered with a protective layer of organic ligands and this must be removed also. Further to this the solvent used for the nanoparticles may also be an organic solution and this should be removed as it too will not be miscible in the aqueous medium.

Several organic solvents have low vapor pressures so it is relatively easy to remove the solvent by heating the samples, removing the solvent by evaporation. To remove the organic ligands that are present on the nanoparticle, choric acid can be used. This is a very strong acid and can break down the organic ligands readily. To digest the particles and get the metal into solution concentrated nitric acid is often used.

A typical protocol may use 0.5 mL of concentrated nanoparticle solution and digest this with 9.5 mL of concentrated nitric acid over the period of a few days. After which 0.5 mL of the digested solution is placed in 9.5 mL of nanopure water. The reason why nanopure water is used is because DI water or regular water will have some amount of metals ions present and these will be detected by the ICP-AES measurement and will lead to figures that are not truly representative of the analyte concentration alone. This is especially pertinent when there is a very a low concentration of metal analyte to be detected, and is even more a problem when the metal to be detected is commonly found in water such as iron. Once the nanopure water and digested solution are prepared then the sample is ready for analysis.

Another point to consider when doing ICP-AES on nanoparticles to determine chemical compositions, includes the potential for wavelength overlap. The energy that is released in the form of light is unique to each element, but elements that are very similar in atomic structure will have emission wavelengths that are very similar to one another. Consider the example of iron and cobalt, these are both transition metals and sit right beside each other on the periodic table. Iron has an emission wavelength at 238.204 nm and cobalt has an emission wavelength at 238.892 nm. So if you were to try determine the amount of each element in an alloy of the two you would have to select another wavelength that would be unique to that element, and not have any wavelength overlap to other analytes in solution. For this case of iron and cobalt it would be wiser to use a wavelength for iron detection of 259.940 nm and a wavelength detection of 228.616 nm. Bearing this in mind a good rule of thumb is to try use the wavelength of the analyte that affords the best detection primarily. But if this value leads to a possible wavelength overlap of within 15 nm wavelength with another analyte in the solution then another choice should be made of the detection wavelength to prevent wavelength overlap from occurring.

Some people have also used the ICP-AES technique to determine the size of nanoparticles. The signal that is detected is determined by the amount of the material that is present in solution. If very dilute solutions of nanoparticles are being analyzed, particles are being analyzed one at a time, i.e., there will be one nanoparticle per droplet in the nebulizer. The signal intensity would then differ according to the size of the particle. In this way the ICP-AES technique could be used to determine the concentration of the particles in the solution as well as the size of the particles.

3.1.1.4 Calculations for ICP concentrations

In order to performe ICP-AES stock solutions must be prepared in dilute nitric acid solutions. To do this a concentrated solution should be diluted with nanopure water to prepare 7 wt% nitric acid solutions. If the concentrated solution is 69.8 wt% (check the assay amount that is written on the side of the bottle) then the amount to dilute the solution will be as such:

- The density (d) of HNO_3 is 1.42 g/mL
- Molecular weight (M_W) of HNO_3 is 63.01

Concentrated percentage 69.8 wt% from assay. First you must determine the molarity of the concentrated solution, (3.2). For the present assay amount, the figure will be calculated from (3.3) and (3.4).

$$\text{Molarity} = [(\%)(d)/(M_W)] * 10 \tag{3.2}$$

$$M = [(69.8)(1.42) / (63.01)] * 10 \tag{3.3}$$

$$\therefore\ M = 15.73 \tag{3.4}$$

This is the initial concentration C_I. To determine the molarity of the 7% solution will be determined by (3.5), i.e., (3.6) is the final concentration C_F.

$$M = [(7)(1.42) / (63.01)] * 10 \tag{3.5}$$

$$\therefore M = 1.58 \tag{3.6}$$

We use these figures in (3.7) to determine the amount of dilution required to dilute the concentrated nitric acid to make it a 7% solution.

$$\text{mass}_I * \text{concentration}_I = \text{mass}_F * \text{concentration}_F \tag{3.7}$$

Now as we are talking about solutions the amount of mass will be measured in mL, and the concentration will be measured as a molarity, (3.8) and (3.9) where M_I and M_F have been calculated above. In addition, the amount of dilute solution will be dependent on the user and how much is required by the user to complete the ICP analysis, for the sake of argument let's say that we need 10 mL of dilute solution, this is mL_F, i.e., (3.10) and (3.11).

$$mL_I * C_I = mL_F * C_F \tag{3.8}$$

$$\therefore mL_I = [mL_F * C_F]/C_I \tag{3.9}$$

$$mL_I = [10 * 1.58] / 15.73 \tag{3.10}$$

$$\therefore mL_I = 10.03 \text{ mL} \tag{3.11}$$

This means that 10.03 mL of the concentrated nitric acid (69.8%) should be diluted up to a total of 100 mL with nanopure water.

Now that you have your stock solution with the correct percentage then you can use this solution to prepare your solutions of varying concentration. Let's take the example that the stock solution that you purchase from a supplier has a concentration of 100 ppm of analyte, which is equivalent to 1 μg/mL.

In order to make your calibration curve more accurate it is important to be aware of two issues. Firstly, as with all straight-line graphs, the more points that are used then the better the statistics is that the line is correct. But, secondly, the more measurements that are used means that more room for error is introduced to the system, to avoid these errors from occurring one should be very vigilant and skilled in the use of pipetting and diluting of solutions. Especially when working with very low concentration solutions a small drop of material making the dilution above or below the exactly required amount can alter the concentration and hence affect the calibration deleteriously. The premise upon which the calculation is done is based on (3.8), whereby C refers to concentration in ppm, and mL refers to mass in mL.

The choice of concentrations to make will depend on the samples and the concentration of analyte within the samples that are being analyzed. For first time users it is wise to make a calibration curve with a large range to encompass all the possible outcomes. When the user is more aware of the kind of concentrations that they are producing in their synthesis then they can narrow down the range to fit the kind of concentrations that they are anticipating.

In this example we will make concentrations ranging from 10 ppm to 0.1 ppm, with a total of five samples. In a typical ICP-AES analysis about 3 mL of solution is used, however if you have situations with substantial wavelength overlap then you may have chosen to do two separate runs and so you will need approximately 6 mL solution. In general it is wise to have at least 10 mL of solution to prepare for any eventuality that may occur. There will also be some extra amount needed for samples that are being used for the quality control check. For this reason 10 mL should be a sufficient amount to prepare of each concentration.

We can define the unknowns in the equation as follows:

- C_I = concentration of concentrated solution (ppm)
- C_F = desired concentration (ppm)
- M_I = initial mass of material (mL)
- M_F = mass of material required for dilution (mL)

The methodology adopted works as follows. Make the high concentration solution then take from that solution and dilute further to the desired concentrations that are required.

Let's say the concentration of the stock solution from the supplier is 100 ppm of analyte. First we should dilute to a concentration of 10 ppm. To make 10 mL of 10 ppm solution we should take 1 mL of the 100

ppm solution and dilute it up to 10 mL with nanopure water, now the concentration of this solution is 10 ppm. Then we can take from the 10 ppm solution and dilute this down to get a solution with 5 ppm. To do this take 5 mL of the 10 ppm solution and dilute it to 10 mL with nanopure water, then you will have a solution of 10 mL that is 5 ppm concentration. And so you can do this successively taking aliquots from each solution working your way down at incremental steps until you have a series of solutions that have concentrations ranging from 10 ppm all the way down to 0.1 ppm or lower, as required.

3.1.1.5 ICP-AES at work

While ICP-AES is a useful method for quantifying the presence of a single metal in a given nanoparticle, another very important application comes from the ability to determine the ratio of metals within a sample of nanoparticles.

In the following examples we can consider the bi-metallic nanoparticles of iron with copper. In a typical synthesis 0.75 mmol of $Fe(acac)_3$ is used to prepare iron-oxide nanoparticle of the form Fe_3O_4. It is possible to replace a quantity of the Fe^{n+} ions with another metal of similar charge. In this manner bi-metallic particles were made with a precursor containing a suitable metal. In this example the additional metal precursor will be $Cu(acac)_2$.

Keep the total metal concentration in this example is 0.75 mmol. So if we want to see the effect of having 10% of the metal in the reaction as copper, then we will use 10% of 0.75 mmol, that is 0.075 mmol $Cu(acac)_2$, and the corresponding amount of iron is 0.675 mmol $Fe(acac)_3$. We can do this for successive increments of the metals until you make 100% copper oxide particles.

Subsequent Fe and Cu ICP-AES of the samples will allow the determination of Fe:Cu ratio that is present in the nanoparticle. This can be compared to the ratio of Fe and Cu that was applied as reactants. The graph Figure 3.2 shows how the percentage of Fe in the nanoparticle changes as a function of how much Fe is used as a reagent.

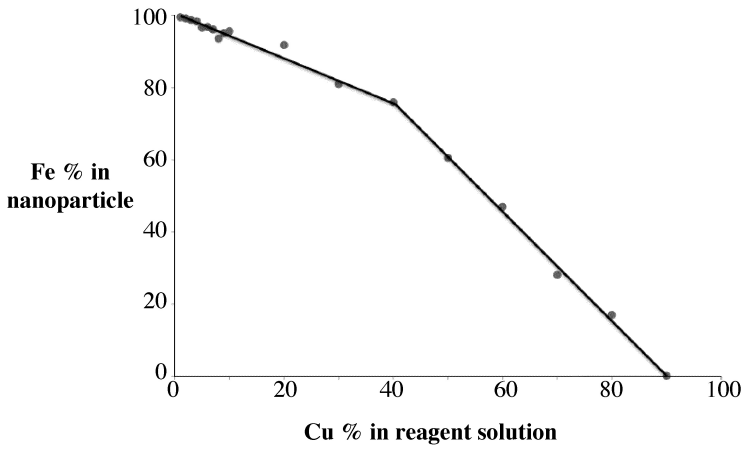

Figure 3.2: Change in iron percentage in the Fe-Cu-O nanoparticles as a function of how much iron precursor is used in the synthesis of the nanoparticles.

3.1.1.5.1 Determining analyte concentration

Once the nanoparticles are digested and the ICP-AES analysis has been completed you must turn the figures from the ICP-AES analysis into working numbers to determine the concentration of metals in the solution that was synthesized initially.

Let's first consider the nanoparticles that are of one metal alone. The figure given by the analysis in this case is given in units of mg/L, this is the value in ppm's. This figure was recorded for the solution that was analyzed, and this is of a dilute concentration compared to the initial synthesized solution because the particles had to be digested in acid first, then diluted further into nanopure water.

As mentioned above in the experimental 0.5 mL of the synthesized nanoparticles were first digested in 9.5 mL of concentrated nitric acid. Then when the digestion was complete 0.5 mL of this solution was dissolved in 9.5 mL of nanopure water. This was the final solution that was analyzed using ICP, and the concentration of metal in this solution will be far lower than that of the original solution. In this case the amount of analyte in the final solution being analyzed is $1/20^{\text{th}}$ that of the total amount of material in the solution that was originally synthesized.

3.1.1.5.2 Calculating concentration in ppm

Let us take an example that upon analysis by ICP-AES the amount of Fe detected is 6.38 mg/L. First convert the figure to mg/mL, using (3.12),

$$6.38 \text{ mg/L} * 1/1000 \text{ L/mL} = 6.38\text{x}10^{-3} \text{ mg/mL} \tag{3.12}$$

The amount of material was diluted to a total volume of 10 mL. Therefore we should multiply this value by 10 mL to see how much mass was in the whole container, (3.13).

$$6.38\text{x}10^{-3} \text{ mg/mL} * 10 \text{ mL} = 6.38\text{x}10^{-2} \text{ mg} \tag{3.13}$$

This is the total mass of iron that was present in the solution that was analyzed using the ICP device. To convert this amount to ppm we should take into consideration the fact that 0.5 mL was initially diluted to 10 mL, to do this we should divide the total mass of iron by this amount that it was diluted to, (3.14).

$$6.38\text{x}10^{-2} \text{ mg} / 0.5 \text{ mL} = 0.1276 \text{ mg/mL} \tag{3.14}$$

This was the total amount of analyte in the 10 mL solution that was analyzed by the ICP device, to attain the value in ppm it should be mulitplied by a thousand, that is then 127.6 ppm of Fe.

3.1.1.5.3 Determining concentration of original solution

We now need to factor in the fact that there were several dilutions of the original solution first to digest the metals and then to dissolve them in nanopure water, in all there were two dilutions and each dilution was equivalent in mass. By diluting 0.5 mL to 10 mL , we are effectively diluting the solution by a factor of 20, and this was carried out twice, i.e., (3.15).

$$0.1276 \text{ mg/mL} * 20 = 2.552 \text{ mg/mL} \tag{3.15}$$

This is the amount of analyte in the solution of digested particles, to covert this to ppm we should multiply it by 1/1000 mL/L, in the following way:

$$2.552 \text{ mg/mL} * 1/1000 \text{ mL/L} = 2552 \text{ mg/L} \tag{3.16}$$

This is essentially your answer now as 2552 ppm. This is the amount of Fe in the solution of digested particles. This was made by diluting 0.5 mL of the original solution into 9.5 mL concentrated nitric acid, which is the same as diluting by a factor of 20. To calculate how much analyte was in the original batch

that was synthesized we multiply the previous value by 20 again, i.e., (3.17). This is the final amount of Fe concentration of the original batch when it was synthesized and made soluble in hexanes.

$$2552 \text{ ppm} * 20 = 51040 \text{ ppm} \tag{3.17}$$

3.1.1.5.4 Calculating stoichiometric ratio

Moving from calculating the concentration of individual elements now we can concentrate on the calculation of stoichiometric ratios in the bi-metallic nanoparticles.

Consider the case when we have the iron and the copper elements in the nanoparticle. The amounts determined by ICP are:

- Iron = 1.429 mg/L.
- Copper = 1.837 mg/L.

We must account for the molecular weights of each element by dividing the ICP obtained value, by the molecular weight for that particular element. For iron this is calculated by (3.18), and thus this is molar ratio of iron. On the other hand the ICP returns a value for copper that is given by (3.19).

$$1.429 \text{ mg/L} / 55.85 = 0.0211 \tag{3.18}$$

$$1.837 \text{ mg/L} / 63.55 = 0.0289 \tag{3.19}$$

To determine the percentage iron we use (3.20), which gives a percentage value of 42.15% Fe.

$$\%\text{Fe} = [(\text{molar ratio of iron})/(\text{sum of molar ratios})] * 100 \tag{3.20}$$

To work out the copper percentage we calculate this amount using (3.21), which leads to an answer of 57.85% Cu.

$$\%\ \text{Cu} = [(\text{molar ratio of copper})/(\text{sum of molar ratios})] * 100 \tag{3.21}$$

In this way the percentage iron in the nanoparticle can be determined as function of the reagent concentration prior to the synthesis (Figure 3.2).

3.1.1.5.5 Determining concentration of nanoparticles in solution

The previous examples have shown how to calculate both the concentration of one analyte and the effective shared concentration of metals in the solution. These figures pertain to the concentration of elemental atoms present in solution. To use this to determine the concentration of nanoparticles we must first consider how many atoms that are being detected are in a nanoparticle. Let us consider that the Fe_3O_4 nanoparticles are of 7 nm diameter. In a 7 nm particle we expect to find 20,000 atoms. However in this analysis we have only detected Fe atoms, so we must still account for the number of oxygen atoms that form the crystal lattice also.

For every 3 Fe atoms, there are 4 O atoms. But as iron is slightly larger than oxygen, it will make up for the fact there is one less Fe atom. This is an over simplification but at this time it serves the purpose to make the reader aware of the steps that are required to take when judging nanoparticles concentration. Let us consider that half of the nanoparticle size is attributed to iron atoms, and the other half of the size is attributed to oxygen atoms.

As there are 20,000 atoms total in a 7 nm particle, and then when considering the effect of the oxide state we will say that for every 10,000 atoms of Fe you will have a 7 nm particle. So now we must find out how many Fe atoms are present in the sample so we can divide by 10,000 to determine how many nanoparticles are present.

In the case from above, we found the solution when synthesized had a concentration 51,040 ppm Fe atoms in solution. To determine how how many atoms this equates to we will use the fact that 1 mole of material has the Avogadro number of atoms present, (3.22).

$$51040 \text{ ppm} = 51040 \text{ mg/L} = 51.040 \text{ g/L} \tag{3.22}$$

1 mole of iron weighs 55.847 g. To determine how many moles we now have, we divide the values like this:

$$(51.040 \text{ g/L}) / (55.847 \text{ g}) = 0.9139 \text{ moles/L} \tag{3.23}$$

The number of atoms is found by multiplying this by Avogadro's number (6.022×10^{23}):

$$(0.9139 \text{ moles/L}) * (6.022 \times 10^{23} \text{ atoms}) = 5.5 \times 10^{23} \text{ atoms/L} \tag{3.24}$$

For every 10,000 atoms we have a nanoparticle (NP) of 7 nm diameter, assuming all the particles are equivalent in size we can then divide the values, (3.25). This is the concentration of nanoparticles per liter of solution as synthesized.

$$(5.5 \times 10^{23} \text{ atoms/L}) / (10{,}000 \text{ atoms/NP}) = 5.5 \times 10^{19} \text{ NP/L} \tag{3.25}$$

3.1.1.5.6 Combined surface area

One very interesting thing about nanotechnology that nanoparticles can be used for is their incredible ratio between the surface areas compared with the volume. As the particles get smaller and smaller the surface area becomes more prominent. And as much of the chemistry is done on surfaces, nanoparticles are good contenders for future use where high aspect ratios are required.

In the example above we considered the particles to be of 7 nm diameters. The surface area of such a particle is 1.539×10^{-16} m^2. So the combined surface area of all the particles is found by multiplying each particle by their individual surface areas.

$$(1.539 \times 10^{-16} \text{ m}^2) * (5.5 \times 10^{19} \text{ NP/L}) = 8465 \text{ m}^2\text{/L} \tag{3.26}$$

To put this into context, an American football field is approximately 5321 m^2. So a liter of this nanoparticle solution would have the same surface area of approximately 1.5 football fields. That is allot of area in one liter of solution when you consider how much material it would take to line the football field with thin layer of metallic iron. Remember there is only about 51 g/L of iron in this solution!

3.1.1.6 Bibliography

- http://www.ivstandards.com/extras/pertable/[2]
- A. Scheffer, C. Engelhard, M. Sperling, and W. Buscher, W. *Anal. Bioanal. Chem.*, 2008, **390**, 249.
- H. Nakamuru, T. Shimizu, M. Uehara, Y. Yamaguchi, and H. Maeda, *Mater. Res. Soc., Symp. Proc.*, 2007, **1056**, 11.
- S. Sun and H. Zeng, *J. Am. Chem. Soc.*, 2002, **124**, 8204.
- C. A. Crouse and A. R. Barron, *J. Mater. Chem.*, 2008, **18**, 4146.

[2] http://www.ivstandards.com/extras/pertable/

3.1.2 TGA/DSC-FTIR Characterization of Oxide Nanaoparticles[3]

3.1.2.1 Metal oxide nanoparticles

The binary compound of one or more oxygen atoms with at least one metal atom that forms a structure ≤100 nm is classified as metal oxide (MO_x) nanoparticle. MO_x nanoparticles have exceptional physical and chemical properties (especially if they are smaller than 10 nm) that are strongly related to their dimensions and to their morphology. These enhanced features are due to the increased surface to volume ratio which has a strong impact on the measured binding energies. Based on theoretical models, binding or cohesive energy is inversely related to particle size with a linear relationship (3.27).

$$E_{\mathrm{NP}} = E_{\mathrm{bulk}} \cdot \left[1 - c \cdot r^{-1}\right] \tag{3.27}$$

where E_{NP} *and* E_{bulk} is the binding energy of the nanoparticle and the bulk binding energy respectively, c is a material constant and r is the radius of the cluster. As seen from (3.27), nanoparticles have lower binding energies than bulk material, which means lower electron cloud density and therefore more mobile electrons. This is one of the features that have been identified to contribute to a series of physical and chemical properties.

3.1.2.1.1 Synthesis of metal oxide nanoparticles

Since today, numerous synthetic methods have been developed with the most common ones presented in Table 3.1. These methods have been successfully applied for the synthesis of a variety of materials with 0-D to 3-D complex structures. Among them, the solvothermal methods are by far the most popular ones due to their simplicity. Between the two classes of solvothermal methods, slow decomposition methods, usually called thermal decomposition methods, are preferred over the hot injection methods since they are less complicated, less dangerous and avoid the use of additional solvents.

Method	Characteristics	Advantages	Disadvantages
Solvothermal a) Slow decomposition b) Hot injection	a) Slow heating of M-precursor in the presence of ligand/surfactant precursor b) Injection of M-precursor into solution at high Temp.	a) Safe, easily carried out, variety of M-precursors to use b) Excellent control of particle distribution	a) Poor control of nucleation/ growth stages – Particle size b) Hazardous, Reproducibility depends on individual

continued on next page

[3]This content is available online at <http://cnx.org/content/m23038/1.2/>.

Template directed	Use of organic molecules or preexistent nanoparticles as templates for directing nanoparticle formation	High yield and high purity of nanoparticles	Template removal in some cases causes particle deformation or loss
Sonochemical	Ultrasound influence particle nucleation	Mild synthesis conditions	Limited applicability
Thermal evaporation	Thermal evaporation of Metal oxides	Monodisperse particle formation, excellent control in shape and structure	Extremely high temperatures, and vacuum system is required
Gas phase catalytic growth	Use of catalyst that serves as a preferential site for absorbing Metal reactants	Excellent control in shape and structure	Limited applicability

Table 3.1: Methods for synthesizing MO_x nanoparticles

A general schematic diagram of the stages involving the nanoparticles formation is shown in Figure 3.3. As seen, first step is the M-atom generation by dissociation of the metal-precursor. Next step is the M-complex formulation, which is carried out before the actual particle assembly stage. Between this step and the final particle formulation, oxidation of the activated complex occurs upon interaction with an oxidant substance. The x-axis is a function of temperature or time or both depending on the synthesis procedure.

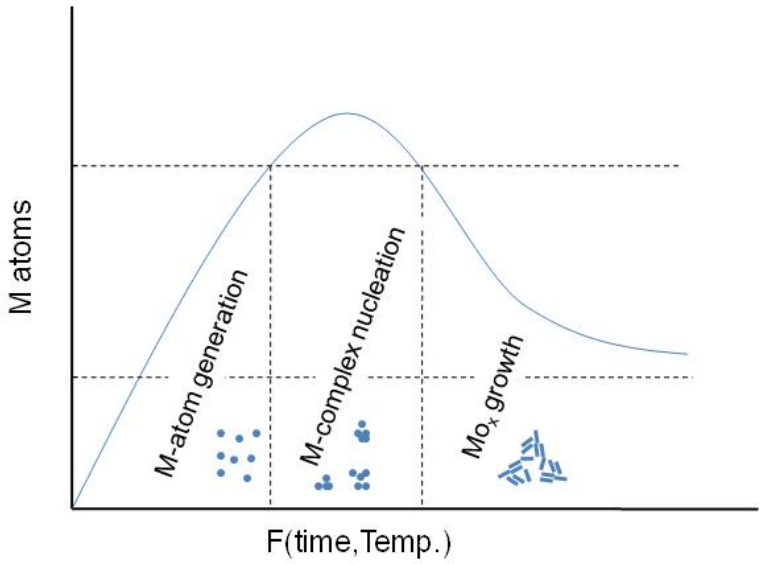

Figure 3.3: Stages of nanoparticle synthesis.

In all cases, the particles synthesized consist of MO_x nanoparticle structures stabilized by one or more types of ligand(s) as seen in Figure 3.4. The ligands are usually long-chained organic molecules that have

one more functional groups. These molecules protect the nanoparticles from attracting each other under van der Waals forces and therefore prevent them from aggregating.

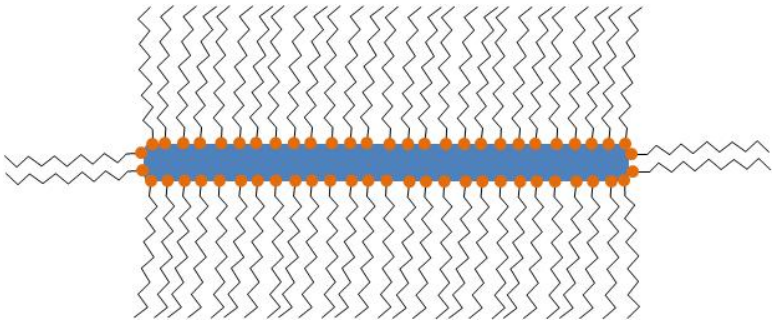

Figure 3.4: Schematic representation of a surfactant/ligand stabilized nanoparticle.

Even though often not referred to specifically, all particles synthesized are stabilized by organic (hydrophilic, hydrophobic or amphoteric) ligands. The detection and the understanding of the structure of these ligands can be of critical importance for understanding the controlling the properties of the synthesized nanoparticles.

3.1.2.1.1.1 Metal oxide nanoparticles synthesized via slow decomposition

In this work, we refer to MO_x nanoparticles synthesized via slow decomposition of a metal complex. In Table 3.2, a number of different MO_x nanoparticles are presented, synthesized via metal complex dissociation. Metal–MO_x and mixed MO_x nanoparticles are not discussed here.

Metal oxide	**Shape**	**Size (approx.)**
Cerium oxide	dots	5-20 nm
Iron oxide	dots, cubes	8.5-23.4 nm
Manganese oxide	Multipods	>50 nm
Zinc oxide	Hexagonal pyramid	15-25 nm
Cobalt oxide	dots	$\sim$ 10 nm
Chromium oxide	dots	12 nm
Vanadium oxide	dots	9-15 nm
Molybdenum oxide	dots	5 nm
Rhodium oxide	dots,rods	16 nm
Palladium oxide	dots	18 nm
Ruthenium oxide	dots	9-14 nm
Zirconium oxide	rods	7x30 nm
Barium oxide	dots	20 nm
Magnesium oxide	dots	4-8 nm
Calcium oxide	dots, rods	7-12 nm
Nickel oxide	dots	8-15 nm
Titanium oxide	dots and rods	2.3-30 nm
Tin oxide	dots	2.0-5.0 nm
Indium oxide	dots	$\sim$ 5 nm
Samaria	Square	$\sim$ 10 nm

Table 3.2: Examples of MO_x nanoparticles synthesized via decomposition of metal complexes.

A significant number of metal oxides synthesized using slow decomposition is reported in literature. If we use the periodic table to map the different MO_x nanoparticles (Figure 3.5), we notice that most of the alkali and transition metals generate MO_x nanoparticles, while only a few of the poor metals seem to do so, using this synthetic route. Moreover, two of the rare earth metals (Ce and Sm) have been reported to successfully give metal oxide nanoparticles via slow decomposition.

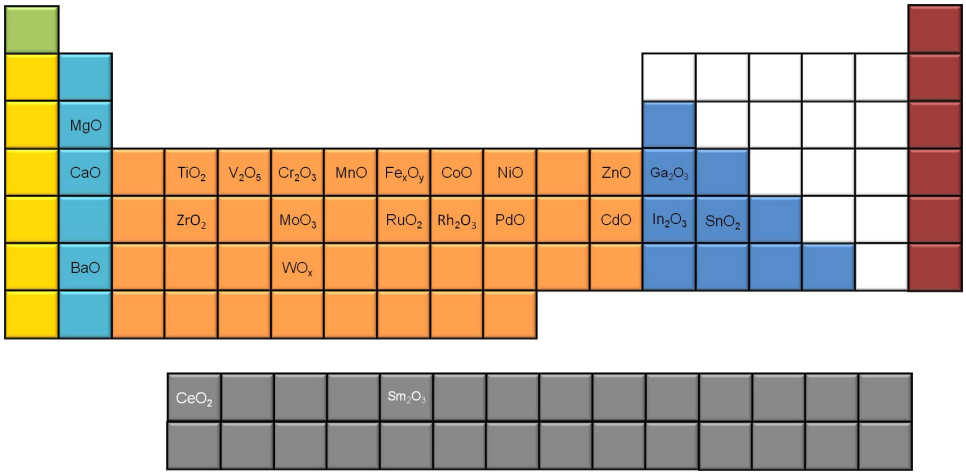

Figure 3.5: "Periodic" table of MO_x nanoparticles synthesized using the slow decomposition technique.

Among the different characterization techniques used for defining these structures, transition electron microscopy (TEM) holds the lion's share. Nevertheless, most of the modern characterization methods are more important when it comes to understanding the properties of nanoparticles. X-ray photoelectron spectroscopy (XPS), X-ray diffraction (XRD), nuclear magnetic resonance (NMR), IR spectroscopy, Raman spectroscopy, and thermogravimetric analysis (TGA) methods are systematically used for characterization.

3.1.2.1.2 Synthesis and characterization of WO_{3-x} nanorods

The synthesis of WO_{3-x} nanorods is based on the method published by Lee et al. A slurry mixture of $Me_3NO \bullet 2H_2O$, oleylamine and $W(CO)_6$ was heated up to 250 °C at a rate of 3 °C/min (Figure 3.6). The mixture was aged at this temperature for 3 hours before cooling down to room temperature.

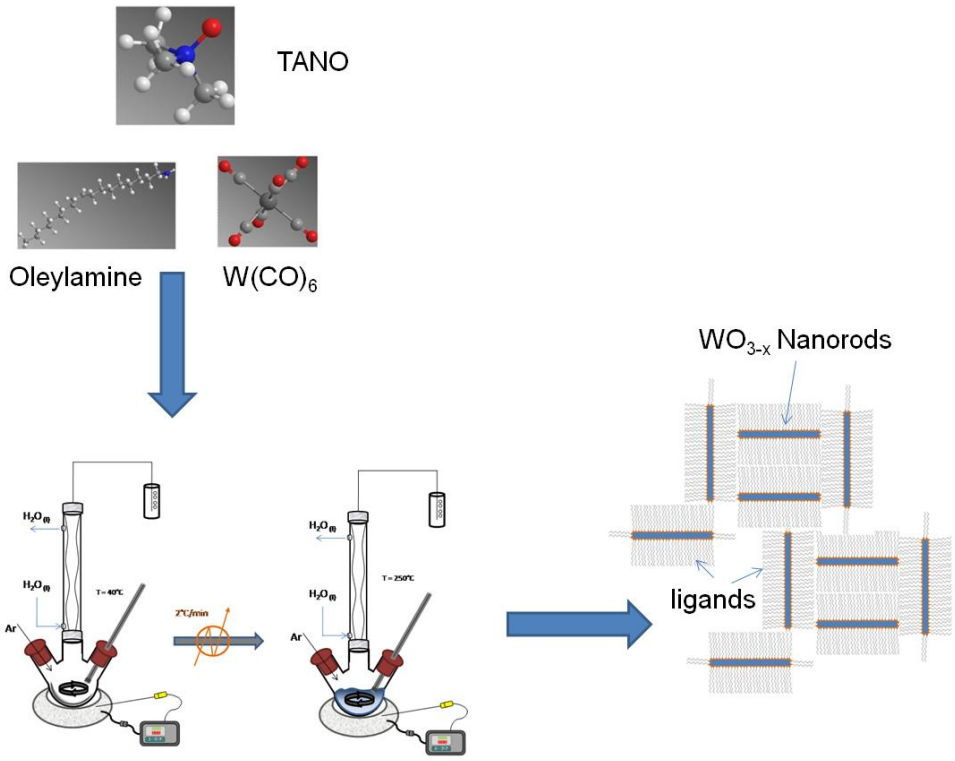

Figure 3.6: Experimental setup for synthesis of WO_{3-x} nanorods.

Multiple color variations were observed between 100 - 250 °C with the final product having a dark blue color. Tungsten oxide nanorods ($W_{18}O_{49}$ identified by XRD) with a diameter of 7±2 nm and 50±2 nm long were acquired after centrifugation of the product solution. A TEM image of the $W_{18}O_{49}$ nanorods is shown in Figure 3.7.

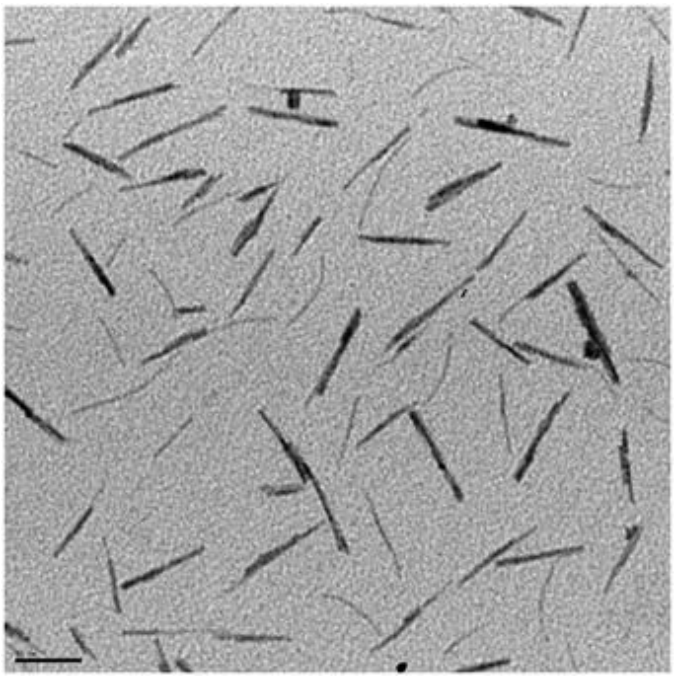

Figure 3.7: TEM image of WO_{3-x} nanorods.

3.1.2.2 Thermogravimetric analysis (TGA)/differential scanning calorimetry (DSC)

Thermogravimetric analysis (TGA) is a technique widely used for determining the organic and inorganic content of various materials. Its basic rule of function is the high precision measurement of weight gain/loss with increasing temperature under inert or reactive atmospheres. Each weight change corresponds to physical (crystallization, phase transformation) or chemical (oxidation, reduction, reaction) processes that take place by increasing the temperature. The sample is placed into platinum or alumina pan and along with an empty or standard pan are placed onto two high precision balances inside a high temperature oven. A method for pretreating the samples is selected and the procedure is initiated. Differential scanning calorimetry (DSC) is a technique usually accompanying TGA and is used for calculating enthalpy energy changes or heat capacity changes associated with phase transitions and/or ligand-binding energy cleavage.

In Figure 3.8 the TGA/DSC plot acquired for the ligand decomposition of WO_{3-x} nanorods is presented. The sample was heated at constant rate under N_2 atmosphere up to 195 °C for removing moisture and then up to 700 °C for removing the oleylamine ligands. It is important to use an inert gas for performing such a study to avoid any premature oxidation and/or capping agent combustion. 26.5% of the weight loss is due to oleylamine evaporations which means about 0.004 moles per gram of sample. After isothermal heating at 700 °C for 25 min the flow was switched to air for oxidizing the ligand-free WO_{3-x} to WO_3. From the DSC curve we noticed the following changes of the weight corrected heat flow:

1. From 0 – 10 min assigned to water evaporation.
2. From 65 – 75 min assigned to OA evaporation.
3. From 155 – 164 min assigned to WO_{3-x} oxidation.
4. From 168 – 175 min is also due to further oxidation of W^{5+} atoms.

The heat flow increase during the WO_{3-x} to WO_3 oxidation is proportional to the crystal phase defects (or W atoms of oxidation state +5) and can be used for performing qualitative studies between different WO_x nanoparticles.

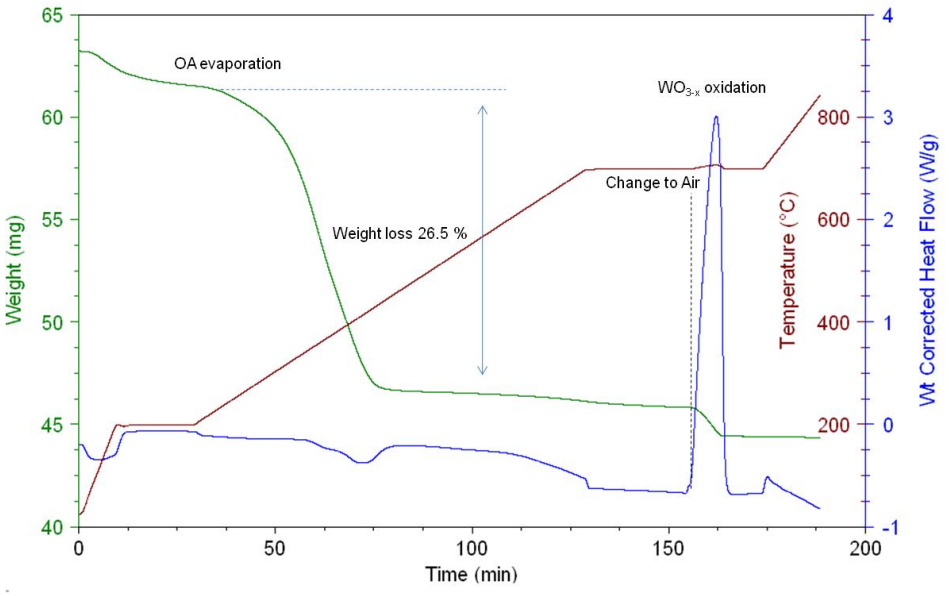

Figure 3.8: TGA/DSC plot for WO_{3-x} nanorods.

The detailed information about the procedure used to acquire the TGA/DSC plot shown in Figure 3.8 is as follows.

Step 1. Select gas (N_2 with flow rate 50 mL/min.)
Step 2. Ramp 20 °C/min to 200 °C.
Step 3. Isothermal for 20 min.
Step 4. Ramp 5 °C/min to 700 °C.
Step 5. Isothermal for 25 min.
Step 6. Select gas (air).
Step 7. Isothermal for 20 min.
Step 8. Ramp 10 °C/min to 850 °C.
Step 9. Cool down

3.1.2.3 Fourier transform infrared spectroscopy

Fourier transform infrared spectroscopy (FTIR) is the most popular spectroscopic method used for characterizing organic and inorganic compounds. The basic modification of an FTIR from a regular IR instrument is a device called interferometer, which generates a signal that allows very fast IR spectrum acquisition. For doing so, the generatated interferogram has to be "expanded" using a Fourier transformation to generate a

complete IR frequency spectrum. In the case of performing FTIR transmission studies the intensity of the transmitted signal is measured and the IR fingerprint is generated (3.28).

$$T = \frac{I}{I_b} = e^{c\varepsilon l} \tag{3.28}$$

Where I is the intensity of the samples, I_b is the intensity of the background, c is the concentration of the compound, ε is the molar extinction coefficient and l is the distance that light travels through the material. A transformation of transmission to absorption spectra is usually performed and the actual concentration of the component can be calculated by applying the Beer-Lambert law (3.29).

$$A = -\ln(T) = c\varepsilon l \tag{3.29}$$

A qualitative IR-band map is presented in Figure 3.9. The absorption bands between 4000 to 1600 cm^{-1} represent the group frequency region and are used to identify the stretching vibrations of different bonds. At lower frequencies (from 1600 to 400 cm^{-1}) vibrations due to intermolecular bond bending occurs upon IR excitation and therefore are usually not taken into account.

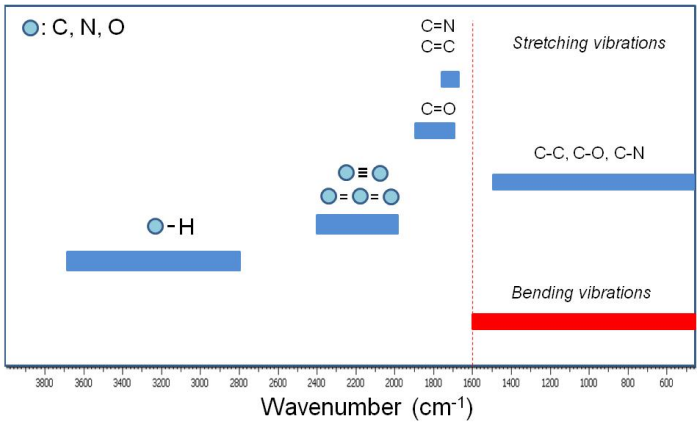

Figure 3.9: Selected FTIR stretching and bending modes associated with the typical ligands used for nanoparticle stabilization.

3.1.2.4 TGA/DSC–FTIR characterization

TGA/DSC is a powerful tool for identifying the different compounds evolved during the controlled pyrolysis and therefore provide qualitative and quantitative information about the volatile components of the sample. In metal oxide nanoparticle synthesis TGA/DSC-FTIR studies can provide qualitative and quantitative information about the volatile compounds of the nanoparticles.

TGA–FTIR results presented below were acquired using a Q600 Simultaneous TGA/DSC (SDT) instrument online with a Nicolet 5700 FTIR spectrometer. This system has a digital mass flow control and two gas inlets giving the capability to switch reacting gas during each run. It allows simultaneous weight change and differential heat flow measurements up to 1500 °C, while at the same time the outflow line is connected to the FTIR for performing gas phase compound identification. Grand-Schmidt thermographs were usually constructed to present the species evolution with time in 3 dimensions.

Selected IR spectra are presented in Figure 3.10. Four regions with intense peaks are observed. Between 4000 – 3550 cm^{-1} due to O-H bond stretching assigned to H_2O that is always present and due to due to N-H group stretching that is assigned to the amine group of oleylamine. Between 2400 – 2250 cm^{-1} due to O=C=O stretching, between 1900 – 1400 cm^{-1} which is mainly to C=O stretching and between 800 – 400 cm^{-1} cannot be resolved as explained previously.

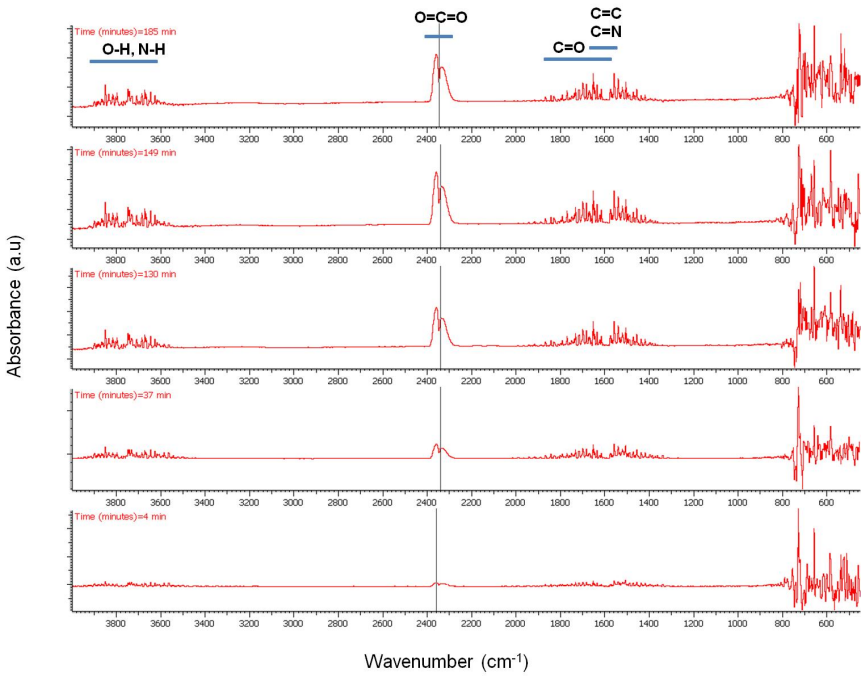

Figure 3.10: FTIR spectra of products from WO_{3-x} pyrolysis.

The peak intensity evolution with time can be more easily observed in Figure 3.11 and Figure 3.12. As seen, CO_2 evolution increases significantly with time especially after switching our flow from N_2 to air. H_2O seems to be present in the outflow stream up to 700 °C while the majority of the N-H amine peaks seem to disappear at about 75 min. C=N compounds are not expected to be present in the stream which leaves bands between 1900 – 1400 cm^{-1} assigned to C=C and C=O stretching vibrations. Unsaturated olefins resulting from the cracking of the oleylamine molecule are possible at elevated temperatures as well as the presence of CO especially under N_2 atmosphere.

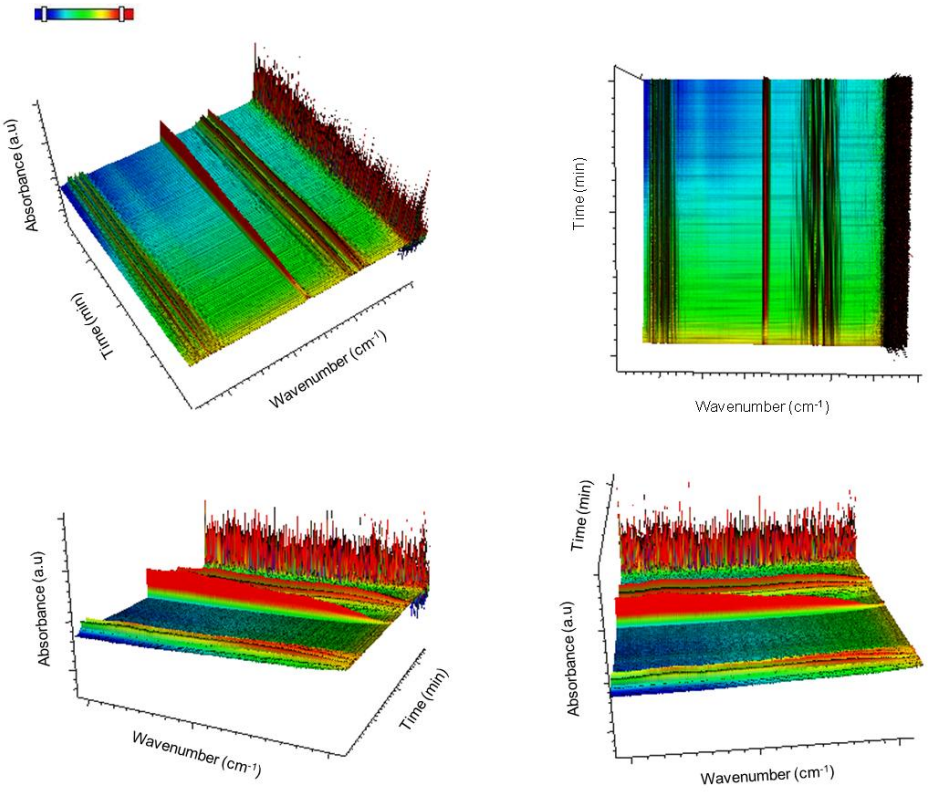

Figure 3.11: 3D representation of FTIR Spectra of the volatile compounds of WO_{3-x}.

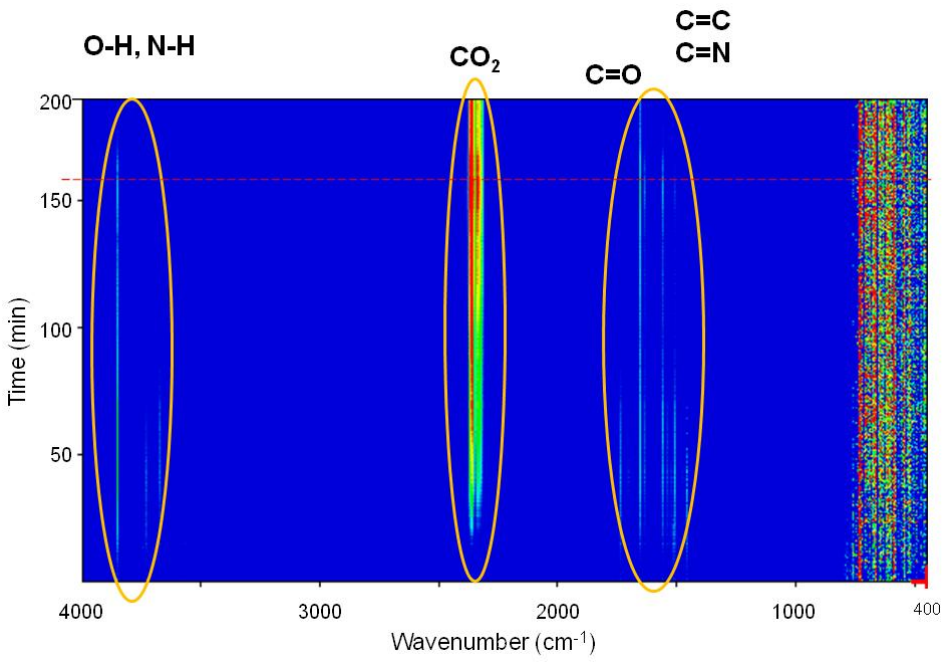

Figure 3.12: Intensity profile of FTIR spectra of the volatile compounds formed from the pyrolysis of WO_{3-x}.

From the above compound identification we can summarize and propose the following applications for TGA-FTIR. First, more complex ligands, containing aromatic rings and maybe other functional groups may provide more insight in the ligand to MO_x interaction. Second, the presence of CO and CO_2 even under N_2 flow means that complete O_2 removal from the TGA and the FTIR cannot be achieved under these conditions. Even though the system was equilibrated for more than an hour, traces of O_2 are existent which create errors in our calculations.

3.1.2.5 Bibliography

- R. D. Parra and H. H. Farrell, *J. Phys. Chem. C*, 2009, **113**, 4786.
- S. C. Vanithakumari and K. K. Nanda, *J. Phys. Chem. B*, 2006, **110**, 6985.
- M. Wautelet and D. Duvivier, *Eur. J. Phys.*, 2007, **28**, 953.
- X. Wang and Y. Li, *J. Am. Chem. Soc.*, 2002, **124**, 2880.
- F. K. R. N. Greta and R. Patzke, *Angew. Chem., Int. Ed.*, 2002, **41**, 2446.
- Z. W. Pan, Z. R. Dai, and Z. L. Wang, *Science*, 2001, **291**, 1947.
- H. Gu and M. D. Soucek, *Chem. Mater.*, 2007, **19**, 1103.
- L. M. Bronstein, X. Huang, J. Retrum, A. Schmucker, M. Pink, B. D. Stein, and B. Dragnea, *Chem. Mater.*, 2007, **19**, 3624.
- D. Zitoun, N. Pinna, N. Frolet, and C. Belin, *J. Am. Chem. Soc.*, 2005, **127**, 15034.
- S. -H. Choi, E. -G. Kim, J. Park, K. An, N. Lee, S. C. Kim, and T. Hyeon, *J. Phys. Chem., B*, 2005, **109**, 14792.
- M. Epifani, J. Arbiol, R. Diaz, M. J. Peralvarez, P. Siciliano, and J. R. Morante, *Chem. Mater.*, 2005, **17**, 6468.

- T. Yu, J. Joo, Y. I. Park, and T. Hyeon, *J. Am. Chem. Soc.*, 2006, **128**, 1786.
- K. Lee, W. S. Seo, and J. T. Park, *J. Am. Chem. Soc.*, 2003, **125**, 3408.
- C. A. Emeis, *J. Catalysis*, 1993, **141**, 347.
- P. R. Griffiths, J. A. De Haseth, *Fourier Transform Infrared Spectrometry*. Wiley-Interscience, New York (2007)

3.1.3 Thermogravimetric Analysis of Single Walled Carbon Nanotubes[4]

Thermogravimetric analysis (TGA) and the associated differential thermal analysis (DTA) are widely used for the characterization of both as-synthesized and side-wall functionalized single walled carbon nanotubes (SWNTs). Under oxygen, SWNTs will pyrolyze leaving any inorganic residue behind. In contrast in an inert atmosphere since most functional groups are labile or decompose upon heating and as SWNTs are stable up to 1200 °C, any weight loss before 800 °C is used to determine the functionalization ratio of side-wall functionalized SWNTs. The following properties of SWNTs can be determined using this TGA;

1. The mass of metal catalyst impurity in as synthesized SWNTs.
2. The number of functional groups per SWNT carbon (C_{SWNT}).
3. The mass of a reactive species absorbed by a functional group on a SWNT.

Quantitative determination of these properties are used to define the purity of SWNTs, and the extent of their functionalization.

3.1.3.1 An overview of thermogravimetric analysis

The main function of TGA is the monitoring of the thermal stability of a material by recording the change in mass of the sample with respect to temperature. Figure 3.13 shows a simple diagram of the inside of a typical TGA.

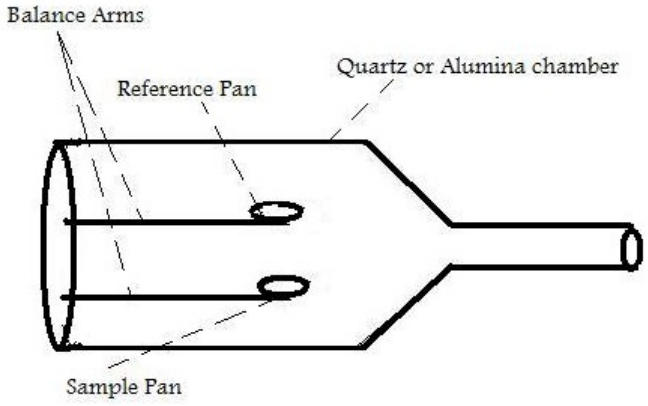

Figure 3.13: Schematic representation of a TGA apparatus.

Inside the TGA, there are two pans, a reference pan and a sample pan. The pan material can be either aluminium or platinum. The type of pan used depends on the maximum temperature of a given run. As

[4]This content is available online at <http://cnx.org/content/m22972/1.2/>.

platinum melts at 1760 °C and alumium melts at 660 °C, platinum pans are chosen when the maximum temperature exceeds 660 °C. Under each pan there is a thermocouple which reads the temperature of the pan. Before the start of each run, each pan is balanced on a balance arm. The balance arms should be calibrated to compensate for the differential thermal expansion between the arms. If the arms are not calibrated, the instrument will only record the temperature at which an event occurred and not the change in mass at a certain time. To calibrate the system, the empty pans are placed on the balance arms and the pans are weighed and zeroed.

As well as recording the change in mass, the heat flow into the sample pan (differential scanning calorimetry, DSC) can also be measured and the difference in temperature between the sample and reference pan (differential thermal analysis, DTA). DSC is quantitative and is a measure of the total energy of the system. This is used to monitor the energy released and absorbed during a chemical reaction for a changing temperature. The DTA shows if and how the sample phase changed. If the DTA is constant, this means that there was no phase change. Figure 3.14 shows a DTA with typical examples of an exotherm and an endotherm.

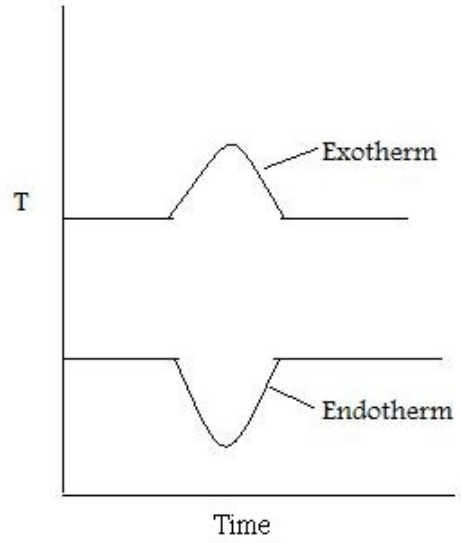

Figure 3.14: Simplified representation of the DTA for an exotherm and an endotherm.

When the sample melts, the DTA dips which signifies an endotherm. When the sample is melting it requires energy from the system. Therefore the temperature of the sample pan decreases compared with the temperature of the reference pan. When the sample has melted, the temperature of the sample pan increases as the sample is releasing energy. Finally the temperatures of the reference and sample pans equilibrate resulting in a constant DTA. When the sample evaporates, there is a peak in the DTA. This exotherm can be explained in the same way as the endotherm.

Typically the sample mass range should be between 0.1 to 10 mg and the heating rate should be 3 to 5 °C/min.

3.1.3.2 Determination of the mass of iron catalyst impurity in HiPCO SWNTs.

SWNTs are typically synthesized using metal catalysts. Those prepared using the HiPco method, contain residual Fe catalyst. The metal (i.e., Fe) is usually oxidized upon exposure to air to the appropriate oxide

(i.e., Fe_2O_3). While it is sometimes unimportant that traces of metal oxide are present during subsequent applications it is often necessary to quantify their presence. This is particularly true if the SWNTs are to be used for cell studies since it has been shown that the catalyst residue is often responsible for observed cellular toxicity.

In order to calculate the mass of catalyst residue the SWNTs are pyrolyzed under air or O_2, and the residue is assumed to be the oxide of the metal catalyst. Water can be added to the raw SWNTs, which enhances the low-temperature catalytic oxidation of carbon. A typical TGA plot of a sample of raw HiPco SWNTs is shown in Figure 3.15.

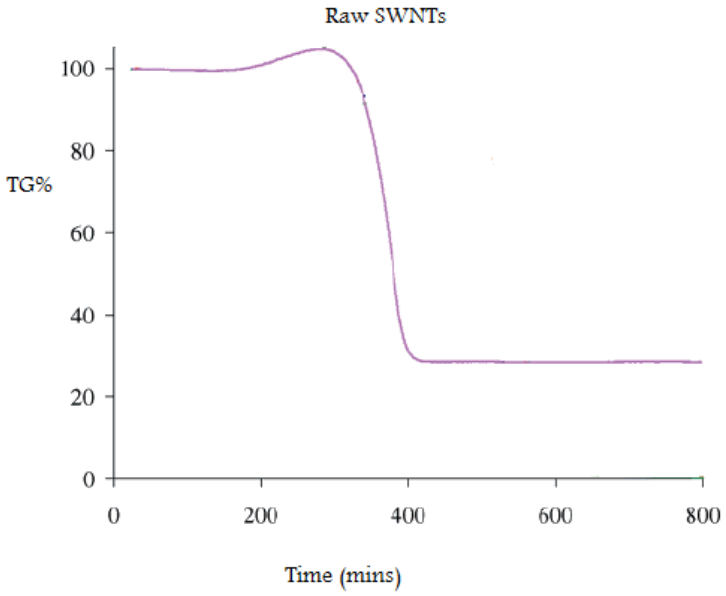

Figure 3.15: The TGA of unpurified HiPco SWNTs under air showing the residual mass associated with the iron catalyst. Adapted from I. W. Chiang, B. E. Brinson, A. Y. Huang, P. A. Willis, M. J. Bronikowski, J. L. Margrave, R. E. Smalley, and R. H. Hauge, *J. Phys. Chem. B*, 2001, **105**, 8297. Adapted from Chiang et al, 2001

The weight gain (of ca. 5%) at 300 °C is due to the formation of metal oxide from the incompletely oxidized catalyst. To determine the mass of iron catalyst impurity in the SWNT, the residual mass must be calculated. The residual mass is the mass that is left in the sample pan at the end of the experiment. From this TGA diagram, it is seen that 70% of the total mass is lost at 400 °C. This mass loss is attributed to the removal of carbon. The residual mass is 30%. Given that this is due to both oxide and oxidized metal, the original total mass of residual catalyst in raw HiPCO SWNTs is ca. 25%.

3.1.3.3 Determining the number of functional groups on SWNTs

The limitation of using SWNTs in any practical applications is their solubility; for example SWNTs have little to no solubility in most solvents due to aggregation of the tubes. Aggregation/roping of nanotubes occurs as a result of the high van der Waals binding energy of ca. 500 eV per μm of tube contact. The van der Waals force between the tubes is so great, that it take tremendous energy to pry them apart, making

it very difficult to make combination of nanotubes with other materials such as in composite applications. The functionalization of nanotubes, i.e., the attachment of "chemical functional groups", provides the path to overcome these barriers. Functionalization can improve solubility as well as processability, and has been used to align the properties of nanotubes to those of other materials. In this regard, covalent functionalization provides a higher degree of fine-tuning for the chemical and physical properties of SWNTs than non-covalent functionalization.

Functionalized nanotubes can be characterized by a variety of techniques, such as atomic force microscopy (AFM), transmission electron microscopy (TEM), UV-vis spectroscopy, and Raman spectroscopy, however, the quantification of the extent of functionalization is important and can be determined using TGA. Because any sample of functionalized-SWNTs will have individual tubes of different lengths (and diameters) it is impossible to determine the number of substituents per SWNT. Instead the extent of functionalization is expressed as number of substituents per SWNT carbon atom (C_{SWNT}), or more often as C_{SWNT}/substituent, since this is then represented as a number greater than 1.

Figure 3.16 shows a typical TGA for a functionalized SWNT. In this case it is polyethyleneimine (PEI) functionalized SWNTs prepared by the reaction of fluorinated SWNTs (F-SWNTs) with PEI in the presence of a base catalyst.

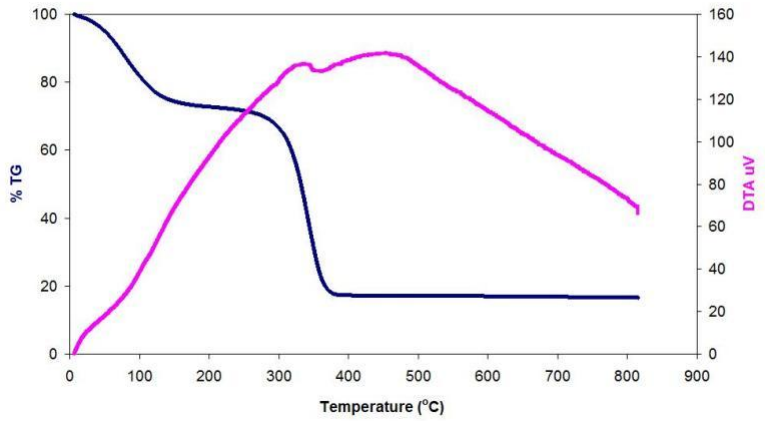

Figure 3.16: The TGA of SWNTs functionalized with polyethyleimine (PEI) under air showing the sequential loss of complexed CO_2 and decomposition of PEI.

In the present case the molecular weight of the PEI is 600 g/mol. When the sample is heated, the PEI thermally decomposes leaving behind the unfunctionalized SWNTs. The initial mass loss below 100 °C is due to residual water and ethanol used to wash the sample.

In the following example the total mass of the sample is 25 mg.

Step 1. The initial mass, M_i = 25 mg = mass of the SWNTs, residues and the PEI.
Step 2. After the initial moisture has evaporated there is 68% of the sample left. 68% of 25 mg is 17 mg. This is the mass of the PEI and the SWNTs.
Step 3. At 300 °C the PEI starts to decompose and all of the PEI has been removed from the SWNTs at 370 °C. The mass loss during this time is 53% of the total mass of the sample. 53% of 25 mg is 13.25 mg.
Step 4. The molecular weight of this PEI is 600 g/mol. Therefore there is 0.013 g / 600 g/mol = 0.022 mmole of PEI in the sample.

Step 5. 15% of the sample is the residual mass, this is the mass of the decomposed SWNTs. 15% of 25 mg is 3.75 mg. The molecular weight of carbon is 12 g/mol. So there is 0.3125 mmole of carbon in the sample.
Step 6. There is 93.4 mol% of carbon and 6.5 mol% of PEI in the sample.

3.1.3.4 Determination of the mass of a chemical absorbed by functionalized SWNTs

Solid-state ^{13}C NMR of PEI-SWNTs shows the presence of carboxylate substituents that can be attributed to carbamate formation as a consequence of the reversable CO_2 absorption to the primary amine substituents of the PEI. Desorption of CO_2 is accomplished by heating under argon at 75 °C.

The quantity of CO_2 absorbed per PEI-SWNT unit may be determined by initially exposing the PEI-SWNT to a CO_2 atmosphere to maximize absorption. The gas flow is switched to either Ar or N_2 and the sample heated to liberate the absorbed CO_2 without decomposing the PEI or the SWNTs. An example of the appropriate TGA plot is shown in Figure 3.17.

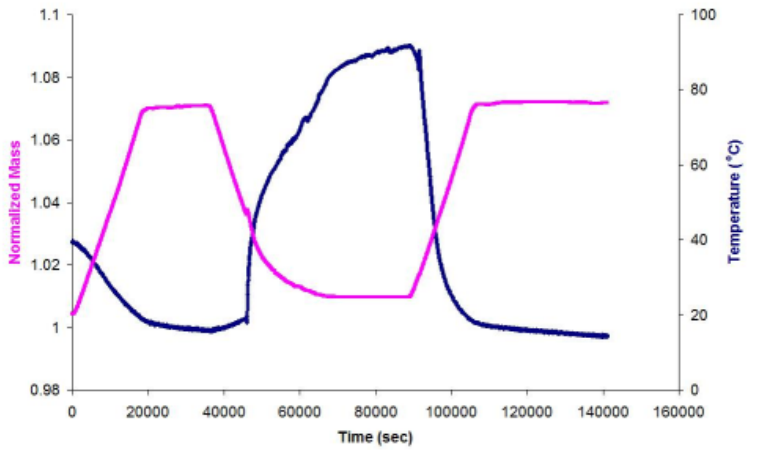

Figure 3.17: The TGA results of PEI(10000)-SWNT absorbing and desorbing CO_2. The mass has been normalized to the lowest mass recorded, which is equivalent to PEI(10000)-SWNT.

The sample was heated to 75 °C under Ar, and an initial mass loss due to moisture and/or atmospherically absorbed CO_2 is seen. In the temperature range of 25 °C to 75 °C the flow gas was switched from an inert gas to CO_2. In this region an increase in mass is seen, the increase is due to CO_2 absorption by the PEI (10000Da)-SWNT. Switching the carrier gas back to Ar resulted in the desorption of the CO_2.

The total normalized mass of CO_2 absorbed by the PEI(10000)-SWNT can be calculated as follows;

Solution Outline

Step 1. Minimum mass = mass of absorbant = $M_{absorbant}$
Step 2. Maximum mass = mass of absorbant and absorbed species = M_{total}
Step 3. Absorbed mass = $M_{absorbed}$ = M_{total} - $M_{absorbant}$
Step 4. % of absorbed species= ($M_{absorbed}$/$M_{absorbant}$)*100
Step 5. 1 mole of absorbed species = MW of absorbed species
Step 6. Number of moles of absorbed species = ($M_{absorbed}$/MW of absorbed species)

Step 7. The number of moles of absorbed species absorbed per gram of absorbant= ($1g/M_{total}$)*(Number of moles of absorbed species)

Solution

Step 1. $M_{absorbant}$ = Mass of PEI-SWNT = 4.829 mg
Step 2. M_{total} = Mass of PEI-SWNT and CO_2 = 5.258 mg
Step 3. $M_{absorbed}$ = M_{total} - $M_{absorbant}$ = 5.258 mg - 4.829 mg = 0.429 mg
Step 4. % of absorbed species= % of CO_2 absorbed = ($M_{absorbed}/M_{absorbant}$)*100 = (0.429/4.829)*100 = 8.8%
Step 5. 1 mole of absorbed species = MW of absorbed species = MW of CO_2 = 44 therefore 1 mole = 44g
Step 6. Number of moles of absorbed species = ($M_{absorbed}$/MW of absorbed species)= (0.429 mg / 44 g) = 9.75 μM
Step 7. The number of moles of absorbed species absorbed per gram of absorbant =(1 g/M_{total})*(Number of moles of absorbed species) = (1 g/5.258 mg)*(9.75)= 1.85 mmol of CO_2 absorbed per gram of absorbant

3.1.3.5 Bibliography

- I. W. Chiang, B. E. Brinson, A. Y. Huang, P. A. Willis, M. J. Bronikowski, J. L. Margrave, R. E. Smalley, and R. H. Hauge, *J. Phys. Chem. B*, 2001, **105**, 8297.
- E. P. Dillon, C. A. Crouse and A. R. Barron, *ACS Nano*, 2008, **2**, 156.

3.1.4 BET Surface Area Analysis of Nanoparticles[5]

3.1.4.1 Introduction

In the past few years, nanotechnology research has expanded out of the chemistry department and into the fields of medicine, energy, aerospace and even computing and information technology. With bulk materials, the surface area to volume is insignificant in relation to the number of atoms in the bulk, however when the particles are only 1 to 100 nm across, different properties begin to arise. For example, commercial grade zinc oxide has a surface area range of 2.5 to 12 m^2/g while nanoparticle zinc oxide can have surface areas as high as 54 m^2/g . The nanoparticles have superior UV blocking properties when compared to the bulk material, making them useful in applications such as sunscreen. Many useful properties of nanoparticles rise from their small size, making it very important to be able to determine their surface area.

3.1.4.2 Overview of BET theory

The BET theory was developed by Stephen Brunauer (Figure 3.18), Paul Emmett (Figure 3.19), and Edward Teller (Figure 3.20) in 1938. The first letter of each publisher's surname was taken to name this theory. The BET theory was an extension of the Langmuir theory, developed by Irving Langmuir (Figure 3.21) in 1916.

[5]This content is available online at <http://cnx.org/content/m38278/1.1/>.

Figure 3.18: Hungarian chemist Stephen Brunauer (1903-1986). Adapted from K. S. Sing, Langmuir, 1987, **3**, 2 (Copyright: American Chemical Society).

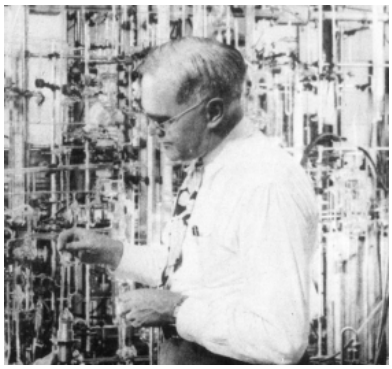

Figure 3.19: American chemical engineer Paul H. Emmett (1900 - 1985). Adapted from B.H. Davis, J. Phys. Chem., 1986, **90**, 4702 (Copyright: American Chemical Society).

Figure 3.20: Hungarian born theoretical physicist Edward Teller (1908 – 2003) shown in 1958 as the director of Lawrence Livermore National Laboratory was known as "the father of the hydrogen bomb".

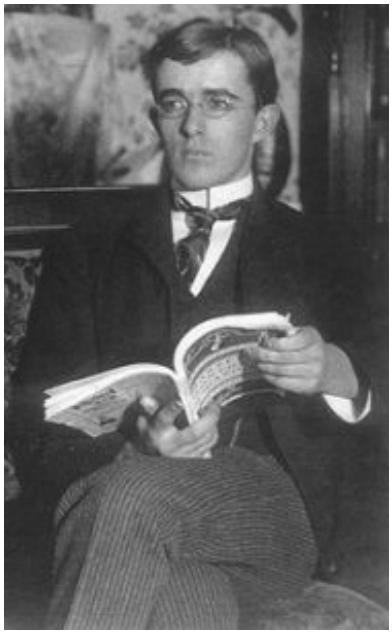

Figure 3.21: American chemist and physicist Irving Langmuir (1881 - 1957). Adapted from *J. Chem. Educ.*, 1933, **10**, 65 (Copyright: American Chemical Society).

The Langmuir theory relates the monolayer adsorption of gas molecules (Figure 3.22), also called adsorbates, onto a solid surface to the gas pressure of a medium above the solid surface at a fixed temperature to

(3.30), where θ is the fractional cover of the surface, P is the gas pressure and α is a constant.

$$\theta = \frac{\alpha \,.\, P}{1 + (\alpha \,.\, P)} \tag{3.30}$$

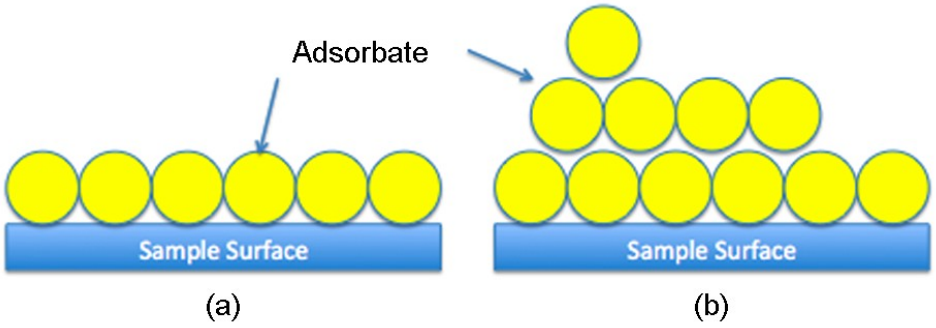

Figure 3.22: Schematic of the adsorption of gas molecules onto the surface of a sample showing (a) the monolayer adsorption model assumed by the Langmuir theory and (b) s the multilayer adsorption model assumed by the BET theory.

The Langmuir theory is based on the following assumptions:

- All surface sites have the same adsorption energy for the adsorbate, which is usually argon, krypton or nitrogen gas. The surface site is defined as the area on the sample where one molecule can adsorb onto.
- Adsorption of the solvent at one site occurs independently of adsorption at neighboring sites.
- Activity of adsorbate is directly proportional to its concentration.
- Adsorbates form a monolayer.
- Each active site can be occupied only by one particle.

The Langmuir theory has a few flaws that are addressed by the BET theory. The BET theory extends the Langmuir theory to multilayer adsorption (Figure 3.22) with three additional assumptions:

- Gas molecules will physically adsorb on a solid in layers infinitely.
- The different adsorption layers do not interact.
- The theory can be applied to each layer.

3.1.4.3 How does BET work?

Adsorption is defined as the adhesion of atoms or molecules of gas to a surface. It should be noted that adsorption is not confused with absorption, in which a fluid permeates a liquid or solid. The amount of gas adsorbed depends on the exposed surface are but also on the temperature, gas pressure and strength of interaction between the gas and solid. In BET surface area analysis, nitrogen is usually used because of its availability in high purity and its strong interaction with most solids. Because the interaction between gaseous and solid phases is usually weak, the surface is cooled using liquid N_2 to obtain detectable amounts of adsorption. Known amounts of nitrogen gas are then released stepwise into the sample cell. Relative

pressures less than atmospheric pressure is achieved by creating conditions of partial vacuum. After the saturation pressure, no more adsorption occurs regardless of any further increase in pressure. Highly precise and accurate pressure transducers monitor the pressure changes due to the adsorption process. After the adsorption layers are formed, the sample is removed from the nitrogen atmosphere and heated to cause the adsorbed nitrogen to be released from the material and quantified. The data collected is displayed in the form of a BET isotherm, which plots the amount of gas adsorbed as a function of the relative pressure. There are five types of adsorption isotherms possible.

3.1.4.3.1 Type I isotherm

Type I is a pseudo-Langmuir isotherm because it depicts monolayer adsorption (Figure 3.23). A type I isotherm is obtained when $P/P_o < 1$ and $c > 1$ in the BET equation, where P/P_o is the partial pressure value and c is the BET constant, which is related to the adsorption energy of the first monolayer and varies from solid to solid. The characterization of microporous materials, those with pore diameters less than 2 nm, gives this type of isotherm.

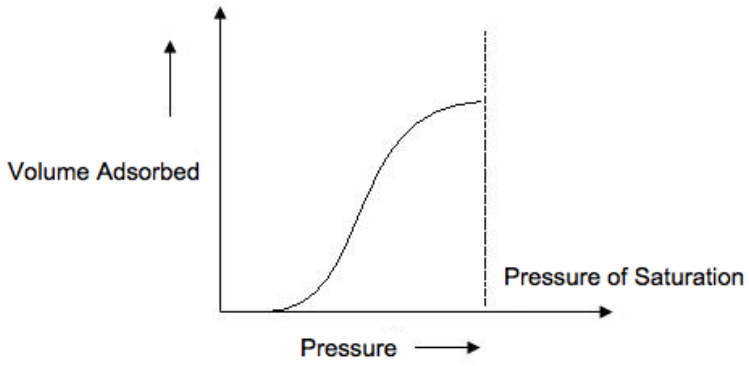

Figure 3.23: The isotherm plots the volume of gas adsorbed onto the surface of the sample as pressure increases. Adapted from S. Brunauer L. S. Deming, W. E. Deming, and E. Teller, *J. Am. Chem. Soc.*, 1940, **62**, 1723.

3.1.4.3.2 Type II isotherm

A type II isotherm (Figure 3.24) is very different than the Langmuir model. The flatter region in the middle represents the formation of a monolayer. A type II isotherm is obtained when $c > 1$ in the BET equation. This is the most common isotherm obtained when using the BET technique. At very low pressures, the micropores fill with nitrogen gas. At the knee, monolayer formation is beginning and multilayer formation occurs at medium pressure. At the higher pressures, capillary condensation occurs.

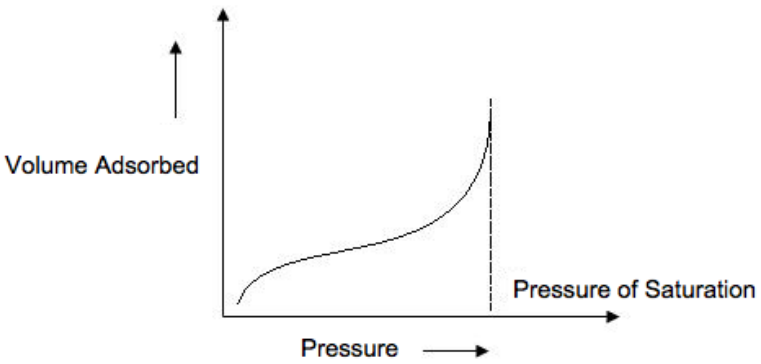

Figure 3.24: The isotherm plots the volume of gas adsorbed onto the surface of the sample as pressure increases. Adapted from S. Brunauer, L. S. Deming, W. E. Deming, and E. Teller, *J. Am. Chem. Soc.*, 1940, **62**, 1723.

3.1.4.3.3 Type III isotherm

A type III isotherm (Figure 3.25) is obtained when the c $<$ 1 and shows the formation of a multilayer. Because there is no asymptote in the curve, no monolayer is formed and BET is not applicable.

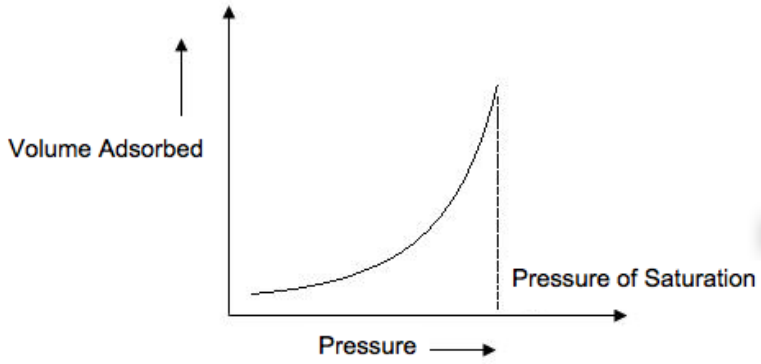

Figure 3.25: Brunauer, L. S. Deming, W. E. Deming, and E. Teller, *J. Am. Chem. Soc.*, 1940, *62*, 1723.

3.1.4.3.4 Type IV isotherm

Type IV isotherms (Figure 3.26) occur when capillary condensation occurs. Gases condense in the tiny capillary pores of the solid at pressures below the saturation pressure of the gas. At the lower pressure regions, it shows the formation of a monolayer followed by a formation of multilayers. BET surface area characterization of mesoporous materials, which are materials with pore diameters between 2 - 50 nm, gives this type of isotherm.

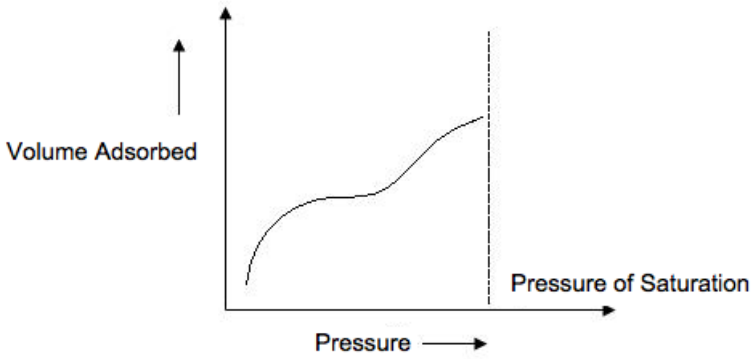

Figure 3.26: Brunauer, L. S. Deming, W. E. Deming, and E. Teller, *J. Am. Chem. Soc.*, 1940, *62*, 1723.

3.1.4.3.5 Type V isotherm

Type V isotherms (Figure 3.27) are very similar to type IV isotherms and are not applicable to BET.

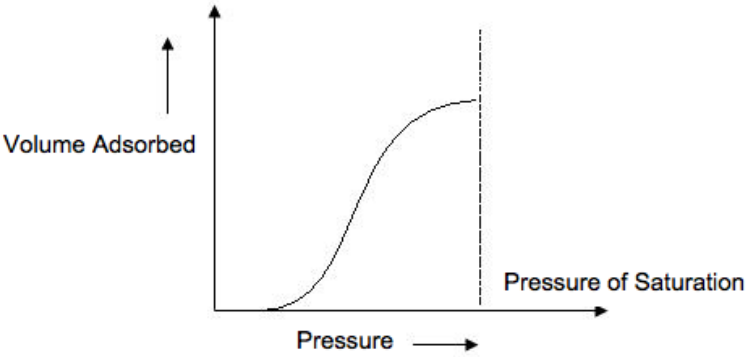

Figure 3.27: Brunauer L. S. Deming, W. E. Deming, and E. Teller, *J. Am. Chem. Soc.*, 1940, **62**, 1723.

3.1.4.4 Calculations

The BET equation, (3.31), uses the information from the isotherm to determine the surface area of the sample, where X is the weight of nitrogen adsorbed at a given relative pressure (P/Po), X_m is monolayer capacity, which is the volume of gas adsorbed at standard temperature and pressure (STP), and C is constant. STP is defined as 273 K and 1 atm.

$$\frac{1}{X[(P_0/P)-1]} = \frac{1}{X_m C} + \frac{C-1}{X_m C}\left(\frac{P}{P_0}\right) \tag{3.31}$$

3.1.4.4.1 Multi-point BET

Ideally five data points, with a minimum of three data points, in the P/P_0 range 0.025 to 0.30 should be used to successfully determine the surface area using the BET equation. At relative pressures higher than 0.5, there is the onset of capillary condensation, and at relative pressures that are too low, only monolayer formation is occurring. When the BET equation is plotted, the graph should be of linear with a positive slope. If such a graph is not obtained, then the BET method was insufficient in obtaining the surface area.

- The slope and y-intercept can be obtained using least squares regression.
- The monolayer capacity X_m can be calculated with (3.32).
- Once X_m is determined, the total surface area S_t can be calculated with the following equation, where L_{av} is Avogadro's number, A_m is the cross sectional area of the adsorbate and equals 0.162 nm^2 for an absorbed nitrogen molecule, and M_v is the molar volume and equals 22414 mL, (3.33).

$$X_m = \frac{1}{s+i} = \frac{C-1}{Cs} \tag{3.32}$$

$$S = \frac{X_m L_{av} A_m}{M_v} \tag{3.33}$$

Single point BET can also be used by setting the intercept to 0 and ignoring the value of C. The data point at the relative pressure of 0.3 will match up the best with a multipoint BET. Single point BET can be used over the more accurate multipoint BET to determine the appropriate relative pressure range for multi-point BET.

3.1.4.5 Sample preparation and experimental setup

Prior to any measurement the sample must be degassed to remove water and other contaminants before the surface area can be accurately measured. Samples are degassed in a vacuum at high temperatures. The highest temperature possible that will not damage the sample's structure is usually chosen in order to shorten the degassing time. IUPAC recommends that samples be degassed for at least 16 hours to ensure that unwanted vapors and gases are removed from the surface of the sample. Generally, samples that can withstand higher temperatures without structural changes have smaller degassing times. A minimum of 0.5 g of sample is required for the BET to successfully determine the surface area.

Samples are placed in glass cells to be degassed and analyzed by the BET machine. Glass rods are placed within the cell to minimize the dead space in the cell. Sample cells typically come in sizes of 6, 9 and 12 mm and come in different shapes. 6 mm cells are usually used for fine powders, 9 mm cells for larger particles and small pellets and 12 mm are used for large pieces that cannot be further reduced. The cells are placed into heating mantles and connected to the outgas port of the machine.

After the sample is degassed, the cell is moved to the analysis port (Figure 3.28). Dewars of liquid nitrogen are used to cool the sample and maintain it at a constant temperature. A low temperature must be

maintained so that the interaction between the gas molecules and the surface of the sample will be strong enough for measurable amounts of adsorption to occur. The adsorbate, nitrogen gas in this case, is injected into the sample cell with a calibrated piston. The dead volume in the sample cell must be calibrated before and after each measurement. To do that, helium gas is used for a blank run, because helium does not adsorb onto the sample.

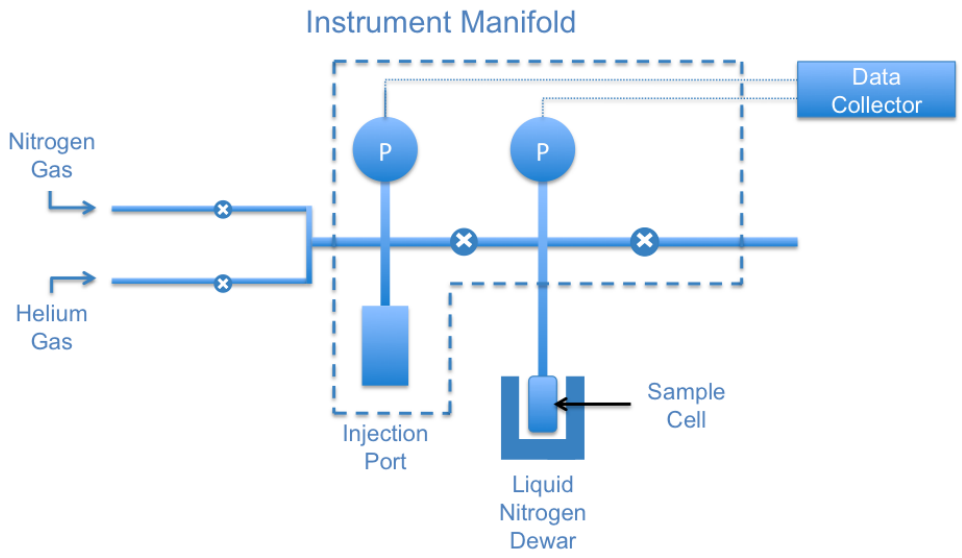

Figure 3.28: Schematic representation of the BET instrument. The degasser is not shown.

3.1.4.6 Shortcomings of BET

The BET technique has some disadvantages when compared to NMR, which can also be used to measure the surface area of nanoparticles. BET measurements can only be used to determine the surface area of dry powders. This technique requires a lot of time for the adsorption of gas molecules to occur. A lot of manual preparation is required.

3.1.4.7 The surface area determination of metal-organic frameworks

The BET technique was used to determine the surface areas of metal-organic frameworks (MOFs), which are crystalline compounds of metal ions coordinated to organic molecules. Possible applications of MOFs, which are porous, include gas purification and catalysis. An isoreticular MOF (IRMOF) with the chemical formula Zn_4O(pyrene-1,2-dicarboxylate)$_3$ (Figure 3.29) was used as an example to see if BET could accurately determine the surface area of microporous materials. The predicted surface area was calculated directly from the geometry of the crystals and agreed with the data obtained from the BET isotherms. Data was collected at a constant temperature of 77 K and a type II isotherm (Figure 3.30) was obtained.

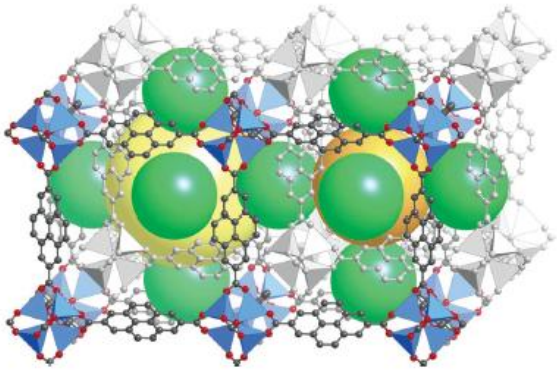

Figure 3.29: The structure of catenated IRMOF-13. Orange and yellow represent non-catenated pore volumes. Green represents catenated pore volume.

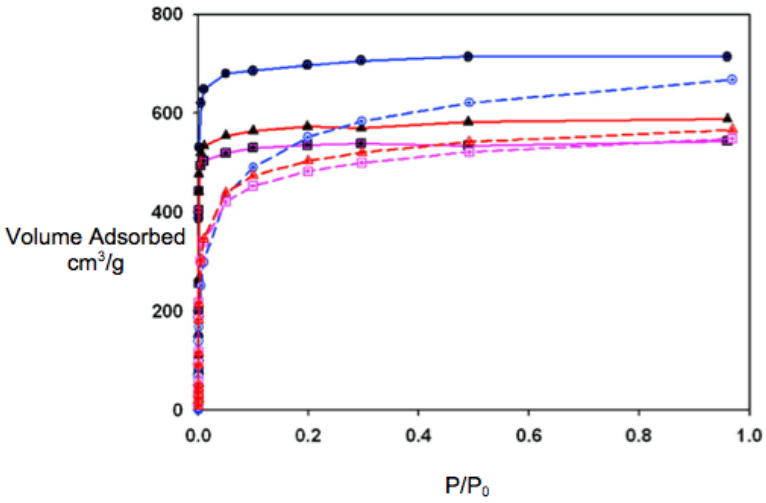

Figure 3.30: The BET isotherms of the zeolites and metal-organic frameworks. IRMOF-13 is symbolized by the black triangle and red line. Adapted from Y.S. Bae, R.Q. Snurr, and O. Yazaydin, *Langmuir*, 2010, **26**, 5478.

The isotherm data obtained from partial pressure range of 0.05 to 0.3 is plugged into the BET equation, (3.31), to obtain the BET plot (Figure 3.31).

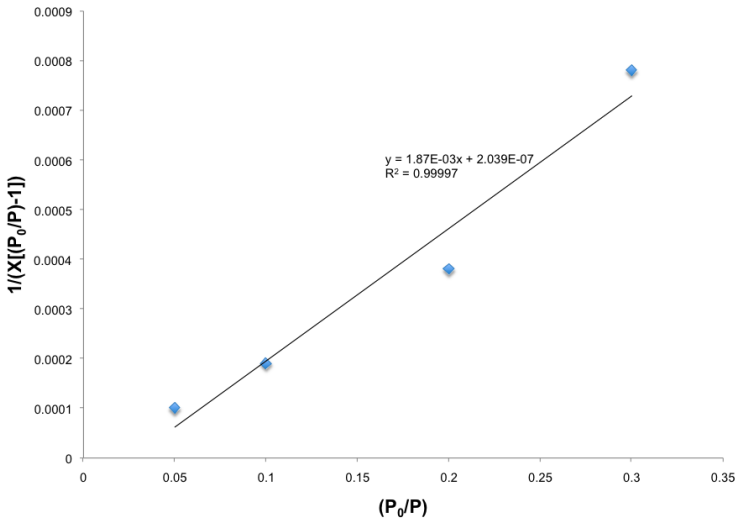

Figure 3.31: BET plot of IRMOF-13 using points collected at the pressure range 0.05 to 0.3. The equation of the best-fit line and R^2 value are shown. Adapted from Y.S. Bae, R.Q. Snurr, and O. Yazaydin, *Langmuir*, 2010, **26**, 5479.

Using (3.34), the monolayer capacity is determined to be 391.2 cm^3/g.

$$X_m = \frac{1}{(2.66E-3)+(-5.512E-05)} \tag{3.34}$$

Now that X_m is known, then (3.35) can be used to determine that the surface area is 1702.3 m^2/g.

$$S = \frac{391.2cm^3 * 0.162nm^2 * 6.02 * 10^{23}}{22.414L} \tag{3.35}$$

3.1.4.8 Bibliography

- B. H. Davis, *J. Phys. Chem.*, 1986, **90**, 4702.
- K. S. Sing, *Langmuir*, 1987, **3**, 2.
- *Brunauer-Emmett-Teller (BET) Surface Area Analysis and Barrett-Joyner-Halenda (BJH) Pore Size and Volume Analysis*, Testing and Analysis Techniques. CERAM.
- S. Brunauer, L. S. Deming, W. E. Deming, and E. Teller, *J. Am. Chem. Soc.*, 1940, **62**, 1723.
- S. Brunauer, P. H. Emmett, and E. Teller, *J. Am. Chem. Soc.*, 1938, **60**, 309.
- Y. S. Bae, R. Q. Snurr, and O. Yazaydin, *Langmuir*, 2010, **26**, 5475.

3.1.5 Measuring the Specific Surface Area of Nanoparticle Suspensions using NMR[6]

3.1.5.1 Introduction

Surface area is a property of immense importance in the nano-world, especially in the area of heterogeneous catalysis. A solid catalyst works with its active sites binding to the reactants, and hence for a given active site reactivity, the higher the number of active sites available, the faster the reaction will occur. In heterogeneous catalysis, if the catalyst is in the form of spherical nanoparticles, most of the active sites are believed to be present on the outer surface. Thus it is very important to know the catalyst surface area in order to get a measure of the reaction time. One expresses this in terms of volume specific surface area, i.e., surface area/volume although in industry it is quite common to express it as surface area per unit mass of catalyst, e.g., m^2/g.

3.1.5.2 Overview of NMR

Nuclear magnetic resonance (NMR) is the study of the nuclei of the response of an atom to an external magnetic field. Many nuclei have a net magnetic moment with $I \neq 0$, along with an angular momentum in one direction where I is the spin quantum number of the nucleus. In the presence of an external magnetic field, a nucleus would precess around the field. With all the nuclei precessing around the external magnetic field, a measurable signal is produced.

NMR can be used on any nuclei with an odd number of protons or neutrons or both, like the nuclei of hydrogen (^{1}H), carbon (^{13}C), phosphorous (^{31}P), etc. Hydrogen has a relatively large magnetic moment (μ = 14.1 x 10^{-27} J/T) and hence it is used in NMR logging and NMR rock studies. The hydrogen nucleus composes of a single positively charged proton that can be seen as a loop of current generating a magnetic field. It is may be considered as a tiny bar magnet with the magnetic axis along the spin axis itself as shown in Figure 3.32. In the absence of any external forces, a sample with hydrogen alone will have the individual magnetic moments randomly aligned as shown in Figure 3.33.

[6]This content is available online at <http://cnx.org/content/m34663/1.1/>.

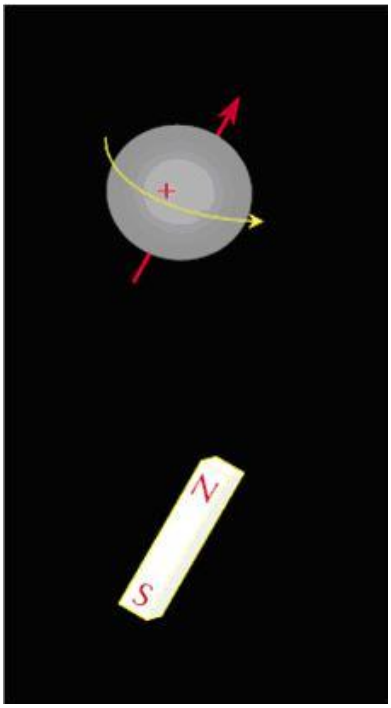

Figure 3.32: A simplistic representation of a spinning nucleus as bar magnet. Copyright: Halliburton Energy Services, Duncan, OK (1999).

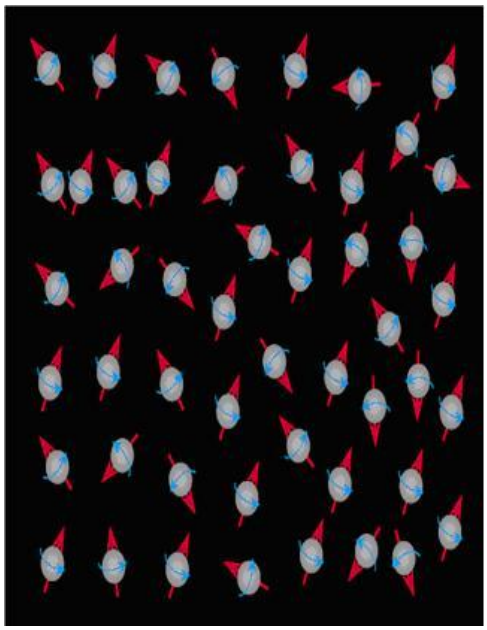

Figure 3.33: Representation of randomly aligned hydrogen nuclei. Copyright: Halliburton Energy Services, Duncan, OK (1999).

3.1.5.3 Advantages of NMR over BET technique

BET measurements follow the BET (Brunner-Emmet-Teller) adsorption isotherm of a gas on a solid surface. Adsorption experiments of a gas of known composition can help determine the specific surface area of the solid particle. This technique has been the main source of surface area analysis used industrially for a long time. However BET techniques take a lot of time for the gas-adsorption step to be complete while one shall see in the course of this module that NMR can give you results in times averaging around 30 minutes depending on the sample. BET also requires careful sample preparation with the sample being in dry powder form, whereas NMR can accept samples in the liquid state as well.

3.1.5.4 How does NMR work?

3.1.5.4.1 Polarization

Polarization involves the alignment of the individual magnetic nuclei in the presence of a static external magnetic field B_o. This external field exerts a torque that forces the spinning nuclei to precess around it by a frequency given by the *Larmor frequency* given by (3.36), where γ is the gyromagnetic ratio which is a characteristic property of the nucleus. For hydrogen, $\gamma/2\pi = 42.58$ MHz/Tesla. This value is different for different elements.

$$f = \frac{\gamma \beta_o}{2\pi} \tag{3.36}$$

Considering the case of a proton under the influence of an external magnetic field, it will be in one of two possible energy states depending on the orientation of the precession axis. If the axis is parallel to B_o, the

proton is in the lower energy state (preferred state) and in the higher energy state if anti-parallel shown by Figure 3.34.

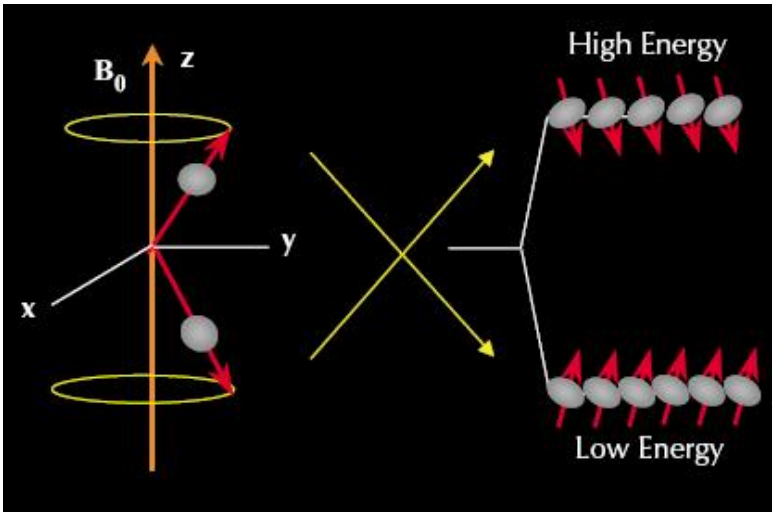

Figure 3.34: Alignment of precession axis. Copyright: Halliburton Energy Services, Duncan, OK (1999).

We define the net magnetization per unit volume of material, M_o, from Curie's law as (3.37), where N = number of protons, h = Planck's constant (6.626 x 10^{-34} Js), I = spin quantum number of the nucleus, k = Boltzmann's constant (1.381 x 10^{-23} m^2 Kg s^{-2} K^{-1}), and T = temperature (K)

$$M_o = \frac{N\gamma^2 h^2 I\left(I+1\right)B_o}{12\Pi^2 kT} \tag{3.37}$$

3.1.5.4.2 T_1 relaxation

The protons are said to be polarized completely once they are all aligned with the static external field. Polarization grows with a time constant called the *longitudinal relaxation time* (T_1) as shown in (3.38), where t = time of exposure to B_o, $M_z(t)$ = magnitude of magnetization at time t, with B_o along z-axis and T_1 = time at which $M_z(t)$ reaches 90% of its final value, i.e., M_o.

$$M_z\left(t\right) = M_o\left(1 - e^{\frac{-t}{T_1}}\right) \tag{3.38}$$

T_1 is the time at which $M_z(t)$ reaches 63% of its final value, M_o. A typical T_1 relaxation experiment involves application of a 90° RF pulse that rotates the magnetization to the transverse direction. With time, the magnetization returns to its original value in the same fashion described by the above equation.

Click on the video below to see the mechanism of T_1 relaxation

[Media Object][7]

[7] This media object is a video file. Please view or download it at

<T1_Relaxation_Video.wmv>

T_1 relaxation mechanism.

3.1.5.4.3 T_2 Relaxation

Once the polarization is complete, the magnetization direction is tipped from the longitudinal plane to a transverse plane by applying an oscillating field B_1 perpendicular to B_o. The frequency of B_1 must equal the Larmor frequency of the material from B_o. This oscillating field causes a possible change in energy state, and in-phase precession. The total phenomenon is called *nuclear magnetic resonance* as shown in Figure 3.35.

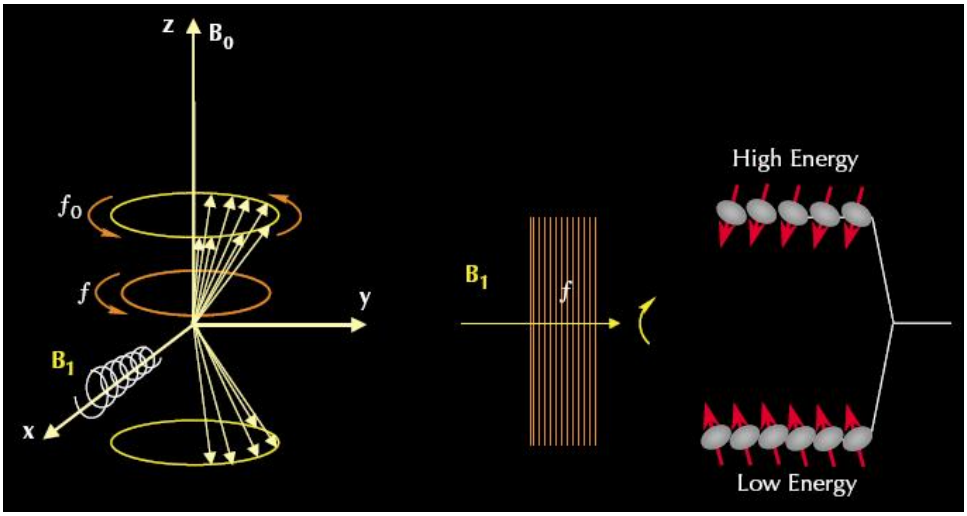

Figure 3.35: A schematic representation of the phenomenon of nuclear magnetic resonance. Copyright: Halliburton Energy Services, Duncan, OK (1999).

The oscillating field is generally pulsed in nature and so terms in books such a 180° pulse or 90° pulse indicates the angle through which the net magnetization gets tipped over. Application of a 90° pulse causes precession in the transverse phase. When the field B_1 is removed, the nuclei begin to de-phase and the net magnetization decreases. Here a receiver coil detects the decaying signal in a process called *free induction decay (FID)*. This exponential decay has an FID time constant (T_2) which is in the order of microseconds.

The time constant of the transverse relaxation is referred as T_2, and the amplitude of the decaying signal is given by (3.39), with symbols as defined earlier.

$$M_x(t) = M_o e^{\frac{-t}{T_2}} \tag{3.39}$$

Click on the video below to see the mechanism of T_2 relaxation

[Media Object][8]
T_2 relaxation mechanism.

[8]This media object is a video file. Please view or download it at

<T2_Relaxation_Video.wmv>

3.1.5.4.4 CPMG sequence

The de-phasing caused by T_1 relaxation can be reversed by applying a 180° pulse after a time τ has passed after application of the initial 90° pulse. Thus the phase of the transverse magnetization vector is now reversed by 180° so that "slower" vectors are now ahead of the "faster" vectors. These faster vectors eventually over-take the slower vectors and cause rephasing which is detected by a receiver coil as a *spin echo*. Thus time τ also passes between the application of the 180° pulse and the maximum peak in the spin echo. The entire sequence is illustrated in Figure 3.36. A single echo decays very quickly and hence a series of 180^0 pulses are applied repeatedly in a sequence called the *Carr-Purcell-Meiboom-Gill (CPMG) sequence*.

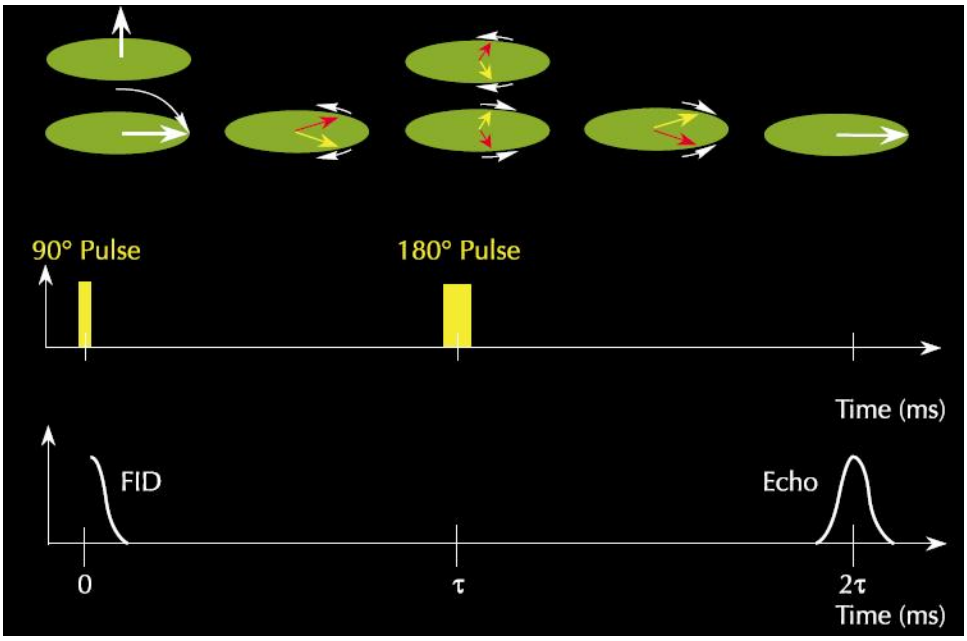

Figure 3.36: A schematic representation of the generation of a spin echo. Copyright: Halliburton Energy Services, Duncan, OK (1999).

3.1.5.5 NMR relaxation mechanism in solid suspensions

3.1.5.5.1 Calculations

From an atomic stand point, T_1 relaxation occurs when a precessing proton transfers energy with its surroundings as the proton relaxes back from higher energy state to its lower energy state. With T_2 relaxation, apart from this energy transfer there is also dephasing and hence T_2 is less than T_1 in general. For solid suspensions, there are three independent relaxation mechanisms involved:-

1) Bulk fluid relaxation, which affects both T_1 and T_2 relaxation.
2) Surface relaxation, which affects both T_1 and T_2 relaxation.
3) Diffusion in the presence of the magnetic field gradients, which affects only T_2 relaxation.

These mechanisms act in parallel so that the net effects are given by (3.40) and (3.41)

$$\frac{1}{T_2} = \frac{1}{T_{2,\text{bulk}}} + \frac{1}{T_{2,\text{surface}}} + \frac{1}{T_{2,\text{diffusion}}} \tag{3.40}$$

$$\frac{1}{T_1} = \frac{1}{T_{1,\text{bulk}}} + \frac{1}{T_{1,\text{surface}}} \tag{3.41}$$

The relative importance of each of these terms depend on the specific scenario. For the case of most solid suspensions in liquid, the diffusion term can be ignored by having a relatively uniform external magnetic field that eliminates magnetic gradients. Theoretical analysis has shown that the surface relaxation terms can be written as (3.42) and (3.43), where ρ = surface relaxivity and s/v = specific surface area.

$$\frac{1}{T_{1,\text{surface}}} = \rho_1 \left(\frac{S}{V}\right)_{\text{particle}} \tag{3.42}$$

$$\frac{1}{T_{2,\text{surface}}} = \rho_2 \left(\frac{S}{V}\right)_{\text{particle}} \tag{3.43}$$

Thus one can use T_1 or T_2 relaxation experiment to determine the specific surface area. We shall explain the case of the T_2 technique further as (3.44).

$$\frac{1}{T_2} = \frac{1}{T_{2,\text{bulk}}} + \rho_2 \left(\frac{S}{V}\right)_{\text{particle}} \tag{3.44}$$

One can determine T_2 by spin-echo measurements for a series of samples of known S/V values and prepare a calibration chart as shown in Figure 3.37, with the intercept as $\frac{1}{T_{2,\text{bulk}}}$ and the slope as ρ_2, one can thus find the specific surface area of an unknown sample of the same material.

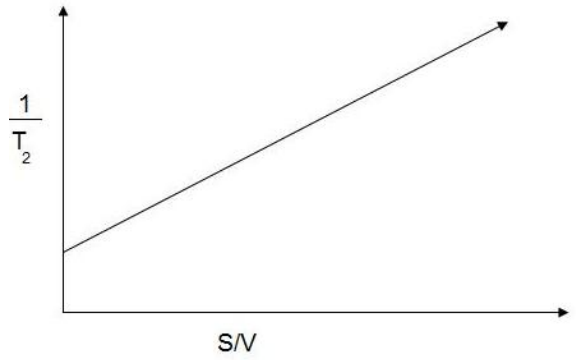

Figure 3.37: Example of a calibration plot of $1/T_2$ versus specific surface area (S/V) of a sample.

3.1.5.6 Sample preparation and experimental setup

The sample must be soluble in the solvent. For proton NMR, about 0.25-1.00 mg/mL are needed depending on the sensitivity of the instrument.

NOTE: The solvent properties will have an impact of some or all of the spectrum. Solvent viscosity affects obtainable resolution, while other solvents like water or ethanol have exchangeable protons that will prevent the observation of such exchangeable protons present in the solute itself. Solvents must be chosen such that the temperature dependence of solute solubility is low in the operation temperature range. Solvents containing aromatic groups like benzene can cause shifts in the observed spectrum compared to non-aromatic solvents.

NMR tubes are available in a wide range of specifications depending on specific scenarios. The tube specifications need to be extremely narrow while operating with high strength magnetic fields. The tube needs to be kept extremely clean and free from dust and scratches to obtain good results, irrespective of the quality of the tube. Tubes can cleaned without scratching by rinsing out the contents and soaking them in a degreasing solution, and by avoiding regular glassware cleaning brushes. After soaking for a while, rinse with distilled water and acetone and dry the tube by blowing filterened nitrogen gas through a pipette or by using a swob of cotton wool.

Filter the sample solution by using a Pasteur pipette stuffed with a piece of cotton wool at the neck. Any suspended material like dust can cause changes in the spectrum. When working with dilute aqueous solutions, sweat itself can have a major effect and so gloves are recommended at all times.

NOTE: Sweat contains mainly water, minerals (sodium 0.9 g/L, potassium 0.2 g/L, calcium 0.015 g/L, magnesium 0.0013 g/L and other trace elements like iron, nickel, zinc, copper, lead and chromium), as well as lactate and urea. In presence of a dilute solution of the sample, the proton-containing substances in sweat (e.g., lactate and urea) can result in a large signal that can mask the signal of the sample.

The NMR probe is the most critical piece of equipment as it contains the apparatus that must detect the small NMR signals from the sample without adding a lot of noise. The size of the probe is given by the diameter of the NMR tube it can accommodate with common sizes 5, 10 and 15 mm. A larger size probe can be used in the case of less sensitive samples in order to get as much solute into the active zone as possible. When the sample is available in less quantity, use a smaller size tube to get an intrinsically higher sensitivity.

3.1.5.6.1 NMR analysis

A result sheet of T_2 relaxation has the plot of magnetization versus time, which will be linear in a semi-log plot as shown in Figure 3.38. Fitting it to the equation, we can find T_2 and thus one can prepare a calibration plot of $1/T_2$ versus S/V of known samples.

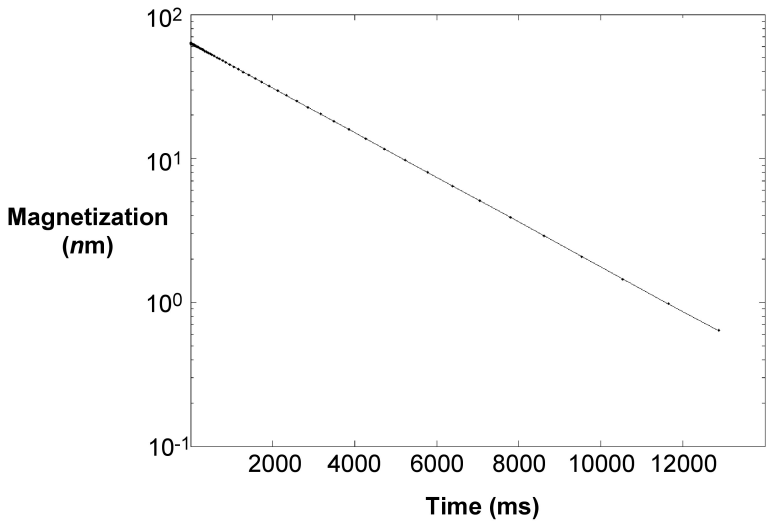

Figure 3.38: Example of T_2 relaxation with magnetization versus time on a semi-log plot.

3.1.5.6.2 Limitations of the T_2 technique

The following are a few of the limitations of the T_2 technique:

- One can't always guarantee no magnetic field gradients, in which case the T_1 relaxation technique is to be used. However this takes much longer to perform than the T_2 relaxation.
- There is the requirement of the odd number of nucleons in the sample or solvent.
- The solid suspension should not have any para- or ferromagnetic substance (for instance, organics like hexane tend to have dissolved O_2 which is paramagnetic).
- The need to prepare a calibration chart of the material with known specific surface area.

3.1.5.6.3 Example of usage

A study of colloidal silica dispersed in water provides a useful example. Figure 3.39 shows a representation of an individual silica particle.

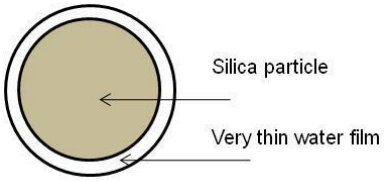

Figure 3.39: A representation of the silica particle with a thin water film surrounding it.

A series of dispersion in DI water at different concentrations was made and surface area calculated. The T_2 relaxation technique was performed on all of them with a typical T_2 plot shown in Figure 3.40 and T_2 was recorded at 2117 milliseconds for this sample.

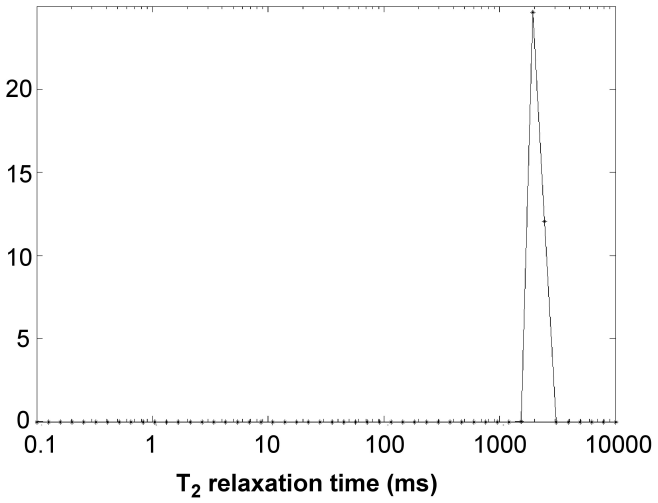

Figure 3.40: T_2 measurement for 2.3 wt% silica in DI water.

A calibration plot was prepared with $1/T_2 - 1/T_{2,bulk}$ as ordinate (the y-axis coordinate) and S/V as abscissa (the x-axis coordinate). This is called the *surface relaxivity plot* and is illustrated in Figure 3.41.

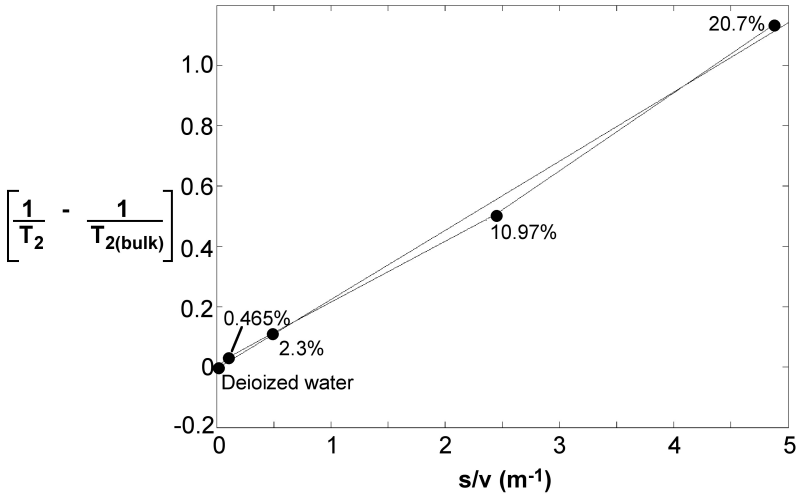

Figure 3.41: Calibration plot of ($1/T_2$ – $1/T_{2,Bulk}$) versus specific surface area for silica in DI water.

Accordingly for the colloidal dispersion of silica in DI water, the best fit resulted in (3.45), from which one can see that the value of surface relaxivity, 2.3 x 10^{-8}, is in close accordance with values reported in literature.

$$\frac{1}{T_2} - \frac{1}{T_{2,\text{bulk}}} = 2.3x10^{-8}\left(\frac{S}{V}\right) - 0.0051 \tag{3.45}$$

The T_2 technique has been used to find the pore-size distribution of water-wet rocks. Information of the pore size distribution helps petroleum engineers model the permeability of rocks from the same area and hence determine the extractable content of fluid within the rocks.

Usage of NMR for surface area determination has begun to take shape with a company, Xigo nanotools, having developed an instrument called the Acorn Area^{TM} to get surface area of a suspension of aluminum oxide. The results obtained from the instrument match closely with results reported by other techniques in literature. Thus the T_2 NMR technique has been presented as a strong case to obtain specific surface areas of nanoparticle suspensions.

3.1.5.7 Bibliography

- G. R Coates, L. Xiao, and M.G. Prammer, *NMR Logging: Principles & Applications*, Halliburton Energy Services, Houston (2001).
- B. Cowan, *Nuclear magnetic resonance and relaxation*, Cambridge University Press, Cambridge UK (2001).
- W. E. Kenyon, *The Log Analyst*, 1997, **6**, 2.
- A. E. Derome, *Modern NMR Techniques for Chemistry Research*, Vol 6, Pergamon Press, Oxford (1988).

3.1.6 Determining the Chemical Formula of Nonstoichiometric Iron Oxide Nanoparticles by Mossbauer Spectroscopy[9]

3.1.6.1 Chemical formula determination

Magnetite (Fe_3O_4) nanoparticles (n-Mag) are nanometer sized, superparamagnetic, have high saturation magnetization, high magnetic susceptibility, and low toxicity. These properties could be utilized for many possible applications; hence, n-Mag has attracted much attention in the scientific community. Some of the potential applications include drug delivery, hyperthermia agents, MRI contrast agents, cell labeling, and cell separation to name a few.

The crystal structure of n-Mag is cubic inverse spinel with Fe^{3+} cations occupying the interstitial tetrahedral sites(A) and Fe^{3+} along with Fe^{2+} occupying the interstitial octahedral sites(B) of an FCC latticed of O^{2-}. Including the site occupation and charge of Fe, the n-Mag chemical formula can be written $(Fe^{3+})_A(Fe^{2+}Fe^{3+})_BO_4$. Non-stoichiometric iron oxide results from B-site vacancies in the crystal structure. To maintain balanced charge and take into account the degree of B-site vacancies the iron oxide formula is written $(Fe^{3+})_A(Fe_{(1-3x)}{}^{2+}\ Fe_{(1+2X)}{}^{3+}Ø_x)_BO_4$ where Ø represents B-site vacancy. The extent of B-site vacancy has a significant effect on the magnetic properties of iron oxide and in the synthesis of n-Mag stoichiometric iron oxide is not guaranteed; therefore, B-site vacancy warrants attention in iron oxide characterization, and can be addressed using Mossbauer spectroscopy.

3.1.7 XAFS Analysis for Arsenic Adsorption onto Iron Oxides[10]

3.1.7.1 Introduction

X-ray absorption fine structure (XAFS) spectroscopy includes both X-ray absorption near edge structure (XANES) and extended X-ray absorption fine structure (EXAFS) spectroscopies. The difference between both techniques is the area to analyze, as shown Figure 3.42 and the information each technique provides. The complete XAFS spectrum is collected across an energy range of around 200 eV before the absorption edge of interest and until 1000 eV after it (Figure 3.42). The absorption edge is defined as the X-ray energy when the absorption coefficient has a pronounced increasing. This energy is equal to the energy required to excite an electron to an unoccupied orbital.

[9] This content is available online at <http://cnx.org/content/m22184/1.4/>.
[10] This content is available online at <http://cnx.org/content/m38287/1.2/>.

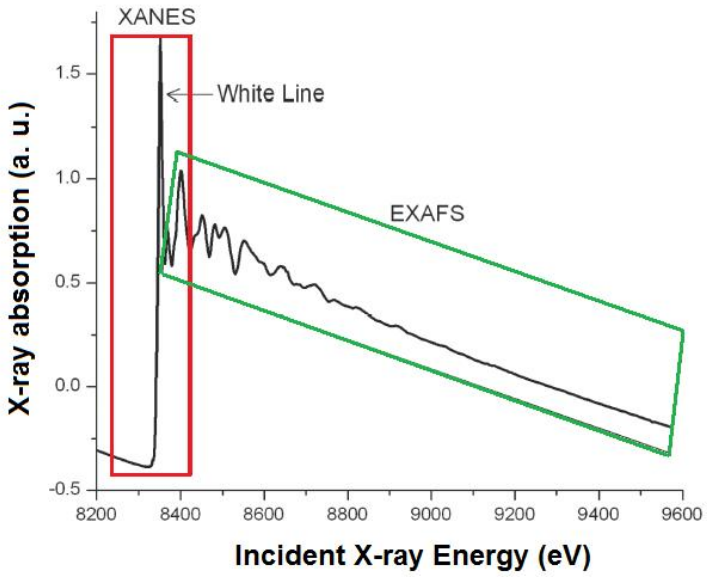

Figure 3.42: Characteristic spectra areas for X-ray absorption near edge structure (XANES) and extended X-ray absorption fine structure (EXAFS) spectroscopies. Adapted from S. D. Kelly, D. Hesterberg, and B. Ravel in *Methods of Soil Analysis: Part 5, Mineralogical Methods*, Ed. A. L. Urely and R. Drees, Soil Science Society of America Book Series, Madison (2008).

X-ray absorption near edge structure (XANES) is used to determine the valence state and coordination geometry, whereas extended X-ray absorption fine structure (EXAFS) is used to determine the local molecular structure of a particular element in a sample.

3.1.7.1.1 X-ray absorption near edge structure (XANES) spectra

XANES is the part of the absorption spectrum closer an absorption edge. It covers from approximately -50 eV to +200 eV relative to the edge energy (Figure 3.42). Because the shape of the absorption edge is related to the density of states available for the excitation of the photoelectron, the binding geometry and the oxidation state of the atom affect the XANES part of the absorption spectrum.

Before the absorption edge, there is a linear and smooth area. Then, the edge appears as a step, which can have other extra shapes as isolated peaks, shoulders or a *white line*, which is a strong peak onto the edge. Those shapes give some information about the atom. For example, the presence of a white line indicates that after the electron releasing, the atomic states of the element is confined by the potential it feels. This peak sharp would be smoothed if the atom could enter to any kind of resonance. Important information is given because of the absorption edge position. Atoms with higher oxidation state have fewer electrons than protons, so, the energy states of the remaining electrons are lowered slightly, which causes a shift of the absorption edge energy up to several eV to a higher X-ray energy.

3.1.7.1.2 Extended X-ray absorption fine structure (EXAFS) spectra

The EXAFS part of the spectrum is the oscillatory part of the absorption coefficient above around 1000 eV of the absorption edge. This region is used to determine the molecular bonding environments of the elements. EXAFS gives information about the types and numbers of atoms in coordination a specific atom and their

inter-atomic distances. The atoms at the same radial distance from a determinate atom form a shell. The number of the atoms in the shell is the coordination number (e.g., Figure 3.43).

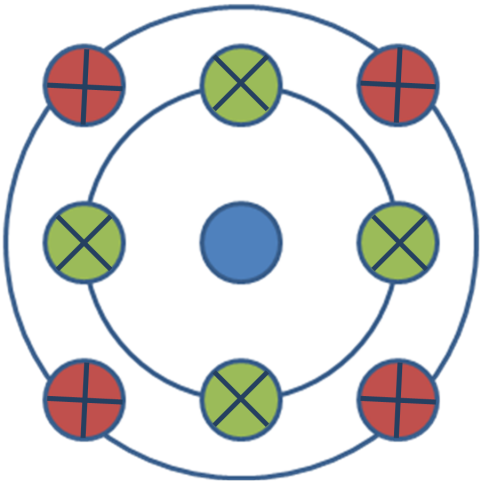

Figure 3.43: A schematic representation of coordination number in different layers in which there are two shells around the center atom. Both shells, green (x) and red (+), have coordination numbers of 4, but the radial distance of the red one (+) is bigger than the green one (x). Based on S. D. Kelly, D. Hesterberg, and B. Ravel in *Methods of Soil Analysis: Part 5, Mineralogical Methods*, Ed. A. L. Urely and R. Drees, Soil Science Society of America Book Series, Madison (2008).

An EXAFS signal is given by the photoelectron scattering generated for the center atom. The phase of the signal is determinate by the distance and the path the photoelectrons travel. A simple scheme of the different paths is shown by Figure 3.44. In the case of two shells around the centered atom, there is a degeneracy of four for the path between the main atom to the first shell, a degeneracy of four for the path between the main atom to the second shell, and a degeneracy of eight for the path between the main atom to the first shell, to the second one and to the center atom.

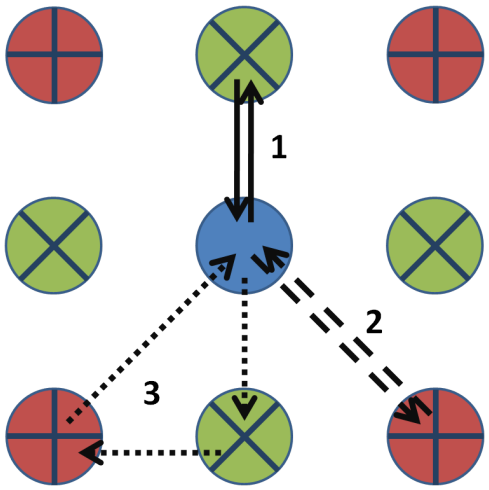

Figure 3.44: A two shell diagram in which there are three kinds of paths. From the center atom to the green one (x) and then going back (1); from the center atom to the red one (+) and the going back (2); and from the center atom to the first shell to the second one, and the returning to the center atom (3). Based on S. D. Kelly, D. Hesterberg, and B. Ravel in *Methods of Soil Analysis: Part 5, Mineralogical Methods*, Ed. A. L. Urely and R. Drees, Soil Science Society of America Book Series, Madison (2008).

The analysis of EXAFS spectra is accomplished using Fourier transformation to fit the data to the EXAFS equation. The EXAFS equation is a sum of the contribution from all scattering paths of the photoelectrons (3.46), where each path is given by (3.47).

$$\chi(k) = \sum_i \chi_i(k) \tag{3.46}$$

$$\chi_i(k) \equiv \frac{\left(N_i S_0^2\right) F_{\mathrm{eff}_i}(k)}{\mathrm{kR}_i^2} \sin\left[2\mathrm{kR}_i + \varphi_i(k)\right] e^{-2\sigma_i^2 k^2} e^{\frac{-2R_i}{\lambda(k)}} \tag{3.47}$$

The terms $F_{\mathrm{eff}}i(\mathrm{k})$, $\phi i(\mathrm{k})$, and $\lambda i(\mathrm{k})$ are the effective scattering amplitude of the photoelectron, the phase shift of the photoelectron, and the mean free path of the photoelectron, respectively. The term R_i is the half path length of the photoelectron (the distance between the centered atom and a coordinating atom for a single-scattering event). And the k^2 is given by the (3.48). The remaining variables are frequently determined by modeling the EXAFS spectrum.

$$k^2 = \frac{2m_e\left(E - E_0 + \Delta\mathrm{E}_0\right)}{\hbar} \tag{3.48}$$

3.1.7.2 XAFS analysis for arsenic adsorption onto iron oxides

The absorption of arsenic species onto iron oxide offers n example of the information that can be obtained by EXAFS. Because the huge impact that the presence of arsenic in water can produce in societies there is a lot of research in the adsorption of arsenic in several kinds of materials, in particular nano materials. Some of the materials more promising for this kind of applications are iron oxides. The elucidation of the

mechanism of arsenic coordination onto the surfaces of those materials has been studied lately using X-ray absorption spectroscopy.

There are several ways how arsenate ($AsO_4{}^{3-}$, Figure 3.45) can be adsorbed onto the surfaces. Figure 3.46 shows the three ways that Sherman proposes arsenate can be adsorbed onto goethite (α-FeOOH): bidentate cornersharing (2C), bidentate edge sharing (2E) and monodentate corner-sharing (1V) shapes. Figure 3.47 shows that the bidentate corner sharing (2C) is the configuration that corresponds with the calculated parameters not only for goethite, but for several iron oxides.

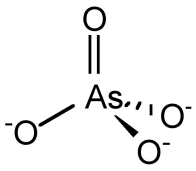

Figure 3.45: Structure of the arsenate anion.

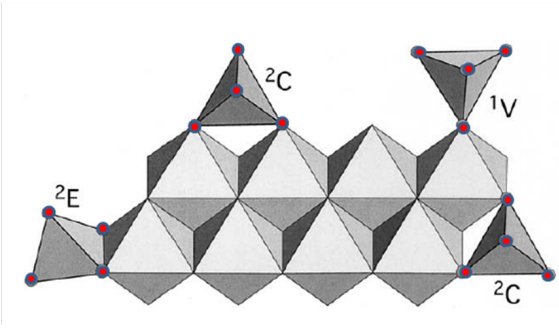

Figure 3.46: Possible configurations of arsenate onto goethite. The tetrahedral with the small spheres represents the arsenate ions. Adapted from D. M. Sherman and S. R. Randal. *Geochim. Cosmochim. Ac.* 2003, **67**, 4223.

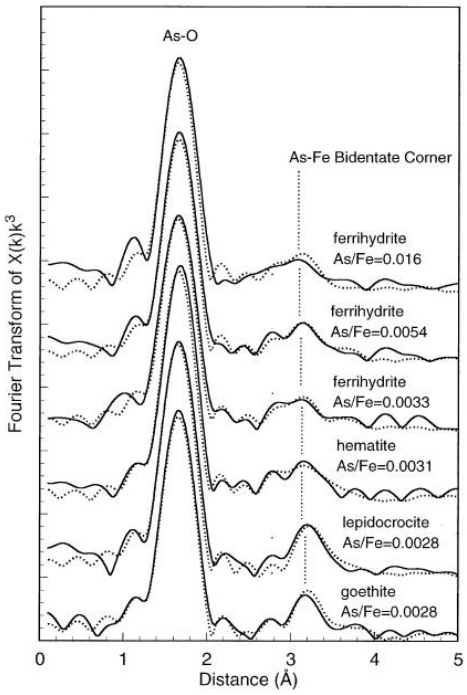

Figure 3.47: Fourier transforms of the EXAFS for arsenate sorbed onto goethite, lepidocrocite, hematite and ferrihydrite. Adapted from D. M. Sherman and S. R. Randal. *Geochim. Cosmochim. Ac.* 2003, **67**, 4223.

Several studies have confirmed that the bidentate corner sharing (2C) is the one present in the arsenate adsorption but also one similar, a tridentate corner sharing complex (3C), for the arsenite adsorption onto most of iron oxides as shows Figure 3.48. Table 3.3 shows the coordination numbers and distances reported in the literature for the As(III) and As(V) onto goethite.

Figure 3.48: Proposed structural model for arsenic(III) tridante. Adapted from G. Morin, Y. Wang, G. Ona-Nguema, F. Juillot, G. Calas, N. Menguy, E. Aubry, J. R. Bargar, and G. E. Brown. *Langmuir* 2009, **25**, 9119.

As	CN As-O	R As-O (Å)	CN As-Fe	R As-Fe (Å)
III	3.06±0.03	1.79±0.8	2.57±0.01	3.34±3
	3.19	1.77±1	1.4	3.34±5
	3	1.78	2	3.55±5
V	1.03.0	1.631.70	2	3.30
	4.6	1.68	–	3.55±5

Table 3.3: Coordination numbers (CN) and inter-atomic distances (R) reported in the literature for the As(III) and As(V) adsorption onto goethite.

3.1.7.3 Bibliography

- G. Bunker. *Introduction to XAFS: A practical guide to X-ray Absorption Fine Structure Spectroscopy*, Cambridge University Press, Cambridge (2010).
- S. D. Kelly, D. Hesterberg, and B. Ravel in *Methods of Soil Analysis: Part 5, Mineralogical Methods*, Ed. A. L. Urely and R. Drees, Soil Science Society of America Book Series, Madison (2008).
- G. A. Waychunas, B. A. Rea, C. C. Fuller, and J. A. Davis. *Geochim. Cosmochim. Ac.* 1993, **57**, 2251.
- B. A. Manning, and S. E. Fendorf, and S.Goldberg, *Environ. Sci. Techn.*, 1998, **32**, 2383.
- D. M. Sherman and S. R. Randal, *Geochim. Cosmochim. Ac.*, 2003, **67**, 4223.
- G. Ona-Nguena, G. Morin F. Juillot, G. Calas, and G. E. Brown, *Environ. Sci. Techn.*, 2005, **39**, 9147.
- M. Stachowicz, T. Hiemstra, and W. H. Van Riemsdijk, *J. Colloid. Interf. Sci.*, 2005, **302**, 62.
- M. Auffan, J. Rose, O. Proux, D. Borschneck, A. Masion, P. Chaurand, J. L. Hazemann, C. Chaneac, J. P. Jolivet, M. R. Wiesner, A. Van Geen, and J. Y. Bottero, *Langmuir*, 2008, **24**, 3215.
- G. Ona-Nguena, G. Morin, Y. Wang, N. Menguy, F. Juillot, L, Olivi, G. Aquilanti, M. Abdelmoula, C. Ruby, J. R. Bargar, F. Guyot, G. Calas, and G. E. Brown, Jr., *Geochim. Cosmochim. Ac.*, 2009, **73**, 1359.

- G. Morin, Y. Wang, G. Ona-Nguema, F. Juillot, G. Calas, N. Menguy, E. Aubry, J. R. Bargar, and G. E. Brown Jr., *Langmuir*, 2009, **25**, 9119.
- J. Rose, M. M. Cortalezzi-Fidalgo, S. Moustier, C. Magnetto, C. D. Jones, A. R. Barron, M. R. Wiesner, and J.-Y. Bottero, *Chem. Mater.*, 2002, **14**, 621.

3.1.8 Nanoparticle Deposition Studies Using a Quartz Crystal Microbalance[11]

3.1.8.1 Overview

The working principle of a quartz crystal microbalance with dissipation (QCM-D) module is the utilization of the resonance properties of some piezoelectric of materials. A piezoelectric material is a material that exhibits an electrical field when a mechanical strain is applied. This phenomenon is also observed in the contrary where an applied electrical field produce a mechanical strain in the material. The material used is α-SiO_2 that produces a very stable and constant frequency. The direction and magnitude of the mechanical strain is directly dependent of the direction of the applied electrical field and the inherent physical properties of the crystal.

A special crystal cut is used, called AT-cut, which is obtain as wafers of the crystal of about 0.1 to 0.3 mm in width and 1 cm in diameter. The AT-cut is obtained when the wafer is cut at 35.25 ° of the main crystallographic axis of SiO_2. This special cut allows only one vibration mode, the shear mode, to be accessed and thus exploited for analytical purposes. When a electrical field is applied to the crystal wafer via metal electrodes, that are vapor-deposited in the surface, a mechanical shear is produced and maintained as long as the electrical field is applied. Since this electric field can be controlled by opening and closing an electrical circuit, a resonance within the crystal is formed (Figure 3.49).

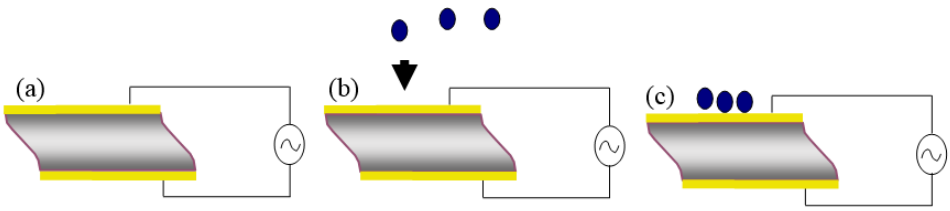

Figure 3.49: Schematic representation of the piezoelectric material: (a) a baseline is obtained by running the sensor without any flow or sample; (b) sample is starting to flow into the sensor; (c) sample deposited in the sensor change the frequency.

Since the frequency of the resonance is dependent of the characteristics of the crystal, an increase of mass, for example when the sample is loaded into the sensor would change the frequency change. This relation (3.49) was obtained by Sauerbrey in 1959, where Δm ($ng.cm^{-2}$) is the areal mass, C (17.7 $ngcm^{-2}Hz^{-1}$) is the vibrational constant (shear, effective area, etc.), n in Hz is the resonant overtone, and Δf is the change in frequency. The dependence of the change in the frequency can be related directly to the change in mass deposited in the sensor only when three conditions are met and assumed:

1. The mass deposited is small compared to the mass of the sensor.
2. It is rigid enough so that it vibrates with the sensor and does not suffer deformation.
3. The mass is evenly distributed among the surface of the sensor.

[11] This content is available online at <http://cnx.org/content/m46155/1.2/>.

$$\Delta m = -C\frac{1}{n}\Delta f \tag{3.49}$$

An important incorporation in recent equipment is the use of the dissipation factor. The inclusion of the dissipation faster takes into account the weakening of the frequency as it travels along the newly deposited mass. In a rigid layer the frequency is usually constant and travels through the newly formed mass without interruption, thus, the dissipation is not important. On the other hand, when the deposited material has a soft consistency the dissipation of the frequency is increased. This effect can be monitored and related directly to the nature of the mass deposited.

The applications of the QCM-D ranges from the deposition of nanoparticles into a surface, from the interaction of proteins within certain substrates. It can also monitors the bacterial amount of products when feed with different molecules, as the flexibility of the sensors into what can be deposited in them include nanoparticle, special functionalization or even cell and bacterias!

3.1.8.2 Experimental planning

In order to use QCM-D for studing the interaction of nanoparticles with a specific surface several steps must be followed. For demonstration purposes the following procedure will describe the use of a Q-Sense E4 with autosampler from Biolin Scientific. A summary is shown below as a quick guide to follow, but further details will be explained:

1. Surface election and cleaning according with the manufacturer recommendations.
2. Sample preparation including having the correct dilutions and enough sample for the running experiment.
3. Equipment cleaning and set up of the correct parameters for the experiment.
4. Data acquisition.
5. Data interpretation.

3.1.8.2.1 Surface election

The decision of what surface of the the sensor to use is the most important decision to make fore each study. Biolin has a large library of available coatings ranging from different compositions of pure elements and oxides (Figure 3.50) to specific binding proteins. It is important to take into account the different chemistries of the sensors and the results we are looking for. For example studying a protein with high sulfur content on a gold sensor can lead to a false deposition results, as gold and sulfur have a high affinity to form bonds. For the purpose of this example, a gold coated sensor will be used in the remainder of the discussion.

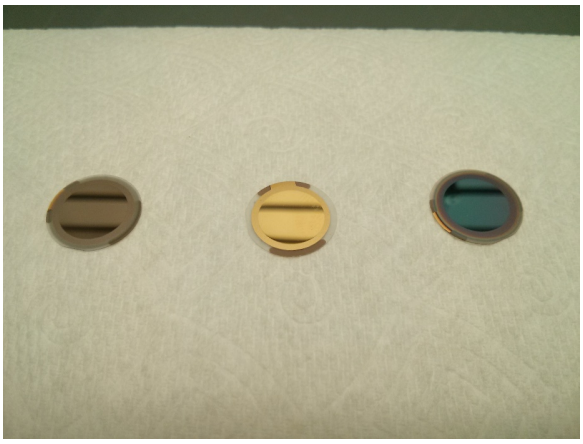

Figure 3.50: From left to right, silica (SiO_2), gold (Au), and iron oxide (Fe_2O_3) coated sensors. Each one is 1 cm in diameter.

3.1.8.2.2 Sensor cleaning

Since QCM-D relies on the amount of mass that is deposited into the surface of the sensor, a thorough cleaning is needed to ensure there is no contaminants on the surface that can lead to errors in the measurement. The procedure the manufacturer established to clean a gold sensor is as follows:

Step 1. Put the sensor in the UV/ozone chamber for 10 minutes
Step 2. Prepare 10 mL of a 5:1:1 solution of hydrogen peroxide:ammonia:water
Step 3. Submerge in this solution at 75 °C for 5 minutes.
Step 4. Rinse with copious amount of milliQ water.
Step 5. Dry with inert gas.
Step 6. Put the sensor in the UV/ozone chamber for 10 minutes as shown in Figure 3.51.

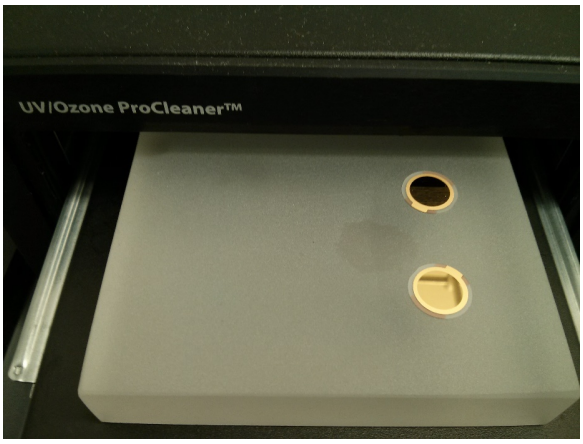

Figure 3.51: Gold sensors in loader of the UV/ozone chamber in the final step of the cleaning process.

Once the sensors are clean, extreme caution should be taken to avoid contamination of the surface. The sensors can be loaded in the flow chamber of the equipment making sure that the T-mark of the sensor matches the T mark of the chamber in order to make sure the electrodes are in constant contact. The correct position is shown in Figure 3.52.

Figure 3.52: Correct position of the sensor in the chamber.

3.1.8.2.3 Sample preparation

As the top range of mass that can be detected is merely micrograms, solutions must be prepared accordingly. For a typical run, a buffer solution is needed in which the deposition will be studied as well as, the sample

itself and a solution of 2% of sodium dodecylsulfate [$CH_3(CH_2)_{10}CH_2OSO_3Na$, SDS]. For this example we will be using nanoparticles of magnetic iron oxide (nMag) coated with PAMS, and as a buffer 8% NaCl in DI water.

- For the nanoparticles sample it is necessary to make sure the final concentration of the nanoparticles will not exceed 1 mM.
- For the buffer solution, it is enough to dissolve 8 g of NaCl in DI water.
- For the SDS solution, 2 g of SDS should be dissolved very slowly in approximate 200 mL of DI water, then 100 mL aliquots of DI water is added until the volume is 1 L. This is in order to avoid the formation of bubbles and foam in the solution.

3.1.8.2.4 Instrument preparation

Due to the sensitivity of the equipment, it is important to rinse and clean the tubing before loading any sample or performing any experiments. To rinse the tubing and the chambers, use a solution of 2% of SDS. For this purpose, a cycle in the autosampler equipment is program with the steps shown in Table 3.4.

Step	**Duration (min)**	**Speed (μL/min)**	**Volume (mL)**
DI water (1:2)	10	100	1
SDS (1:1)	20	300	6
DI water (1:2)	10	100	1

Table 3.4: Summary of cleaning processes.

Once the equipment is cleaned, it is ready to perform an experiment, a second program in the autosampler is loaded with the parameters shown in Table 3.5.

Step	**Duration (min)**	**Speed (μL/min)**	**Volume (mL)**
Buffer (1:3)	7	100	0.7
Nanoparticles (1:4)	30	100	3.0

Table 3.5: Experimental set-up.

The purpose of flowing the buffer in the beginning is to provide a background signal to take into account when running the samples. Usually a small quantity of the sample is loaded into the sensor at a very slow flow rate in order to let the deposition take place.

3.1.8.2.5 Data acquisition

Example data obtained with the above parameters is shown in Figure 3.53. The blue squares depict the change in the frequency. As the experiment continues, the frequency decreases as more mass is deposited. On the other hand, shown as the red squares, the dissipation increases, describing the increase of both the height and certain loss of the rigidity in the layer from the top of the sensor. To illustrate the different steps of the experiment, each section has been color coded. The blue part of the data obtained corresponds to the flow of the buffer, while the yellow part corresponds to the deposition equilibrium of the nanoparticles onto the gold surface. After certain length of time equilibrium is reached and there is no further change. Once equilibrium indicates no change for about five minutes, it is safe to say the deposition will not change.

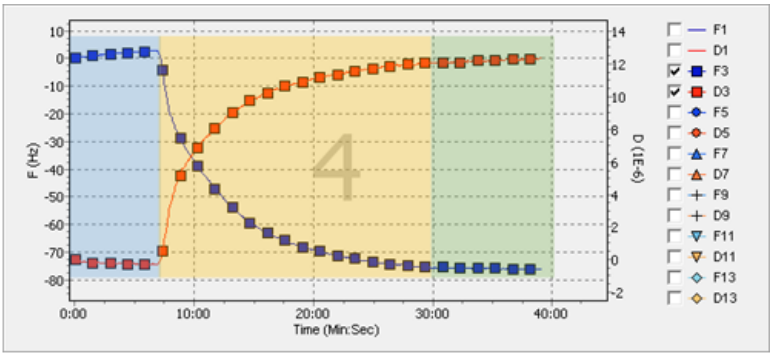

Figure 3.53: Data of deposition of nMag in a gold surface.

3.1.8.2.6 Instrument clean-up

As a measure preventive care for the equipment, the same cleaning procedure should be followed as what was done before loading the sample. Use of a 2% solution of SDS helps to ensure the equipment remains as clean as possible.

3.1.8.3 Data modeling

Once the data has been obtained, QTools (software that is available in the software suit of the equipment) can be used to convert the change in the frequency to areal mass, via the Sauerbrey equation, (3.49). The correspondent graph of areal mass is shown in Figure 3.54. From this graph we can observe how the mass is increasing as the nMag is deposited in the surface of the sensor. The blue section again illustrates the part of the experiment where only buffer was been flown to the chamber. The yellow part illustrates the deposition, while the green part shows no change in the mass after a period of time, which indicates the deposition is finished. The conversion from areal mass to mass is a simple process, as gold sensors come with a definite area of 1 cm^2, but a more accurate measure should be taken when using functionalized sensors.

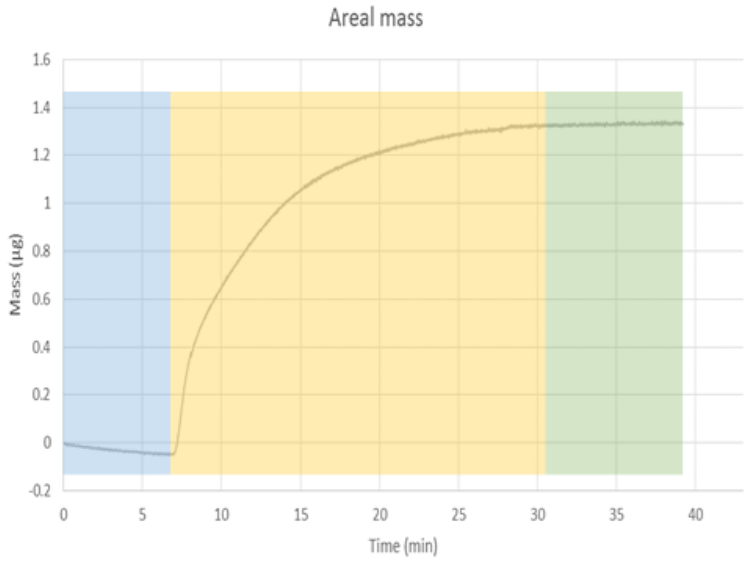

Figure 3.54: Areal mass of deposition of nMag into gold surface.

It is important to take into account the limitations of the Saubery equation, because the equation accounts for a uniform layer on top of the surface of the sensor. Deviations due to clusters of material deposited in one place or the formation of partial multilayers in the sensor cannot be calculated through this model. Further characterization of the surface should be done to have a more accurate model of the phenomena.

3.1.8.4 Bibliography

- Biolin Scientific, *Cleaning and Immobilization Protocols* (2004).
- F. Hook, *Development of a Novel QCM Technique for Protein Adsorption Studies*, Chalmers University (1997).
- C. Ziez, *Theoretical and Experimental Analysis on Nanoparticle-Nanoparticle and Nanoparticle-Surface Interactions and their Role in Defining their Stability and Mobility*, Rice University (2013).

3.2 Spectroscopy

3.2.1 Optical Properties of Group 12-16 (II-VI) Semiconductor Nanoparticles[12]

3.2.1.1 What are Group 12-16 semiconductors?

Semiconductor materials are generally classified on the basis of the periodic table group that their constituent elements belong to. Thus, Group 12-16 semiconductors, formerly called II-VI semiconductors, are materials whose cations are from the Group 12 and anions are from Group 16 in the periodic table (Figure 3.55). Some examples of Group 12-16 semiconductor materials are cadmium selenide (CdSe), zinc sulfide (ZnS), cadmium teluride (CdTe), zinc oxide (ZnO), and mercuric selenide (HgSe) among others.

[12] This content is available online at <http://cnx.org/content/m34553/1.1/>.

NOTE: The new IUPAC (International Union of Pure and Applied Chemistry) convention is being followed in this document, to avoid any confusion with regard to conventions used earlier. In the old IUPAC convention, Group 12 was known as Group IIB with the roman numeral 'II' referring to the number of electrons in the outer electronic shells and B referring to being on the right part of the table. However, in the CAS (Chemical Abstracts Service), the alphabet B refers to transition elements as compared to main group elements, though the roman numeral has the same meaning. Similarly, Group 16 was earlier known as Group VI because all the elements in this group have 6 valence shell electrons.

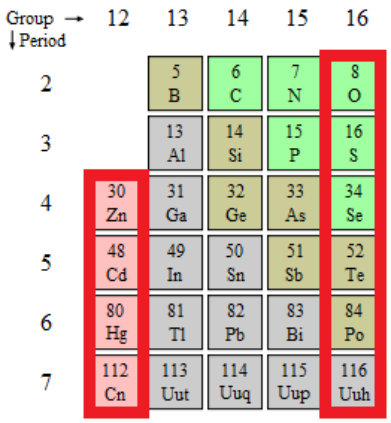

Figure 3.55: The red box indicates the Group 12 and Group 16 elements in the periodic table.

3.2.1.2 What are Group 12-16 (II-VI) semiconductor nanoparticles?

From the Greek word *nanos* - meaning "dwarf" this prefix is used in the metric system to mean 10^{-9} or one billionth (1/1,000,000,000). Thus a nanometer is 10^{-9} or one billionth of a meter, and a nanojoule is 10^{-9} or one billionth of a Joule, etc. A nanoparticle is ordinarily defined as any particle with at least one of its dimensions in the 1 - 100 nm range.

Nanoscale materials often show behavior which is intermediate between that of a bulk solid and that of an individual molecule or atom. An inorganic nanocrystal can be imagined to be comprised of a few atoms or molecules. It thus will behave differently from a single atom; however, it is still smaller than a macroscopic solid, and hence will show different properties. For example, if one would compare the chemical reactivity of a bulk solid and a nanoparticle, the latter would have a higher reactivity due to a significant fraction of the total number of atoms being on the surface of the particle. Properties such as boiling point, melting point, optical properties, chemical stability, electronic properties, etc. are all different in a nanoparticle as compared to its bulk counterpart. In the case of Group 12-16 semiconductors, this reduction in size from bulk to the nanoscale results in many size dependent properties such as varying band gap energy, optical and electronic properties.

3.2.1.3 Optical properties of semiconductor quantum nanoparticles

In the case of semiconductor nanocrystals, the effect of the size on the optical properties of the particles is very interesting. Consider a Group 12-16 semiconductor, cadmium selenide (CdSe). A 2 nm sized CdSe

crystal has a blue color fluorescence whereas a larger nanocrystal of CdSe of about 6 nm has a dark red fluorescence (Figure 3.56). In order to understand the size dependent optical properties of semiconductor nanoparticles, it is important to know the physics behind what is happening at the nano level.

Figure 3.56: Fluorescing CdSe quantum dots synthesized in a heat transfer liquid of different sizes (M. S. Wong, Rice University).

3.2.1.3.1 Energy levels in a semiconductor

The electronic structure of any material is given by a solution of Schrödinger equations with boundary conditions, depending on the physical situation. The electronic structure of a semiconductor (Figure 3.57) can be described by the following terms:

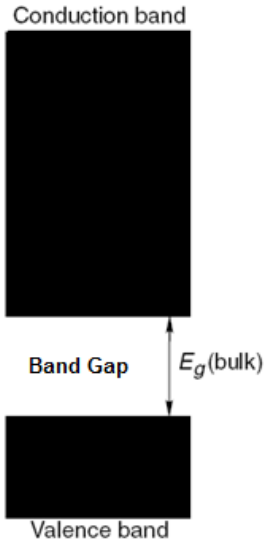

Figure 3.57: Simplified representation of the energy levels in a bulk semiconductor.

3.2.1.3.1.1 Energy level

By the solution of Schrödinger's equations, the electrons in a semiconductor can have only certain allowable energies, which are associated with energy levels. No electrons can exist in between these levels, or in other words can have energies in between the allowed energies. In addition, from Pauli's Exclusion Principle, only 2 electrons with opposite spin can exist at any one energy level. Thus, the electrons start filling from the lowest energy levels. Greater the number of atoms in a crystal, the difference in allowable energies become very small, thus the distance between energy levels decreases. However, this distance can never be zero. For a bulk semiconductor, due to the large number of atoms, the distance between energy levels is very small and for all practical purpose the energy levels can be described as continuous (Figure 3.57).

3.2.1.3.1.2 Band gap

From the solution of Schrödinger's equations, there are a set of energies which is not allowable, and thus no energy levels can exist in this region. This region is called the band gap and is a quantum mechanical phenomenon (Figure 3.57). In a bulk semiconductor the bandgap is fixed; whereas in a quantum dot nanoparticle the bandgap varies with the size of the nanoparticle.

3.2.1.3.1.3 Valence band

In bulk semiconductors, since the energy levels can be considered as continuous, they are also termed as energy bands. Valence band contains electrons from the lowest energy level to the energy level at the lower edge of the bandgap (Figure 3.57). Since filling of energy is from the lowest energy level, this band is usually almost full.

3.2.1.3.1.4 Conduction band

The conduction band consists of energy levels from the upper edge of the bandgap and higher (Figure 3.57). To reach the conduction band, the electrons in the valence band should have enough energy to cross the band gap. Once the electrons are excited, they subsequently relax back to the valence band (either radiatively or non-radiatively) followed by a subsequent emission of radiation. This property is responsible for most of the applications of quantum dots.

3.2.1.3.1.5 Exciton and exciton Bohr radius

When an electron is excited from the valence band to the conduction band, corresponding to the electron in the conduction band a hole (absence of electron) is formed in the valence band. This electron pair is called an exciton. Excitons have a natural separation distance between the electron and hole, which is characteristic of the material. This average distance is called exciton Bohr radius. In a bulk semiconductor, the size of the crystal is much larger than the exciton Bohr radius and hence the exciton is free to move throughout the crystal.

3.2.1.3.2 Energy levels in a quantum dot semiconductor

Before understanding the electronic structure of a quantum dot semiconductor, it is important to understand what a quantum dot nanoparticle is. We earlier studied that a nanoparticle is any particle with one of its dimensions in the 1 - 100 nm. A quantum dot is a nanoparticle with its diameter on the order of the materials exciton Bohr radius. Quantum dots are typically 2 - 10 nm wide and approximately consist of 10 to 50 atoms. With this understanding of a quantum dot semiconductor, the electronic structure of a quantum dot semiconductor can be described by the following terms.

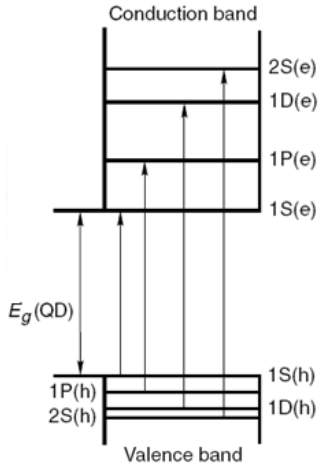

Figure 3.58: Energy levels in quantum dot. Allowed optical transitions are shown. Adapted from T. Pradeep, *Nano: The Essentials. Understanding Nanoscience and Nanotechnology*, Tata McGraw-Hill, New Delhi (2007).

3.2.1.3.2.1 Quantum confinement

When the size of the semiconductor crystal becomes comparable or smaller than the exciton Bohr radius, the quantum dots are in a state of quantum confinement. As a result of quantum confinement, the energy levels in a quantum dot are discrete (Figure 3.58) as opposed to being continuous in a bulk crystal (Figure 3.57).

3.2.1.3.2.2 Discrete energy levels

In materials that have small number of atoms and are considered as quantum confined, the energy levels are separated by an appreciable amount of energy such that they are not continuous, but are discrete (see Figure 3.58). The energy associated with an electron (equivalent to conduction band energy level) is given by is given by (3.50), where h is the Planck's constant, m_e is the effective mass of electron and n is the quantum number for the conduction band states, and n can take the values 1, 2, 3 and so on. Similarly, the energy associated with the hole (equivalent to valence band energy level) is given by (3.51), where n' is the quantum number for the valence states, and n' can take the values 1, 2, 3, and so on. The energy increases as one goes higher in the quantum number. Since the electron mass is much smaller than that of the hole, the electron levels are separated more widely than the hole levels.

$$E^e = \frac{h^2 n^2}{8\pi^2 m_e d^2} \tag{3.50}$$

$$E^h = \frac{h^2 n'^2}{8\pi^2 m_h d^2} \tag{3.51}$$

3.2.1.3.2.3 Tunable band gap

As seen from (3.50) and (3.51), the energy levels are affected by the diameter of the semiconductor particles. If the diameter is very small, since the energy is dependent on inverse of diameter squared, the energy levels of the upper edge of the band gap (lowest conduction band level) and lower edge of the band gap (highest valence band level) change significantly with the diameter of the particle and the effective mass of the electron and the hole, resulting in a size dependent tunable band gap. This also results in the discretization of the energy levels.

Qualitatively, this can be understood in the following way. In a bulk semiconductor, the addition or removal of an atom is insignificant compared to the size of the bulk semiconductor, which consists of a large number of atoms. The large size of bulk semiconductors makes the changes in band gap so negligible on the addition of an atom, that it is considered as a fixed band gap. In a quantum dot, addition of an atom does make a difference, resulting in the tunability of band gap.

3.2.1.3.3 UV-visible absorbance

Due to the presence of discrete energy levels in a QD, there is a widening of the energy gap between the highest occupied electronic states and the lowest unoccupied states as compared to the bulk material. As a consequence, the optical properties of the semiconductor nanoparticles also become size dependent.

The minimum energy required to create an exciton is the defined by the band gap of the material, i.e., the energy required to excite an electron from the highest level of valence energy states to the lowest level of the conduction energy states. For a quantum dot, the bandgap varies with the size of the particle. From (3.50) and (3.51), it can be inferred that the band gap becomes higher as the particle becomes smaller. This means that for a smaller particle, the energy required for an electron to get excited is higher. The relation between energy and wavelength is given by (3.52), where h is the Planck's constant, c is the speed of light, λ

is the wavelength of light. Therefore, from (3.52) to cross a bandgap of greater energy, shorter wavelengths of light are absorbed, i.e., a blue shift is seen.

$$E = \frac{hc}{\lambda} \tag{3.52}$$

For Group 12-16 semiconductors, the bandgap energy falls in the UV-visible range. That is ultraviolet light or visible light can be used to excite an electron from the ground valence states to the excited conduction states. In a bulk semiconductor the band gap is fixed, and the energy states are continuous. This results in a rather uniform absorption spectrum (Figure 3.59a).

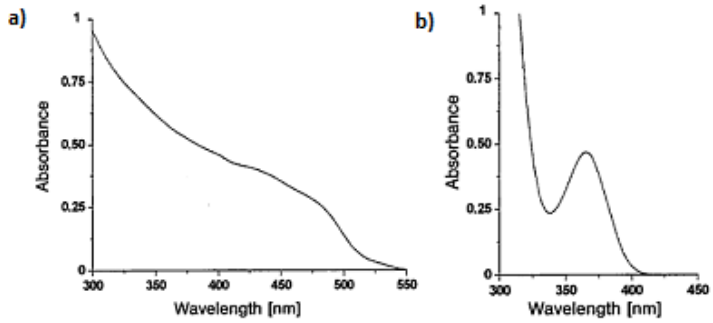

Figure 3.59: UV-vis spectra of (a) bulk CdS and (b) 4 nm CdS. Adapted from G. Kickelbick, *Hybrid Materials: Synthesis, Characterization and Applications*, Wiley-VCH, Weinheim (2007).

In the case of Group 12-16 quantum dots, since the bandgap can be changed with the size, these materials can absorb over a range of wavelengths. The peaks seen in the absorption spectrum (Figure 3.59b) correspond to the optical transitions between the electron and hole levels. The minimum energy and thus the maximum wavelength peak corresponds to the first exciton peak or the energy for an electron to get excited from the highest valence state to the lowest conduction state. The quantum dot will not absorb wavelengths of energy longer than this wavelength. This is known as the absorption onset.

3.2.1.3.4 Fluorescence

Fluorescence is the emission of electromagnetic radiation in the form of light by a material that has absorbed a photon. When a semiconductor quantum dot (QD) absorbs a photon/energy equal to or greater than its band gap, the electrons in the QD's get excited to the conduction state. This excited state is however not stable. The electron can relax back to its ground state by either emitting a photon or lose energy via heat losses. These processes can be divided into two categories – radiative decay and non-radiative decay. Radiative decay is the loss of energy through the emission of a photon or radiation. Non-radiative decay involves the loss of heat through lattice vibrations and this usually occurs when the energy difference between the levels is small. Non-radiative decay occurs much faster than radiative decay.

Usually the electron relaxes to the ground state through a combination of both radiative and non-radiative decays. The electron moves quickly through the conduction energy levels through small non-radiative decays and the final transition across the band gap is via a radiative decay. Large nonradiative decays don't occur across the band gap because the crystal structure can't withstand large vibrations without breaking the bonds of the crystal. Since some of the energy is lost through the non-radiative decay, the energy of the emitted photon, through the radiative decay, is much lesser than the absorbed energy. As a result the

wavelength of the emitted photon or fluorescence is longer than the wavelength of absorbed light. This energy difference is called the Stokes shift. Due this Stokes shift, the emission peak corresponding to the absorption band edge peak is shifted towards a higher wavelength (lower energy), i.e., Figure 3.60.

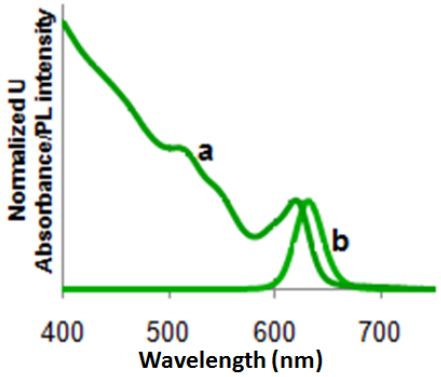

Figure 3.60: Absorption spectra (a) and emission spectra (b) of CdSe tetrapod.

Intensity of emission versus wavelength is a bell-shaped Gaussian curve. As long as the excitation wavelength is shorter than the absorption onset, the maximum emission wavelength is independent of the excitation wavelength. Figure 3.60 shows a combined absorption and emission spectrum for a typical CdSe tetrapod.

3.2.1.3.5 Factors affecting the optical properties of NPs

There are various factors that affect the absorption and emission spectra for Group 12-16 semiconductor quantum crystals. Fluorescence is much more sensitive to the background, environment, presence of traps and the surface of the QDs than UV-visible absorption. Some of the major factors influencing the optical properties of quantum nanoparticles include:

- **Surface defects, imperfection of lattice, surface charges** – The surface defects and imperfections in the lattice structure of semiconductor quantum dots occur in the form of unsatisfied valencies. Similar to surface charges, unsatisfied valencies provide a sink for the charge carriers, resulting in unwanted recombinations.
- **Surface ligands** – The presence of surface ligands is another factor that affects the optical properties. If the surface ligand coverage is a 100%, there is a smaller chance of surface recombinations to occur.
- **Solvent polarity** – The polarity of solvents is very important for the optical properties of the nanoparticles. If the quantum dots are prepared in organic solvent and have an organic surface ligand, the more non-polar the solvent, the particles are more dispersed. This reduces the loss of electrons through recombinations again, since when particles come in close proximity to each other, increases the non-radiative decay events.

3.2.1.3.6 Applications of the optical properties of Group 12-16 semiconductor NPs

The size dependent optical properties of NP's have many applications from biomedical applications to solar cell technology, from photocatalysis to chemical sensing. Most of these applications use the following unique properties.

For applications in the field of nanoelectronics, the sizes of the quantum dots can be tuned to be comparable to the scattering lengths, reducing the scattering rate and hence, the signal to noise ratio. For Group 12-16 QDs to be used in the field of solar cells, the bandgap of the particles can be tuned so as to form absorb energy over a large range of the solar spectrum, resulting in more number of excitons and hence more electricity. Since the nanoparticles are so small, most of the atoms are on the surface. Thus, the surface to volume ratio is very large for the quantum dots. In addition to a high surface to volume ratio, the Group 12-16 QDs respond to light energy. Thus quantum dots have very good photocatalytic properties. Quantum dots show fluorescence properties, and emit visible light when excited. This property can be used for applications as biomarkers. These quantum dots can be tagged to drugs to monitor the path of the drugs. Specially shaped Group 12-16 nanoparticles such as hollow shells can be used as drug delivery agents. Another use for the fluorescence properties of Group 12-16 semiconductor QDs is in color-changing paints, which can change colors according to the light source used.

3.2.1.3.7 Bibliography

- M. J. Schulz, V. N. Shanov, and Y. Yun, *Nanomedicine - Design of Particles, Sensors, Motors, Implants, Robots, and Devices*, Artech House, London (2009).
- S. V. Gapoenko, *Optical Properties of Semiconductor Nanocrystals*, Cambridge University Press, Cambridge (2003).
- T. Pradeep, *Nano: The Essentials. Understanding Nanoscience and Nanotechnology*, Tata McGraw-Hill, New Delhi (2007).
- G. Schmid, *Nanoparticles: From Theory to Application*, Wiley-VCH, Weinheim (2004).
- A. L. Rogach, *Semiconductor Nanocrystal Quantum Dots. Synthesis, Assembly, Spectroscopy and Applications*, Springer Wien, New York (2008).
- G. Kickelbick, *Hybrid Materials: Synthesis, Characterization and Applications*, Wiley-VCH, Weinheim (2007).

3.2.2 Band Gap Measurement[13]

3.2.2.1 Introduction

In solid state physics a *band gap* also called an energy gap, is an energy range in an ideal solid where no electron states can exist. As shown in Figure 3.61 for an insulator or semiconductor the band gap generally refers to the energy difference between the top of the valence band and the bottom of the conduction band. This is equivalent to the energy required to free an outer shell electron from its orbit about the nucleus to become a mobile charge carrier, able to move freely within the solid material.

[13] This content is available online at <http://cnx.org/content/m43554/1.1/>.

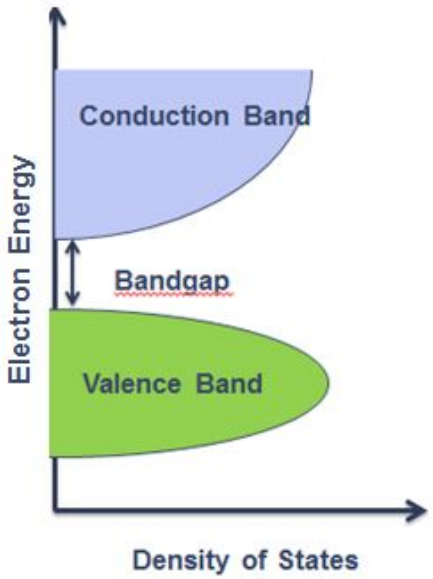

Figure 3.61: Schematic explanation of band gap.

The band gap is a major factor determining the electrical conductivity of a solid. Substances with large band gaps are generally insulators (i.e., dielectric), those with smaller band gaps are semiconductors, while conductors either have very small band gaps or no band gap (because the valence and conduction bands overlap as shown in Figure 3.62).

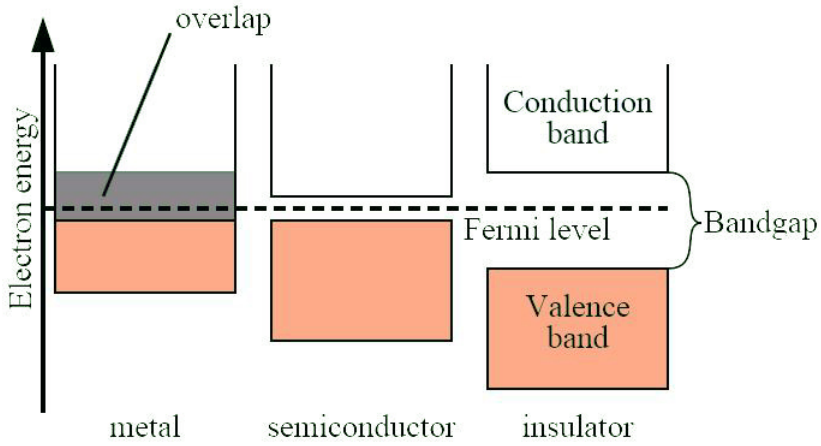

Figure 3.62: Schematic representation of the band gap difference in a metal, a semiconductor and an insulator.

The theory of bands in solids is one of the most important steps in the comprehension of the properties of solid matter. The existence of a forbidden energy gap in semiconductors is an essential concept in order to be able to explain the physics of semiconductor devices. For example, the magnitude of the bad gap of solid determines the frequency or wavelength of the light, which will be adsorbed. Such a value is useful for photocatalysts and for the performance of a dye sensitized solar cell.

Nanocomposites materials are of interest to researchers the world over for various reasons. One driver for such research is the potential application in next-generation electronic and photonic devices. Particles of a nanometer size exhibit unique properties such as quantum effects, short interface migration distances (and times) for photoinduced holes and electrons in photochemical and photocatalytic systems, and increased sensitivity in thin film sensors.

3.2.2.2 Measurement methods

3.2.2.2.1 Electrical measurement method

For a p-n junction, the essential electrical characteristic is that it constitutes a rectifier, which allows the easy flow of a charge in one direction but restrains the flow in the opposite direction. The voltage-current characteristic of such a device can be described by the Shockley equation, (3.53), in which,I_0 is the reverse bias saturation current, q the charge of the electron, k is Boltzmann's constant, and T is the temperature in Kelvin.

$$I = I_0(\exp(qV/kT)-1) \tag{3.53}$$

When the reverse bias is very large, the current I is saturated and equal to I_0. This saturation current is the sum of several different contributions. They are diffusion current, generation current inside the depletion zone, surface leakage effects and tunneling of carriers between states in the band gap. In a first approximation at a certain condition, I_0 can be interpreted as being solely due to minority carriers accelerated by the depletion zone field plus the applied potential difference. Therefore it can be shown that, (3.54), where A is a constant, E_g the energy gap (slightly temperature dependent), and γ an integer depending on the

temperature dependence of the carrier mobility μ.

$$I_0 = AT^{(3+\gamma/2)}\exp(-E_g(T)/KT) \tag{3.54}$$

We can show that γ is defined by the relation by a more advanced treatment, (3.55).

$$T\mu^2 = T^{\gamma} \tag{3.55}$$

After substituting the value of I_0 given by (3.54) into (3.53), we take the napierian logarithm of the two sides and multiply them by kT for large forward bias ($qV > 3kT$); thus, rearranging, we have (3.56).

$$qV = E_g(T) + T[k\ \mathrm{In}(l/A)] - (3+\gamma/2)k\mathrm{InT} \tag{3.56}$$

As InT can be considered as a slowly varying function in the 200 - 400 K interval, therefore for a constant current, I, flowing through the junction a plot of qV versus the temperature should approximate a straight line, and the intercept of this line with the qV axis is the required value of the band gap E_g extrapolated to 0 K. Through (3.57) instead of qV, we can get a more precise value of Eg.

$$qV_c = qV + (3+\gamma/2)k\mathrm{InT} \tag{3.57}$$

(3.55) shows that the value of γ depends on the temperature and μ that is a very complex function of the particular materials, doping and processing. In the 200 - 400 K range, one can estimate that the variation ΔE_g produced by a change of $\Delta\gamma$ in the value of γ is (3.58). So a rough value of γ is sufficient for evaluating the correction. By taking the experimental data for the temperature dependence of the mobility μ, a mean value for γ can be found. Then the band gap energy qV can be determined.

$$\Delta E_g = 10^{-2}\,\mathrm{eV}\ \Delta\gamma \tag{3.58}$$

The electrical circuit required for the measurement is very simple and the constant current can be provided by a voltage regulator mounted as a constant current source (see Figure 3.63). The potential difference across the junction can be measured with a voltmeter. Five temperature baths were used: around 90 °C with hot water, room temperature water, water-ice mixture, ice-salt-water mixture andmixture of dry ice and acetone. The result for GaAs is shown in Figure 3.64. The plot $qV_{corrected}$ (qV_c) versus temperature gives $E_1 = 1.56 \pm 0.02$ eV for GaAs. This may be compared with literature value of 1.53 eV.

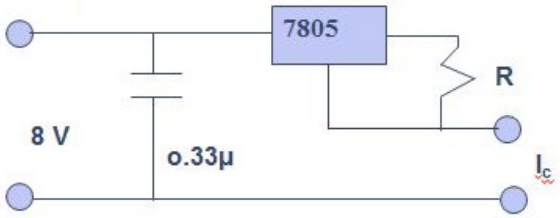

Figure 3.63: Schematic of the constant current source. ($I_c = 5V/R$). Adapted from Y. Canivez, *Eur. J. Phys.*, 1983, **4**, 42.

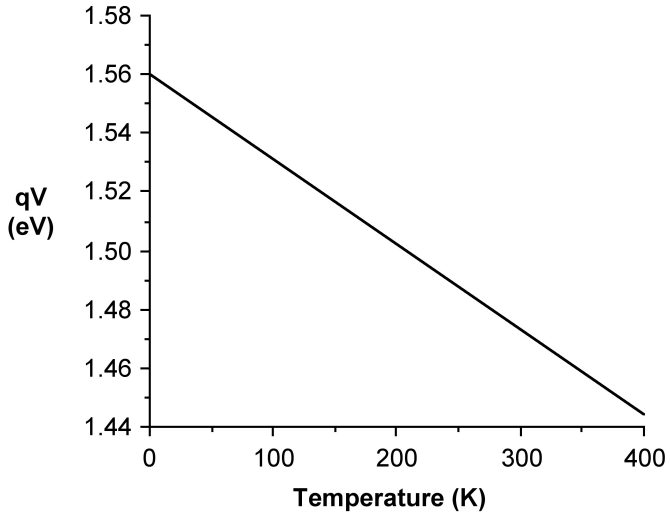

Figure 3.64: Plot of corrected voltage versus temperature for GaAs. Adapted from Y. Canivez, *Eur. J. Phys.*, 1983, **4**, 42.

3.2.2.2.2 Optical measurement method

Optical method can be described by using the measurement of a specific example, e.g., hexagonal boron nitride (h-BN, Figure 3.65). The UV-visible absorption spectrum was carried out for investigating the optical energy gap of the h-BN film based on its optically induced transition.

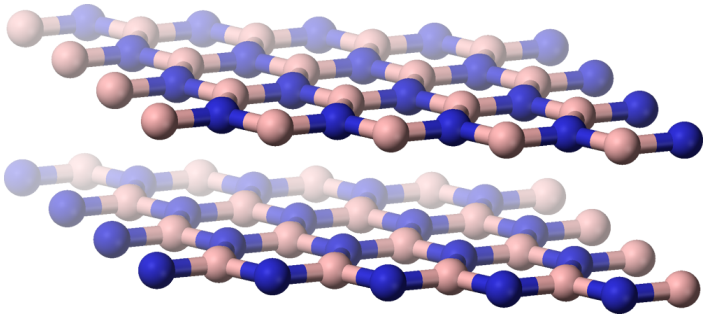

Figure 3.65: The structure of hexagonal boron nitride (h-BN).

For this study, a sample of h-BN was first transferred onto an optical quartz plate, and a blank quartz

plate was used for the background as the reference substrate. The following Tauc's equation was used to determine the optical band gap E_g , (3.59), where ε is the optical absorbance, λ is the wavelength and $\omega = 2\pi/\lambda$ is the angular frequency of the incident radiation.

$$\omega^2\varepsilon = (\hbar\omega - E_g)^2 \tag{3.59}$$

As Figure 3.66a shows, the absorption spectrum has one sharp absorption peak at 201 - 204 nm. On the basis of Tauc's formulation, it is speculated that the plot of $\varepsilon^{1/2}/\lambda$ versus $1/\lambda$ should be a straight line at the absorption range. Therefore, the intersection point with the x axis is $1/\lambda_g$ (λ_g is defined as the gap wavelength). The optical band gap can be calculated based on E_g) hc/λ_g. The plot in Figure 3.66b shows $\varepsilon^{1/2}/\lambda$ versus $1/\lambda$ curve acquired from the thin h-BN film. For more than 10 layers sample, he calculated gap wavelength λ_g is about 223 nm, which corresponds to an optical band gap of 5.56 eV.

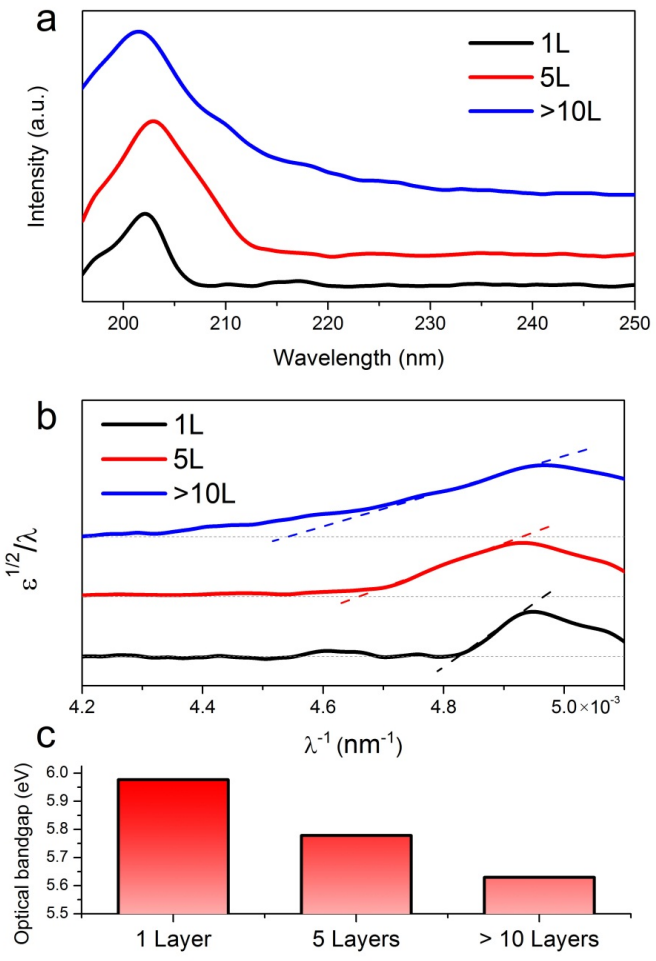

Figure 3.66: Ultraviolet-visible adsorption spectra of h-BN films of various thicknesses taken at room temperature. (a) UV adsorption spectra of 1L, 5L and thick (>10L) h-BN films. (b) Corresponding plots of $\varepsilon^{1/2}/\lambda$ versus $1/\lambda$. (c) Calculated optical band gap for each h-BN films.

Previous theoretical calculations of a single layer of h-BN shows 6 eV band gap as the result. The thickness of h-BN film are 1 layer, 5 layers and thick (>10 layers) h-BN films, the measured gap is about 6.0, 5.8, 5.6 eV, respectively, which is consistent with the theoretical gap value. For thicker samples, the layer-layer interaction increases the dispersion of the electronic bands and tends to reduce the gap. From this example, we can see that the band gap is relative to the size of the materials, this is the most important feature of nano material.

3.2.2.3 Bibliography:

- Y. Canivez, *Eur. J. Phys.* 1983, **4**, 42.
- S. U. M. Khan, M. Al-Shahry, and W. B. Ingler Jr., *Science*, 2002, **297**, 2243.
- B. O'Regan and M. Grätzel, *Nature*, 1991, **353**, 737.
- S. Uchida, Y. Yamamoto, Y. Fujishiro, A. Watanabe, O. Ito, and T. Sato, *J. Chem. Soc., Farady Trans.*, 1997, **93**, 3229.
- T. Sato, Y. Yamamoto, Y. Fujishiro, and S. Uchida, *J. Chem. Soc., Farady Trans.*, 1996, **92**, 5089.
- T. Sato, K. Masaki, K. Sato, Y. Fujishiro, and A. Okuwaki, *J. Chem. Tech. Biotechnol.*, 1996, **67**, 339.
- L. Song, L. Ci, and P. M. Ajayan, *Nano Lett.* 2010, **10**, 3209.
- J. Tauc, R. Grigorovici, and A. Vancu, *Phys. Status Solidi.* 1996, **15**, 627.
- X. Blase, A. Rubio, S. G. Louie, and M. L. Cohen, *Phys. Rev. B*, 1995, **51**, 6868.
- D. M. Hoffman, G. L. Doll, and P. C. Eklund, *Phys. Rev. B*, 1984, **30**, 6051.

3.2.3 Using UV-vis for the detection and characterization of silicon quantum dots[14]

3.2.3.1 What are quantum dots?

Quantum dots (QDs) are small semiconductor nanoparticles generally composed of two elements that have extremely high quantum efficiencies when light is shined on them. The most common quantum dots are CdSe, PbS, and ZnSe, but there are many many other varieties of these particles that contain other elements as well. QDs can also be made of just three elements or just one element such as silicon.

3.2.3.2 Synthesis of silicon quantum dots

Silicon quantum dots are synthesized in inverse micelles. $SiCl_4$ is reduced using a two fold excess of $LiAlH_4$ (Figure 3.67). After the silicon has been fully reduced and the excess reducing agent quenched, the particles are capped with hydrogens and are hydrophobic. A platinum catalyzed ligand exchange of hydrogen for allylamine will produce hydrophilic particles (Figure 3.68). All reactions in making these particles are extremely air sensitive, and silica is formed readily, so the reactions should be performed in a highly controlled atmosphere, such as a glove box. The particles are then washed in DMF, and finally filtered and stored in deionized water. This will allow the Si QDs to be pure in water, and the particles are ready for analysis. This technique yields Si QDs of 1 - 2 nm in size.

[14]This content is available online at <http://cnx.org/content/m34655/1.1/>.

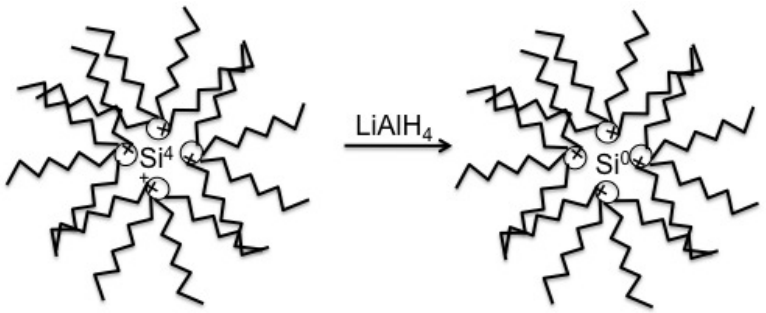

Figure 3.67: A schematic representation of the inverse micelle used for the synthesis of Si QDs.

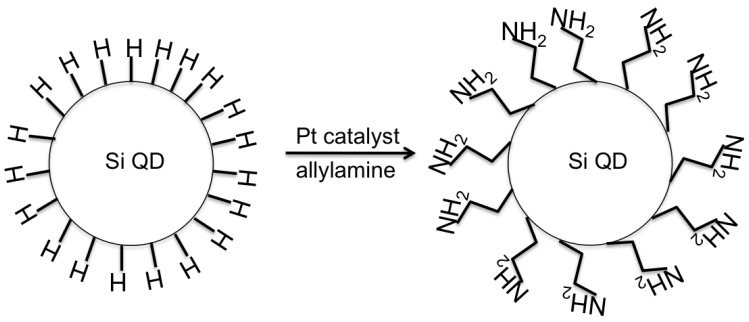

Figure 3.68: Conversion of hydrophobic Si QDs to hydrophillic Si QDs. Adapted from J. H. Warner, A. Hoshino, K. Yamamoto, and R. D. Tilley, *Angew. Chem., Int. Ed.*, 2005, **44**, 4550. Copyright: American Chemical Society (2005).

3.2.3.2.1 Sample preparation of Si QDs

The reported absorbtion wavelength for 1 - 2 nm Si QDs absorb is 300 nm. With the hydrophobic Si QDs, UV-vis absorbance analysis in toluene does not yield an acceptable spectrum because the UV-vis absorbance cutoff is 287 nm, which is very close to 300 nm for the peaks to be resolvable. A better hydrophobic solvent would be hexanes. All measurements of these particles would require a quartz cuvette since the glass aborbance cutoff (300 nm) is exactly where the particles would be observed. Hydrophilic substituted particles do not need to be transferred to another solvent because water's absorbance cutoff is much lower. There is usually a slight impurity of DMF in the water due to residue on the particles after drying. If there is a DMF peak in the spectrum with the Si QDs the wavelengths are far enough apart to be resolved.

3.2.3.3 What information can be obtained from UV-visible spectra?

Quantum dots are especially interesting when it comes to UV-vis spectroscopy because the size of the quantum dot can be determined from the position of the absorbtion peak in the UV-vis spectrum. Quantum dots absorb different wavelengths depending on the size of the particles (e.g., Figure 3.69). Many calibration curves would need to be done to determine the exact size and concentration of the quantum dots, but it is entirely possible and very useful to be able to determine size and concentration of quantum dots in this way since other ways of determining size are much more expensive and extensive (electron microscopy is most widely used for this data).

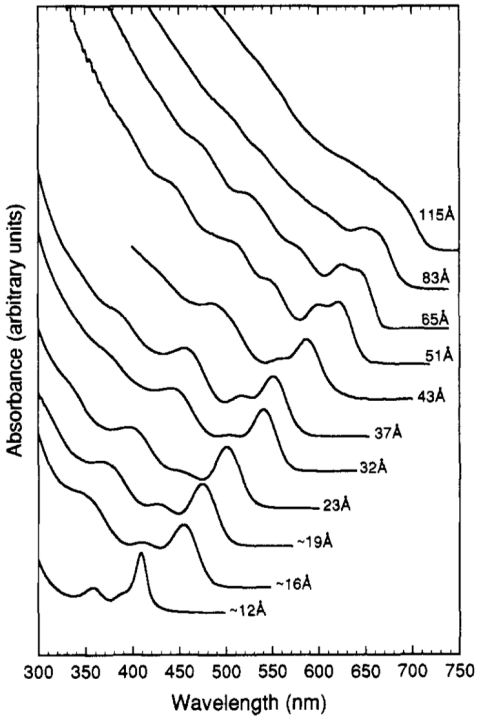

Figure 3.69: Absorbance of different sized CdSe QDs. Reprinted with permission from C. B. Murray, D. J. Norris, and M. G. Bawendi, *J. Am. Chem. Soc.*, 1993, **115**, 8706. Copyright: American Chemical Society (1993).

An example of silicon quantum dot data can be seen in Figure 3.70. The wider the absorbance peak is, the less monodispersed the sample is.

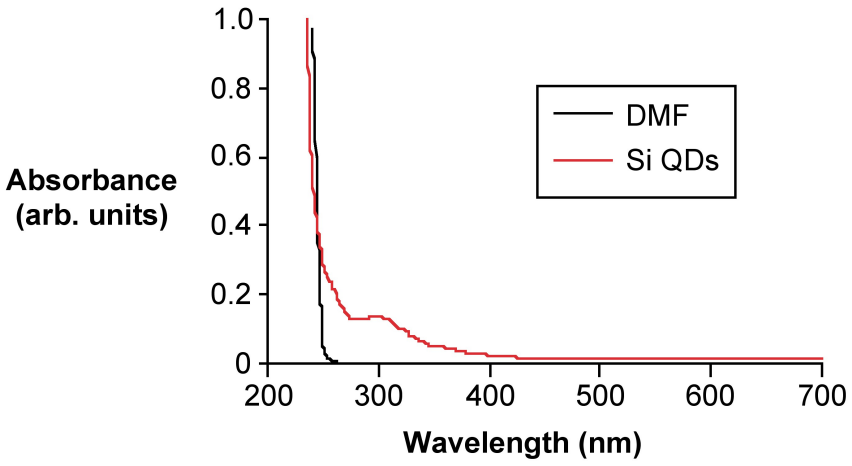

Figure 3.70: UV-vis absorbance spectrum of 1 - 2 nm Si QDs with a DMF reference spectrum.

3.2.3.3.1 Why is knowing the size of QDs important?

Different size (different excitation) quantum dots can be used for different applications. The absorbance of the QDs can also reveal how monodispersed the sample is; more monodispersity in a sample is better and more useful in future applications. Silicon quantum dots in particular are currently being researched for making more efficient solar cells. The monodispersity of these quantum dots is particularly important for getting optimal absorbance of photons from the sun or other light source. Different sized quantum dots will absorb light differently, and a more exact energy absorption is important in the efficiency of solar cells. UV-vis absorbance is a quick, easy, and cheap way to determine the monodispersity of the silicon quantum dot sample. The peak width of the absorbance data can give that information. The other important information for future applications is to get an idea about the size of the quantum dots. Different size QDs absorb at different wavelengths; therefore, specific size Si QDs will be required for different cells in tandem solar cells.

3.2.3.4 Bibliography

- J. H. Warner, A. Hoshino, K. Yamamoto, and R. D. Tilley, *Angew. Chem., Int. Ed.*, 2005, **44**, 4550.
- C. B. Murray, D. J. Norris, and M. G. Bawendi, *J. Am. Chem. Soc.*, 1993, **115**, 8706.

3.2.4 Characterization of Group 12-16 (II-VI) Semiconductor Nanoparticles by UV-visible Spectroscopy[15]

Quantum dots (QDs) as a general term refer to nanocrystals of semiconductor materials, in which the size of the particles are comparable to the natural characteristic separation of an electron-hole pair, otherwise known as the exciton Bohr radius of the material. When the size of the semiconductor nanocrystal becomes this small, the electronic structure of the crystal is governed by the laws of quantum physics. Very small Group 12-16 (II-VI) semiconductor nanoparticle quantum dots, in the order of 2 - 10 nm, exhibit significantly different optical and electronic properties from their bulk counterparts. The characterization of size dependent optical

[15]This content is available online at <http://cnx.org/content/m34601/1.1/>.

properties of Group 12-16 semiconductor particles provide a lot of qualitative and quantitative information about them – size, quantum yield, monodispersity, shape and presence of surface defects. A combination of information from both the UV-visible absorption and fluorescence, complete the analysis of the optical properties.

3.2.4.1 UV-visible absorbance spectroscopy

Absorption spectroscopy, in general, refers to characterization techniques that measure the absorption of radiation by a material, as a function of the wavelength. Depending on the source of light used, absorption spectroscopy can be broadly divided into infrared and UV-visible spectroscopy. The band gap of Group 12-16 semiconductors is in the UV-visible region. This means the minimum energy required to excite an electron from the valence states of the Group 12-16 semiconductor QDs to its conduction states, lies in the UV-visible region. This is also a reason why most of the Group 12-16 semiconductor quantum dot solutions are colored.

This technique is complementary to fluorescence spectroscopy, in that UV-visible spectroscopy measures electronic transitions from the ground state to the excited state, whereas fluorescence deals with the transitions from the excited state to the ground state. In order to characterize the optical properties of a quantum dot, it is important to characterize the sample with both these techniques

In quantum dots, due to the very small number of atoms, the addition or removal of one atom to the molecule changes the electronic structure of the quantum dot dramatically. Taking advantage of this property in Group 12-16 semiconductor quantum dots, it is possible to change the band gap of the material by just changing the size of the quantum dot. A quantum dot can absorb energy in the form of light over a range of wavelengths, to excite an electron from the ground state to its excited state. The minimum energy that is required to excite an electron, is dependent on the band gap of the quantum dot. Thus, by making accurate measurements of light absorption at different wavelengths in the ultraviolet and visible spectrum, a correlation can be made between the band gap and size of the quantum dot. Group 12-16 semiconductor quantum dots are of particular interest, since their band gap lies in the visible region of the solar spectrum.

The UV-visible absorbance spectroscopy is a characterization technique in which the absorbance of the material is studied as a function of wavelength. The visible region of the spectrum is in the wavelength range of 380 nm (violet) to 740 nm (red) and the near ultraviolet region extends to wavelengths of about 200 nm. The UV-visible spectrophotometer analyzes over the wavelength range $200 - 900$ nm.

When the Group 12-16 semiconductor nanocrystals are exposed to light having an energy that matches a possible electronic transition as dictated by laws of quantum physics, the light is absorbed and an exciton pair is formed. The UV-visible spectrophotometer records the wavelength at which the absorption occurs along with the intensity of the absorption at each wavelength. This is recorded in a graph of absorbance of the nanocrystal versus wavelength.

3.2.4.2 Instrumentation

A working schematic of the UV-visible spectrophotometer is shown in Figure 3.71.

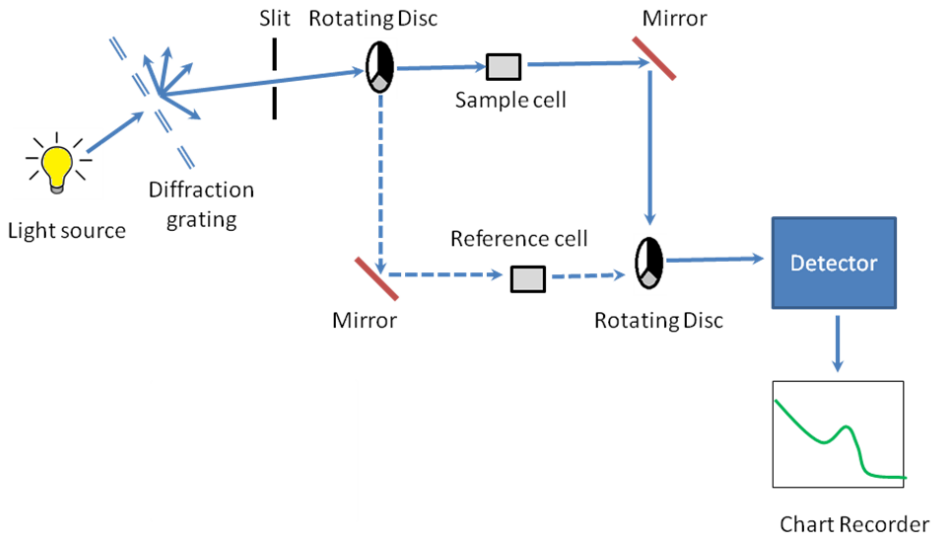

Figure 3.71: Schematic of UV-visible spectrophotometer.

3.2.4.2.1 The light source

Since it is a UV-vis spectrophotometer, the light source (Figure 3.71) needs to cover the entire visible and the near ultra-violet region (200 - 900 nm). Since it is not possible to get this range of wavelengths from a single lamp, a combination of a deuterium lamp for the UV region of the spectrum and tungsten or halogen lamp for the visible region is used. This output is then sent through a diffraction grating as shown in the schematic.

3.2.4.2.2 The diffraction grating and the slit

The beam of light from the visible and/or UV light source is then separated into its component wavelengths (like a very efficient prism) by a diffraction grating (Figure 3.71). Following the slit is a slit that sends a monochromatic beam into the next section of the spectrophotometer.

3.2.4.2.3 Rotating discs

Light from the slit then falls onto a rotating disc (Figure 3.71). Each disc consists of different segments – an opaque black section, a transparent section and a mirrored section. If the light hits the transparent section, it will go straight through the sample cell, get reflected by a mirror, hits the mirrored section of a second rotating disc, and then collected by the detector. Else if the light hits the mirrored section, gets reflected by a mirror, passes through the reference cell, hits the transparent section of a second rotating disc and then collected by the detector. Finally if the light hits the black opaque section, it is blocked and no light passes through the instrument, thus enabling the system to make corrections for any current generated by the detector in the absence of light.

3.2.4.2.4 Sample cell, reference cell and sample preparation

For liquid samples, a square cross section tube sealed at one end is used. The choice of cuvette depends on the following factors:

- **Type of solvent -** For aqueous samples, specially designed rectangular quartz, glass or plastic cuvettes are used. For organic samples glass and quartz cuvettes are used.
- **Excitation wavelength** – Depending on the size and thus, bandgap of the 12-16 semiconductor nanoparticles, different excitation wavelengths of light are used. Depending on the excitation wavelength, different materials are used

Cuvette	Wavelength (nm)
Visible only glass	380 - 780
Visible only plastic	380 - 780
UV plastic	220 - 780
Quartz	200 - 900

Table 3.6: Cuvette materials and their wavelengths.

- **Cost** – Plastic cuvettes are the least expensive and can be discarded after use. Though quartz cuvettes have the maximum utility, they are the most expensive, and need to reused. Generally, disposable plastic cuvettes are used when speed is more important than high accuracy.

The best cuvettes need to be very clear and have no impurities that might affect the spectroscopic reading. Defects on the cuvette such as scratches, can scatter light and hence should be avoided. Some cuvettes are clear only on two sides, and can be used in the UV-Visible spectrophotometer, but cannot be used for fluorescence spectroscopy measurements. For Group 12-16 semiconductor nanoparticles prepared in organic solvents, the quartz cuvette is chosen.

In the sample cell the quantum dots are dispersed in a solvent, whereas in the reference cell the pure solvent is taken. It is important that the sample be very dilute (maximum first exciton absorbance should not exceed 1 au) and the solvent is not UV-visible active. For these measurements, it is required that the solvent does not have characteristic absorption or emission in the region of interest. Solution phase experiments are preferred, though it is possible to measure the spectra in the solid state also using thin films, powders, etc. The instrumentation for solid state UV-visible absorption spectroscopy is slightly different from the solution phase experiments and is beyond the scope of discussion.

3.2.4.2.5 Detector

Detector converts the light into a current signal that is read by a computer. Higher the current signal, greater is the intensity of the light. The computer then calculates the absorbance using the in (3.60), where A denotes absorbance, I is sample cell intensity and I_o is the reference cell intensity.

$$A = \log_{10}(I_0/I) \tag{3.60}$$

The following cases are possible:

- Where $I < I_0$ and $A < 0$. This usually occurs when the solvent absorbs in the wavelength range. Preferably the solvent should be changed, to get an accurate reading for actual reference cell intensity.
- Where $I = I_0$ and $A = 0$. This occurs when pure solvent is put in both reference and sample cells. This test should always be done before testing the sample, to check for the cleanliness of the cuvettes.
- When $A = 1$. This occurs when 90% or the light at a particular wavelength has been absorbed, which means that only 10% is seen at the detector. So I_0/I becomes $100/10 = 10$. Log_{10} of 10 is 1.
- When $A > 1$. This occurs in extreme case where more than 90% of the light is absorbed.

3.2.4.2.6 Output

The output is the form of a plot of absorbance against wavelength, e.g., Figure 3.72.

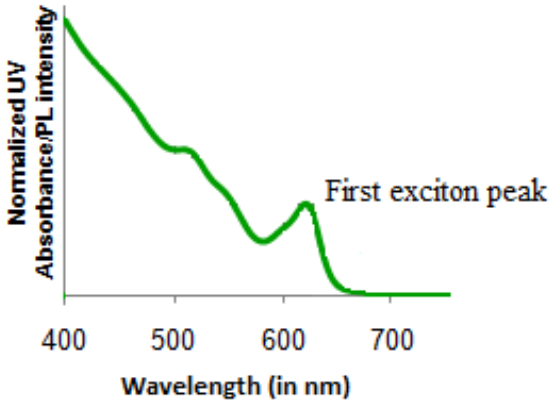

Figure 3.72: Representative UV-visble absorption spectrum for CdSe tetrapods.

3.2.4.3 Beer-Lambert law

In order to make comparisons between different samples, it is important that all the factors affecting absorbance should be constant except the sample itself.

3.2.4.3.1 Effect of concentration on absorbance

The extent of absorption depends on the number of absorbing nanoparticles or in other words the concentration of the sample. If it is a reasonably concentrated solution, it will have a high absorbance since there are lots of nanoparticles to interact with the light. Similarly in an extremely dilute solution, the absorbance is very low. In order to compare two solutions, it is important that we should make some allowance for the concentration.

3.2.4.3.2 Effect of container shape

Even if we had the same concentration of solutions, if we compare two solutions – one in a rectagular shaped container (e.g., Figure 3.73) so that light travelled 1 cm through it and the other in which the light travelled 100 cm through it, the absorbance would be different. This is because if the length the light travelled is greater, it means that the light interacted with more number of nanocrystals, and thus has a higher absorbance. Again, in order to compare two solutions, it is important that we should make some allowance for the concentration.

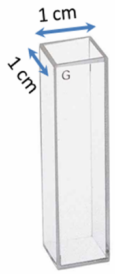

Figure 3.73: A typical rectangular cuvette for UV-visible spectroscopy.

3.2.4.3.3 The law

The Beer-Lambert law addresses the effect of concentration and container shape as shown in (3.60), (3.61) and (3.62), where A denotes absorbance; ε is the molar absorptivity or molar absorption coefficient; l is the path length of light (in cm); and c is the concentration of the solution (mol/dm^3).

$$\log_{10}(I_0/I) = \varepsilon l c \tag{3.61}$$

$$A = \varepsilon l c \tag{3.62}$$

3.2.4.3.4 Molar absorptivity

From the Beer-Lambert law, the molar absorptivity 'ε' can be expressed as shown in (3.63).

$$c = A/l\varepsilon \tag{3.63}$$

Molar absorptivity corrects for the variation in concentration and length of the solution that the light passes through. It is the value of absorbance when light passes through 1 cm of a 1 mol/dm^3 solution.

3.2.4.3.5 Limitations of Beer-Lambert law

The linearity of the Beer-Lambert law is limited by chemical and instrumental factors.

- At high concentrations ($>$ 0.01 M), the relation between absorptivity coefficient and absorbance is no longer linear. This is due to the electrostatic interactions between the quantum dots in close proximity.
- If the concentration of the solution is high, another effect that is seen is the scattering of light from the large number of quantum dots.
- The spectrophotometer performs calculations assuming that the refractive index of the solvent does not change significantly with the presence of the quantum dots. This assumption only works at low concentrations of the analyte (quantum dots).
- Presence of stray light.

3.2.4.4 Analysis of data

The data obtained from the spectrophotometer is a plot of absorbance as a function of wavelength. Quantitative and qualitative data can be obtained by analysing this information

3.2.4.4.1 Quantitative Information

The band gap of the semiconductor quantum dots can be tuned with the size of the particles. The minimum energy for an electron to get excited from the ground state is the energy to cross the band gap. In an absorption spectra, this is given by the first exciton peak at the maximum wavelength (λ_{max}).

3.2.4.4.1.1 Size of the quantum dots

The size of quantum dots can be approximated corresponding to the first exciton peak wavelength. Emperical relationships have been determined relating the diameter of the quantum dot to the wavelength of the first exciton peak. The Group 12-16 semiconductor quantum dots that they studied were cadmium selenide (CdSe), cadmium telluride (CdTe) and cadmium sulfide (CdS). The empirical relationships are determined by fitting experimental data of absorbance versus wavelength of known sizes of particles. The empirical equations determined are given for CdTe, CdSe, and CdS in (3.64), (3.65) and (3.66) respectively, where D is the diameter and λ is the wavelength corresponding to the first exciton peak. For example, if the first exciton peak of a CdSe quantum dot is 500 nm, the corresponding diameter of the quantum dot is 2.345 nm and for a wavelength of 609 nm, the corresponding diameter is 5.008 nm.

$$D = (9.8127 \times 10^{-7})\lambda^3 - (1.7147 \times 10^{-3})\lambda^2 + (1.0064)\lambda - 194.84 \quad (3.64)$$

$$D = (1.6122 \times 10^{-7})\lambda^3 - (2.6575 \times 10^{-6})\lambda^2 + (1.6242 \times 10^{-3})\lambda + 41.57 \quad (3.65)$$

$$D = (-6.6521 \times 10^{-8})\lambda^3 + (1.9577 \times 10^{-4})\lambda^2 - (9.2352 \times 10^{-2})\lambda + 13.29 \quad (3.66)$$

3.2.4.4.1.2 Concentration of sample

Using the Beer-Lambert law, it is possible to calculate the concentration of the sample if the molar absorptivity for the sample is known. The molar absorptivity can be calculated by recording the absorbance of a standard solution of 1 mol/dm^3 concentration in a standard cuvette where the light travels a constant distance of 1 cm. Once the molar absorptivity and the absorbance of the sample are known, with the length the light travels being fixed, it is possible to determine the concentration of the sample solution.

Empirical equations can be determined by fitting experimental data of extinction coefficient per mole of Group 12-16 semiconductor quantum dots, at 250 °C, to the diameter of the quantum dot, (3.67), (3.68), and (3.69).

$$\varepsilon = 10043 \times D^{2.12} \quad (3.67)$$

$$\varepsilon = 5857 \times D^{2.65} \quad (3.68)$$

$$\varepsilon = 21536 \times D^{2.3} \quad (3.69)$$

The concentration of the quantum dots can then be then be determined by using the Beer Lambert law as given by (3.63).

3.2.4.4.2 Qualitative Information

Apart from quantitative data such as the size of the quantum dots and concentration of the quantum dots, a lot of qualitative information can be derived from the absorption spectra.

3.2.4.4.2.1 Size distribution

If there is a very narrow size distribution, the first exciton peak will be very sharp (Figure 3.74). This is because due to the narrow size distribution, the differences in band gap between different sized particles will be very small and hence most of the electrons will get excited over a smaller range of wavelengths. In addition, if there is a narrow size distribution, the higher exciton peaks are also seen clearly.

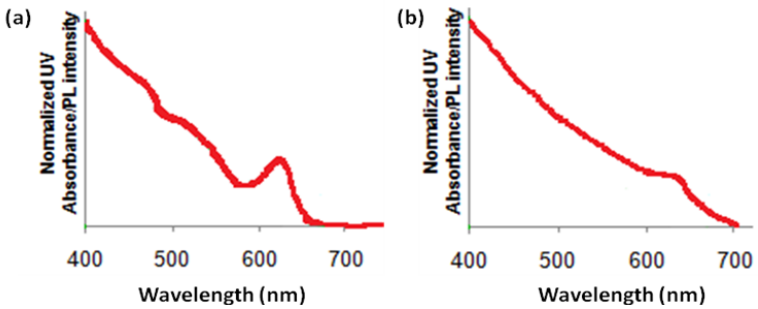

Figure 3.74: Narrow emission spectra (a) and broad emission spectra (b) of CdSe QDs.

3.2.4.4.2.2 Shaped particles

In the case of a spherical quantum dot, in all dimensions, the particle is quantum confined (Figure 3.75). In the case of a nanorod, whose length is not in the quantum regime, the quantum effects are determined by the width of the nanorod. Similar is the case in tetrapods or four legged structures. The quantum effects are determined by the thickness of the arms. During the synthesis of the shaped particles, the thickness of the rod or the arm of the tetrapod does not vary among the different particles, as much as the length of the rods or arms changes. Since the thickness of the rod or tetrapod is responsible for the quantum effects, the absorption spectrum of rods and tetrapods has sharper features as compared to a quantum dot. Hence, qualitatively it is possible to differentiate between quantum dots and other shaped particles.

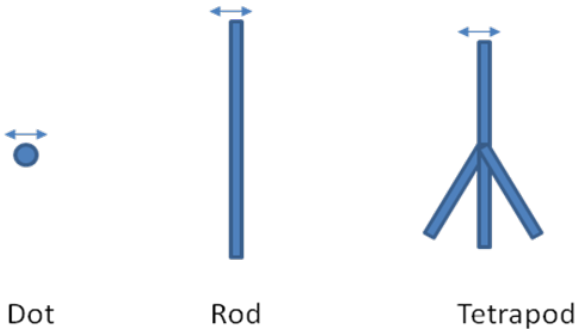

Figure 3.75: Different shaped nanoparticles with the arrows indicating the dimension where quantum confinement effects are observed.

3.2.4.4.2.3 Crystal lattice information

In the case of CdSe semiconductor quantum dots it has been shown that it is possible to estimate the crystal lattice of the quantum dot from the adsorption spectrum (Figure 3.76), and hence determine if the structure is zinc blend or wurtzite.

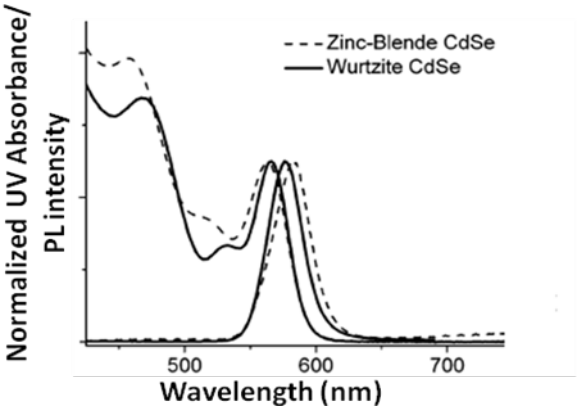

Figure 3.76: Zinc blende and wurtzite CdSe absorption spectra. Adapted from J. Jasieniak, C. Bullen, J. van Embden, and P. Mulvaney, *J. Phys. Chem. B*, 2005, **109**, 20665.

3.2.4.5 UV-vis absorption spectra of Group 12-16 semiconductor nanoparticles

3.2.4.5.1 Cadmium selenide

Cadmium selenide (CdSe) is one of the most popular Group 12-16 semiconductors. This is mainly because the band gap (712 nm or 1.74 eV) energy of CdSe. Thus, the nanoparticles of CdSe can be engineered

to have a range of band gaps throughout the visible range, corresponding to the major part of the energy that comes from the solar spectrum. This property of CdSe along with its fluorescing properties is used in a variety of applications such as solar cells and light emitting diodes. Though cadmium and selenium are known carcinogens, the harmful biological effects of CdSe can be overcome by coating the CdSe with a layer of zinc sulfide. Thus CdSe, can also be used as bio-markers, drug-delivery agents, paints and other applications.

A typical absorption spectrum of narrow size distribution wurtzite CdSe quantum dot is shown in Figure 3.77. A size evolving absorption spectra is shown in Figure 3.78. However, a complete analysis of the sample is possible only by also studying the fluorescence properties of CdSe.

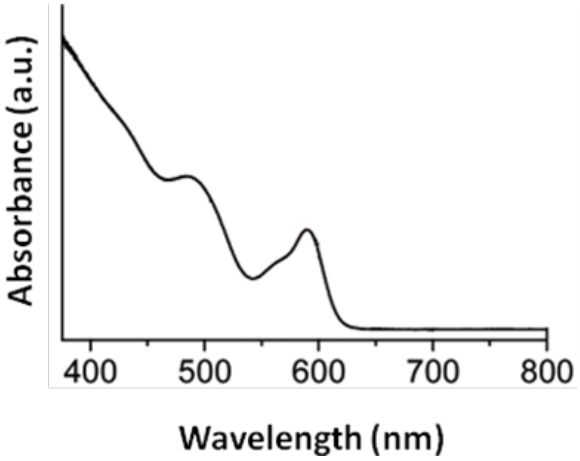

Figure 3.77: Wurtzite CdSe quantum dot. Adapted from X. Zhong, Y. Feng, and Y. Zhang, *J. Phys. Chem. C*, 2007, **111**, 526.

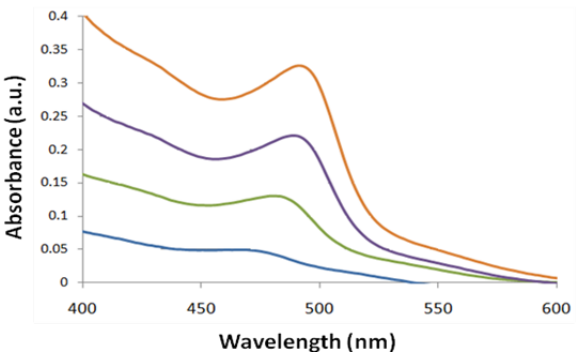

Figure 3.78: Size evolving absorption spectra of CdSe quantum dots.

3.2.4.5.2 Cadmium telluride (CdTe)

Cadmium telluride has a band gap of 1.44 eV (860 nm) and as such it absorbs in the infrared region. Like CdSe, the sizes of CdTe can be engineered to have different band edges and thus, different absorption spectra as a function of wavelength. A typical CdTe spectra is shown in Figure 3.79. Due to the small bandgap energy of CdTe, it can be used in tandem with CdSe to absorb in a greater part of the solar spectrum.

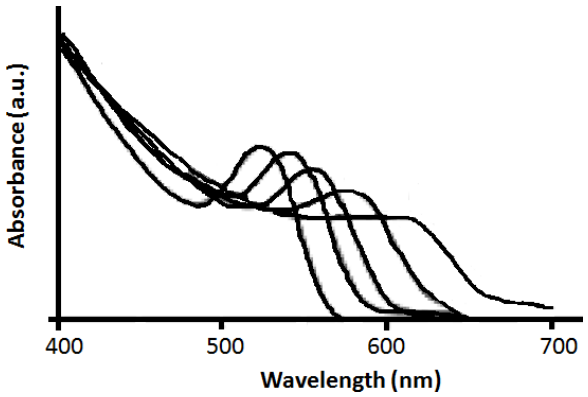

Figure 3.79: Size evolving absorption spectra of CdTe quantum dots from 3 nm to 7 nm. Adapted from C. Qi-Fan, W. Wen-Xing, G. Ying-Xin, L. Meng-Ying, X. Shu-Kun and Z. Xiu-Juan, *Chin. J. Anal. Chem.*, 2007, **35**, 135.

3.2.4.5.3 Other Group 12-16 semiconductor systems

Table 3.7 shows the bulk band gap of other Group 12-16 semiconductor systems. The band gap of ZnS falls in the UV region, while those of ZnSe, CdS, and ZnTe fall in the visible region.

Material	Band gap (eV)	Wavelength (nm)
ZnS	3.61	343.2
ZnSe	2.69	460.5
ZnTe	2.39	518.4
CdS	2.49	497.5
CdSe	1.74	712.1
CdTe	1.44	860.3

Table 3.7: Bulk band gaps of different Group 12-16 semiconductors.

3.2.4.5.4 Heterostructures of Group 12-16 semiconductor systems

It is often desirable to have a combination of two Group 12-16 semiconductor system quantum heterostructures of different shapes like dots and tetrapods, for applications in solar cells, bio-markers, etc. Some of the most interesting systems are ZnS shell-CdSe core systems, such as the CdSe/CdS rods and tetrapods.

Figure 3.80 shows a typical absorption spectra of CdSe-ZnS core-shell system. This system is important because of the drastically improved fluorescence properties because of the addition of a wide band gap ZnS shell than the core CdSe. In addition with a ZnS shell, CdSe becomes bio-compatible.

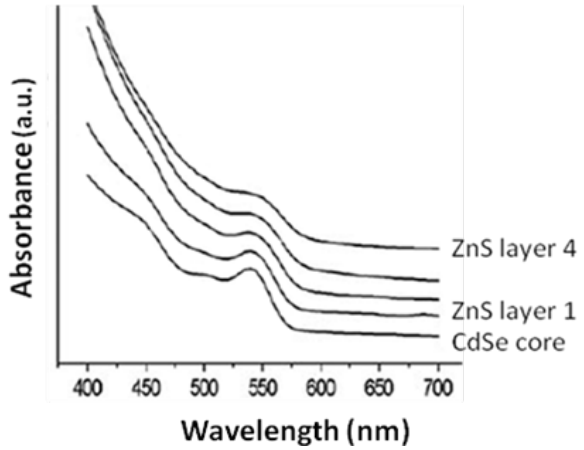

Figure 3.80: Absorption spectra of CdSe core, ZnS shell. Adapted from C. Qing-Zhu, P. Wang, X. Wang and Y. Li, *Nanoscale Res. Lett.*, 2008, **3**, 213.

A CdSe seed, CdS arm nanorods system is also interesting. Combining CdSe and CdS in a single nanostructure creates a material with a mixed dimensionality where holes are confined to CdSe while electrons can move freely between CdSe and CdS phases.

3.2.4.6 Bibliography

- S. V. Gapoenko, *Optical Properties of Semiconductor Nanocrystals*, Cambridge University Press, Cambridge (2003).
- W. W. Yu, L. Qu, W. Guo, and X. Peng, *Chem. Mater.*, 2003, **15**, 2854.
- J. Jasieniak, C. Bullen, J. van Embden, and P. Mulvaney, *J. Phys. Chem. B*, 2005, **109**, 20665.
- X. Zhong, Y. Feng, and Y. Zhang, *J. Phys. Chem. C*, 2007, **111**, 526.
- D. V. Talapin, J. H. Nelson, E. V. Shevchenko, S. Aloni, B. Sadtler, and A. P. Alivisatos, *Nano Lett.*, 2007, **7**, 2951.
- C. Qing-Zhu, P. Wang, X. Wang, and Y. Li, *Nanoscale Res. Lett.*, 2008, **3**, 213.
- C. Qi-Fan, W. Wen-Xing, G. Ying-Xin, L. Meng-Ying, X. Shu-Kun, and Z. Xiu-Juan, *Chin. J. Anal. Chem.*, 2007, **35**, 135.

3.2.5 Characterization of Covalently Functionalized Single-Walled Carbon Nanotubes[16]

3.2.5.1 Introduction

Characterization of nanoparticles in general, and carbon nanotubes in particular, remains a technical challenge even though the chemistry of covalent functionalization has been studied for more than a decade. It

[16] This content is available online at <http://cnx.org/content/m22299/1.4/>.

has been noted by several researchers that the characterization of products represents a constant problem in nanotube chemistry. A systematic tool or suites of tools are needed for adequate characterization of chemically functionalized single-walled carbon nanotubes (SWNTs), and is necessary for declaration of success or failure in functionalization trials.

So far, a wide range of techniques have been applied to characterize functionalized SWNTs: infra red (IR), Raman, and UV/visible spectroscopies, thermogravimetric analysis (TGA), atomic force microscopy (AFM), transmission electron microscopy (TEM), X-ray photoelectron spectroscopy (XPS), etc. A summary of the attribute of each of the characterization method is given in Table 3.8.

Method	**Sample**	**Information**	**Limitations**
TGA	solid	functionalization ratio	no evidence for covalent functionalization, not specific
XPS	solid	elements, functionalization ratio	no evidence of covalent functionalization, not specific, quantification complicated
Raman	solid	sp^3 indicated by D mode	not specific, quantification not reliable
Infra red (IR)	solid for (ATR-IR) or solution	substituent groups	no direct evidence for covalent functionalization, quantification not possible
UV/visible	solution	sidewall functionalization	not specific or quantitative, need highly dispersed sample
Solution NMR	solution	substituents	no evidence of covalent functionalization, high solubility of sample
Solid state NMR	solid	substituents, sp^3 molecular motions, quantification at high level of funcitionalization	high functionalization needed, long time for signal acquisition, quantification not available for samples with protons on side chains

continued on next page

AFM	solid on substrate	topography	only a small portion of sample characterized, no evidence of covalent functionalization, no chemical identity
TEM	solid on substrate	image of sample distribution dispersion	only a small portion of sample characterized, no evidence of covalent functionalization, no chemical identity dispersion information complicated
STM	solid on substrate	distribution	no chemical identity of functional groups small portion of sample conductive sample only

Table 3.8: Common characterization methodology for functionalized SWNTs.

3.2.5.2 Elemental and Physical Analysis

3.2.5.2.1 Thermogravimetric analysis (TGA)

Thermogravimetric analysis (TGA) is the mostly widely used method to determine the level of sidewall functionalization. Since most functional groups are labile or decompose upon heating, while the SWNTs are stable up to 1200 °C under Ar atmosphere. The weight loss at 800 °C under Ar is often used to determine functionalization ratio using this indirect method. Unfortunately, quantification can be complicated with presence of multiple functional groups. Also, TGA does not provide direct evidence for covalent functionalization since it cannot differentiate between covalent attachment and physical adsorption.

3.2.5.2.2 X-ray photoelectron spectroscopy (XPS)

XPS confirms the presence of different elements in functionalized SWNTs. This is useful for identification of heteroatom elements such as F and N, and then XPS can be used for quantification with simple substituent groups and used indirectly. Deconvolution of XPS is useful to study fine structures on SWNTs. However, the overlapping of binding energies in the spectrum complicates quantification.

3.2.5.3 Spectroscopy

3.2.5.3.1 Raman spectroscopy

Raman spectroscopy is very informative and important for characterizing functionalized SWNTs. The tangential G mode (*ca.* $1550 - 1600$ cm^{-1}) is characteristic of sp^2 carbons on the hexagonal graphene network. The D-band, so-called disorder mode (found at *ca.* 1295 cm^{-1}) appears due to disruption of the hexagonal sp^2 network of SWNTs. The D-band was largely used to characterize functionalized SWNTs and ensure functionalization is covalent and occurred at the sidewalls. However, the observation of D band in Raman can also be related to presence of defects such as vacancies, 5-7 pairs, or dopants. Thus, using Raman to provide evidence of covalent functionalization needs to be done with caution. In particular, the use of Raman spectroscopy for a determination of the degree of functionalization is not reliable.

It has been shown that quantification with Raman is complicated by the distribution of functional groups on the sidewall of SWNTs. For example, if fluorinated-SWNTs (F-SWNTs) are functionalized with thiol or thiophene terminated moieties, TGA shows that they have similar level of functionalization. However, their

relative intensities of D:G in Raman spectrum are quite different. The use of sulfur substituents allow for gold nanoparticles with 5 nm in diameter to be attached as a "chemical marker" for direct imaging of the distribution of functional groups. AFM and STM suggest that the functional groups of thio-SWNTs are group together while the thiophene groups are widely distributed on the sidewall of SWNTs. Thus the difference is not due to significant difference in substituent concentration but on substituent distribution, while Raman shows different D:G ratio.

3.2.5.3.2 Infra red spectroscopy

IR spectroscopy is useful in characterizing functional groups bound to SWNTs. A variety of organic functional groups on sidewall of SWNTs have been identified by IR, such as COOH(R), -CH_2, -CH_3, -NH_2, -OH, etc. However, it is difficult to get direct functionalization information from IR spectroscopy. The C-F group has been identified by IR in F-SWNTs. However, C-C, C-N, C-O groups associated with the side-wall functionalization have not been observed in the appropriately functionalized SWNTs.

3.2.5.3.3 UV/visible spectroscopy

UV/visible spectroscopy is maybe the most accessible technique that provides information about the electronic states of SWNTs, and hence functionalization. The absorption spectrum shows bands at *ca.* 1400 nm and 1800 nm for pristine SWNTs. A complete loss of such structure is observed after chemical alteration of SWNTs sidewalls. However, such information is not quantitative and also does not show what type of functional moiety is on the sidewall of SWNTs.

3.2.5.3.4 Nuclear magnetic resonance

NMR can be considered as a "new" characterization technique as far as SWNTs are concerned. Solution state NMR is limited for SWNT characterization because low solubility and slow tumbling of the SWNTs results in broad spectra. Despite this issue, there are still solution ^{1}H NMR reported of SWNTs functionalized by carbenes, nitrenes and azomethine ylides because of the high solubility of derivatized SWNTs. However, proof of covalent functionalization cannot be obtained from the ^{1}H NMR. As an alternative, solid state ^{13}C NMR has been employed to characterize several functionalized SWNTs and show successful observation of sidewall organic functional groups, such as carboxylic and alkyl groups. But there has been a lack of direct evidence of sp^3 carbons on the sidewall of SWNTs that provides information of covalent functionalization.

Solid state ^{13}C NMR has been successfully employed in the characterization of F-SWNTs through the direct observation of the sp^3C-F carbons on sidewall of SWNTs. This methodology has been transferred to more complicated systems; however, it has been found that longer side chain length increases the ease to observe sp^3C-X sidewall carbons.

Solid state NMR is a potentially powerful technique for characterizing functionalized SWNTs because molecular dynamic information can also be obtained. Observation that higher side chain mobility can be achieved by using a longer side chain length offers a method of exploring functional group conformation. In fact, there have been reports using solid state NMR to study molecular mobility of functionalized multi-walled carbon nanotubes.

3.2.5.4 Microscopy

AFM, TEM and STM are useful imaging techniques to characterize functionalized SWNTs. As techniques, they are routinely used to provide an "image" of an individual nanoparticle, as opposed to an average of all the particles.

3.2.5.4.1 Atomic force microscopy

AFM shows morphology on the surface of SWNTs. The height profile on AFM is often used to show presence of functional groups on sidewall of SWNTs. Individual SWNTs can be probed by AFM and sometimes provide

information of dispersion and exfoliation of bundles. Measurement of heights along an individual SWNT can be correlated with the substituent group, i.e., the larger an alkyl chain of a sidewall substituent the greater the height measured. AFM does not distinguish whether those functional groups are covalently attached or physically adsorbed on the surface of SWNTs.

3.2.5.4.2 Transmission electron microscopy

TEM can be used to directly image SWNTs and at high resolution clearly shows the sidewall of individual SWNT. However, the resolution of TEM is not sufficient to directly observe covalent attachment of chemical modification moieties, i.e., to differentiate between sp^2 and sp^3 carbon atoms. TEM can be used to provide information of functionalization effect on dispersion and exfoliation of ropes.

Samples are usually prepared from very dilute concentration of SWNTs. Sample needs to be very homogeneous to get reliable data. As with AFM, TEM only shows a very small portion of sample, using them to characterize functionalized SWNTs and evaluate dispersion of samples in solvents needs to be done with caution.

3.2.5.4.3 Scanning tunneling microscopy

STM offers a lot of insight on structure and surface of functionalized SWNTs. STM measures electronic structure, while sometimes the topographical information can be indirectly inferred by STM images. STM has been used to characterize F-SWNTs gold-marked SWNTs, and organic functionalized SWNTs. Distribution of functional groups can be inferred from STM images since the location of a substituent alters the localized electronic structure of the tube. STM images the position/location of chemical changes to the SWNT structure. The band-like structure of F-SWNTs was first disclosed by STM.

STM has the same problem that is inherent with AFM and TEM, that when using small sample size, the result may not be statistically relevant. Also, chemical identity of the features on SWNTs cannot be determined by STM; rather, they have to be identified by spectroscopic methods such as IR or NMR. A difficulty with STM imaging is that the sample has to be conductive, thus deposition of the SWNT onto a gold (or similar) surface is necessary.

3.2.5.5 Bibliography

- L. B. Alemany, L. Zhang, L. Zeng, C. L. Edwards, and A. R. Barron, *Chem. Mater.*, 2007, **19**, 735.
- J. L. Bahr and J. M. Tour, *J. Mater. Chem.*, 2002, **12**, 1952.
- M. S. Dresselhaus, G. Dresselhaus, and A. Jorio, *J. Phys. Chem. C*, 2007, **111**, 17887.
- A. Hirsch, *Angew. Chem. Int. Ed.*, 2002, **41**, 1853.
- M. Holzinger, J. Abraham, P. Whelan, R. Graupner, L. Ley, F. Hennrich, M. Kappes, and A. Hirsch, *J. Am. Chem. Soc.*, 2003, **125**, 8566.
- K. F. Kelly, I. W. Chiang, E. T. Mickelson, R. H. Hauge, J. L. Margrave, X. Wang, G. E. Scuseria, C. Radloff, and N. J. Halas, *Chem. Phys. Lett.*, 1999, **313**, 455.
- V. N. Khabashesku, W. E. Billups, and J. L. Margrave, *Acc. Chem. Res.*, 2002, **35**, 1087.
- F. Liang, L. B. Alemany, J. M. Beach, and W. E. Billups, *J. Am. Chem. Soc.*, 2005, **127**, 13941.
- D. Tasis, N. Tagmatarchis, A. Bianco, and M. Prato, *Chem. Rev.*, 2006, **106**, 1105.
- H-L. Wu, Y-T. Yang, C-C. M. Ma, and H-C. Kuan, *J. Polym. Sci. A. Polym. Chem.*, 2005, 6084.
- L. Zeng, L. Zhang, and A. R. Barron, *Nano Lett.*, 2005, **5**, 2001.
- L. Zhang, J. Zhang, N. Schmandt, J. Cratty, V. N. Khabashesku, K. F. Kelly, and A. R. Barron, *Chem. Commun.*, 2005, 5429.

3.2.6 Characterization of Single-Walled Carbon Nanotubes by Raman Spectroscopy[17]

3.2.6.1 Introduction

Carbon nanotubes (CNTs) have proven to be a unique system for the application of Raman spectroscopy, and at the same time Raman spectroscopy has provided an exceedingly powerful tool useful in the study of the vibrational properties and electronic structures of CNTs. Raman spectroscopy has been successfully applied for studying CNTs at single nanotube level.

The large van der Waals interactions between the CNTs lead to an agglomeration of the tubes in the form of bundles or ropes. This problem can be solved by wrapping the tubes in a surfactant or functionalizing the SWNTs by attaching appropriate chemical moieties to the sidewalls of the tube. Functionalization causes a local change in the hybridization from sp^2 to sp^3 of the side-wall carbon atoms, and Raman spectroscopy can be used to determine this change. In addition information on length, diameter, electronic type (metallic or semiconducting), and whether nanotubes are separated or in bundle can be obtained by the use of Raman spectroscopy. Recent progress in understanding the Raman spectra of single walled carbon nanotubes (SWNT) have stimulated Raman studies of more complicated multi-wall carbon nanotubes (MWNT), but unfortunately quantitative determination of the latter is not possible at the present state of art.

3.2.6.2 Characterizing SWNTs

Raman spectroscopy is a single resonance process, i.e., the signals are greatly enhanced if either the incoming laser energy (E_{laser}) or the scattered radiation matches an allowed electronic transition in the sample. For this process to occur, the phonon modes are assumed to occur at the center of the Brillouin zone (q = 0). Owing to their one dimensional nature, the Π-electronic density of states of a perfect, infinite, SWNTs form sharp singularities which are known as van Hove singularities (vHs), which are energetically symmetrical with respect to Fermi level (E_f) of the individual SWNTs. The allowed optical transitions occur between matching vHs of the valence and conduction band of the SWNTs, i.e., from first valence band vHs to the first conduction band vHs (E_{11}) or from the second vHs of the valence band to the second vHs of the conduction band (E_{22}). Since the quantum state of an electron (k) remains the same during the transition, it is referred to as k-selection rule.

The electronic properties, and therefore the individual transition energies in SWNTs are given by their structure, i.e., by their chiral vector that determines the way SWNT is rolled up to form a cylinder. Figure 3.81 shows a SWNT having vector R making an angle θ, known as the chiral angle, with the so-called zigzag or r_1 direction.

[17] This content is available online at <http://cnx.org/content/m22925/1.2/>.

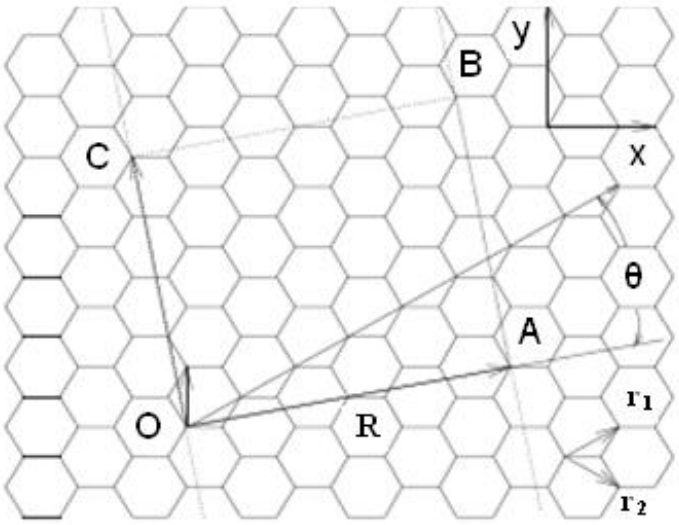

Figure 3.81: The unrolled honeycomb lattice of a nanotube. When the sites O and A, and the sites B and C are connected, a portion of a graphene sheet can be rolled seamlessly to form a SWNT. The vectors OA and OB define the chiral vector R of the nanotube, respectively. The rectangle OABC defines the unit cell if the nanotube. The figure is constructed for (n,m) = (4,2) nanotube. Adapted from M. S. Dresselhaus, G. Dresselhaus, R. Saito, and A. Jorio, *Physics Reports*, 2004, **2**, 47.

Raman spectroscopy of an ensemble of many SWNTs having different chiral vectors is sensitive to the subset of tubes where the condition of allowed transition is fulfilled. A 'Kataura-Plot' gives the allowed electronic transition energies of individual SWNTs as a function of diameter d, hence information on which tubes are resonant for a given excitation wavelength can be inferred. Since electronic transition energies vary roughly as $1/d$, the question whether a given laser energy probes predominantly semiconducting or metallic tubes depends on the mean diameter and diameter distribution in the SWNT ensemble. However, the transition energies that apply to an isolated SWNT do not necessarily hold for an ensemble of interacting SWNTs owing to the mutual van der Waals interactions.

Figure 3.82 shows a typical Raman spectrum from 100 to 3000 cm^{-1} taken of SWNTs produced by catalytic decomposition of carbon monoxide (HiPco-process). The two dominant Raman features are the radial breathing mode (RBM) at low frequencies and tangential (G-band) multifeature at higher frequencies. Other weak features, such as the disorder induced D-band and the G' band (an overtone mode) are also shown.

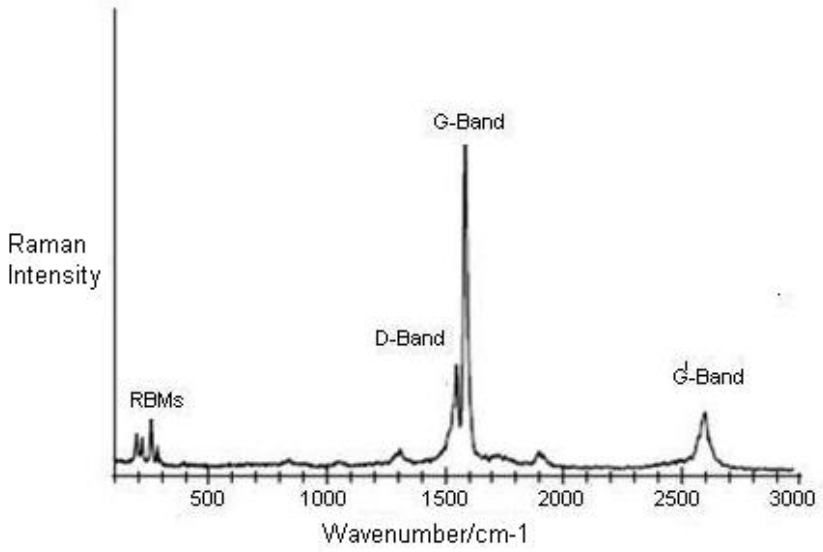

Figure 3.82: Raman spectrum of HiPco SWNTs using a laser of wavelength of $\lambda_{exc} = 633$ nm. Adapted from R. Graupner, *J. Raman Spectrosc.*, 2007, **38**, 673.

3.2.6.3 Modes in the Raman spectra of SWNTs

3.2.6.3.1 Radial breathing modes (RBMs)

Out of all Raman modes observed in the spectra of SWNTs, the radial breathing modes are unique to SWNTs. They appear between 150 $cm^{-1} < \omega_{RBM} < 300$ cm^{-1} from the elastically scattered laser line. It corresponds to the vibration of the C atoms in the radial direction, as if the tube is breathing (Figure 3.83). An important point about these modes is the fact that the energy (or wavenumber) of these vibrational modes depends on the diameter (d) of the SWNTs, and not on the way the SWNT is rolled up to form a cylinder, i.e., they do not depend on the θ of the tube.

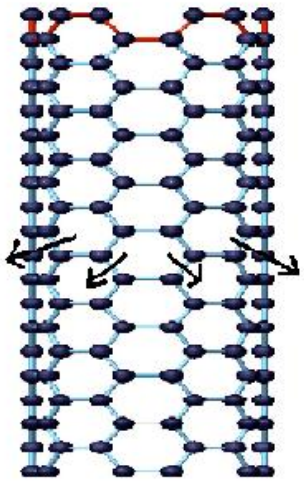

Figure 3.83: Schematic picture showing vibration for RBM. Adapted from A. Jorio, M. A. Pimenta, A. G. S. Filho, R. Saito, G. Dresselhaus, and M. S. Dresselhaus, *New J. Phys.*, 2003, **5**, 139.

These features are very useful for characterizing nanotube diameters through the relation $\omega_{\mathrm{RBM}} = \mathrm{A}/d + \mathrm{B}$, where A and B are constants and their variations are often attributed to environmental effects, i.e., whether the SWNTs are present as individual tubes wrapped in a surfactant, isolated on a substrate surface, or in the form of bundles. However, for typical SWNT bundles in the diameter range, $d = 1.5 \pm 0.2$ nm, A = 234 cm^{-1} nm and B = 10 cm^{-1} (where B is an upshift coming from tube-tube interactions). For isolated SWNTs on an oxidized Si substrate, A= 248 cm^{-1} nm and B = 0. As can be seen from Figure 3.84, the relation $\omega_{\mathrm{RBM}} = \mathrm{A/d} + \mathrm{B}$ holds true for the usual diameter range i.e., when d lies between 1 and 2 nm. However, for d less than 1 nm, nanotube lattice distortions lead to chirality dependence of ω_{RBM} and for large diameters tubes when, d is more than 2 nm the intensity of RBM feature is weak and is hardly observable.

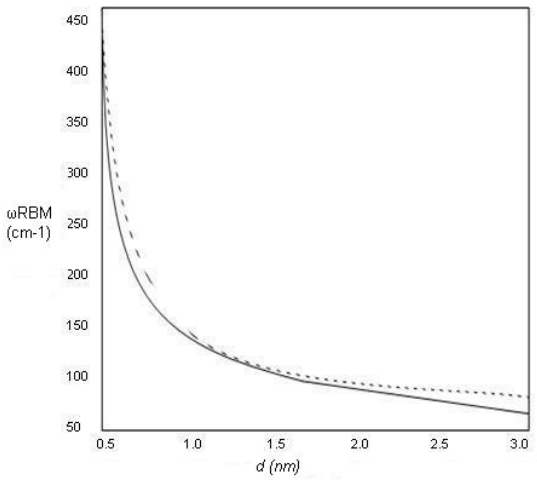

Figure 3.84: RBM frequencies $\omega_{\mathrm{RBM}} = \mathrm{A}/d + \mathrm{B}$ versus nanotube diameter for (i) A = 234 cm^{-1} nm and B = 10 cm^{-1}, for SWNT bundles (dashed curve); (ii) A = 248 cm^{-1} nm and B = 0, for isolated SWNTs (solid curve). Adapted from A. Jorio, M. A. Pimenta, A. G. S. Filho, R. Saito, G. Dresselhaus, and M. S. Dresselhaus, *New J. Phys.*, 2003, **5**, 139.

Hence, a single Raman measurement gives an idea of the tubes that are in resonance with the laser line, but does not give a complete characterization of the diameter distribution of the sample. However, by taking Raman spectra using many laser lines, a good characterization of the diameter distributions in the sample can be obtained. Also, natural line widths observed for isolated SWNTs are $\omega_{\mathrm{RBM}} = 3$ cm^{-1}, but as the tube diameter is increased, broadening is observed which is denoted by Γ_{RBM}. It has been observed that for $d > 2$ nm, $\Gamma_{\mathrm{RBM}} > 20$ cm^{-1}. For SWNT bundles, the line width does not reflect Γ_{RMB}, it rather reflects an ensemble of tubes in resonance with the energy of laser.

3.2.6.3.1.1 Variation of RBM intensities upon functionalization

Functionalization of SWNTs leads to variations of relative intensities of RBM compared to the starting material (unfunctionalized SWNTs). Owing to the diameter dependence of the RBM frequency and the resonant nature of the Raman scattering process, chemical reactions that are sensitive to the diameter as well as the electronic structure, i.e., metallic or semiconducting of the SWNTs can be sorted out. The difference in Raman spectra is usually inferred by thermal defunctionalization, where the functional groups are removed by annealing. The basis of using annealing for defunctionalizing SWNTs is based on the fact that annealing restores the Raman intensities, in contrast to other treatments where a complete disintegration of the SWNTs occurs. Figure 3.85 shows the Raman spectra of the pristine, functionalized and annealed SWNTs. It can be observed that the absolute intensities of the radial breathing modes is drastically reduced after functionalization. This decrease can be attributed to vHs, which themselves are a consequence of translational symmetry of the SWNTs. Since the translational symmetry of the SWNTs is broken as a result of irregular distribution of the sp^3-sites due to the functionalization, these vHs are broadened and strongly reduced in intensity. As a result, the resonant Raman cross section of all modes is strongly reduced as well.

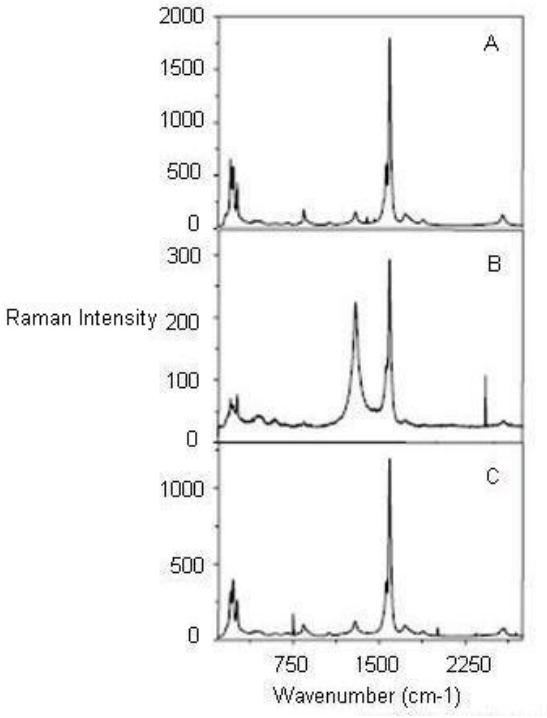

Figure 3.85: Raman spectra of sidewall functionalized SWNTs of (A) pristine material, (B) functionalized SWNTs, and (C) after annealing at 750 °C in Ar. Adapted from R. Graupner, *J. Raman Spectrosc.*, 2007, **38**, 673.

For an ensemble of functionalized SWNTs, a decrease in high wavenumber RBM intensities has been observed which leads to an inference that destruction of small diameter SWNT takes place. Also, after prolonged treatment with nitric acid and subsequent annealing in oxygen or vacuum, diameter enlargement of SWNTs is observed from the disappearance of RBMs from small diameter SWNTs and the appearance of new RBMs characteristic of SWNTs with larger diameters. In addition, laser irradiation seems to damage preferentially small diameter SWNTs. In all cases, the decrease of RBM intensities is either attributed to the complete disintegration of SWNTs or reduction in resonance enhancement of selectively functionalized SWNTs. However, change in RBM intensities can also have other reasons. One reason is doping induced bleaching of electronic transitions in SWNTs. When a dopant is added, a previously occupied electronic state can be filled or emptied, as a result of which E_f in the SWNTs is shifted. If this shift is large enough and the conduction band vHs corresponding to the respective E_{ii} transition that is excited by the laser light gets occupied (n-type doping) or the valence band vHs is emptied (p-type doping), the resonant enhancement is lost as the electronic transitions are quenched.

Sample morphology has also seen to affect the RBMs. The same unfunctionalized sample in different aggregation states gives rise to different spectra. This is because the transition energy, E_{ii} depends on the aggregation state of the SWNTs.

3.2.6.3.2 Tangential modes (G-band)

The tangential modes are the most intensive high-energy modes of SWNTs and form the so-called G-band, which is typically observed at around 1600 cm^{-1}. For this mode, the atomic displacements occur along the cicumferential direction (Figure 3.86). Spectra in this frequency can be used for SWNT characterization, independent of the RBM observation. This multi-peak feature can, for example, also be used for diameter characterization, although the information provided is less accurate than the RBM feature, and it gives information about the metallic character of the SWNTs in resonance with laser line.

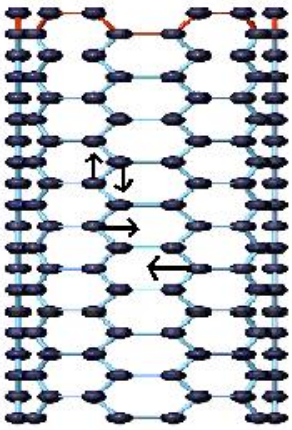

Figure 3.86: Schematic picture showing the atomic vibrations for the G-band. Adapted from A. Jorio, M. A. Pimenta, A. G. S. Filho, R. Saito, G. Dresselhaus, and M. S. Dresselhaus, *New J. Phys.*, 2003, **5**, 139.

The tangential modes are useful in distinguishing semiconducting from metallic SWNTs. The difference is evident in the G- feature (Figure 3.87 and Figure 3.88) which broadens and becomes asymmetric for metallic SWNTs in comparison with the Lorentzian lineshape for semiconducting tubes, and this broadening is related to the presence of free electrons in nanotubes with metallic character. This broadened G-feature is usually fit using a Breit-Wigner-Fano (BWF) line that accounts for the coupling of a discrete phonon with a continuum related to conduction electrons. This BWF line is observed in many graphite-like materials with metallic character, such as n-doped graphite intercalation compounds (GIC), n-doped fullerenes, as well as metallic SWNTs. The intensity of this G- mode depends on the size and number of metallic SWNTs in a bundle (Figure 3.89).

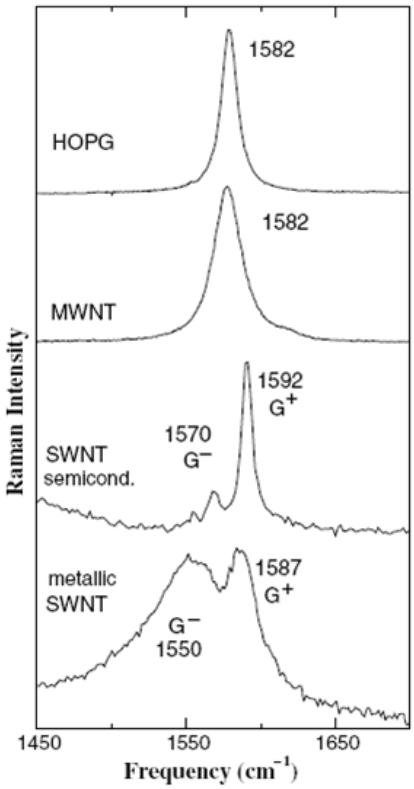

Figure 3.87: G-band for highly ordered pyrolytic graphite (HOPG), MWNT bundles, one isolated semiconducting SWNT and one isolated metallic SWNT. The multi-peak G-band feature is not clear for MWNTs due to the large tube size. A. Jorio, M. A. Pimenta, A. G. S. Filho, R. Saito, G. Dresselhaus, and M. S. Dresselhaus, *New J. Phys.*, 2003, **5**, 139. Copyright Institute of Physics (2005).

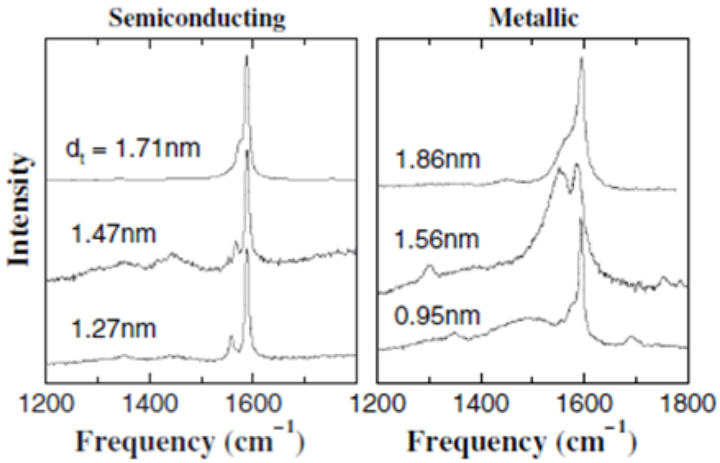

Figure 3.88: Raman signal from three isolated semiconducting and three isolated metallic SWNTs showing the G-and D-band profiles. SWNTs in good resonance (strong signal with low signal to noise ratio) show practically no D-band. A. Jorio, M. A. Pimenta, A. G. S. Filho, R. Saito, G. Dresselhaus, and M. S. Dresselhaus, *New J. Phys.*, 2003, **5**, 139. Copyright Institute of Physics (2005).

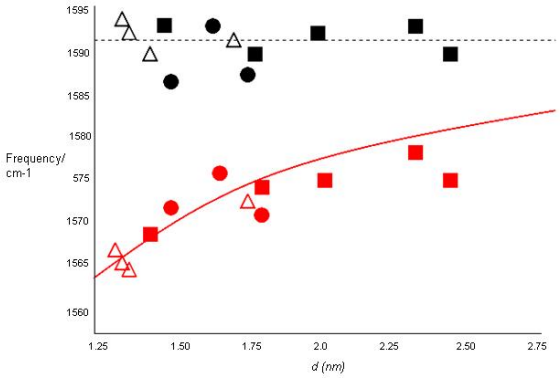

Figure 3.89: Dependence of G+ (black symbols) and G- (red symbols) frequencies as a function of diameter. Adapted from M. Paillet, T. Michel, J. C. Meyer, V. N. Popov, L. Henrad, S. Roth, and J. L. Sauvajol, *Phy. Rev. Lett.*, 2006, **96**, 257401.

3.2.6.3.2.1 Change of G-band line shape on functionalization

Chemical treatments are found to affect the line shape of the tangential line modes. Selective functionalization of SWNTs or a change in the ratio of metallic to semiconducting SWNTs due to selective etching is responsible for such a change. According to Figure 3.90, it can be seen that an increase or decrease of the BWF line shape is observed depending on the laser wavelength. At $\lambda_{exc} = 633$ nm, the preferentially functionalized small diameter SWNTs are semiconducting, therefore the G-band shows a decrease in the BWG asymmetry. However, the situation is reversed at 514 nm, where small metallic tubes are probed. BWF resonance intensity of small bundles increases with bundle thickness, so care should be taken that the effect ascribed directly to functionalization of the SWNTs is not caused by the exfoliation of the previously bundles SWNT.

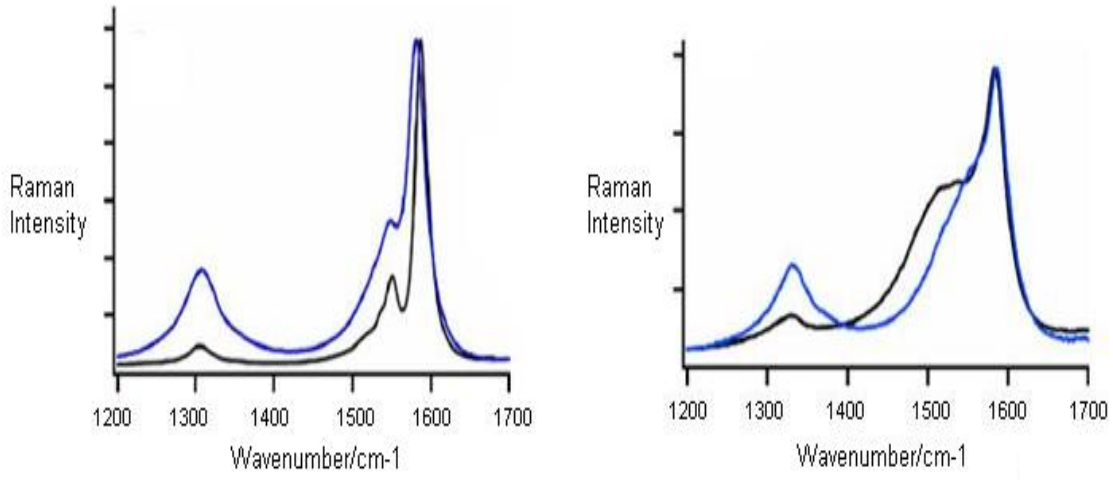

Figure 3.90: G-and D-band spectra of pristine (black) and ozonized (blue) SWNTs at 633 nm (left) and 514 nm (right) excitation. Adapted from R. Graupner, *J. Raman Spectrosc.*, 2007, **38**, 673.

3.2.6.3.3 Disorder-induced D-band

This is one of the most discussed modes for the characterization of functionalized SWNTs and is observed at 1300-1400 cm^{-1}. Not only for functionalized SWNTs, D-band is also observed for unfunctionalized SWNTs. From a large number of Raman spectra from isolated SWNTs, about 50% exhibit observable D-band signals with weak intensity (Figure 3.88). A large D-peak compared with the G-peak usually means a bad resonance condition, which indicates the presence of amorphous carbon.

The appearance of D-peak can be interpreted due to the breakdown of the k-selection rule. It also depends on the laser energy and diameter of the SWNTs. This behavior is interpreted as a double resonance effect, where not only one of the direct, k-conserving electronic transitions, but also the emission of phonon is a resonant process. In contrast to single resonant Raman scattering, where only phonons around the center of the Brillouin zone (q = 0) are excited, the phonons that provoke the D-band exhibit a non-negligible q vector. This explains the double resonance theory for D-band in Raman spectroscopy. In few cases, the overtone of the D-band known as the G'-band (or D*-band) is observed at 2600-2800 cm^{-1}, and it does not

require defect scattering as the two phonons with q and –q are excited. This mode is therefore observed independent of the defect concentration.

The presence of D-band cannot be correlated to the presence of various defects (such as hetero-atoms, vacancies, heptagon-pentagon pairs, kinks, or even the presence of impurities, etc). Following are the two main characteristics of the D-band found in carbon nanotubes:

1. Small linewidths: Γ_D values for SWNTs range from 40 cm^{-1} down to 7 cm^{-1}.
2. Lower frequencies: D-band frequency is usually lower than the frequency of sp^2-based carbons, and this downshift of frequency shows $1/d$ dependence.

3.2.6.3.3.1 D-Band intensity as a measure of functionalization versus defect density

Since D-peak appears due to the presence defects, an increase in the intensity of the band is taken as a fingerprint for successful functionalization. But, whether D-band intensity is a measure of degree of functionalization or not is still sure. So, it is not correct to correlate D-peak intensity or D-peak area to the degree of functionalization. From Figure 3.91, it can be observed that for lower degree of functionalization, intensity of the D-band scales linearly with defect density. As the degree of functionalization is further increased, both D and G-band area decrease, which is explained by the loss of resonance enhancement due to functionalization. Also, normalization of the D-peak intensity to the G-band in order to correct for changes in resonance intensities also leads to a decrease for higher densities of functional groups.

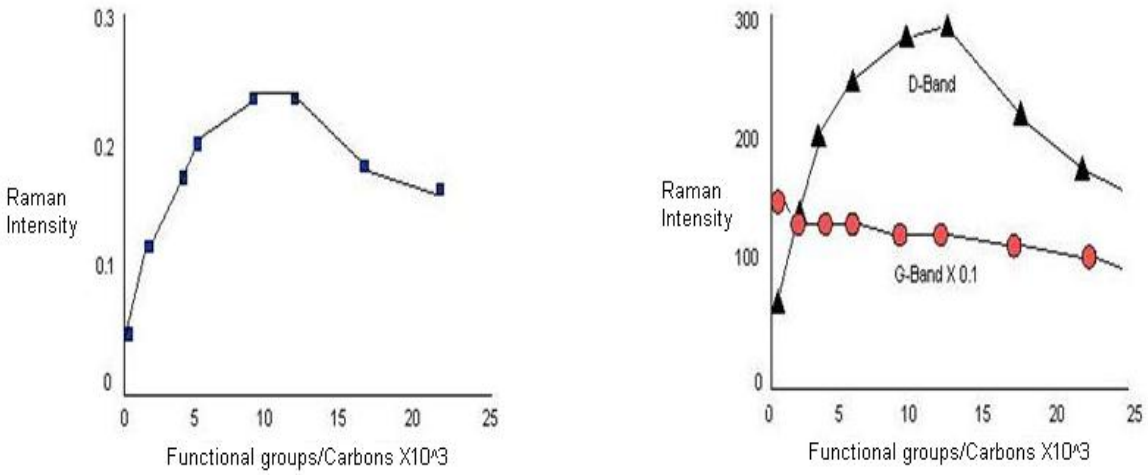

Figure 3.91: The left figure shows the intensity ratio I_D/I_G and the right figure shows D- and G-band intensity at $\lambda_{exc} = 532$ nm with respect to degree of functionalization using diazonium reagents. Adapted from R. Graupner, *J. Raman Spectrosc.*, 2007, **38**, 673.

3.2.6.3.4 Limitations of Raman spectroscopy

Though Raman spectroscopy has provides an exceedingly important tool for characterization of SWNTs, however, it suffers from few serious limitations. One of the main limitations of Raman spectroscopy is that it does not provide any information about the extent of functionalization in the SWNTs. The presence of

D-band indicates disorder, i.e. side wall distribution, however it cannot differentiate between the number of substituents and their distribution. Following are the two main limitations of Raman Spectroscopy:

3.2.6.3.4.1 Quantification of substituents

This can be illustrated by the following examples. Purified HiPco tubes may be fluorinated at 150 °C to give F-SWNTs with a C:F ratio of approximately 2.4:1. The Raman spectra (using 780 nm excitation) for F-SWNTs shows in addition to the tangential mode at ~1587 cm^{-1} an intense broad D (disorder) mode at ~ 1295 cm^{-1} consistent with the side wall functionalization. Irrespective of the arrangements of the fluorine substituents, thermolysis of F-SWNTs results in the loss of fluorine and the re-formation of unfunctionalized SWNTs alnog with their cleavage into shorter length tubes. As can be seen from Figure 3.92, the intensity of the D-band decreases as the thermolysis temperature increases. This is consistent with the loss of F-substituents. The G-band shows a concomitant sharpening and increase in intensity.

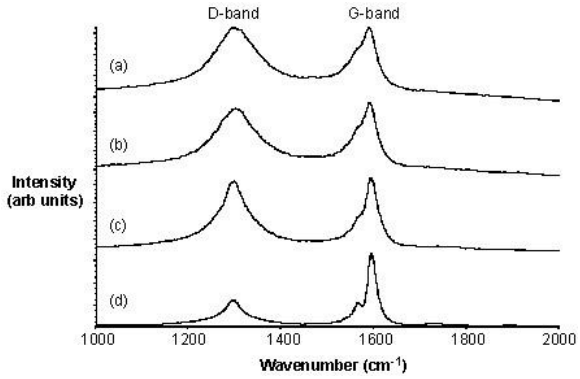

Figure 3.92: Raman spectra of F-SWNTs (a) as prepared at 150 °C and after heating to (b) 400, (c) 450 and (d) 550 °C.

As discussed above, the presence of a significant D mode has been the primary method for determining the presence of sidewall functionalization. It has been commonly accepted that the relative intensity of the D mode *versus* the tangential G mode is a quantitative measure of level of substitution. However, as discussed below, the G:D ratio is also dependent on the distribution of substituents. Using Raman spectroscopy in combination with XPS analysis of F-SWNTs that have been subjected to thermolysis at different temperatures, a measure of the accuracy of Raman as a quantitative tool for determining substituent concentration can be obtained. As can be seen from Figure 3.93, there is essentially no change in the G:D band ratio despite a doubling amount of functional groups.Thus, at low levels of functionalization the use of Raman spectroscopy to quantify the presence of fluorine substituents is a clearly suspect.

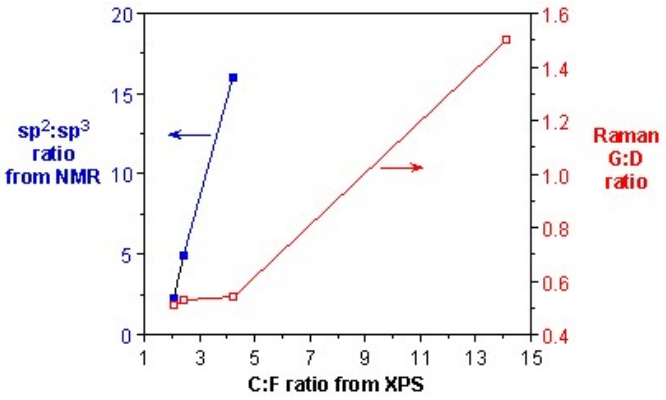

Figure 3.93: C(sp^2):C-F(sp^3) ratio (blue) and Raman G-band:D-band ratio (red) as a function of C:F ratio from XPS.

On the basis of above data it can be concluded that Raman spectroscopy does not provide an accurate quantification of small differences at low levels of functionalization, whereas when a comparison between samples with high levels of functionalization or large differences in degree of functionalization is requires Raman spectroscopy provides a good quantification.

3.2.6.3.4.2 Number versus distribution

Fluorinated nanotubes may be readily functionalized by reaction with the appropriate amine in the presence of base according to the scheme shown in Figure 3.94.

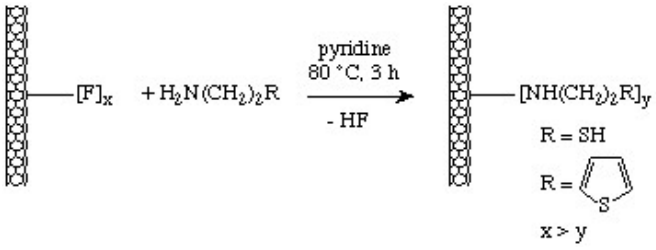

Figure 3.94: Synthesis of functionalized SWNTs.

When the Raman spectra of the functionalized SWNTs is taken (Figure 3.95), it is found out that the relative intensity of the disorder D-band at ~1290 cm^{-1} *versus* the tangential G-band (1500 - 1600 cm^{-1}) is much higher for thiophene-SWNT than thiol-SWNT. If the relative intensity of the D mode is the measure of the level of substitution, it can be concluded that there are more number of thiophene groups present per C than thiol groups. However, from the TGA weight loss data the SWNT-C:substituent ratios are calculated to be 19:1 and 17.5:1. Thus, contrary to the Raman data the TGA suggest that the number of substituents per C (in the SWNT) is actually similar for both substituents.

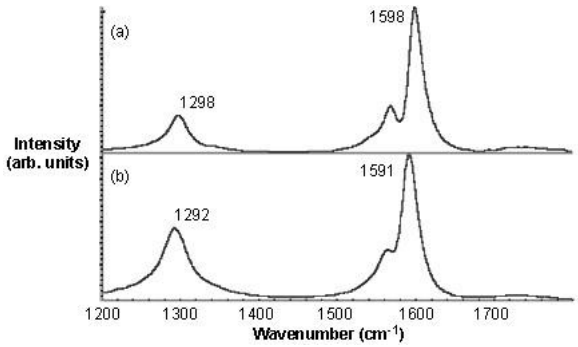

Figure 3.95: Raman spectrum of (a) thiol-SWNT and (b)thiophene-SWNT using 780 nm excitation showing the relative intensity of D-band at ~1300 cm^{-1} versus the G-band at ~1590 cm^{-1}.

This result would suggest that Raman spectroscopy is potentially unsuccessful in correctly providing the information about the number of substituents on the SWNTs. Subsequent imaging of the functionalized SWNTs by STM showed that the distribution of the functional groups was the difference between the thiol and thiphene functionalized SWNTs Figure 3.96. Thus, relative ratio of the D- and G-bands is a measure of concentration and distribution of functional groups on SWNTs.

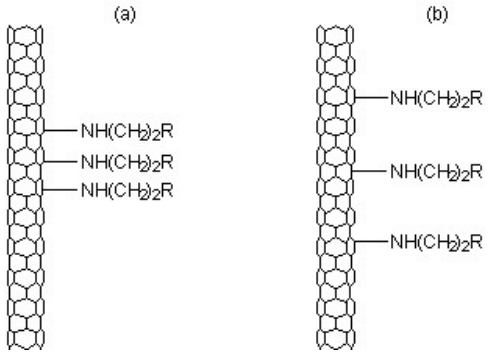

Figure 3.96: Schematic representation of the functional group distribution for (a) thiol-SWNT and (b) thiophene-SWNT.

3.2.6.4 Multi-walled carbon nanotubes (MWNTs)

Most of the characteristic differences that distinguish the Raman spectra in SWNTs from the spectra of graphite are not so evident for MWNTs. It is because the outer diameter for MWNTs is very large and the ensemble of CNTs in them varies from small to very large. For example, the RBM Raman feature associated with a small diameter inner tube (less than 2 nm) can sometimes be observed when a good resonance condition is established, but since the RBM signal from large diameter tubes is usually too weak

to be observable and the ensemble average of inner tube diameter broadens the signal, a good signal is not observed. However, when hydrogen gas in the arc discharge method is used, a thin innermost nanotube within a MWNT of diameter 1 nm can be obtained which gives strong RBM peaks in the Raman spectra.

Thereas the G+ - G- splitting is large for small diameter SWNT, the corresponding splitting of the G-band in MWNTs is both small in intensity and smeared out due to the effect of the diameter distribution. Therefore the G-band feature predominantly exists a weakly asymmetric characteristic lineshape, and a peak appearing close to the graphite frequency of 1582 cm^{-1}.however for isolated MWNTs prepared in the presence of hydrogen gas using the arc discharge method, it is possible to observe multiple G-band splitting effects even more clearly than for the SWNTs, and this is because environmental effects become relatively small for the innermost nanotube in a MWNT relative to the interactions occurring between SWNTs and different environments. The Raman spectroscopy of MWNTs has not been well investigated up to now. The new directions in this field are yet to be explored.

3.2.6.5 Bibliography

- R. Graupner, *J. Ramn Spectrosc.*, 2007, **38**, 673.
- S. Costa, B. Palen, M. Kruszynska, A. Bachmatiuk, and R.J. Kalenczuk, *Mat. Sci. Poland*, 2008, **26**, 433.
- M. Paillet, T. Michel , J. C. Meyer, V. N. Popov, L. Henrad, S. Roth, and J. L. Sauvajol, *Phy. Rev. Lett.*, 2006, **96**, 257401.
- L. Zhang, J. Zhang, N. Schmandt, J. Cratty, V. N. Khabashesku, K. F. Kelly, and A. R. Barron, *Chem. Commun.*, 2005, 5429.
- L. B. Alemany, L. Zhang, L. Zeng, C. L. Edwards, and A. R. Barron, *Chem. Mater.*, 2006, **19**, 735.
- M. S. Dresselhaus, G. Dresselhaus, R. Saito, and A. Jorio, *J. Phys. Rep.*, 2005, **2**, 47.
- A. Jorio, M. A. Pimenta, A. G. S. Filho, R. Saito, G. Dresselhaus, and M. S. Dresselhaus, *New J. Phys.*, 2003, **5**, 139.

3.2.7 Characterization of Graphene by Raman Spectroscopy[18]

3.2.7.1 Introduction

Graphene is a quasi-two-dimensional material, which comprises layers of carbon atoms arranged in six-member rings (Figure 3.97). Since being discovered by Andre Geim and co-wokers at the University of Manchester, graphene has become one of the most exciting topics of research because of its distinctive band structure and physical properties, such as the observation of a quantum hall effect at room temperature, a tunable band gap, and a high carrier mobility.

[18] This content is available online at <http://cnx.org/content/m34667/1.2/>.

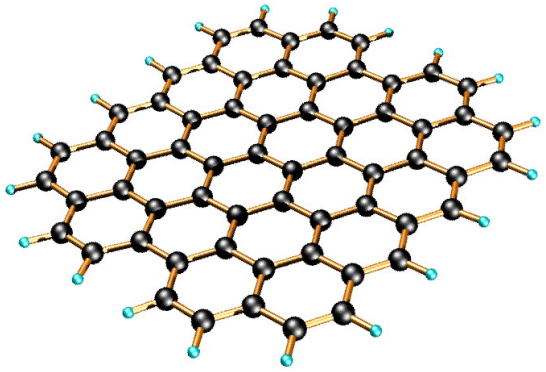

Figure 3.97: Idealized structure of a single graphene sheet.

Graphene can be characterized by many techniques including atomic force microscopy (AFM), transmission electron microscopy (TEM) and Raman spectroscopy. AFM can be used to determine the number of the layers of the graphene, and TEM images can show the structure and morphology of the graphene sheets. In many ways, however, Raman spectroscopy is a much more important tool for the characterization of graphene. First of all, Raman spectroscopy is a simple tool and requires little sample preparation. What's more, Raman spectroscopy can not only be used to determine the number of layers, but also can identify if the structure of graphene is perfect, and if nitrogen, hydrogen or other fuctionalization is successful.

3.2.7.2 Raman spectrum of graphene

While Raman spectroscopy is a useful technique for characterizing sp^2 and sp^3 hybridized carbon atoms, including those in graphite, fullerenes, carbon nanotubes, and graphene. Single, double, and multi-layer graphenes have also been differentiated by their Raman fingerprints.

shows a typical Raman spectrum of N-doped single-layer graphene. The D-mode, appears at approximately 1350 cm-1, and the G-mode appears at approximately 1583 cm^{-1}. The other Raman modes are at 1620 cm^{-1} (D'- mode), 2680 cm^{-1} (2D-mode), and 2947 cm^{-1} (D+G-mode).

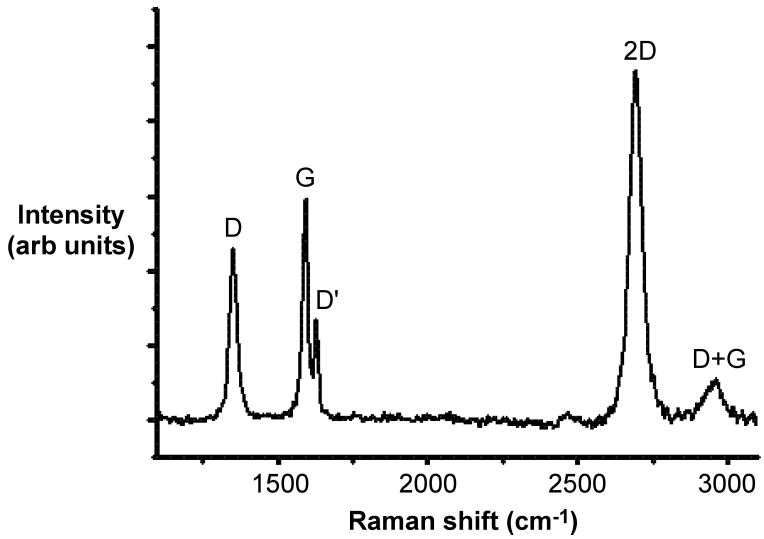

Figure 3.98: Raman spectrum with a 514.5 nm excitation laser wavelength of N-doped single-layer graphene.

3.2.7.2.1 The G-band

The G-mode is at about 1583 cm^{-1}, and is due to E2g mode at the Γ-point. G-band arises from the stretching of the C-C bond in graphitic materials, and is common to all sp^2 carbon systems. The G-band is highly sensitive to strain effects in sp^2 system, and thus can be used to probe modification on the flat surface of graphene.

3.2.7.2.2 Disorder-induced D- band and D'- band

The D-mode is caused by disordered structure of graphene. The presence of disorder in sp^2-hybridized carbon systems results in resonance Raman spectra, and thus makes Raman spectroscopy one of the most sensitive techniques to characterize disorder in sp^2 carbon materials. As is shown by a comparison of and , there is no D peak in the Raman spectra of graphene with a perfect structure.

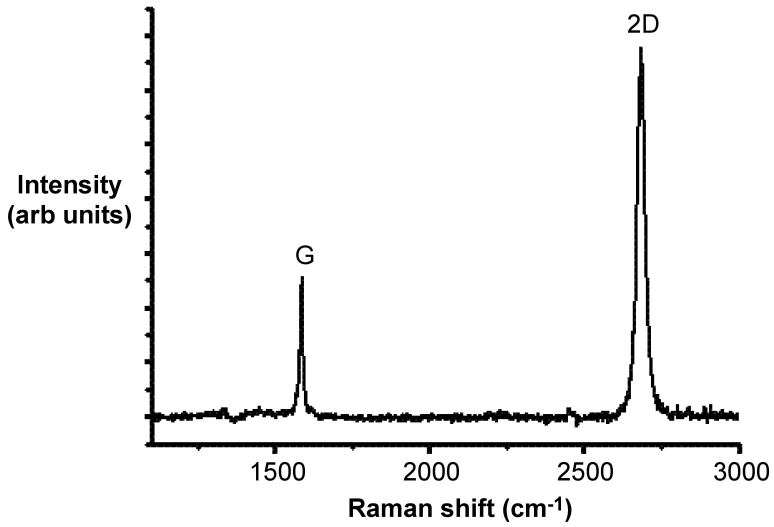

Figure 3.99: Raman spectrum with a 514.5 nm excitation laser wavelengthof pristine single-layer graphene.

If there are some randomly distributed impurities or surface charges in the graphene, the G-peak can split into two peaks, G-peak (1583 cm^{-1}) and D'-peak (1620 cm^{-1}). The main reason is that the localized vibrational modes of the impurities can interact with the extended phonon modes of graphene resulting in the observed splitting.

3.2.7.2.3 The 2D-band

All kinds of sp^2 carbon materials exhibit a strong peak in the range 2500 - 2800 cm^{-1} in the Raman spectra. Combined with the G-band, this spectrum is a Raman signature of graphitic sp^2 materials and is called 2D-band. 2D-band is a second-order two-phonon process and exhibits a strong frequency dependence on the excitation laser energy.

What's more, the 2D band can be used to determine the number of layer of graphene. This is mainly because in the multi-layer graphene, the shape of 2D band is pretty much different from that in the single-layer graphene. As shown in , the 2D band in the single-layer graphene is much more intense and sharper as compared to the 2D band in multi-layer graphene.

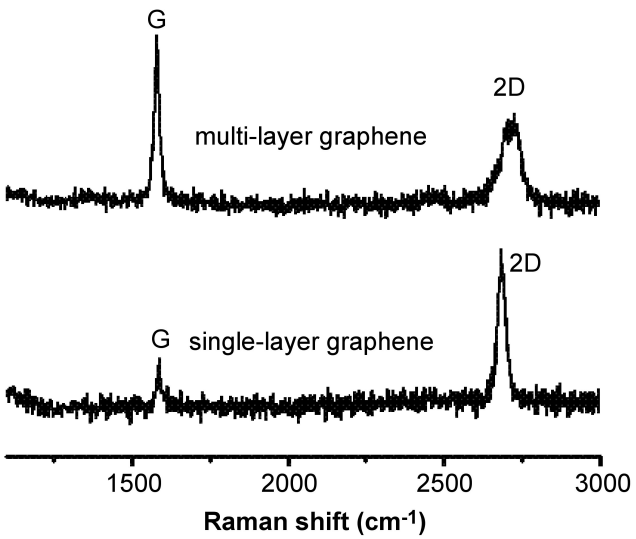

Figure 3.100: Raman spectrum with a 514.5 nm excitation laser wavelength of pristine single-layer and multi-layer graphene.

3.2.7.3 Bibliography

- G. G. Chen, P. Joshi, S. Tadigadapa, and P. C. Eklund, *Nano Lett.*, 2006, **6** , 2667.
- C. Ferrari, J. C. Meyer, V. Scardaci, C. Casiraghi, M. Lazzeri, F. Mauri, S. Piscanec, D. Jiang, K. S. Novoselov, and S. Roth, A. K. Geim, *Phys. Rev. Lett.*, 2006, **97**, 187401.
- M. A. Pimenta, G. Dresselhaus, M. S. Dresselhaus, L. A.Cancado, A. Jorio, and R. Sato, *Phys. Chem. Chem. Phys.*, 2007, **9**, 1276.

3.2.8 Optical Characterization of Group 12-16 (II-VI) Semiconductor Nanoparticles by Fluorescence Spectroscopy[19]

Group 12-16 semiconductor nanocrystals when exposed to light of a particular energy absorb light to excite electrons from the ground state to the excited state, resulting in the formation of an electron-hole pair (also known as excitons). The excited electrons relax back to the ground state, mainly through radiative emission of energy in the form of photons.

Quantum dots (QD) refer to nanocrystals of semiconductor materials where the size of the particles is comparable to the natural characteristic separation of an electron-hole pair, otherwise known as the exciton Bohr radius of the material. In quantum dots, the phenomenon of emission of photons associated with the transition of electrons from the excited state to the ground state is called fluorescence.

3.2.8.1 Fluorescence spectroscopy

Emission spectroscopy, in general, refers to a characterization technique that measures the emission of radiation by a material that has been excited. Fluorescence spectroscopy is one type of emission spectroscopy

[19]This content is available online at <http://cnx.org/content/m34656/1.1/>.

which records the intensity of light radiated from the material as a function of wavelength. It is a nondestructive characterization technique.

After an electron is excited from the ground state, it needs to relax back to the ground state. This relaxation or loss of energy to return to the ground state, can be achieved by a combination of non-radiative decay (loss of energy through heat) and radiative decay (loss of energy through light). Non-radiative decay by vibrational modes typically occurs between energy levels that are close to each other. Radiative decay by the emission of light occurs when the energy levels are far apart like in the case of the band gap. This is because loss of energy through vibrational modes across the band gap can result in breaking the bonds of the crystal. This phenomenon is shown in Figure 3.101.

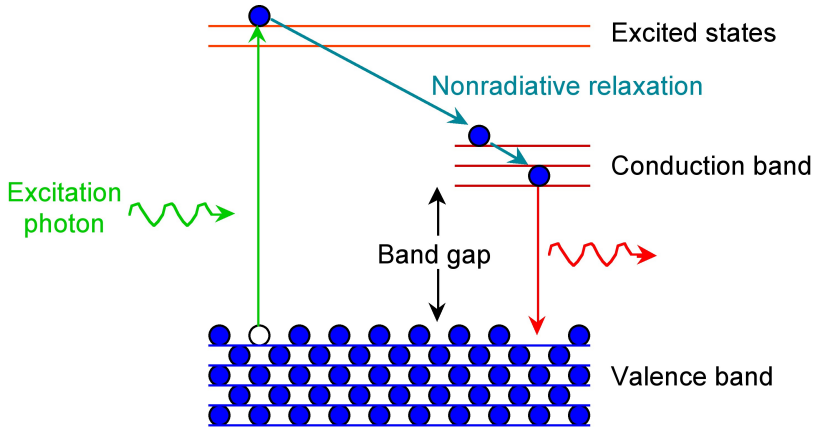

Figure 3.101: Emission of luminescence photon for Group 12-16 semiconductor quantum dot.

The band gap of Group 12-16 semiconductors is in the UV-visible region. Thus, the wavelength of the emitted light as a result of radiative decay is also in the visible region, resulting in fascinating fluorescence properties.

A fluorimeter is a device that records the fluorescence intensity as a function of wavelength. The fluorescence quantum yield can then be calculated by the ratio of photons absorbed to photons emitted by the system. The quantum yield gives the probability of the excited state getting relaxed via fluorescence rather than by any other non-radiative decay.

3.2.8.2 Difference between fluorescence and phosphorescence

Photoluminescence is the emission of light from any material due to the loss of energy from excited state to ground state. There are two main types of luminescence – fluorescence and phosphorescence. Fluorescence is a fast decay process, where the emission rate is around 10^8 s^{-1} and the lifetime is around 10^{-9} - 10^{-7} s. Fluorescence occurs when the excited state electron has an opposite spin compared to the ground state electrons. From the laws of quantum mechanics, this is an allowed transition, and occurs rapidly by emission of a photon. Fluorescence disappears as soon as the exciting light source is removed.

Phosphorescence is the emission of light, in which the excited state electron has the same spin orientation as the ground state electron. This transition is a forbidden one and hence the emission rates are slow (10^3 - 10^0 s^{-1}). So the phosphorescence lifetimes are longer, typically seconds to several minutes, while the excited phosphors slowly returned to the ground state. Phosphorescence is still seen, even after the exciting light

source is removed. Group 12-16 semiconductor quantum dots exhibit fluorescence properties when excited with ultraviolet light.

3.2.8.3 Instrumentation

The working schematic for the fluorometer is shown in Figure 3.102.

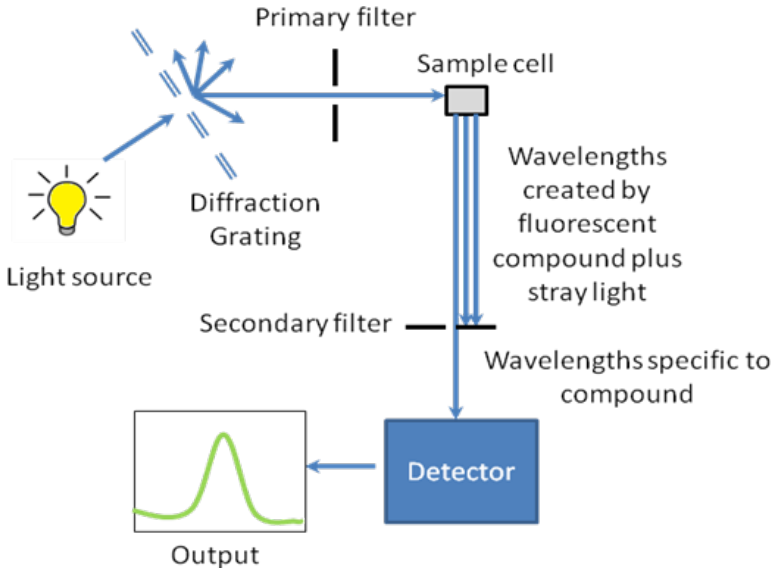

Figure 3.102: Schematic of fluorometer.

3.2.8.3.1 The light source

The excitation energy is provided by a light source that can emit wavelengths of light over the ultraviolet and the visible range. Different light sources can be used as excitation sources such as lasers, xenon arcs and mercury-vapor lamps. The choice of the light source depends on the sample. A laser source emits light of a high irradiance at a very narrow wavelength interval. This makes the need for the filter unnecessary, but the wavelength of the laser cannot be altered significantly. The mercury vapor lamp is a discrete line source. The xenon arc has a continuous emission spectrum between the ranges of 300 - 800 nm.

3.2.8.3.2 The diffraction grating and primary filter

The diffraction grating splits the incoming light source into its component wavelengths (Figure 3.102). The monochromator can then be adjusted to choose with wavelengths to pass through. Following the primary filter, specific wavelengths of light are irradiated onto the sample

3.2.8.3.3 Sample cell and sample preparation

A proportion of the light from the primary filter is absorbed by the sample. After the sample gets excited, the fluorescent substance returns to the ground state, by emitting a longer wavelength of light in all directions (Figure 3.102). Some of this light passes through a secondary filter. For liquid samples, a square cross section

tube sealed at one end and all four sides clear, is used as a sample cell. The choice of cuvette depends on three factors:

1. **Type of solvent** - For aqueous samples, specially designed rectangular quartz, glass or plastic cuvettes are used. For organic samples glass and quartz cuvettes are used.
2. **Excitation wavelength** – Depending on the size and thus, bandgap of the Group 12-16 semiconductor nanoparticles, different excitation wavelengths of light are used. Depending on the excitation wavelength, different materials are used (Table 3.9).

Cuvette	Wavelength (nm)
Visible only glass	380 - 780
Visible only plastic	380 - 780
UV plastic	220 - 780
Quartz	200 - 900

Table 3.9: Cuvette materials and their wavelengths.

3. **Cost** – Plastic cuvettes are the least expensive and can be discarded after use. Though quartz cuvettes have the maximum utility, they are the most expensive, and need to reused. Generally, disposable plastic cuvettes are used when speed is more important than high accuracy.

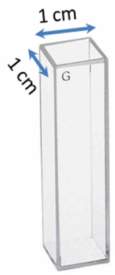

Figure 3.103: A typical cuvette for fluorescence spectroscopy.

The cuvettes have a 1 cm path length for the light (Figure 3.103). The best cuvettes need to be very clear and have no impurities that might affect the spectroscopic reading. Defects on the cuvette, such as scratches, can scatter light and hence should be avoided. Since the specifications of a cuvette are the same for both, the UV-visible spectrophotometer and fluorimeter, the same cuvette that is used to measure absorbance can be used to measure the fluorescence. For Group 12-16 semiconductor nanoparticles preparted in organic solvents, the clear four sided quartz cuvette is used. The sample solution should be dilute (absorbance <1 au), to avoid very high signal from the sample to burn out the detector. The solvent used to disperse the nanoparticles should not absorb at the excitation wavelength.

3.2.8.3.4 Secondary filter

The secondary filter is placed at a 90° angle (Figure 3.102) to the original light path to minimize the risk of transmitted or reflected incident light reaching the detector. Also this minimizes the amount of stray light,

and results in a better signal-to-noise ratio. From the secondary filter, wavelengths specific to the sample are passed onto the detector.

3.2.8.3.5 Detector

The detector can either be single-channeled or multichanneled (Figure 3.102). The single-channeled detector can only detect the intensity of one wavelength at a time, while the multichanneled detects the intensity at all wavelengths simultaneously, making the emission monochromator or filter unnecessary. The different types of detectors have both advantages and disadvantages.

3.2.8.3.6 Output

The output is the form of a plot of intensity of emitted light as a function of wavelength as shown in Figure 3.104.

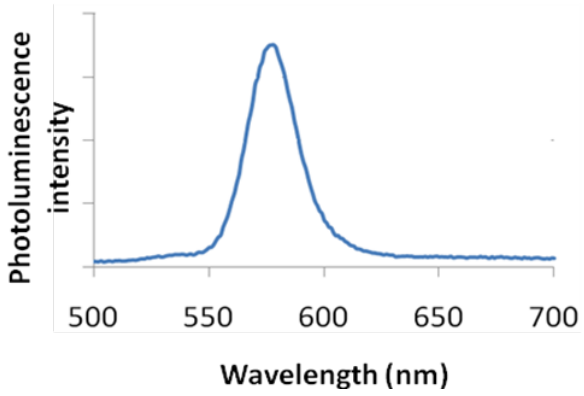

Figure 3.104: Emission spectra of CdSe quantum dot.

3.2.8.4 Analysis of data

The data obtained from fluorimeter is a plot of fluorescence intensity as a function of wavelength. Quantitative and qualitative data can be obtained by analysing this information.

3.2.8.4.1 Quantitative information

From the fluorescence intensity versus wavelength data, the quantum yield (Φ_F) of the sample can be determined. Quantum yield is a measure of the ratio of the photons absorbed with respect to the photons emitted. It is important for the application of Group 12-16 semiconductor quantum dots using their fluorescence properties, for e.g., bio-markers.

The most well-known method for recording quantum yield is the comparative method which involves the use of well characterized standard solutions. If a test sample and a standard sample have similar absorbance values at the same excitation wavelength, it can be assumed that the number of photons being absorbed by both the samples is the same. This means that a ratio of the integrated fluorescence intensities of the test and standard sample measured at the same excitation wavelength will give a ratio of quantum yields. Since

the quantum yield of the standard solution is known, the quantum yield for the unknown sample can be calculated.

A plot of integrated fluorescence intensity versus absorbance at the excitation wavelength is shown in Figure 3.105. The slope of the graphs shown in Figure 3.105 are proportional to the quantum yield of the different samples. Quantum yield is then calculated using (3.70), where subscripts ST denotes standard sample and X denotes the test sample; QY is the quantum yield; RI is the refractive index of the solvent.

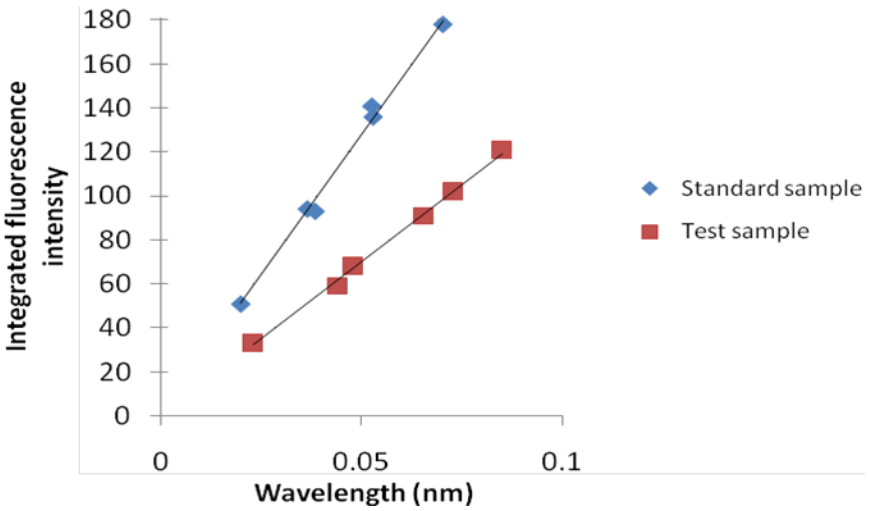

Figure 3.105: Integrated fluoresncene intensity as a function of absorbance.

$$\frac{QY_X}{QY_{ST}} = \frac{\text{slope}_X\ (\text{RI}_X)^2}{\text{slope}_{ST}\ (\text{RI}_{ST})^2} \tag{3.70}$$

Take the example of Figure 3.105. If the same solvent is used in both the sample and the standard solution, the ratio of quantum yields of the sample to the standard is given by (3.71). If the quantum yield of the standard is known to 0.95, then the quantum yield of the test sample is 0.523 or 52.3%.

$$\frac{QY_X}{QY_{ST}} = \frac{1.41}{2.56} \tag{3.71}$$

The assumption used in the comparative method is valid only in the Beer-Lambert law linear regime. Beer-Lambert law states that absorbance is directly proportional to the path length of light travelled within the sample, and concentration of the sample. The factors that affect the quantum yield measurements are the following:

- **Concentration** – Low concentrations should be used (absorbance < 0.2 a.u.) to avoid effects such as self quenching.
- **Solvent** – It is important to take into account the solvents used for the test and standard solutions. If the solvents used for both are the same then the comparison is trivial. However, if the solvents in the test and standard solutions are different, this difference needs to be accounted for. This is done by incorporating the solvent refractive indices in the ratio calculation.
- **Standard samples** – The standard samples should be characterized thoroughly. In addition, the standard sample used should absorb at the excitation wavelength of the test sample.

- **Sample preparation** – It is important that the cuvettes used are clean, scratch free and clear on all four sides. The solvents used must be of spectroscopic grade and should not absorb in the wavelength range.
- **Slit width** – The slit widths for all measurements must be kept constant.

The quantum yield of the Group 12-16 semiconductor nanoparticles are affected by many factors such as the following.

- **Surface defects** – The surface defects of semiconductor quantum dots occur in the form of unsatisfied valencies. Thus resulting in unwanted recombinations. These unwanted recombinations reduce the loss of energy through radiative decay, and thus reducing the fluorescence.
- **Surface ligands** – If the surface ligand coverage is a 100%, there is a smaller chance of surface recombinations to occur.
- **Solvent polarity** – If the solvent and the ligand have similar solvent polarities, the nanoparticles are more dispersed, reducing the loss of electrons through recombinations.

3.2.8.4.2 Qualitative Information

Apart from quantum yield information, the relationship between intensity of fluorescence emission and wavelength, other useful qualitative information such as size distribution, shape of the particle and presence of surface defects can be obtained.

As shown in Figure 3.106, the shape of the plot of intensity versus wavelength is a Gaussian distribution. In Figure 3.106, the full width at half maximum (FWHM) is given by the difference between the two extreme values of the wavelength at which the photoluminescence intensity is equal to half its maximum value. From the full width half max (FWHM) of the fluorescence intensity Gaussian distribution, it is possible to determine qualitatively the size distribution of the sample. For a Group 12-16 quantum dot sample if the FWHM is greater than 30, the system is very polydisperse and has a large size distribution. It is desirable for all practical applications for the FWHM to be lesser than 30.

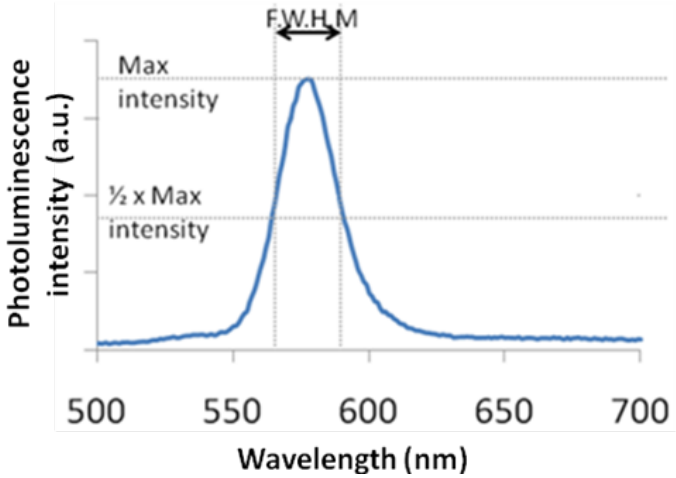

Figure 3.106: Emission spectra of CdSe QDs showing the full width half maximum (FWHM).

From the FWHM of the emission spectra, it is also possible to qualitatively get an idea if the particles are spherical or shaped. During the synthesis of the shaped particles, the thickness of the rod or the arm of the tetrapod does not vary among the different particles, as much as the length of the rods or arms changes. The thickness of the arm or rod is responsible for the quantum effects in shaped particles. In the case of quantum dots, the particle is quantum confined in all dimensions. Thus, any size distribution during the synthesis of quantum dots greatly affects the emission spectra. As a result the FWHM of rods and tetrapods is much smaller as compared to a quantum dot. Hence, qualitatively it is possible to differentiate between quantum dots and other shaped particles.

Another indication of branched structures is the decrease in the intensity of fluorescence peaks. Quantum dots have very high fluorescence values as compared to branched particles, since they are quantum confined in all dimensions as compared to just 1 or 2 dimensions in the case of branched particles.

3.2.8.5 Fluorescence spectra of different Group 12-16 semiconductor nanoparticles

The emission spectra of all Group 12-16 semiconductor nanoparticles are Gaussian curves as shown in Figure 3.104 and Figure 3.106. The only difference between them is the band gap energy, and hence each of the Group 12-16 semiconductor nanoparticles fluoresce over different ranges of wavelengths

3.2.8.5.1 Cadmium selenide

Since its bulk band gap (1.74 eV, 712 nm) falls in the visible region cadmium Selenide (CdSe) is used in various applications such as solar cells, light emitting diodes, etc. Size evolving emission spectra of cadmium selenide is shown in Figure 3.107. Different sized CdSe particles have different colored fluorescence spectra. Since cadmium and selenide are known carcinogens and being nanoparticles are easily absorbed into the human body, there is some concern regarding these particles. However, CdSe coated with ZnS can overcome all the harmful biological effects, making cadmium selenide nanoparticles one of the most popular 12-16 semiconductor nanoparticle.

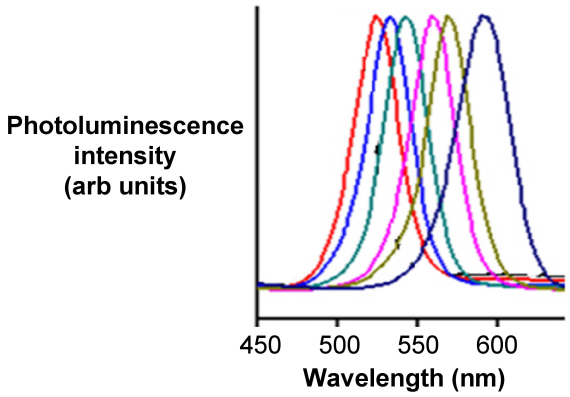

Figure 3.107: Size evolving CdSe emission spectra. Adapted from http://www.physics.mq.edu.au.

A combination of the absorbance and emission spectra is shown in Figure 3.108 for four different sized particles emitting green, yellow, orange, and red fluorescence.

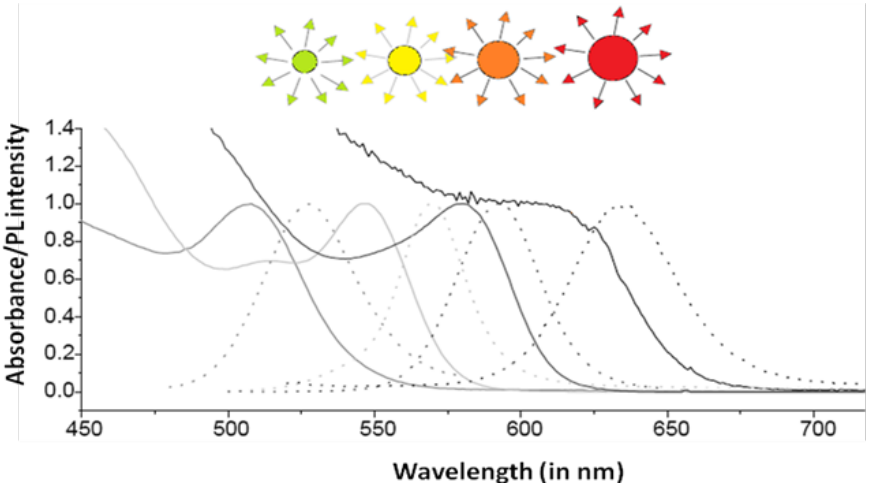

Figure 3.108: Absorption and emission spectra of CdSe quantum dots. Adapted from G. Schmid, *Nanoparticles: From Theory to Application*, Wiley-VCH, Weinham (2004).

3.2.8.5.2 Cadmium telluride

Cadmium Telluride (CdTe) has a band gap of 1.44 eV and thus absorbs in the infra red region. The size evolving CdTe emission spectra is shown in Figure 3.109.

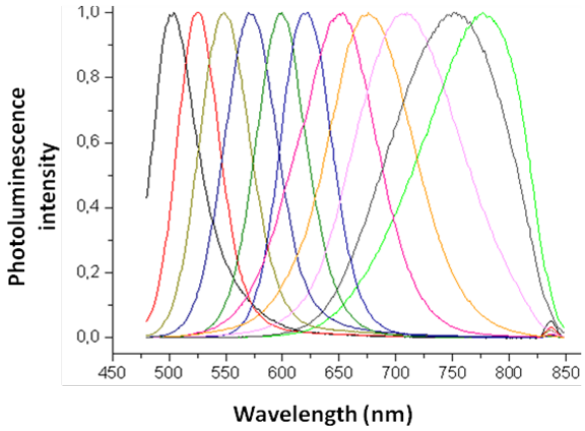

Figure 3.109: Size evolution spectra of CdTe quantum dots.

3.2.8.5.3 Adding shells to QDs

Capping a core quantum dot with a semiconductor material with a wider bandgap than the core, reduces the nonradiative recombination and results in brighter fluorescence emission. Quantum yields are affected by the presences of free surface charges, surface defects and crystal defects, which results in unwanted recombinations. The addition of a shell reduces the nonradiative transitions and majority of the electrons relax radiatively to the valence band. In addition, the shell also overcomes some of the surface defects.

For the CdSe-core/ZnS-shell systems exhibit much higher quantum yield as compared to core CdSe quantum dots as seen in Figure 3.110.

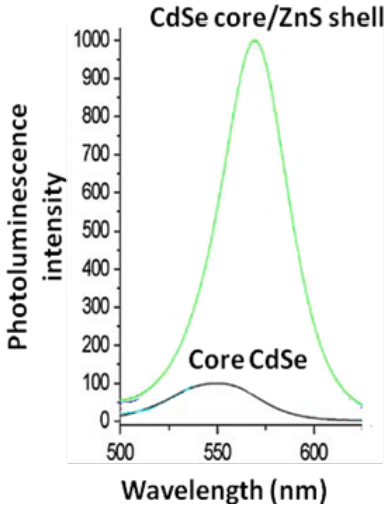

Figure 3.110: Emission spectra of core CdSe only and CdSe-core/ZnS-shell.

3.2.8.6 Bibliography

- A. T. R. Williams, S. A. Winfield, and J. N. Miller, *Analyst*, 1983, **108**, 1067.
- G. Schmid, *Nanoparticles: From Theory to Application*, Wiley-VCH, Weinham, (2004).
- J. Y. Hariba, *A Guide to Recording Fluorescence Quantum Yield*, Jobin Yvon Hariba Limited, Stanmore (2003).
- C. Qing Zhu, P. Wang, X. Wang, and Y. Li, *Nanoscale Res. Lett.*., 2008, **3**, 213.

3.2.9 XPS of Carbon Nanomaterials[20]

3.2.9.1 Introduction

X-ray photoelectron spectroscopy (XPS), also called electron spectroscopy for chemical analysis (ESCA), is a method used to determine the elemental composition of a material's surface. It can be further applied to determine the chemical or electronic state of these elements.

The photoelectric effect is the ejection of electrons from the surface of a material upon exposure to electromagnetic radiation of sufficient energy. Electrons emitted have characteristic kinetic energies proportional to

[20] This content is available online at <http://cnx.org/content/m34549/1.2/>.

the energy of the radiation, according to (3.72), where KE is the kinetic energy of the electron, h is Planck's constant, ν is the frequency of the incident radiation, E_b is the ionization, or binding, energy, and ϕ is the work function. The work function is a constant which is dependent upon the spectrometer.

$$KE = h\nu - E_b - \varphi \tag{3.72}$$

In photoelectron spectroscopy, high energy radiation is used to expel core electrons from a sample. The kinetic energies of the resulting core electrons are measured. Using the equation with the kinetic energy and known frequency of radiation, the binding energy of the ejected electron may be determined. By Koopman's theorem, which states that ionization energy is equivalent to the negative of the orbital energy, the energy of the orbital from which the electron originated is determined. These orbital energies are characteristic of the element and its state.

3.2.9.2 Basics of XPS

3.2.9.2.1 Sample preparation

As a surface technique, samples are particularly susceptible to contamination. Furthermore, XPS samples must be prepared carefully, as any loose or volatile material could contaminate the instrument because of the ultra-high vacuum conditions. A common method of XPS sample preparation is embedding the solid sample into a graphite tape. Samples are usually placed on 1 x 1 cm or 3 x 3 cm sheets.

3.2.9.2.2 Experimental set-up

Monochromatic aluminum ($h\nu$ = 1486.6 eV) or magnesium ($h\nu$ = 1253.6 eV) K_α X-rays are used to eject core electrons from the sample. The photoelectrons ejected from the material are detected and their energies measured. Ultra-high vacuum conditions are used in order to minimize gas collisions interfering with the electrons before they reach the detector.

3.2.9.2.3 Measurement specifications

XPS analyzes material between depths of 1 and 10 nm, which is equivalent to several atomic layers, and across a width of about 10 μm. Since XPS is a surface technique, the orientation of the material affects the spectrum collected.

3.2.9.2.4 Data collection

X-ray photoelectron (XP) spectra provide the relative frequencies of binding energies of electrons detected, measured in electron-volts (eV). Detectors have accuracies on the order of $\pm$0.1 eV. The binding energies are used to identify the elements to which the peaks correspond. XPS data is given in a plot of intensity versus binding energy. Intensity may be measured in counts per unit time (such as counts per second, denoted c/s). Often, intensity is reported as arbitrary units (arb. units), since only relative intensities provide relevant information. Comparing the areas under the peaks gives relative percentages of the elements detected in the sample. Initially, a survey XP spectrum is obtained, which shows all of the detectable elements present in the sample. Elements with low detection or with abundances near the detection limit of the spectrometer may be missed with the survey scan. Figure 3.111 shows a sample survey XP scan of fluorinated double-walled carbon nanotubes (DWNTs).

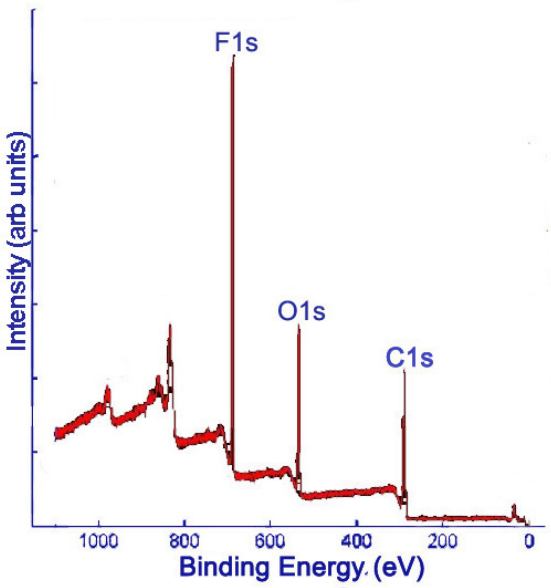

Figure 3.111: Survey XP spectrum of F-DWNTs (O. Kuznetsov, Rice University).

Subsequently, high resolution scans of the peaks can be obtained to give more information. Elements of the same kind in different states and environments have slightly different characteristic binding energies. Computer software is used to fit peaks within the elemental peak which represent different states of the same element, commonly called deconvolution of the elemental peak. Figure 3.112 and Figure 3.113 show high resolutions scans of C1s and F1s peaks, respectively, from Figure 3.111, along with the peak designations.

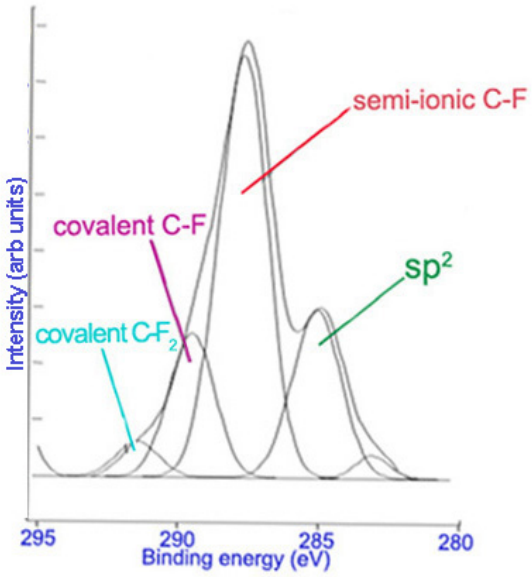

Figure 3.112: Deconvoluted high resolution C1s spectrum of F-DWNTs (O. Kuznetsov, Rice University).

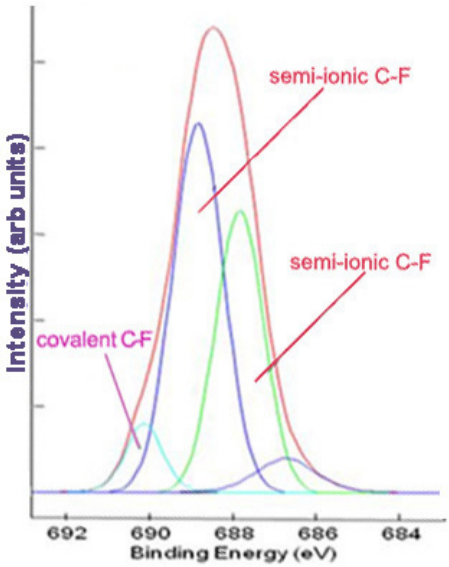

Figure 3.113: Deconvoluted high resolution F1s spectrum of F-DWNTs (O. Kuznetsov, Rice University).

3.2.9.2.5 Limitations

Both hydrogen and helium cannot be detected using XPS. For this reason, XPS can provide only relative, rather than absolute, ratios of elements in a sample. Also, elements with relatively low atomic percentages close to that of the detection limit or low detection by XPS may not be seen in the spectrum. Furthermore, each peak represents a distribution of observed binding energies of ejected electrons based on the depth of the atom from which they originate, as well as the state of the atom. Electrons from atoms deeper in the sample must travel through the above layers before being liberated and detected, which reduces their kinetic energies and thus increases their apparent binding energies. The width of the peaks in the spectrum consequently depends on the thickness of the sample and the depth to which the XPS can detect; therefore, the values obtained vary slightly depending on the depth of the atom. Additionally, the depth to which XPS can analyze depends on the element being detected.

High resolution scans of a peak can be used to distinguish among species of the same element. However, the identification of different species is discretionary. Computer programs are used to deconvolute the elemental peak. The peaks may then be assigned to particular species, but the peaks may not correspond with species in the sample. As such, the data obtained must be used cautiously, and care should be taken to avoid over-analyzing data.

3.2.9.3 XPS for carbon nanomaterials

Despite the aforementioned limitations, XPS is a powerful surface technique that can be used to accurately detect the presence and relative quantities of elements in a sample. Further analysis can provide information about the state and environment of atoms in the sample, which can be used to infer information about the surface structure of the material. This is particularly useful for carbon nanomaterials, in which surface

structure and composition greatly influence the properties of the material. There is much research interest in modifying carbon nanomaterials to modulate their properties for use in many different applications.

3.2.9.3.1 Sample preparation

Carbon nanomaterials present certain issues in regard to sample preparation. The use of graphite tape is a poor option for carbon nanomaterials because the spectra will show peaks from the graphite tape, adding to the carbon peak and potentially skewing or overwhelming the data. Instead, a thin indium foil (between 0.1 and 0.5 mm thick) is used as the sample substrate. The sample is simply pressed onto a piece of the foil.

3.2.9.4 Analysis and applications for carbon nanomaterials

3.2.9.4.1 Chemical Speciation

The XP survey scan is an effective way to determine the identity of elements present on the surface of a material, as well as the approximate relative ratios of the elements detected. This has important implications for carbon nanomaterials, in which surface composition is of greatest importance in their uses. XPS may be used to determine the purity of a material. For example, nanodiamond powder is a created by detonation, which can leave nitrogenous groups and various oxygen containing groups attached to the surface. Figure 3.114 shows a survey scan of a nanodiamond thin film with the relative atomic percentages of carbon, oxygen, and nitrogen being 91.25%, 6.25%, and 1.7%, respectively. Based on the XPS data, the nanodiamond material is approximately 91.25% pure.

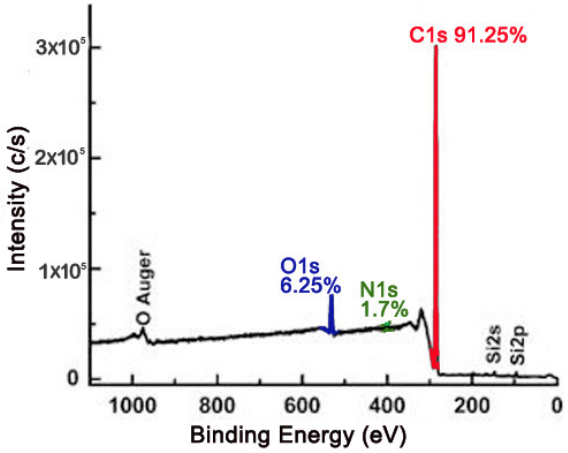

Figure 3.114: Survey XPS of a nanodiamond thin film. Adapted from F. Y. Xie, W. G. Xie, J. Chen, X. Liu, D. Y. Lu, and W. H. Zhang, *J. Vac. Sci. Tech. B*, 2008, **26**, 102.

XPS is a useful method to verify the efficacy of a purification process. For example, high-pressure CO conversion single-walled nanotubes (HiPco SWNTs) are made using iron as a catalyst. Figure 3.115 shows the Fe2p XP spectra for pristine and purified HiPco SWNTs.

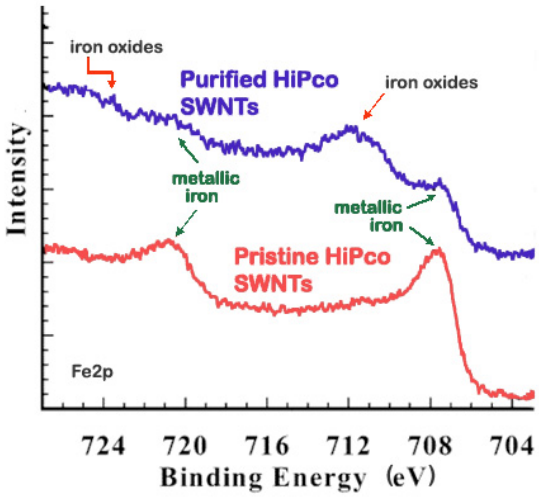

Figure 3.115: High resolution scan of Fe2p peak for pristine and purified HiPco SWNTs. Adapted with permission from C. M. Yang, H. Kanoh, K. Kaneko, M. Yudasaka, and S. Iijima, *J. Phys. Chem. B*, 2002, **106**, 8994. Copyright: American Chemical Society (2002).

For this application, XPS is often done in conjunction with thermogravimetric analysis (TGA), which measures the weight lost from a sample at increasing temperatures. TGA data serves to corroborate the changes observed with the XPS data by comparing the percentage of weight loss around the region of the impurity suspected based on the XP spectra. The TGA data support the reduction in iron content with purification suggested by the XP spectra above, for the weight loss at temperatures consistent with iron loss decreases from 27% in pristine SWNTs to 18% in purified SWNTs. Additionally, XPS can provide information about the nature of the impurity. In Figure 3.115, the Fe2p spectrum for pristine HiPco SWNTs shows two peaks characteristic of metallic iron at 707 and 720 eV. In contrast, the Fe2p spectrum for purified HiPco SWNTs also shows two peaks at 711 and 724 eV, which are characteristic of either Fe_2O_3 or Fe_3O_4. In general, the atomic percentage of carbon obtained from the XPS spectrum is a measure of the purity of the carbon nanomaterials.

3.2.9.4.2 Bonding and functional groups

XP spectra give evidence of functionalization and can provide insight into the identity of the functional groups. Carbon nanomaterials provide a versatile surface which can be functionalized to modulate their properties. For example, the sodium salt of phenyl sulfonated SWNTs is water soluble. In the XP survey scan of the phenyl sulfonated SWNTs, there is evidence of functionalization owing to the appearance of the S2p peak. Figure 3.116 shows the survey XP spectrum of phenyl sulfonated SWNTs.

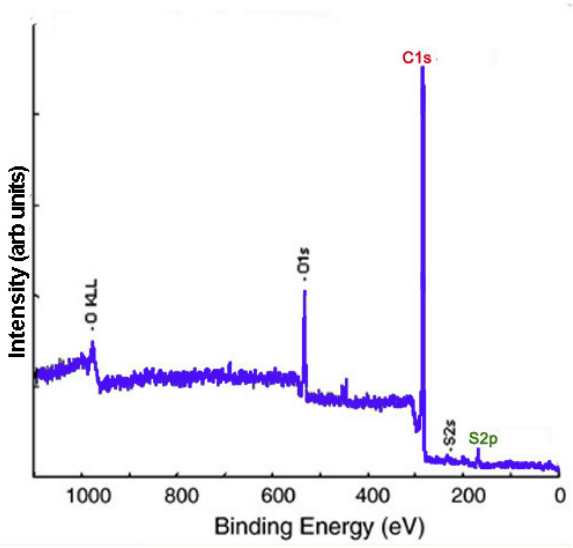

Figure 3.116: Survey XP spectrum of phenyl sulfonated SWNTs. Adapted with permission from F. Liang, J. M. Beach, P. K. Rai, W. H. Guo, R. H. Hauge, M. Pasquali, R. E. Smalley, and W. E. Billups, *Chem. Mater.*, 2006, **18**, 1520. Copyright: American Chemical Society (2006).

The survey XP spectrum of the sodium salt shows a Na1s peak (Figure 3.117) and the high resolution scans of Na1s and S2p show that the relative atomic percentages of Na1s and S2p are nearly equal (Figure 3.118), which supports the formation of the sodium salt.

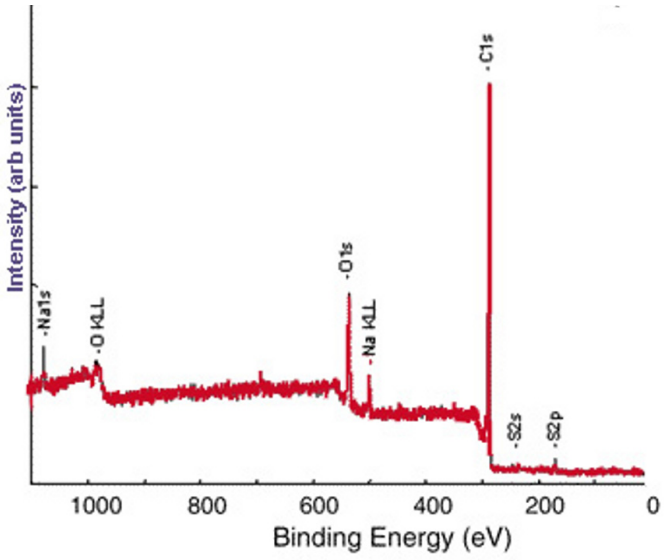

Figure 3.117: Survey XP spectrum of phenyl sulfonated SWNTs. Adapted with permission from F. Liang, J. M. Beach, P. K. Rai, W. H. Guo, R. H. Hauge, M. Pasquali, R. E. Smalley, and W. E. Billups, *Chem. Mater.*, 2006, **18**, 1520. Copyright: American Chemical Society (2006).

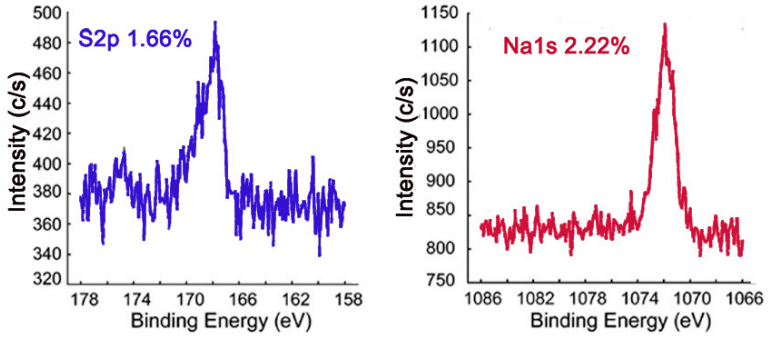

Figure 3.118: High resolution S2p (left) and Na1s (right) XP spectra of phenyl sulfonated SWNTs. Adapted with permission from F. Liang, J. M. Beach, P. K. Rai, W. H. Guo, R. H. Hauge, M. Pasquali, R. E. Smalley, and W. E. Billups, *Chem. Mater.*, 2006, **18**, 1520. Copyright: American Chemical Society (2006).

3.2.9.4.3 Further characterization

High resolution scans of each of the element peaks of interest can be obtained to give more information about the material. This is a way to determine with high accuracy the presence of elements as well as relative ratios of elements present in the sample. This can be used to distinguish species of the same element in different chemical states and environments, such as through bonding and hybridization, present in the material. The distinct peaks may have binding energies that differ slightly from that of the convoluted elemental peak. Assignment of peaks can be done using XPS databases, such as that produced by NIST[21] . The ratios of the intensities of these peaks can be used to determine the percentage of atoms in a particular state. Discrimination between and identity of elements in different states and environments is a strength of XPS that is of particular interest for carbon nanomaterials.

3.2.9.4.3.1 Hybridization

The hybridization of carbons influences the properties of a carbon nanomaterial and has implications in its structure. XPS can be used to determine the hybridization of carbons on the surface of a material, such as graphite and nanodiamond. Graphite is a carbon material consisting of sp^2 carbons. Thus, theoretically the XPS of pure graphite would show a single C1s peak, with a binding energy characteristic of sp^2 carbon (around 284.2 eV). On the other hand, nanodiamond consists of sp^3 bonded carbons. The XPS of nanodiamond should show a single C1s peak, with a binding energy characteristic of sp^3 carbon (around 286 eV). The ratio of the sp^2 and sp^3 peaks in the C1s spectrum gives the ratio of sp^2 and sp^3 carbons in the nanomaterial. This ratio can be altered and compared by collecting the C1s spectra. For example, laser treatment of graphite creates diamond-like material, with more sp^3 character when a higher laser power is used. This can be observed in Figure 3.119, in which the C1s peak is broadened and shifted to higher binding energies as increased laser power is applied.

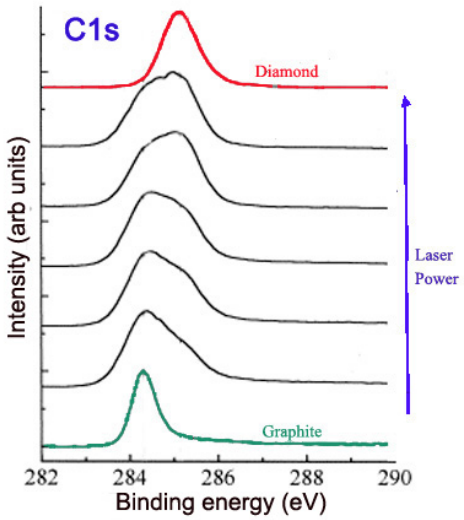

Figure 3.119: C1s high resolution XP spectra of graphite, nanodiamond, and graphite samples with increasing laser power treatment. Adapted from P. Merel, M. Tabbal, M. Chaker, S. Moisa, and J. Margot, *Appl. Surf. Sci.*, 1998, **136**, 105.

[21] http://srdata.nist.gov/xps/Default.aspx

Alternatively, annealing nanodiamond thin films at very high temperatures creates graphitic layers on the nanodiamond surface, increasing sp^2 content. The extent of graphitization increases with the temperature at which the sample is annealed, as shown in Figure 3.120.

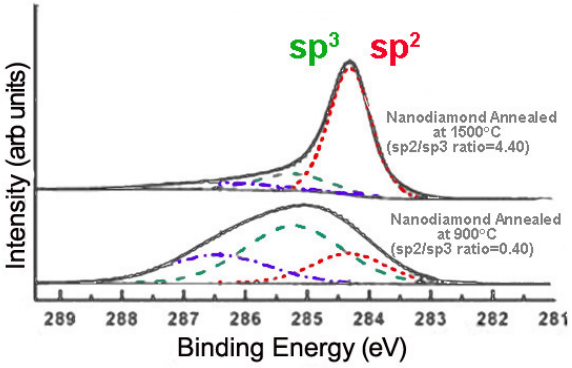

Figure 3.120: Deconvoluted high resolution C1s XP spectra for annealed nanodiamond. Adapted from F. Y. Xie, W. G. Xie, J. Chen, X. Liu, D. Y. Lu, and W. H. Zhang, *J. Vac. Sci. Tech. B*, 2008, **26**, 102.

3.2.9.4.3.2 Reaction completion

Comparing the relative intensities of various C1s peaks can be powerful in verifying that a reaction has occurred. Fluorinated carbon materials are often used as precursors to a broad range of variously functionalized materials. Reaction of fluorinated SWNTs (F-SWNTs) with polyethyleneimine (PEI) leads to decreases in the covalent carbon-fluoride C1s peak, as well as the evolution of the amine C1s peak. These changes are observed in the C1s spectra of the two samples (Figure 3.121).

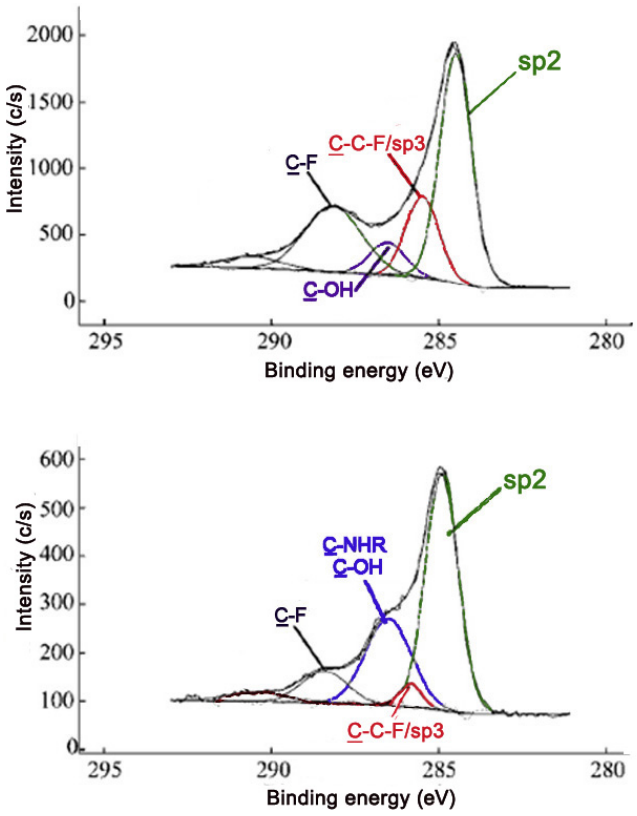

Figure 3.121: High resolution C1s XP spectra of F-SWNTs (top) and PEI-SWNTs (bottom). Adapted with permission from E. P. Dillon, C. A. Crouse, and A. R. Barron, *ACS Nano*, 2008, **2**, 156. Copyright: American Chemical Society (2008).

3.2.9.4.3.3 Nature and extent of functionalization

XPS can also be applied to determine the nature and extent of functionalization. In general, binding energy increases with decreasing electron density about the atom. Species with more positive oxidation states have higher binding energies, while more reduced species experience a greater degree of shielding, thus increasing the ease of electron removal.

The method of fluorination of carbon materials and such factors as temperature and length of fluorination affect the extent of fluoride addition as well as the types of carbon-fluorine bonds present. A survey scan can be used to determine the amount of fluorine compared to carbon. High resolution scans of the C1s and F1s peaks can also give information about the proportion and types of bonds. A shift in the peaks, as well as changes in peak width and intensity, can be observed in spectra as an indication of fluorination of graphite. Figure 3.122 shows the Cls and F1s spectra of samples containing varying ratios of carbon to fluorine.

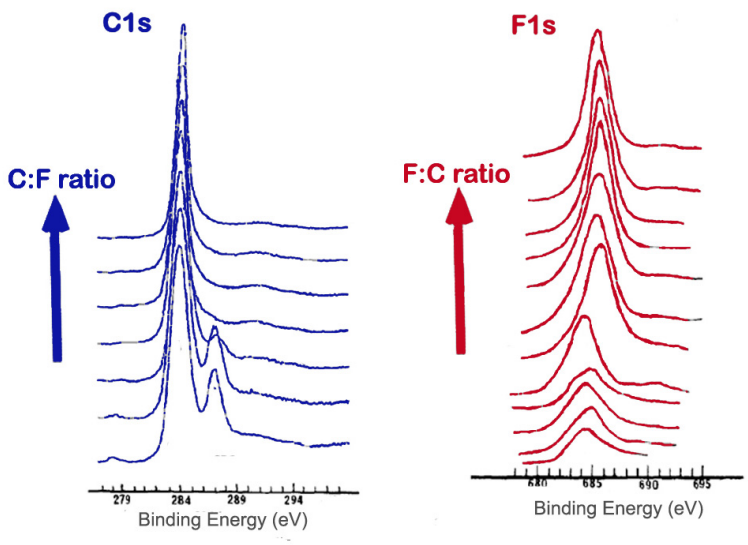

Figure 3.122: C1s and F1s high resolution XP spectra for graphite fluorides. Adapted from I. Palchan, M. Crespin, H. Estrade-Szwarckopf, and B. Rousseau. *Chem. Phys. Lett.*, 1989, **157**, 321.

Furthermore, different carbon-fluorine bonds show characteristic peaks in high resolution C1s and F1s spectra. The carbon-fluorine interactions in a material can range from ionic to covalent. Covalent carbon-fluorine bonds show higher core electron binding energies than bonds more ionic in character. The method of fluorination affects the nature of the fluorine bonds. Graphite intercalation compounds are characterized by ionic carbon-fluorine bonding. Figure 3.123 shows the F1s spectra for two fluorinated exfoliated graphite samples prepared with different methods.

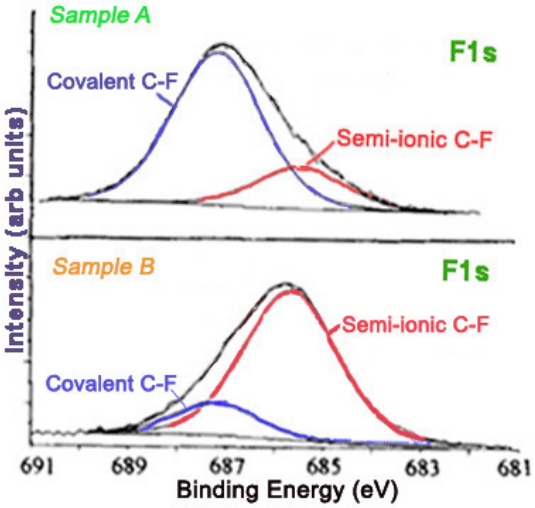

Figure 3.123: High resolution F1s XP spectra of two fluorinated exfoliated graphite samples. Adapted from A. Tressaud, F. Moguet, S. Flandrois, M. Chambon, C. Guimon, G. Nanse, E. Papirer, V. Gupta, and O.P. Bahl. *J. Phys. Chem. Solids*, 1996, **57**, 745.

Also, the peaks for carbons attached to a single fluorine atom, two fluorine atoms, and carbons attached to fluorines have characteristic binding energies. These peaks are seen in that C1s spectra of F- and PEI-SWNTs shown in Figure 3.124.

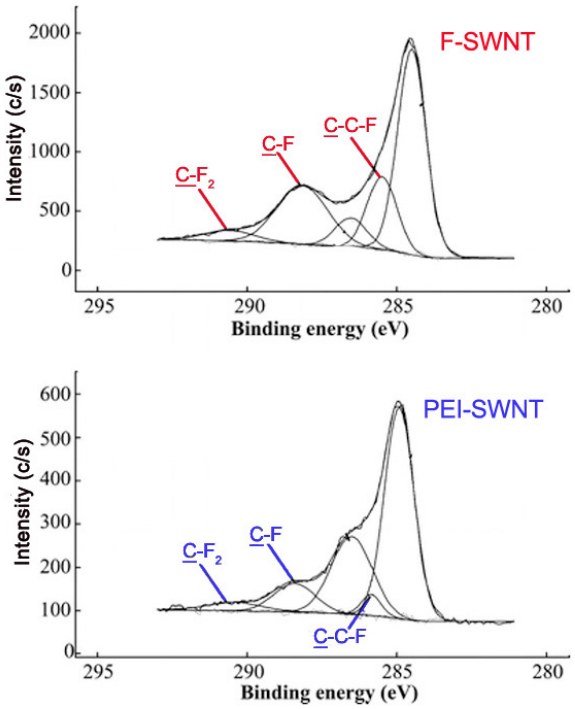

Figure 3.124: High resolution C1s XP spectra of F-SWNTs (top) and PEI-SWNTs (bottom). Adapted with permission from E. P. Dillon, C. A. Crouse, and A. R. Barron, *ACS Nano*, 2008, **2**, 156. Copyright: American Chemical Society (2008).

Table 3.10 lists various bonds and functionalities and the corresponding C1s binding energies, which may be useful in assigning peaks in a C1s spectrum, and consequently in characterizing the surface of a material.

Bond/Group	**Binding Energy (eV)**
C-C	**284.0-286.0**
C-C (sp^2)	284.3-284.6
C-C (sp^3)	285.0-286.0
C-N	**285.2-288.4**
C-NR_2 (amine)	285.5-286.4
O=C-NH (amide)	287.9-288.6
-C≡N (nitrile)	266.3-266.8
C-O	**286.1-290.0**
O=C-OH (carboxyl)	288.0-289.4
-C-O (epoxy)	286.1-287.1
-C-OH (hydroxyl)	286.4-286.7
-C-O-C- (ether)	286.1-288.0
-C=O (aldehyde/ketone)	287.1-288.1
C-F	**287.0-293.4**
-C-F (covalent)	287.7-290.2
-C-F (ionic)	287.0-287.4
C≡C-F	286.0-287.7
C-F_2	291.6-292.4
C-F_3	292.4-293.4
C-S	**285.2-287.5**
C-Cl	**287.0-287.2**

Table 3.10: Summary of selected C1s binding energies.

3.2.9.4.4 Conclusion

X-ray photoelectron spectroscopy is a facile and effective method for determining the elemental composition of a material's surface. As a quantitative method, it gives the relative ratios of detectable elements on the surface of the material. Additional analysis can be done to further elucidate the surface structure. Hybridization, bonding, functionalities, and reaction progress are among the characteristics that can be inferred using XPS. The application of XPS to carbon nanomaterials provides much information about the material, particularly the first few atomic layers, which are most important for the properties and uses of carbon nanomaterials.

3.2.9.5 Bibliography

- J. Bockris, *Modern Electrochemistry 2A*, 2nd ed., Springer (2001).
- E. P. Dillon, C. A. Crouse, and A. R. Barron, *ACS Nano*, 2008, **2**, 156.
- Y. G. Gogotsi, and I. V. Uvarova, *Nanostructured materials and coatings for biomedical and sensor applications*, Kluwer Academic Publishing (2003).
- F. Liang, J. M. Beach, P. K. Rai, W. H. Guo, R. H. Hauge, M. Pasquali, R. E. Smalley, and W. E. Billups, *Chem. Mater.*, 2006, **18**, 1520.

- P. Merel, M. Tabbal, M. Chaker, S. Moisa, and J. Margot, *Appl. Surf. Sci.*, 1998, **136**, 105.
- T. Nakajima, *Graphite fluorides and carbon-fluorine compounds*, CRC Press, Boca Raton (1991).
- I. Palhan, M. Crespin, H. Estrade-Szwarckopf, and B. Rousseau. *Chem. Phys. Lett.*, 1989, **157**, 321.
- A. Tressaud, F. Moguet, S. Flandrois, M. Chambon, C. Guimon, G. Nanse, E. Papirer, V. Gupta, and O. P. Bahl. *J. Phys. Chem. Solids*, 1996, **57**, 745.
- F. Y. Xie, W. G. Xie, J. Chen, X. Liu, D. Y. Lu, and W. H. Zhang, *J. Vac. Sci. Tech. B*, 2008, **26**, 102.
- C. M. Yang, H. Kanoh, K. Kaneko, M. Yudasaka, and S. Iijima, *J. Phys. Chem. B*, 2002, **106**, 8994.

3.2.10 Using XPS to Analyze Metal Nanoparticles[22]

3.2.10.1 Introduction

X-ray photoelectron spectroscopy (XPS) is a surface technique developed for use with thin films. More recently, however, it has been used to analyze the chemical and elemental composition of nanoparticles. The complication of nanoparticles is that they are neither flat nor larger than the diameter of the beam, creating issues when using the data obtained at face value. Samples of nanoparticles will often be large aggregates of particles. This creates problems with the analysis acquisition, as there can be a variety of cross-sections, as seen in Figure 3.125. This acquisition problem is also compounded by the fact that the surfactant may not be completely covering the particle, as the curvature of the particle creates defects and divots. Even if it is possible to create a monolayer of particles on a support, other issues are still present. The background support will be analyzed with the particle, due to their small size and the size of the beam and the depth at which it can penetrate.

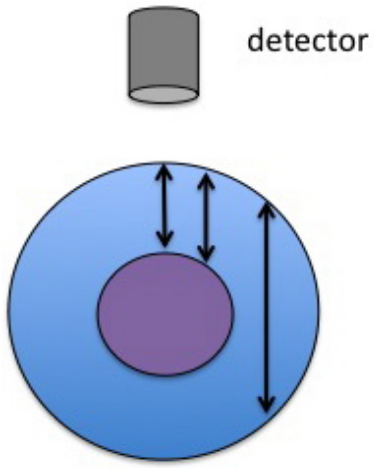

Figure 3.125: Different cross-sections of analysis possible on a nanoparticle.

Many other factors can introduce changes in nanoparticles and their properties. There can be probe, environmental, proximity, and sample preparation effects. The dynamics of particles can wildly vary depending on the reactivity of the particle itself. Sputtering can also be a problem. The beam used to sputter

[22] This content is available online at <http://cnx.org/content/m34526/1.1/>.

will be roughly the same size or larger than the particles. This means that what appears in the data is not a section of particle, but an average composition of several particles.

Each of these issues needs to be taken into account and preventative measures need to be used so the data is the best representation possible.

3.2.10.2 Sample preparation

Sample preparation of nanoparticles is very important when using XPS. Certain particles, such as iron oxides without surfactants, will interact readily with oxygen in the air. This causes the particles to gain a layer of oxygen contamination. When the particles are then analyzed, oxygen appears where it should not and the oxidation state of the metal may be changed. As shown by these particles, which call for handling, mounting and analysis without exposure to air, knowing the reactivity of the nanoparticles in the sample is very important even before starting analysis. If the reactivity of the nanoparticle is known, such as the reactivity of oxygen and iron, then preventative steps can be taken in sample preparation in order to obtain the best analysis possible.

When preparing a sample for XPS, a powder form is often used. This preparation, however, will lead to aggregation of nanoparticles. If analysis is performed on such a sample, the data obtained will be an average of composition of each nanoparticle. If composition of a single particle is what is desired, then this average composition will not be sufficient. Fortunately, there are other methods of sample preparation. Samples can be supported on a substrate, which will allow for analysis of single particles. A pictorial representation in Figure 3.126 shows the different types of samples that can occur with nanoparticles.

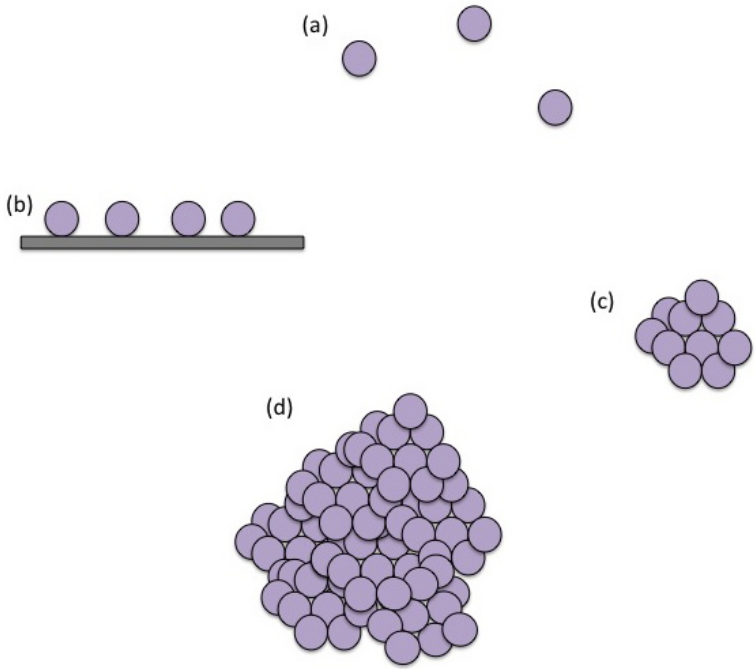

Figure 3.126: Representation of (a) a theoretical isolated nanoparticles, (b) nanoparticles suspended on a substrate, (c) an aggregate of nanoparticles, and (d) a powdered form of nanoparticles.

3.2.10.3 Analysis limitations

Nanoparticles are dynamic; their properties can change when exposed to new chemical environments, leading to a new set of applications. It is the dynamics of nanoparticles that makes them so useful and is one of the reasons why scientists strive to understand their properties. However, it is this dynamic ability that makes analysis difficult to do properly. Nanoparticles are easily damaged and can change properties over time or with exposure to air, light or any other environment, chemical or otherwise. Surface analysis is often difficult because of the high rate of contamination. Once the particles are inserted into XPS, even more limitations appear.

3.2.10.3.1 Probe effects

There are often artifacts introduced from the simple mechanism of conducting the analysis. When XPS is used to analyze the relatively large surface of thin films, there is small change in temperature as energy is transferred. The thin films, however, are large enough that this small change in energy has to significant change to its properties. A nanoparticle is much smaller. Even a small amount of energy can drastically change the shape of particles, in turn changing the properties, giving a much different set of data than expected.

The electron beam itself can affect how the particles are supported on a substrate. Theoretically, nanoparticles would be considered separate from each other and any other chemical environments, such as solvents or substrates. This, however, is not possible, as the particles must be suspended in a solution or placed on a substrate when attempting analysis. The chemical environment around the particle will have some amount of interaction with the particle. This interaction will change characteristics of the nanoparticles, such as oxidation states or partial charges, which will then shift the peaks observed. If particles can be separated and suspended on a substrate, the supporting material will also be analyzed due to the fact that the X-ray beam is larger than the size of each individual particle. If the substrate is made of porous materials, it can adsorb gases and those will be detected along with the substrate and the particle, giving erroneous data.

3.2.10.3.2 Environmental effects

Nanoparticles will often react, or at least interact, with their environments. If the particles are highly reactive, there will often be induced charges in the near environment of the particle. Gold nanoparticles have a well-documented ability to undergo plasmon interactions with each other. When XPS is performed on these particles, the charges will change the kinetic energy of the electrons, shifting the apparent binding energy. When working with nanoparticles that are well known for creating charges, it is often best to use an ion gun or a coating of gold. The purpose of the ion gun or gold coating is to try to move peaks back to their appropriate energies. If the peaks do not move, then the chance of there being no induced charge is high and thus the obtained data is fairly reliable.

3.2.10.3.3 Proximity effects

The proximity of the particles to each other will cause interactions between the particles. If there is a charge accumulation near one particle, and that particle is in close proximity with other particles, the charge will become enhanced as it spreads, affecting the signal strength and the binding energies of the electrons. While the knowledge of charge enhancement could be useful to potential applications, it is not beneficial if knowledge of the various properties of individual particles is sought.

Less isolated (i.e., less crowded) particles will have different properties as compared to more isolated particles. A good example of this is the plasmon effect in gold nanoparticles. The closer gold nanoparticles are to each other, the more likely they will induce the plasmon effect. This can change the properties of the particles, such as oxidation states and partial charges. These changes will then shift peaks seen in XPS spectra. These proximity effects are often introduced in the sample preparation. This, of course, shows why it is important to prepare samples correctly to get desired results.

3.2.10.4 Conclusions

Unfortunately there is no good general procedure for all nanoparticles samples. There are too many variables within each sample to create a basic procedure. A scientist wanting to use XPS to analyze nanoparticles must first understand the drawbacks and limitations of using their sample as well as how to counteract the artifacts that will be introduced in order to properly use XPS.

One must never make the assumption that nanoparticles are flat. This assumption will only lead to a misrepresentation of the particles. Once the curvature and stacking of the particles, as well as their interactions with each other are taken into account, XPS can be run.

3.2.10.5 Bibliography

- D. R. Baer and M. H. Engelhard. *J. Electron Spectrosc. Rel. Phenom.*, 2009, **178-179**, 415.
- D. R. Baer, J. E. Amonette, M. H. Engelhard, D. J. Gaspar, A. S. Karakoti, S. Kuchibhatla, P. Nachimuthu, J. T. Nurmi, Y. Qiang, V. Sarathy, S. Seal, A. Sharma. P. G. Tratnyek, and C. M. Wang. *Surf. Interface Anal.*, 2008, **40**, 529.

3.2.11 Mossbauer Analysis of Iron Oxide Nanoparticles[23]

3.2.11.1 Spectra and formula calculations

Due to the potential applications of magnetite nanoparticles (Fe_3O_4, nMag) many methods have been devised for its synthesis. However, stoichiometric Fe_3O_4 is not always achieved by different synthetic methods. B-site vacancies introduced into the cubic inverse spinel crystal structure of nMag result in nonstoichiometric iron oxide of the formula $(Fe^{3+})_A(Fe_{(1-3x)}{}^{2+}\ Fe_{(1+2X)}{}^{3+}Ø_x)_BO_4$ where Ø represents B-site vacancy. The magnetic susceptibility which is key to most nMag applications decreases with increased B-site vacancy hence the extent of B-site vacancy is important. The very high sensitivity of the Mossbauer spectrum to the oxidation state and site occupancy of Fe^{3+} in cubic inverse spinel iron oxides makes Mossbauer spectroscopy valuable for addressing the issues of whether or not the product of a synthetic method is actually nMag and the extent of B-site vacancy.

As with most analysis using multiple instrumental methods in conjunction is often helpful. This is exemplified by the use of XRD along with Mossbauer spectroscopy in the following analysis. Figure 3.127 shows the XRD results and Mossbauer spectra "magnetite" samples prepared by a Fe^{2+}/Fe^{3+} co-precipitation (Mt025), hematite reduction by hydrogen (MtH2) and hematite reduction with coal(MtC). The XRD analysis shows MtH2 and MT025 exhibiting only magnetite peaks while MtC shows the presence of magnetite, maghemite, and hematite. This information becomes very useful when fitting peaks to the Mossbauer spectra because it gives a chemical basis for peak fitting parameters and helps to fit the peaks correctly.

[23] This content is available online at <http://cnx.org/content/m22619/1.3/>.

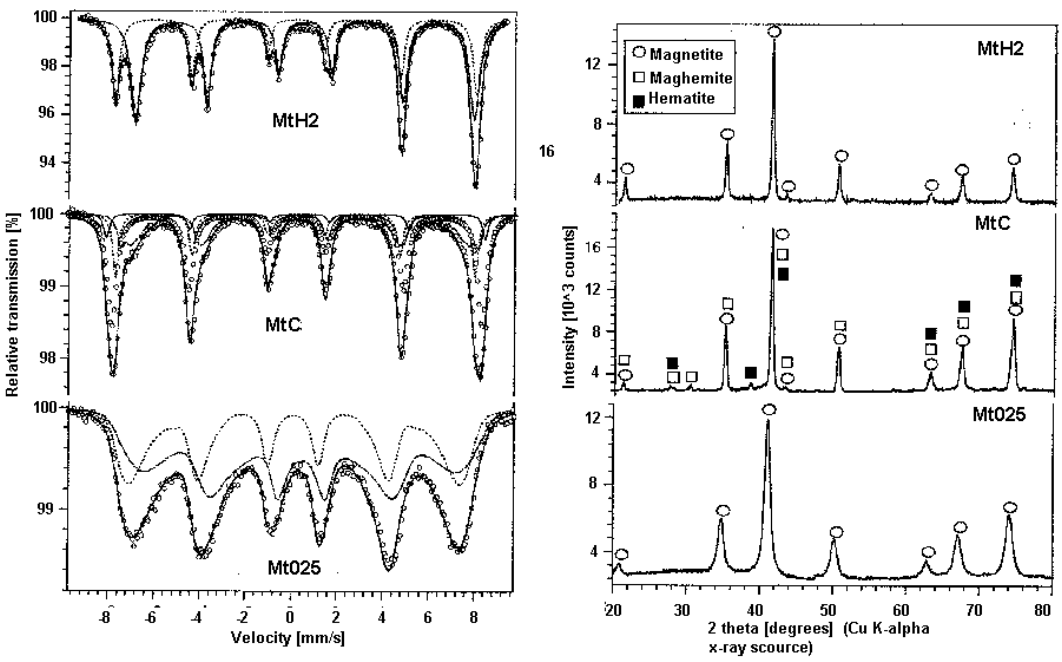

Figure 3.127: Mossbauer spectra (left) and corresponding XRD spectra of iron oxide sample prepared by different methods. Adapted from A. L. Andrade, D. M. Souza, M. C. Pereira, J. D. Fabris, and R. Z. Domingues. *J. Nanosci. Nanotechnol.*, 2009, **9**, 2081.

Being that the iron occupies two local environments, the A-site and B site, and two species (Fe^{2+} and Fe^{3+}) occupy the B-site one might expect the spectrum to be a combination of 3 spectra, however delocalization of electrons or electron hopping between Fe^{2+} and Fe^{3+} in the B site causes the nuclei to sense an average valence in the B site thus the spectrum are fitted with two curves accordingly. This is most easily seen in the Mt025 spectrum. The two fitted curves correspond to Fe^{3+} in the A-site and mixed valance $Fe^{2.5+}$ in the B-site. The isomer shift of the fitted curves can be used to determined which curve corresponds to which valence. The isomer shift relative to the top fitted curve is reported to be 0.661 and the bottom fitted curve is 0.274 relative to αFe thus the top fitted curve corresponds to less s-electron dense $Fe^{2.5+}$. The magnetic splitting is quite apparent. In each of the spectra, six peaks are present due to magnetic splitting of the nuclear energy states as explained previously. Quadrupole splitting is not so apparent, but actually is present in the spectra. The three peaks to the left of the center of a spectrum should be spaced the same as those to the right due to magnetic splitting alone since the energy level spacing between sublevels is equal. This is not the case in the above spectra, because the higher energy I = 3/2 sublevels are split unevenly due to magnetic and quadrupole splitting interactions.

Once the peaks have been fitted appropriately, determination of the extent of B-site vacancy in $(Fe^{3+})_A(Fe_{(1-3x)}{}^{2+}\ Fe_{(1+2X)}{}^{3+}\emptyset_x)_B O_4$ is a relatively simple matter. All one has to due to determine the number of vacancies (x) is solve the equation:

$\frac{RA_B}{RA_A} = \frac{2-6x}{1-5x}$ where $RA_{B\text{ or }A}$ = relative area ($\frac{Area\ A\ or\ B\ site\ curve}{Area\ of\ both\ curves}$) of the curve for the B or A site respectively

The reasoning for this equation is as follows. Taking into account that the mixed valance $Fe^{2.5+}$

curve is a result of paired interaction between Fe^{2+} and Fe^{3+} the nonstochiometric chemical formula is $(Fe^{3+})_A(Fe_{(1-3x)}{}^{2+}\ Fe_{(1+2X)}{}^{3+}\emptyset_x)_BO_4$. The relative intensity (or relative area) of the Fe-A and Fe-B curves is very sensitive to stoichiometry because vacancies in the B-site reduce the Fe-A curve and increase Fe-B curve intensities. This is due to the unpaired $Fe_{5x}{}^{3+}$ adding to the intensity of the Fe-A curve rather than the Fe-B curve. Since the relative area is directly proportional to the number of Fe contributing to the spectrum the ratio of the relative areas is equal to stoichiometric ratio of $Fe^{2.5+}$ to Fe^{3+}, which yields the above formula.

Example Calculation:

For MtH2 $RA_A/RA_B = 1.89$

Plugging x into the nonstoichiometric iron oxide formula yeilds:

$$\frac{RA_B}{RA_A}=\frac{2\text{-}6x}{1\text{-}5x} \quad \text{solving for x yeilds} \quad x=\frac{2-\frac{RA_A}{RA_B}}{5\frac{RA_A}{RA_B}+6}=\frac{2\text{-}1.89}{5(1.89)+6}=0.00712$$

$(Fe^{3+})_A(Fe_{1.9572}{}^{2+}\ Fe_{0.0356}{}^{3+})_BO_4$ (very close to stoichiometric)

Sample	RA_B/RA_A	X	Chemical formula
MtH2	1.89	0.007	$(Fe^{3+})_A(Fe_{0.979}{}^{2+}\ Fe_{1.014}{}^{3+})_BO_4$
MtC	1.66	0.024	$(Fe^{3+})_A(Fe_{0.929}{}^{2+}\ Fe_{1.048}{}^{3+})_BO_4$
Mt025	1.60	0.029	$(Fe^{3+})_A(Fe_{0.914}{}^{2+}\ Fe_{1.057}{}^{3+})_BO_4$

Table 3.11: Parameters and nonstoichiometric formulas for MtC, Mt025, and MtH2

3.2.11.2 Bibliography

- F. C. Voogt, T. Fujii, P. J. M. Smulders, L. Niesen, M. A. James, and T. Hibma, *Phys. Rev. B*, 1999, **60**, 11193.
- A. L. Andrade, D. M. Souza, M. C. Pereira, J. D. Fabris, and R. Z. Domingues, *J. Nanosci. Nanotechnol.*, 2009, **9**, 2081.
- J. B. Yang, X. D. Zhou, W. B. Yelon, W. fJ. James, Q. Cai, K. V. Gopalakrishnan, S. K. Malik, X. C. Sun, and D. E. Nikles, *J. Appl. Phys.*, 2004, **95**, 7540.
- R.E. Vandenberghe, I. Nedkov, T. Merodiiska, and L. Slavov, *Hyperfine Interact.* 2005, **165**, 267.

3.2.12 Using 13-C NMR to Study Carbon Nanomaterials[24]

3.2.12.1 Introduction

3.2.12.1.1 Carbon nanomaterial

There are several types of carbon nanomaterial. Members of this family are graphene, single-walled carbon nanotubes (SWNT), multi-walled carbon nanotubes (MWNT), and fullerenes such as C_{60}. Nano materials have been subject to various modification and functionalizations, and it has been of interest to develop methods that could observe these changes. Herein we discuss selected applications of ^{13}C NMR in studying graphene and SWNTs. In addition, a discussion of how ^{13}C NMR could be used to analyze a thin film of amorphous carbon during a low-temperature annealing process will be presented.

[24] This content is available online at <http://cnx.org/content/m46153/1.2/>.

3.2.12.1.2 ^{13}C NMR versus ^{1}H NMR

Since carbon is found in any organic molecule NMR that can analyze carbon could be very helpful, unfortunately the major isotope, ^{12}C, is not NMR active. Fortunately, ^{13}C with a natural abundance of 1.1% is NMR active. This low natural abundance along with lower gyromagnetic ratio for ^{13}C causes sensitivity to decrease. Due to this lower sensitivity, obtaining a ^{13}C NMR spectrum with a specific signal-to-noise ratio requires averaging more spectra than the number of spectra that would be required to average in order to get the same signal to noise ratio for a ^{1}H NMR spectrum. Although it has a lower sensitivity, it is still highly used as it discloses valuable information.

Peaks in a ^{1}H NMR spectrum are split to $n + 1$ peak, where n is the number of hydrogen atoms on the adjacent carbon atom. The splitting pattern in ^{13}C NMR is different. First of all, C-C splitting is not observed, because the probability of having two adjacent ^{13}C is about 0.01%. Observed splitting patterns, which is due to the hydrogen atoms on the same carbon atom not on the adjacent carbon atom, is governed by the same $n + 1$ rule.

In ^{1}H NMR, the integral of the peaks are used for quantitative analysis, whereas this is problematic in ^{13}C NMR. The long relaxation process for carbon atoms takes longer comparing to that of hydrogen atoms, which also depends on the order of carbon (i.e., 1 °, 2 °, etc.). This causes the peak heights to not be related to the quantity of the corresponding carbon atoms.

Another difference between ^{13}C NMR and ^{1}H NMR is the chemical shift range. The range of the chemical shifts in a typical NMR represents the different between the minimum and maximum amount of electron density around that specific nucleus. Since hydrogen is surrounded by fewer electrons in comparison to carbon, the maximum change in the electron density for hydrogen is less than that for carbon. Thus, the range of chemical shift in ^{1}H NMR is narrower than that of ^{13}C NMR.

3.2.12.1.3 Solid state NMR

^{13}C NMR spectra could also be recorded for solid samples. The peaks for solid samples are very broad because the sample, being solid, cannot have all anisotropic, or orientation-dependent, interactions canceled due to *rapid random tumbling*. However, it is still possible to do high resolution solid state NMR by spinning the sample at 54.74 ° with respect to the applied magnetic field, which is called the *magic angle*. In other words, the sample can be spun to artificially cancel the orientation-dependent interaction. In general, the spinning frequency has a considerable effect on the spectrum.

3.2.12.2 ^{13}C NMR of carbon nanotubes

Single-walled carbon nanotubes contain sp^2 carbons. Derivatives of SWNTs contain sp^3 carbons in addition. There are several factors that affect the ^{13}C NMR spectrum of a SWNT sample, three of which will be reviewed in this module: ^{13}C percentage, diameter of the nanotube, and functionalization.

3.2.12.2.1 ^{13}C percentage

For sp^2 carbons, there is a slight dependence of ^{13}C NMR peaks on the percentage of ^{13}C in the sample. Samples with lower ^{13}C percentage are slighted shifted downfield (higher ppm). Data are shown in Table 3.12. Please note that these peaks are for the sp^2 carbons.

Sample	δ **(ppm)**
SWNTs(100%)	116±1
SWNTs(1%)	118±1

Table 3.12: Effects of ^{13}C percentage on the sp^2 peak. Data from S. Hayashi, F. Hoshi, T. Ishikura, M. Yumura, and S. Ohshima, *Carbon*, 2003, **41**, 3047.

3.2.12.2.2 Diameter of the nanotubes

The peak position for SWNTs also depends on the diameter of the nanotubes. It has been reported that the chemical shift for sp^2 carbons decreases as the diameter of the nanotubes increases. Figure 3.128 shows this correlation. Since the peak position depends on the diameter of nanotubes, the peak broadening can be related to the diameter distribution. In other words, the narrower the peak is, the smaller the diameter distribution of SWNTs is. This correlation is shown in Figure 3.129.

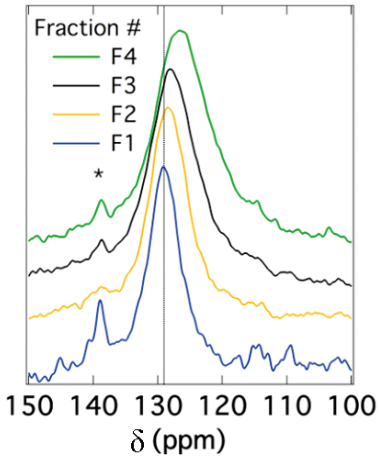

Figure 3.128: Correlation between the chemical shift of the sp^2 carbon and the diameter of the nanotubes. The diameter of the nanotubes increases from F1 to F4. Image from C. Engtrakul, V. M. Irurzun, E. L. Gjersing, J. M. Holt, B. A. Larsen, D. E. Resasco, and J. L. Blackburn, *J. Am. Chem. Soc.*, 2012, **134**, 4850. Copyright: American Chemical Society (2012).

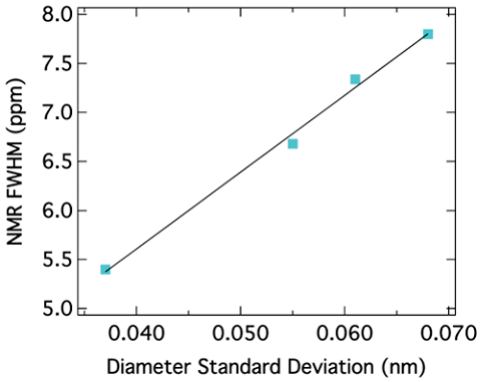

Figure 3.129: Correlation between FWHM and the standard deviation of the diameter of nanotubes. Image from C. Engtrakul, V. M. Irurzun, E. L. Gjersing, J. M. Holt, B. A. Larsen, D. E. Resasco, and J. L. Blackburn, *J. Am. Chem. Soc.*, 2012, **134**, 4850. Copyright: American Chemical Society (2012).

3.2.12.2.3 Functionalization

Solid stated ^{13}C NMR can also be used to analyze functionalized nanotubes. As a result of functionalizing SWNTs with groups containing a carbonyl group, a slight shift toward higher fields (lower ppm) for the sp^2 carbons is observed. This shift is explained by the perturbation applied to the electronic structure of the whole nanotube as a result of the modifications on only a fraction of the nanotube. At the same time, a new peak emerges at around 172 ppm, which is assigned to the carboxyl group of the substituent. The peak intensities could also be used to quantify the level of functionalization. Figure 3.130 shows these changes, in which the substituents are $-(CH_2)_3COOH$, $-(CH_2)_2COOH$, and $-(CH_2)_2CONH(CH_2)_2NH_2$ for the spectra Figure 3.130b, Figure 3.130c, and Figure 3.130d, respectively. Note that the bond between the nanotube and the substituent is a C-C bond. Due to low sensitivity, the peak for the sp^3 carbons of the nanotube, which does not have a high quantity, is not detected. There is a small peak around 35 ppm in Figure 3.130, can be assigned to the aliphatic carbons of the substituent.

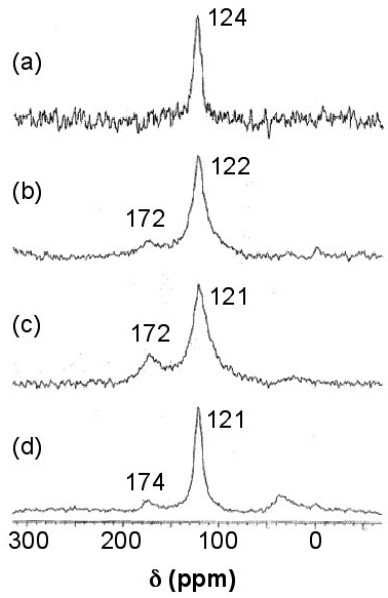

Figure 3.130: ^{13}C NMR spectra for (a) pristine SWNT, (b) SWNT functionalized with $-(CH_2)_3COOH$, (c) SWNT functionalized with $-(CH_2)_2COOH$, and (d) SWNT functionalized with $-(CH_2)_2CONH(CH_2)_2NH_2$. Image from H. Peng, L. B. Alemany, J. L. Margrave, and V. N. Khabashesku, *J. Am. Chem. Soc.*, 2003, **125**, 15174. Copyright: American Chemical Society (2003).

For substituents containing aliphatic carbons, a new peak around 35 ppm emerges, as was shown in Figure 3.130, which is due to the aliphatic carbons. Since the quantity for the substituent carbons is low, the peak cannot be detected. Small substituents on the sidewall of SWNTs can be chemically modified to contain more carbons, so the signal due to those carbons could be detected. This idea, as a strategy for enhancing the signal from the substituents, can be used to analyze certain types of sidewall modifications. For example, when Gly ($-NH_2CH_2CO_2H$) was added to F-SWNTs (fluorinated SWNTs) to substitute the fluorine atoms, the ^{13}C NMR spectrum for the Gly-SWNTs was showing one peak for the sp^2 carbons. When the aliphatic substituent was changed to 6-aminohexanoic acid with five aliphatic carbons, the peak was detectable, and using 11-aminoundecanoic acid (ten aliphatic carbons) the peak intensity was in the order of the size of the peak for sp^2 carbons. In order to use ^{13}C NMR to enhance the substituent peak (for modification quantification purposes as an example), Gly-SWNTs was treated with 1-dodecanol to modify Gly to an amino ester. This modification resulted in enhancing the aliphatic carbon peak at around 30 ppm. Similar to the results in Figure 3.130, a peak at around 170 emerged which was assigned to the carbonyl carbon. The sp^3 carbon of the SWNTs, which was attached to nitrogen, produced a small peak at around 80 ppm, which is detected in a cross-polarization magic angle spinning (CP-MAS) experiment.

F-SWNTs (fluorinated SWNTs) are reported to have a peak at around 90 ppm for the sp^3 carbon of nanotube that is attached to the fluorine. The results of this part are summarized in Table 3.13 (approximate values).

Group	δ (ppm)	Intensity
sp^2 carbons of SWNTs	120	Strong
$–NH_2(CH_2)_nCO_2H$ (aliphatic carbon, n=1,5, 10)	20-40	Depends on 'n'
$–NH_2(CH_2)_nCO_2H$ (carboxyl carbon, n=1,5, 10)	170	Weak
sp^3 carbon attached to nitrogen	80	Weak
sp^3 carbon attached to fluorine	90	Weak

Table 3.13: Chemical shift for different types of carbons in modified SWNTs. Note that the peak for the aliphatic carbons gets stronger if the amino acid is esterified. Data are obtained from: H. Peng, L. B. Alemany, J. L. Margrave, and V. N. Khabashesku, *J. Am. Chem. Soc.*, 2003, **125**, 15174; L. Zeng, L. Alemany, C. Edwards, and A. Barron, *Nano. Res.*, 2008, **1**, 72; L. B. Alemany, L. Zhang, L. Zeng, C. L. Edwards, and A. R. Barron, *Chem. Mater.*, 2007, **19**, 735.

The peak intensities that are weak in Table 3.13 depend on the level of functionalization and for highly functionalized SWNTs, those peaks are not weak. The peak intensity for aliphatic carbons can be enhanced as the substituents get modified by attaching to other molecules with aliphatic carbons. Thus, the peak intensities can be used to quantify the level of functionalization.

3.2.12.3 ^{13}C NMR of functionalized graphene

Graphene is a single layer of sp^2 carbons, which exhibits a benzene-like structure. Functionalization of graphene sheets results in converting some of the sp^2 carbons to sp^3. The peak for the sp^2 carbons of graphene shows a peak at around 140 ppm. It has been reported that fluorinated graphene produces an sp^3 peak at around 82 ppm. It has also been reported for graphite oxide (GO), which contains –OH and epoxy substituents, to have peaks at around 60 and 70 ppm for the epoxy and the –OH substituents, respectively. There are chances for similar peaks to appear for graphene oxide. Table 3.14 summarizes these results.

Type of carbon	δ (ppm)
sp^2	140
sp^3 attached to fluorine	80
sp^3 attached to –OH (for GO)	70
sp^3 attached to epoxide (for GO)	60

Table 3.14: Chemical shifts for functionalized graphene. Data are obtained from: M. Dubois, K. Guérin, J. P. Pinheiro, Z. Fawal, F. Masin, and A. Hamwi, *Carbon*, 2004, **42**, 1931; L. B. Casabianca, M. A. Shaibat, W. W. Cai, S. Park, R. Piner, R. S. Ruoff, and Y. Ishii, *J. Am. Chem. Soc.*, 2010, **132**, 5672.

3.2.12.4 Analyzing annealing process using ^{13}C NMR

^{13}C NMR spectroscopy has been used to study the effects of low-temperature annealing (at 650 °C) on thin films of amorphous carbon. The thin films were synthesized from a ^{13}C enriched carbon source (99%). There were two peaks in the ^{13}C NMR spectrum at about 69 and 142 ppm which were assigned to sp^3 and sp^2 carbons, respectively (Figure 3.131). The intensity of each peak was used to find the percentage of each type of hybridization in the whole sample, and the broadening of the peaks was used to estimate the distribution of different types of carbons in the sample. It was found that while the composition of the sample didn't change during the annealing process (peak intensities didn't change, see Figure 3.131b), the full width at half maximum (FWHM) did change (Figure 3.131a). The latter suggested that the structure became more

ordered, i.e., the distribution of sp^2 and sp^3 carbons within the sample became more homogeneous. Thus, it was concluded that the sample turned into a more homogenous one in terms of the distribution of carbons with different hybridization, while the fraction of sp^2 and sp^3 carbons remained unchanged.

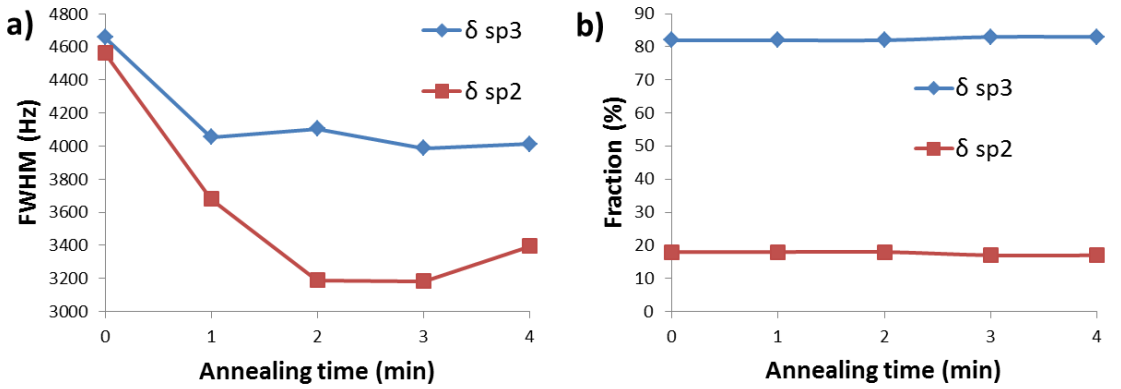

Figure 3.131: a) Effect of the annealing process on the FWHM, which represents the change in the distribution of sp^2 and sp^3 carbons. b) Fractions of sp^2 and sp^3 carbon during the annealing process. Data are obtained from T. M. Alam, T. A. Friedmann, P. A. Schultz, and D. Sebastiani, *Phys. Rev. B.*, 2003, **67**, 245309.

Aside from the reported results from the paper, it can be concluded that ^{13}C NMR is a good technique to study annealing, and possibly other similar processes, in real time, if the kinetics of the process is slow enough. For these purposes, the peak intensity and FWHM can be used to find or estimate the fraction and distribution of each type of carbon respectively.

3.2.12.5 Summary

^{13}C NMR can reveal important information about the structure of SWNTs and graphene. ^{13}C NMR chemical shifts and FWHM can be used to estimate the diameter size and diameter distribution. Though there are some limitations, it can be used to contain some information about the substituent type, as well as be used to quantify the level of functionalization. Modifications on the substituent can result in enhancing the substituent signal. Similar type of information can be achieved for graphene. It can also be employed to track changes during annealing and possibly during other modifications with similar time scales. Due to low natural abundance of ^{13}C it might be necessary to synthesize ^{13}C-enhanced samples in order to obtain suitable spectra with a sufficient signal-to-noise ratio. Similar principles could be used to follow the annealing process of carbon nano materials. C_{60} will not be discussed herein.

3.2.12.6 Bibliography

- T. M. Alam, T. A. Friedmann, P. A. Schultz, and D. Sebastiani, *Phys. Rev. B.*, 2003, **67**, 245309.
- L. B. Alemany, L. Zhang, L. Zeng, C. L. Edwards, and A. R. Barron, *Chem. Mater.*, 2007, **19**, 735.
- L. B. Casabianca, M. A. Shaibat, W. W. Cai, S. Park, R. Piner, R. S. Ruoff, and Y. Ishii, *J. Am. Chem. Soc.*, 2010, **132**, 5672.
- M. Dubois, K. Guérin, J. P. Pinheiro, Z. Fawal, F. Masin, and A. Hamwi, *Carbon*, 2004, **42**, 1931.

- C. Engtrakul, V. M. Irurzun, E. L. Gjersing, J. M. Holt, B. A. Larsen, D. E. Resasco, and J. L. Blackburn, *J. Am. Chem. Soc.*, 2012, **134**, 4850.
- S. Hayashi, F. Hoshi, T. Ishikura, M. Yumura, and S. Ohshima, *Carbon*, 2003, **41**, 3047.
- H. Peng, L. B. Alemany, J. L. Margrave, and V. N. Khabashesku, *J. Am. Chem. Soc.*, 2003, **125**, 15174.
- L. Zeng, L. Alemany, C. Edwards, and A. Barron, *Nano. Res.*, 2008, **1**, 72.

3.3 Microscopy

3.3.1 Beyond Optical Microscopy[25]

NOTE: "This module was developed as part of a Rice University Class called "Nanotechnology: Content and Context[26] " initially funded by the National Science Foundation under Grant No. EEC-0407237. It was conceived, researched, written and edited by students in the Fall 2005 version of the class, and reviewed by participating professors."

Figure 3.132: Dell Butcher Hall, home of the SEA fish tank, where the SEM, AFM, and STM reside.

[25] This content is available online at <http://cnx.org/content/m14353/1.2/>.
[26] http://frazer.rice.edu/nanotech

3.3.1.1 Introduction

Light microscopes are used in a number of areas such as medicine, science, and engineering. However, light microscopes cannot give us the high magnifications needed to see the tiniest objects like atoms. As the study of both microstructures and macrostructures of materials have come to the forefront of materials research and development new methods and equipment have been developed. Both the usage of electrons and atomic force rather than light permits advanced degrees of observations than would allow an optical microscope. As the interest in new materials in general and nanomaterials in particular is growing alternatives to optical microscopy are proving fundamental to the advancement of nanoscale science and technology.

3.3.1.2 Scanning Electron Microscope

SEM: A Brief History

The scanning electron microscope is an incredible tool for seeing the unseen worlds of microspace. The scanning electron microscope reveals new levels of detail and complexity in the world of micro-organisms and miniature structures. While conventional light microscopes use a series of glass lenses to bend light waves and create a magnified image, the scanning electron microscope creates magnified images by using electrons instead of light waves.

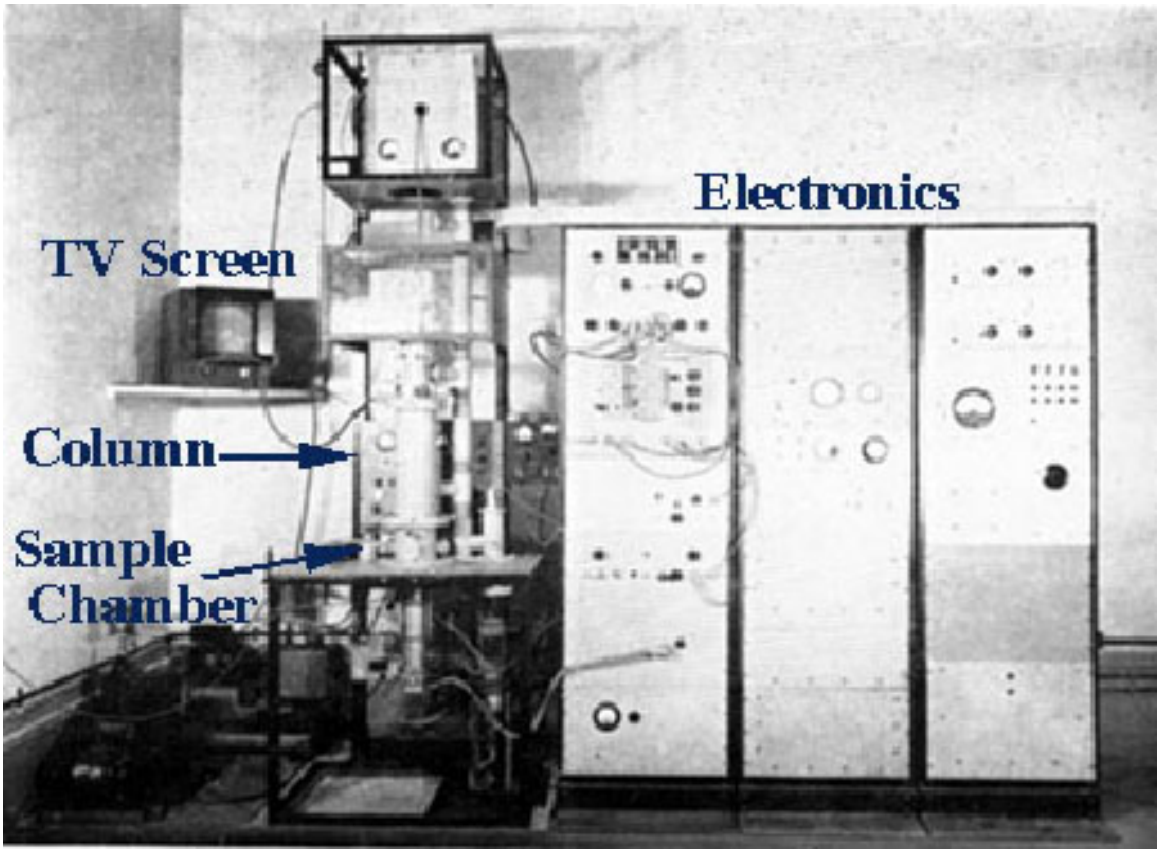

Figure 3.133: One of the first SEMs

The earliest known work describing the conceptualization of the scanning electron microscope was in 1935 by M. Knoll who, along with other pioneers in the field of electron optics, was working in Germany. Although it was Manfred von Ardenne who laid the foundations of both transmission and surface scanning electron microscopy just before World War II, it is Charles Oatley who is recognized as the great innovator of scanning electron microscopy. Oatley's involvement with the SEM began immediately after World War II when, his recent wartime experience in the development of radar, allowed him to develop new techniques that could be brought to overcome some of the fundamental problems encountered by von Ardenne in his pre-war research.

Von Ardenne (1938) constructed a scanning transmission electron microscope (STEM) by adding scan coils to a transmission electron microscope. [1][27] In the late 1940s Oatley, then a lecturer in the Engineering Department of Cambridge University, England, showed interest in conducting research in the field of electron optics and decided to re-investigate the SEM as an accompaniment to the work being done on the TEM (by V. E. Cosslett, also being developed in Cambridge at the Physics Department). One of Oatley's students, Ken Sander, began working on a column for a transmission electron microscope using electrostatic lenses, but after a long period of illness was forced to suspend his research. His work then was taken up by Dennis McMullan in 1948, when he and Oatley built their first SEM by 1951. By 1952 this instrument had achieved a resolution of 50 nm.

How the SEM works

In the SEM, electromagnets are used to bend an electron beam which is then utilized to produce the image on a screen. The beam of electrons is produced at the top of the microscope by heating a metallic filament. The electron beam follows a vertical path through the column of the microscope. It makes its way through electromagnetic lenses which focus and direct the beam down towards the sample. Once it hits the sample, other electrons are ejected from the sample. Detectors collect the secondary or backscattered electrons, and convert them to a signal that is sent to a viewing screen similar to the one in an ordinary television, producing an image.

[27] http://www2.eng.cam.ac.uk/~bcb/history.htm

Figure 3.134: JEOL 5300 Scanning Electron Microscope, Rice University Mechanical Engineering Building

By using electromagnets an observer can have more control over how much magnification he/she obtains. The SEM has a large depth of field, which allows a large amount of the sample to be in focus at one time. The electron beam also provides greater clarity in the image produced. The SEM allows a greater depth of focus than the optical microscope. For this reason the SEM can produce an image that is a good representation of the three-dimensional sample.

The SEM also produces images of high resolution, which means that closely spaced features can be examined at a high magnification. Preparation of the samples is relatively easy since most SEMs only require the sample to be conductive. The combination of higher magnification, larger depth of focus, greater resolution, and ease of sample observation makes the SEM one of the most heavily used instruments in research areas today.

SEM Usage

The SEM is designed for direct studying of:

- Topography: study of the surfaces of solid objects
- Morphology: study of shape and size
- Brief history of each microscope
- Composition: analysis of elements and compounds
- Crystallographic information: how atoms are arranged in a sample

SEM has become one of the most widely utilized instruments for material characterization. Given the overwhelming importance and widespread use of the SEM, it has become a fundamental instrument in universities and colleges with materials-oriented programs. [2][28] Institutions of higher learning and research have been forced to take extremely precautious measures with their equipment as it is expensive and maintenance is also costly.

Rice University, for example, has created what is called the Rice Shared Equipment Authority (SEA) to organize schedules, conduct training sessions, collect usage fees and maintain the usage of its high tech microscopic equipment. The following chart indicates prices, location, and necessary training for three of the most popular instruments under SEA jurisdiction:

SEM 6500	SEM 5300	AFM
The JEOL 6500F is a high resolution (1.5 nm) thermal field emission electron microscope capable of imaging at voltages from 200 V to 30 kV. It is also equipped with a back-scattered electron detector for compositional and topographical imaging. The 6500F has a high speed electrostatic beam blanker and is configured for electron beam lithography via the Nabity NPGS system. Lithography resolution is approximately 20 nm.	The JEOL 5300 is a simple medium resolution (5 nm) tungsten filament electron microscope. It is useful for general secondary electron imaging on properly prepared samples.	Atomic force microscopy measures the topographic features of a surface under ambient conditions, or in some cases the features of materials immersed in liquids; typical resolution with these instruments is 10's of nanometers lateral (x y) and .3 nanometers in z.
$25/hr for academic use $125/hr for external users Dell Butcher Hall, 160A Training consists of 2-3, 2 hour sessions spread out over 3 weeks.	$10/hour academic use $125/hour external use Sputter coating available Mechanical Engineering Building, 204 To begin training, contact a super-user or faculty in charge.	$7.50/hour academic use, $50/hour + tip cost external use. Dell Butcher Hall, 160A Training for this instrument usually consists of 2 or 3 two-hour sessions at $15.00/hour.

Figure 3.135: Chart comparing costs, location, and training for three instruments

Advantages and Disadvantages

Among the advantages is the most obvious, better resolution and depth of field than light microscopes. The SEM also provides compositional information for small areas, is relatively easy to use (after training), and the coatings make it semi non-destructive to beam damage. Its disadvantages, however, are all related to the specimen being examined. There are occasions when vacuum compatibility does not allow clear visibility. Specimen preparation can also cause contamination by introducing unwanted artifacts. Lastly, specimen must also be conductive for maximum visibility.

[28] http://www.tms.org/pubs/journals/JOM/9509/Chumbley-9509.html

Questions for Review

- What makes the SEM such a useful instrument? What can it do that a normal optical microscope cannot?
- Explain the usage of the electron beam in the SEM.
- What is meant by "images of high resolution"?

3.3.1.3 Scanning Tunneling Microscopes

A Brief Historical Note

The scanning tunneling microscope (STM) had its birth in 1981, invented by Gerd Binnig and Heinrich Rohrer of IBM, in Zurich, Germany. They won the 1986 Nobel Prize in physics for this accomplishment, but use of the microscope itself was somewhat slow to spread into the academic world. STM is used to scan surfaces at the atomic level, producing a map of electron densities; the surface science community was somewhat skeptical and resistant of such a pertinent tool coming from an outside, industrial source. There were questions as to the interpretations of the early images (how are we really sure those are the individual silicon atoms?), as well as the difficulty of interpreting them in the first place – the original STMs did not include computers to integrate the data. The older electron microscopes were generally easier to use, and more reliable; hence they retained preference over STMs for several years after the STM development. STM gained publicity slowly, through accomplishments such as IBM's famous xenon atom arrangement feat (see fig. 3) in 1990, and the determination of the structure of "crystalline" silicon.

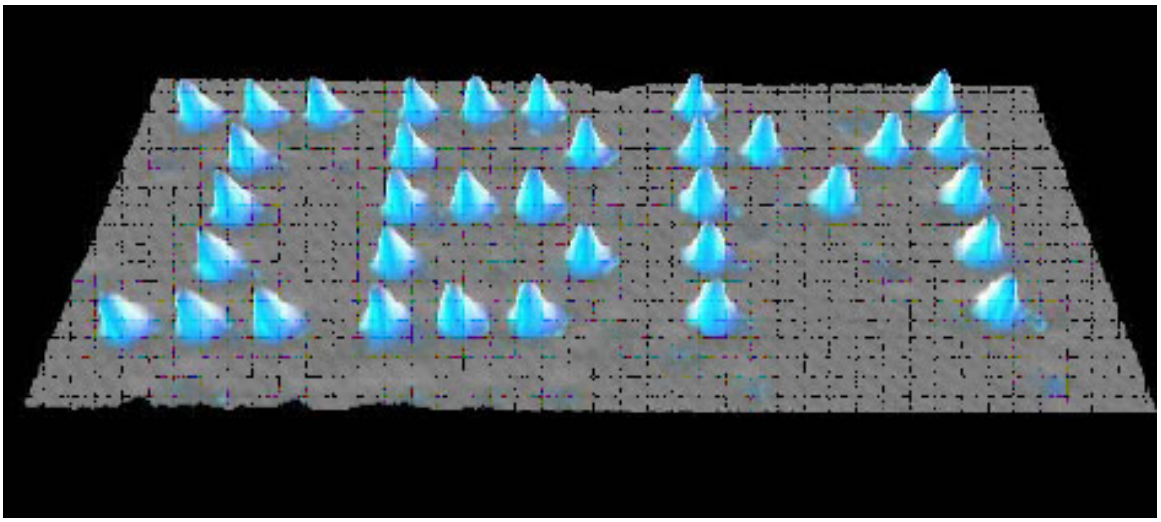

Figure 3.136: false-color STM image of xenon atoms arranged on a nickel background. From: D.M. Eigler, E.K. Schweizer. Positioning single atoms with a scanning tunneling microscope. Nature 344, 524-526 (1990).

How STMs Work: The Basic Ideas

I. The Probe - Scanning Tunneling Microscopy relies on a tiny probe of tungsten, platinum-iridium, or another conductive material to collect the data. The probe slowly "scans" across a surface, yielding an electron-density map of the nanoscale features of the surface. To achieve this resolution, the probe must be a wire with a protruding peak of a single atom; the sharper the peak, the

better the resolution. A voltage difference between the tip and the sample results in an electron "tunneling" current when the tip comes close enough (within around 10 Å). This "tunneling" is a phenomenon explained by the quantum mechanical properties of particles; the current is either held constant and probe height recorded, or the probe's height is maintained and the change in current is measured to produce the scanning data. In constant current microscopy, the probe height must be constantly adjusted, which makes for relatively slow scanning, but allows fairly irregular surfaces to be examined. By contrast, constant height mode allows for faster scanning, but will only be effective for relatively smooth sample surfaces.

II. Piezoelectric Scanner - In order to make the sub-nanometer vertical adjustments required for STM, piezoelectric ceramics are used in the scanning platform on which the sample is held. Piezoelectric materials undergo infinitesimally small mechanical changes under an applied voltage; therefore in the positioning device of a STM, they provide the motion to change the tip height at small enough increments that collision with the sample surface can be avoided. A data feedback loop is maintained between probe and piezoelectric positioner, so that the tip's height can be adjusted as necessary in constant-current mode, and can be brought close enough to the sample to begin scanning in the first place.

III. The Computer - Though the earliest STMs did not include a computer with the scanning apparatus, current models have one attached to filter and integrate the data as it is received, as well as to monitor and control the actual scanning process. Grayscale primary images can be colored to give contrast to different types of atoms in the sample; most published STM images have been enhanced in this way.

The very high degree of focus of a STM allows it to be used as a spectroscopic tool as well as a larger scale image producer. Properties of a single point on a sample surface can be analyzed through focused examination of the electronic structure.

Complications and Caveats

The integral use of the tunneling current in STM requires that both the probe and the sample be conductive, so the electrons can move between them. Non-conductive samples, therefore, must be coated in a metal, which obscures details as well as masks the actual properties of the sample. Furthermore, like with the SEM, oxidation and other contamination of the sample surface can be a problem, depending on the material(s) being studied. To avoid this, STM work is often carried out in an ultra-high vacuum (UHV) environment rather than in air. Some samples, however, are fairly well-suited to study in ambient conditions; one can strip away successive levels of a layered sample material in order to "clean" the surface as the study is being conducted.

Another seemingly simple problem involved in STM is control of vibration. Since the distances between probe and sample are so minute, the tiniest shake can result in data errors or cause the tip to collide with the surface, damaging the sample and possibly ruining the tip of the probe. A variety of systems have been implemented to control vibration, often involving frames with springs, or a sling in which the microscope is hung.

STM is plagued by artifacts, systematic errors in the observed data due to the mechanistic details of the microscope. For example, repetition of a particular shape in the same orientation throughout the image may be a case of tip artifacts, where a feature on the sample was sharper than the tip itself, resulting in the tip's shape being recorded rather than that of the sample feature. Lack of optimization of the microscope's feedback loop can produce large amounts of noise in the data, or, alternatively, cause a surface to be much smoother than it is. Finally, while sophisticated image processing software lends much-needed clarity to STM data, it can be misused such that meaning is created where there is none. Image filters used must be carefully evaluated against more "raw" image data to affirm their utility.

Counterbalancing the technique's obvious usefulness is the general difficulty of STM as a process. Whereas a scanning electron microscope can be operated successfully by a researcher with minimum skills as a technician, STMs are notoriously finicky and require expertise, time, and patience to produce a decent image. They are therefore not particularly popular research tools, though improvements in design and artifact control have been and are being made, making STM increasingly more practical.

Questions for Review

- In what types of situations would constant current microscopy be preferred over constant height? And vice-versa?
- What are potential problems of the large amount of data filtering and processing involved in STM?
- What errors are likely to be present in data from a particularly jagged, sharp-featured sample, and why?

3.3.1.4 Atomic Force Microscope

Another New Microscope

The requirement to have a conducting sample limited the usefulness of the STM. Gerd Binnig, Christoph Gerber, and Calvin Quate solved this problem with the invention of the Atomic Force Microscope (AFM) in 1986. [3][29] As suggested by its name, the AFM uses atomic forces—not the flow of electrons—to scan a sample, so it can be inductive as well as conductive. Still, the set up of the two microscopes is similar (see Figure 6). The AFM has a sharp tip a few micrometers long and usually a diameter less than 100 Å. It is attached to the end of a flexible tube 100-200 μm in length called a cantilever. The tip is brought close enough to the sample to feel forces that contribute to atomic bonds, called van der Waals forces. These are due to the attraction and repulsion of positively-charged protons and negatively-charged electrons. As electrons zip around an atom, they create temporary regions of positive and negative charges, which attract oppositely-charged regions on other atoms. If the atoms get too close, though, the repulsive force of the electrons overshadows this weaker attraction. In terms of the AFM, the temporary positive and negative charges attract the atoms in the tip and sample when they are far apart (several angstroms), but if they come too close (1-2 Å, less than the length of an atomic bond), the electrons on the tip and sample repel each other. This feature led to the development of two types of AFM: contact and non-contact.

[29] http://www.ieee-virtual-museum.org/

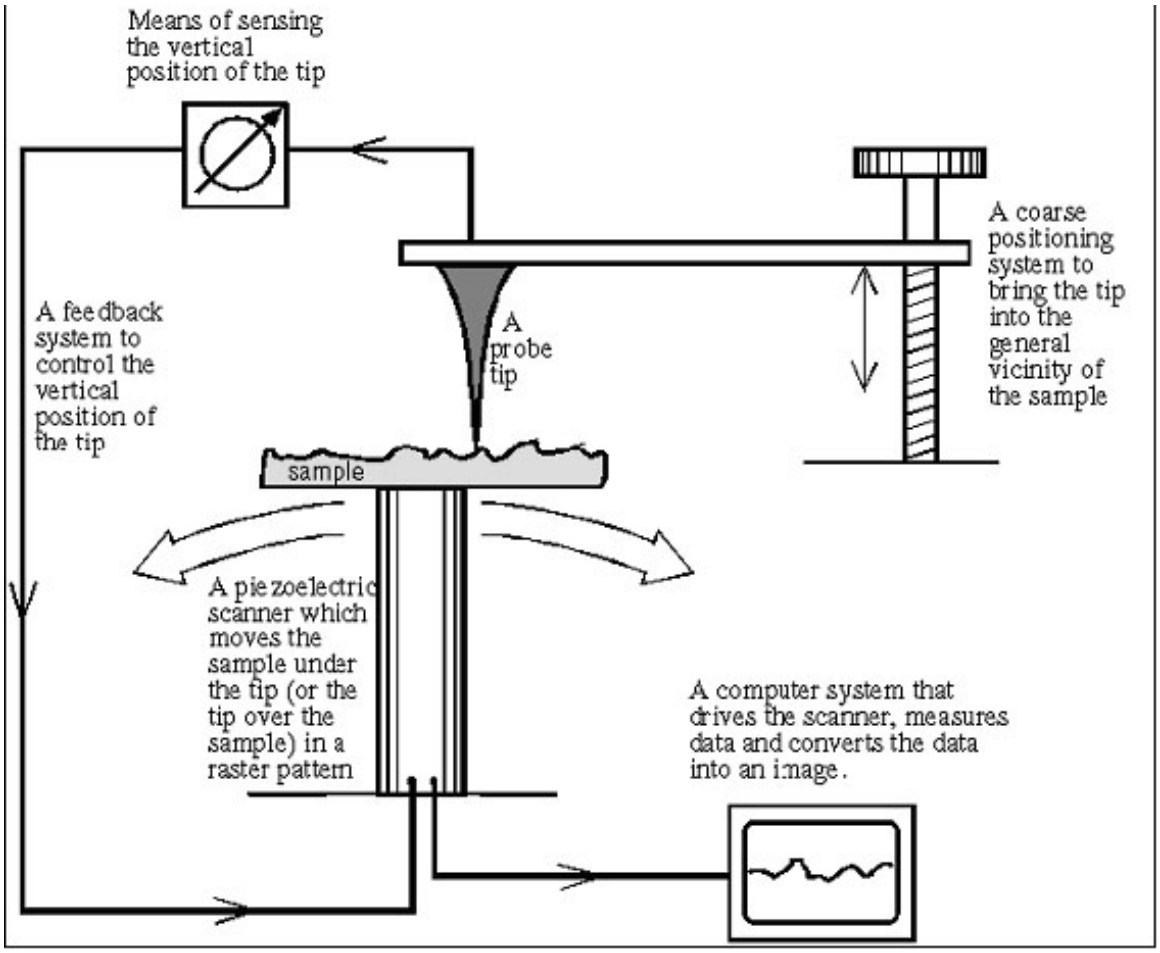

Figure 3.137: General schematic of AFM or STM, http://web.mit.edu/cortiz/www/AFMGallery/PracticalGuide.pdf[30]

[30] http://web.mit.edu/cortiz/www/AFMGallery/PracticalGuide.pdf

Figure 3.138: Digital Instrument Nanoscope, Rice University Dell Butcher Hall (Fish Tank)

The Contact AFM

A contact AFM is so called because the tip and the sample are closer to each other than atoms of the same molecule are. (It is difficult to define "contact" at the molecular level; bonds form when electrons from different atoms overlap. There is no rubbing together of atoms as we think of it at the macrolevel.) Since the cantilever is flexible, it is sensitive to the mutually repulsive force exerted between the tip and sample. This force varies with the topography of the latter–bumps bring the sample closer to the tip, increasing the force between them, while dips decrease the force. The variance in force is measured in two ways. In "constant-height" mode, the cantilever moves across the sample at a constant height, subjecting the tip to stronger and weaker forces, which cause the cantilever end to bend. This movement is measured by a laser beam that bounces off the reflective cantilever and onto a detector. In "constant-force" mode, the height of the cantilever is adjusted to keep the force between the tip and sample constant. Thus, the bend in the tip stays the same and the height adjustment is measured instead.

The Non-Contact AFM

As suggested by its name, the tip and sample are farther apart in a non-contact AFM. The cantilever vibrates so that the tip is tens to hundreds of angstroms from the sample, greater than the distance of a typical atomic bond, meaning that the force between them is attractive (compare to the 1-2 Å distance of the contact AFM). As the tip vibrates, it is pulled by this force, affecting its vibration frequency. A bump in the sample will cause a greater attractive force than a dip, so the topography is analyzed by recording

the vibration frequency.

Comparing the Two

Contact and non-contact AFMs generate similar pictures of a sample, which can be roughly interpreted as a topographical map (though other factors affect the force readings, such as local deviations in the electron density of the sample). However, each has its advantages and disadvantages that better suit it for certain sample types. In non-contact, the sample and tip remain far enough apart that the force between them is low and does not significantly affect the sample itself. This makes changes in topography more difficult to detect, but it also preserves the sample, which is especially important if it is soft and elastic, as well as the tip. In addition, the cantilever must be stiffer than for a contact AFM, otherwise it may bend too much, causing the tip to "contact" the sample. A contact AFM is more useful for sample surfaces that may be covered with a thin layer of water. Even in a high vacuum, this can occur when gaseous water condenses upon it. A non-contact AFM will not penetrate the water layer and will record its topography instead of the sample, but a contact AFM gets close enough to break through this problem.

Questions for Review

- What was significant about the invention of the AFM (what could be done that was not possible before)?
- Why is are the names "contact" and "non-contact" associated with these types of AFM?
- AFM tips are commonly composed of silicon or silicon nitride. Given that the latter is a tougher, more durable material, which would be more appropriate for a contact AFM?

3.3.2 TEM Imaging of Carbon Nanomaterials[31]

3.3.2.1 Introduction to TEM

Transmission electron microscopy (TEM) is a form of microscopy that uses an high energy electron beam (rather than optical light). A beam of electrons is transmitted through an ultra thin specimen, interacting with the specimen as it passes through. The image (formed from the interaction of the electrons with the sample) is magnified and focused onto an imaging device, such as a photographic film, a fluorescent screen,or detected by a CCD camera. In order to let the electrons pass through the specimen, the specimen has to be ultra thin, usually thinner than 10 nm.

The resolution of TEM is significantly higher than light microscopes. This is because the electron has a much smaller de Broglie wavelength than visible light (wavelength of 400∼700 nm). Theoretically, the maximum resolution, d, has been limited by λ, the wavelength of the detecting source (light or electrons) and NA, the numerical aperture of the system.

$$d = \frac{\lambda}{2n\sin\alpha} \approx \frac{\lambda}{2NA} \tag{3.73}$$

For high speed electrons (in TEM, electron velocity is close to the speed of light, c, so that the special theory of relativity has to be considered), the λ_e:

$$\lambda_e = \frac{h}{\sqrt{(2m_0E(1+E/2m_0c^2))}} \tag{3.74}$$

According to this formula, if we increase the energy of the detecting source, its wavelength will decrease, and we can get higher resolution. Today, the energy of electrons used can easily get to 200 keV, sometimes as high as 1 MeV, which means the resolution is good enough to investigate structure in sub-nanometer scale. Because the electrons is focused by several electrostatic and electromagnetic lenses, like the problems optical camera usually have, the image resolution is also limited by aberration, especially the spherical aberration called C_s. Equipped with a new generation of aberration correctors, transmission electron aberration-corrected microscope (TEAM) can overcome spherical aberration and get to half angstrom resolution.

[31] This content is available online at <http://cnx.org/content/m22963/1.5/>.

Although TEAM can easily get to atomic resolution, the first TEM invented by Ruska in April 1932 could hardly compete with optical microscope, with only $3.6 \times 4.8 = 14.4$ magnification. The primary problem was the electron irradiation damage to sample in poor vacuum system. After World War II, Ruska resumed his work in developing high resolution TEM. Finally, this work brought him the Nobel Prize in physics 1986. Since then, the general structure of TEM hasn't changed too much as shown in Figure 3.139. The basic components in TEM are: electron gun, condenser system, objective lens (most important len in TEM which determines the final resolution), diffraction lens, projective lenses (all lens are inside the equipment column, between apertures), image recording system (used to be negative films, now is CCD cameras) and vacuum system.

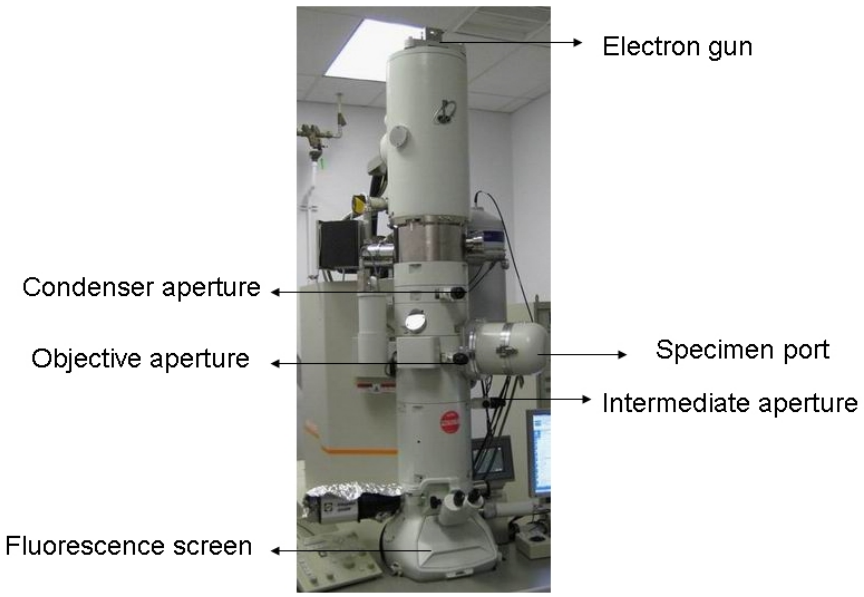

Figure 3.139: Position of the basic components in a TEM.

3.3.2.2 The family of carbon allotropes and carbon nanomaterials

Common carbon allotropes include diamond, graphite, amorphrous C (a-C), fullerene (also known as buckyball), carbon nanotube (CNT, including single wall CNT and multi wall CNT), graphene. Most of them are chemically inert and have been found in nature. We can also define carbon as sp^2 carbon (which is graphite), sp^3 carbon (which is diamond) or hybrids of sp^2 and sp^3 carbon. As shown in Figure 3.140, (a) is the structure of diamond, (b) is the structure of graphite, (c) graphene is a single sheet of graphite, (d) is amorphous carbon, (e) is C_{60}, and (f) is single wall nanotube. As for carbon nanomaterials, fullerene, CNT and graphene are the three most well investigated, due to their unique properties in both mechanics and electronics. Under TEM, these carbon nanomaterials will display three different projected images.

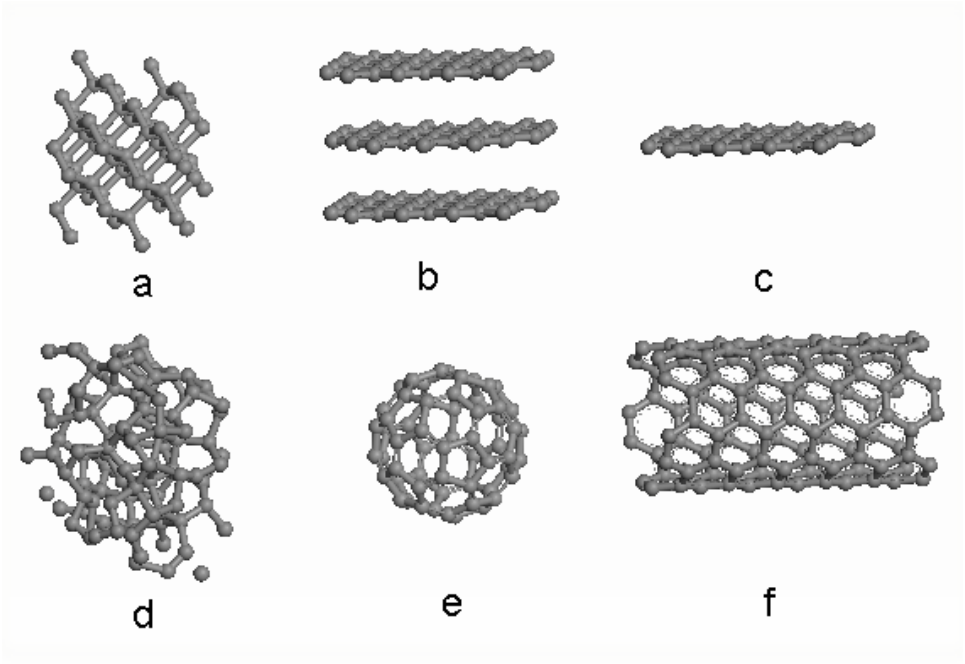

Figure 3.140: Six allotropes of carbon: a) diamond, b) graphite, c) graphene, d) amorphous carbon, e) C_{60} (Buckminsterfullerene or buckyball), f) single-wall carbon nanotube or buckytube.

3.3.2.3 Atomic structure of carbon nanomaterials under TEM

All carbon naomaterials can be investigated under TEM. Howerver, because of their difference in structure and shape, specific parts should be focused in order to obtain their atomic structure.

For C_{60}, which has a diameter of only 1 nm, it is relatively difficult to suspend a sample over a lacey carbon grid (a common kind of TEM grid usually used for nanoparticles). Even if the C_{60} sits on a thin a-C film, it also has some focus problems since the surface profile variation might be larger than 1 nm. One way to solve this problem is to encapsulate the C_{60} into single wall CNTs, which is known as nano peapods. This method has two benefits:

1. CNT helps focus on C_{60}. Single wall is aligned in a long distance (relative to C_{60}). Once it is suspended on lacey carbon film, it is much easier to focus on it. Therefore, the C_{60} inside can also be caught by minor focus changes.
2. The CNT can protect C_{60} from electron irradiation. Intense high energy electrons can permanently change the structure of the CNT. For C_{60}, which is more reactive than CNTs, it can not survive after exposing to high dose fast electrons.

In studying CNT cages, C_{92} is observed as a small circle inside the walls of the CNT. While a majority of electron energy is absorbed by the CNT, the sample is still not irradiation-proof. Thus, as is seen in Figure 3.141, after a 123 s exposure, defects can be generated and two C_{92} fused into one new larger fullerene.

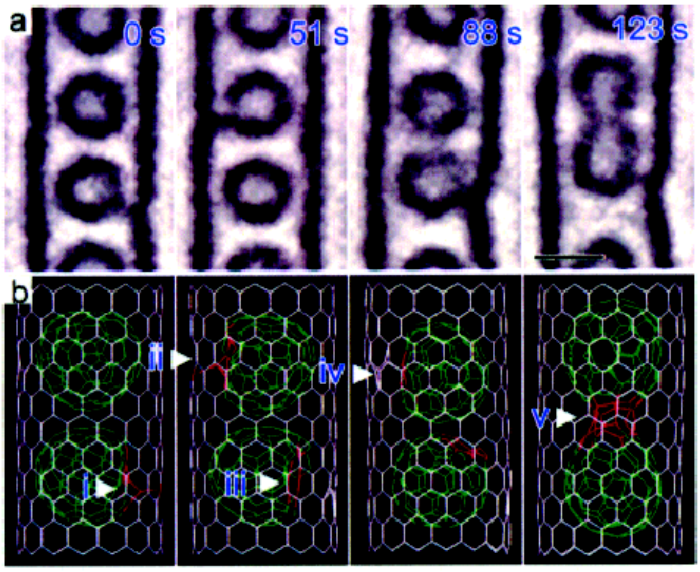

Figure 3.141: C_{92} encapsulated in SWNTs under different electron irradiation time. Courtesy of Dr. Kazutomo SUENAGA, adapted from K. Urita, Y. Sato, K. Suenaga, A. Gloter, A. Hasimoto, M. Ishida, T. Shimada, T. Shinohara, S. Iijima, *Nano Lett.*, 2004, **4**, 2451. Copyright American Chemical Society (2004).

Although, the discovery of C_{60} was first confirmed by mass spectra rather than TEM. When it came to the discovery of CNTs, mass spectra was no longer useful because CNTs shows no individual peak in mass spectra since any sample contains a range of CNTs with different lengths and diameters. On the other hand, HRTEM can provide a clear image evidence of their existence. An example is shown in Figure 3.142.

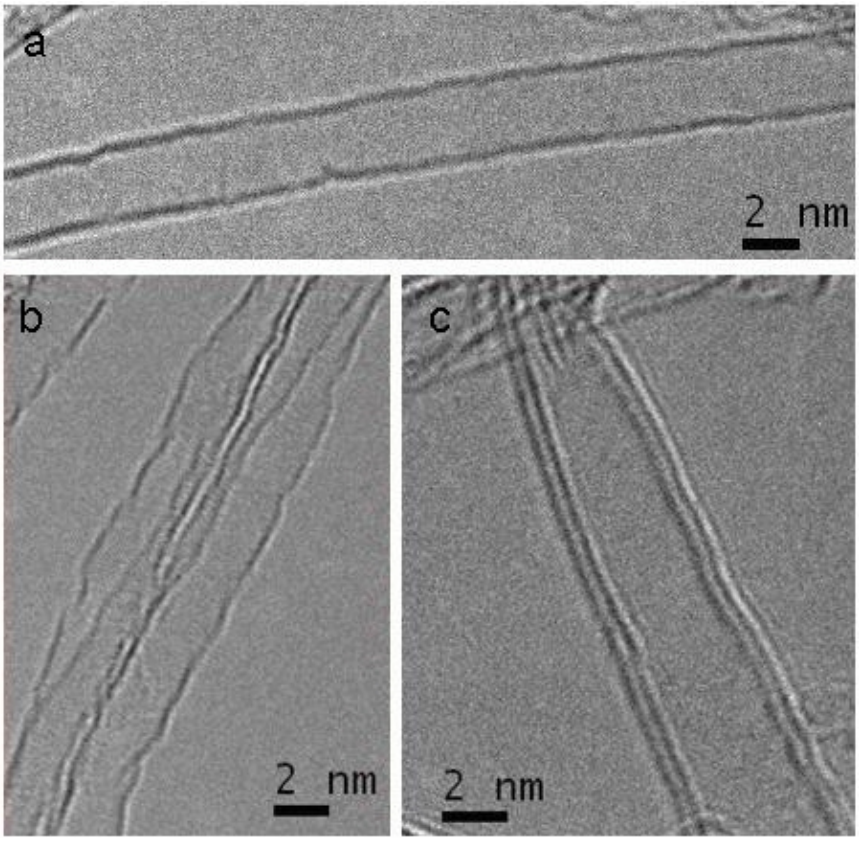

Figure 3.142: TEM images of SWNT and DWCNTs. Parallel dark lines corresponds to (002) lattice image of graphite. (a) and (b) SWNTs have 1 layer graphene sheet, diameter 3.2 nm. (c) DWCNT, diameter 4.0 nm.

Graphene is a planar fullerene sheet. Until recently, Raman, AFM and optical microscopy (graphene on 300 nm SiO_2 wafer) were the most convenient methods to characterize samples. However, in order to confirm graphene's atomic structure and determine the difference between mono-layer and bi-layer, TEM is still a good option. In Figure 3.143, a monolayer suspended graphene is observed with its atomic structure clearly shown. Inset is the FFT of the TEM image, which can be used as a filter to get an optimized structure image. High angle annular dark field (HAADF) image usually gives better contrast for different particles on it. It is also sensitive with changes of thickness, which allows a determination of the number of graphene layers.

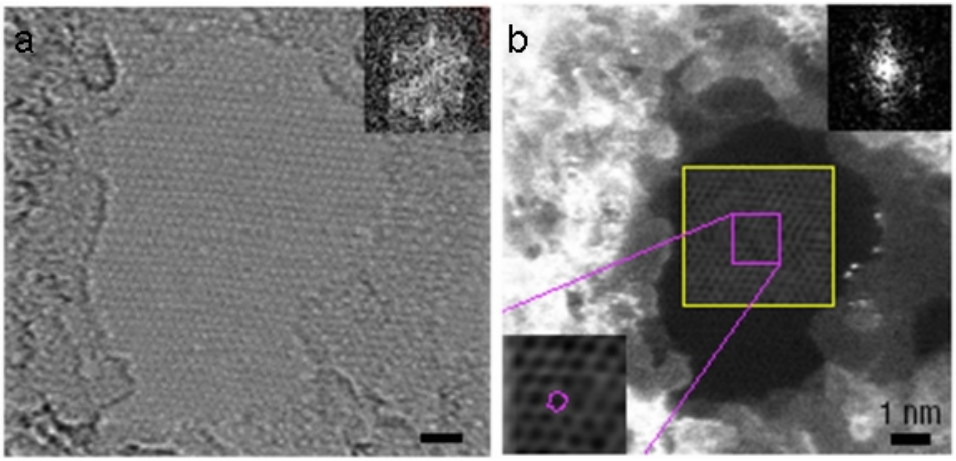

Figure 3.143: HRTEM of monolayer graphene. (a) Bright filed. (b) High Angle Annular Dark Field. Courtesy of Dr M. H. Gass, adapted from M. H. Gass, U. Bangert, A. L. Bleloch, P. Wang, R. R. Nair, and A. K. Geim, *Nature Nanotechnol.*, 2008, **3**, 676.

3.3.2.4 Graphene stacking and edges direction

Like the situation in CNT, TEM image is a projected image. Therefore, even with exact count of edge lines, it is not possible to conclude that a sample is a single layer graphene or multi-layer. If folding graphene has AA stacking (one layer is superposed on the other), with a projected direction of [001], one image could not tell the thickness of graphene. In order to distinguish such a bilayer of graphene from a single layer of graphene, a series of tilting experiment must be done. Different stacking structures of graphene are shown in Figure 3.144a.

Theoretically, graphene has the potential for interesting edge effects. Based upon its sp^2 structure, its edge can be either that of a zigzag or armchair configuration. Each of these possess different electronic properties similar to that observed for CNTs. For both research and potential application, it is important to control the growth or cutting of graphene with one specific edge. But before testing its electronic properties, all the edges have to be identified, either by directly imaging with STM or by TEM. Detailed information of graphene edges can be obtained with HRTEM, simulated with fast fourier transform (FFT). In Figure 3.144b, armchair directions are marked with red arrow respectively. A clear model in Figure 3.144c shows a 30 degree angle between zigzag edge and armchair edge.

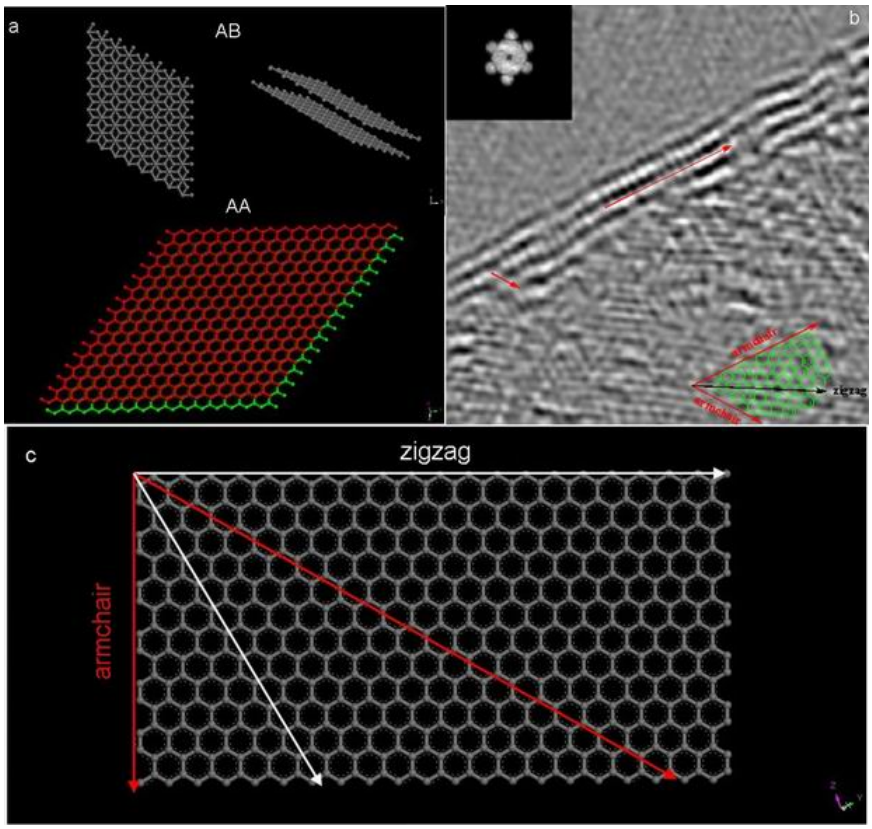

Figure 3.144: (a) Graphene stacking structure; (b) HRTEM image of graphene edges: zigzag and armchain (inset is FFT); (c) graphene edge model, a 30 ° angle between zigzag and armchair direction.

3.3.2.5 Bibliography

- K. Urita, Y. Sato, K. Suenaga, A. Gloter, A. Hasimoto, M. Ishida, T. Shimada, T. Shinohara, and S. Iijima, *Nano Lett.*, 2004, **4**, 2451.
- H. W. Kroto, J. R. Heath, S. C. O'Brien, R. F. Curl, and R. E. Smalley, *Nature*, 1985, **318**, 162.
- S. Iijima, *Nature*, 1991, **354**, 56.
- M. H. Gass, U. Bangert, A. L. Bleloch, P. Wang, R. R. Nair, and A. K. Geim, *Nature Nanotechnol.*, 2008, **3**, 676.
- L. Zheng and S. Iijima, *Phys. Rev. Lett.*, 2009, **102**, 015501.
- J. Campos-Delgado, J. M. Romo-Herrera, X. Jia, D. A. Cullen, H. Muramatsu, Y. A. Kim, T. Hayashi, Z. Ren, D. J. Smith, Y. Okuno, T. Ohba, H. Kanoh, K. Kaneko, M. Endo, H. Terrones, M. S. Dresselhaus, and M. Terrones, *Nano Lett.*, 2008, **8**, 2773.

3.3.3 Transmission Electron Microscopy Image for Multilayer-Nanomaterials[32]

Although, TEMs can only provide 2D analysis for a 3D specimen; magnifications of 300,000 times can be routinely obtained for many materials making it an ideal methodfor the study of nanomaterials. Besides from the TEM images, darker areas of the image show that the sample is thicker or denser in these areas, so we can observe the different components and structures of the specimen by the difference of color. For investigating multilayer-nanomaterials, a TEM is usually the first choice, because not only does it provide a high resolution image for nanomaterials but also it can distinguish each layer within a nanostructured material.

3.3.3.1 Observations of multilayer-nanomaterials

TEM was been used to analyze the depth-graded W/Si multilayer films. Multilayer films were grown on polished, 100 mm thick Si wafers by magnetron sputtering in argon gas. The individual tungsten and silicon layer thicknesses in periodic and depth-graded multilayers are adjusted by varying the computer-controlled rotational velocity of the substrate platen. The deposition times required to produce specific layer thicknesses were determined from detailed rate calibrations. Samples for TEM were prepared by focused ion beam milling at liquid N_2 temperature to prevent any beam heating which might result in re-crystallization and/or re-growth of any amorphous or fine grained polycrystalline layers in the film.

TEM measurements were made using a JEOL-4000 high-resolution transmission electron microscope operating at 400 keV; this instrument has a point-to-point resolution of 0.16 nm. Large area cross-sectional images of a depth-graded multilayer film obtained under medium magnification ($\sim$100 kX) were acquired at high resolution. A cross-sectional TEM image showed 150 layers W/Si film with the thickness of layers in the range of 3.33 $\sim$ 29.6 nm (Figure 3.145 shows a part of layers). The dark layers are tungsten and the light layers are silicon and they are separated by the thin amorphous W–Si interlayers (gray bands). By the high resolution of the TEM and the nature characteristics of the material, each layer can be distinguished clearly with their different darkness.

[32] This content is available online at <http://cnx.org/content/m34524/1.1/>.

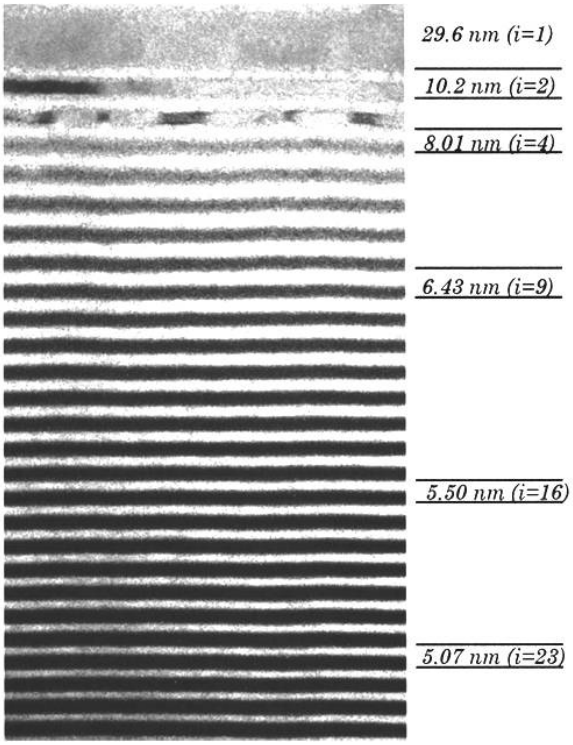

Figure 3.145: Cross-sectional transmission electron micrograph of the top portion of a depth-graded W/Si multilayer structure. Selected bilayer indices and thicknesses are indicated. The tungsten (dark bands) and silicon (light bands) layers are separated by thin amorphous W–Si interlayers (gray bands). The topmost silicon layer is not completely visible in this image. Adapted from D. L. Windt, F. E. Christensen, W. W. Craig, C. Hailey, F. A. Harrison, M. Jimenez-Garate, R. Kalyanaraman, and P. H. Mao, *J. Appl. Phys.*, 2000, **88**, 460.

Not all kinds of multilayer nanomaterials can be observed clearly under TEM. A materials consist of pc-Si:H multilayers were prepared by a photo-assisted chemical vapor deposition (photo-CVD) using a low-pressure mercury lamp as an UV light source to dissociate the gases. The pc-Si:H multilayer included low H_2-diluted a-Si:H sublayers (SL's) and highly H_2-diluted a-Si:H sublayers (SH's). Control of the CVD gas flow ($H_2|SiH_4$) under continuous UV irradiation resulted in the deposition of multilayer films layer by layer.

For a TEM measurement, a 20 nm thick undiluted a-Si:H film on a c-Si wafer before the deposition of multilayer to prevent from any epitaxial growth. Figure 3.146 shows a cross-sectional TEM image of a six-cycled pc-Si:H multilayer specimen. The white dotted lines are used to emphasize the horizontal stripes, which have periodicity in the TEM image. As can be seen, there are no significant boundaries between SL and SH could be observed because all sublayers are prepared in H_2 gas. In order to get the more accurate thickness of each sublayer, other measurements might be necessary.

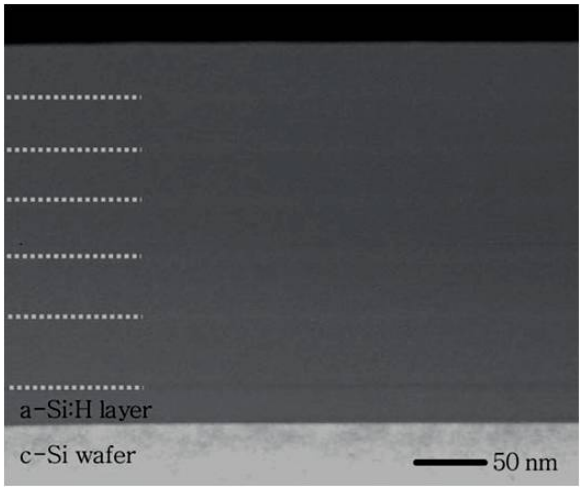

Figure 3.146: Cross-sectional TEM image of a 6-cycled pc-Si:H multilayer. Before the multilayer deposition, a 20 nm thick a-Si:H was deposited on a c-Si substrate. Adapted from S. W. Kwon, J. Kwak, S. Y. Myong, and K. S. Lim, *J. Non-Cryst. Solid*, 2006, **352**, 1132.

3.3.3.2 Bibliography

- D. L. Windt, F. E. Christensen, W. W. Craig, C. Hailey, F. A. Harrison, M. Jimenez-Garate, R. Kalyanaraman, and P. H. Mao, *J. Appl. Phys.*, 2000, **88**, 460.
- S. W. Kwon, J. Kwak, S. Y. Myong, and K. S. Lim, *J. Non-Cryst. Solid*, 2006, **352**, 1132.

3.3.4 Atomic Force Microscopy[33]

3.3.4.1 Introduction

Atomic force microscopy (AFM) is a high-resolution form of scanning probe microscopy, also known as scanning force microscopy (SFM). The instrument uses a cantilever with a sharp tip at the end to scan over the sample surface (Figure 3.147). As the probe scans over the sample surface, attractive or repulsive forces between the tip and sample, usually in the form of van der Waal forces but also can be a number of others such as electrostatic and hydrophobic/hydrophilic, cause a deflection of the cantilever. The deflection is measured by a laser (Figure 3.147) which is reflected off the cantilever into photodiodes. As one of the photodiodes collects more light, it creates an output signal that is processed and provides information about the vertical bending of the cantilever. This data is then sent to a scanner that controls the height of the probe as it moves across the surface. The variance in height applied by the scanner can then be used to produce a three-dimensional topographical representation of the sample.

[33] This content is available online at <http://cnx.org/content/m34664/1.1/>.

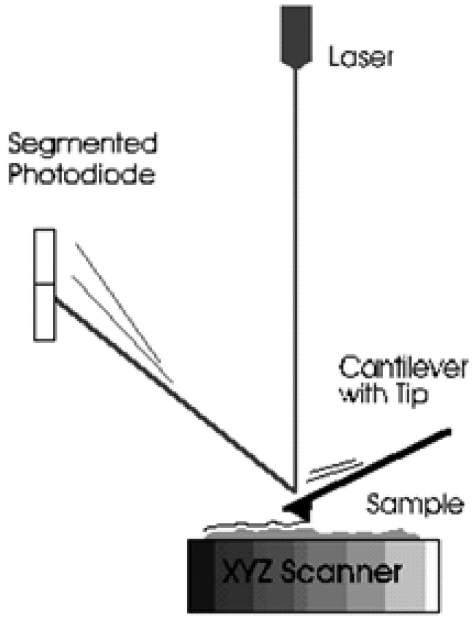

Figure 3.147: Simple schematic of atomic force microscope (AFM) apparatus. Adapted from H. G. Hansma, Department of Physics, University of California, Santa Barbara.

3.3.4.2 Modes of operation

3.3.4.2.1 Contact mode

The contact mode method utilizes a constant force for tip-sample interactions by maintaining a constant tip deflection (Figure 3.148.). The tip communicates the nature of the interactions that the probe is having at the surface via feedback loops and the scanner moves the entire probe in order to maintain the original deflection of the cantilever. The constant force is calculated and maintained by using Hooke's Law, (3.75). This equation relates the force (F), spring constant (k), and cantilever deflection (x). Force constants typically range from 0.01 to 1.0 N/m. Contact mode usually has the fastest scanning times but can deform the sample surface. It is also only the only mode that can attain "atomic resolution."

$$F = -kx \tag{3.75}$$

Figure 3.148: Schematic diagram of probe and surface interaction in contact mode.

3.3.4.2.2 Tapping mode

In the tapping mode the cantilever is externally oscillated at its fundamental resonance frequency (Figure 3.149). A piezoelectric on top of the cantilever is used to adjust the amplitude of oscillation as the probe scans across the surface. The deviations in the oscillation frequency or amplitude due to interactions between the probe and surface are measured, and provide information about the surface or types of material present in the sample. This method is gentler than contact AFM since the tip is not dragged across the surface, but it does require longer scanning times. It also tends to provide higher lateral resolution than contact AFM.

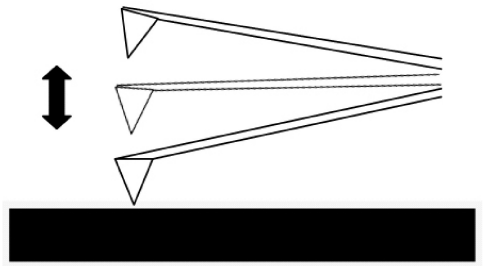

Figure 3.149: Diagram of probe and surface interaction in tapping mode.

3.3.4.2.3 Noncontact mode

For noncontact mode the cantilever is oscillated just above its resonance frequency and this frequency is decreased as the tip approaches the surface and experiences the forces associated with the material (Figure 3.150). The average tip-to-sample distance is measured as the oscillation frequency or amplitude is kept constant, which then can be used to image the surface. This method exerts very little force on the sample, which extends the lifetime of the tip. However, it usually does not provide very good resolution unless placed under a strong vacuum.

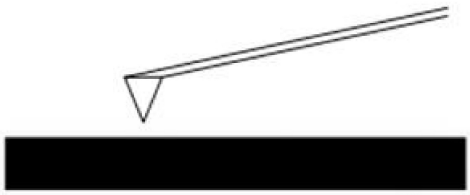

Figure 3.150: Diagram of probe and surface interaction in noncontact mode.

3.3.4.3 Experimental limitations

A common problem seen in AFM images is the presence of artifacts which are distortions of the actual topography, usually either due to issues with the probe, scanner, or image processing. The AFM scans slowly which makes it more susceptible to external temperature fluctuations leading to thermal drift. This leads to artifacts and inaccurate distances between topographical features.

It is also important to consider that the tip is not perfectly sharp and therefore may not provide the best aspect ratio, which leads to a convolution of the true topography. This leads to features appearing too large or too small since the width of the probe cannot precisely move around the particles and holes on the surface. It is for this reason that tips with smaller radii of curvature provide better resolution in imaging. The tip can also produce false images and poorly contrasted images if it is blunt or broken.

The movement of particles on the surface due to the movement of the cantilever can cause noise, which forms streaks or bands in the image. Artifacts can also be made by the tip being of inadequate proportions compared to the surface being scanned. It is for this reason that it is important to use the ideal probe for the particular application.

3.3.4.4 Sample size and preparation

The sample size varies with the instrument but a typical size is 8 mm by 8 mm with a typical height of 1 mm. Solid samples present a problem for AFM since the tip can shift the material as it scans the surface. Solutions or dispersions are best for applying as uniform of a layer of material as possible in order to get the most accurate value of particles' heights. This is usually done by spin-coating the solution onto freshly cleaved mica which allows the particles to stick to the surface once it has dried.

3.3.4.5 Applications of AFM

AFM is particularly versatile in its applications since it can be used in ambient temperatures and many different environments. It can be used in many different areas to analyze different kinds of samples such as semiconductors, polymers, nanoparticles, biotechnology, and cells amongst others. The most common application of AFM is for morphological studies in order to attain an understanding of the topography of the sample. Since it is common for the material to be in solution, AFM can also give the user an idea of the ability of the material to be dispersed as well as the homogeneity of the particles within that dispersion. It also can provide a lot of information about the particles being studied such as particle size, surface area, electrical properties, and chemical composition. Certain tips are capable of determining the principal mechanical, magnetic, and electrical properties of the material. For example, in magnetic force microscopy (MFM) the probe has a magnetic coating that senses magnetic, electrostatic, and atomic interactions with the surface. This type of scanning can be performed in static or dynamic mode and depicts the magnetic structure of the surface.

3.3.4.5.1 AFM of carbon nanotubes

Atomic force microscopy is usually used to study the topographical morphology of these materials. By measuring the thickness of the material it is possible to determine if bundling occurred and to what degree. Other dimensions of the sample can also be measured such as the length and width of the tubes or bundles. It is also possible to detect impurities, functional groups (Figure 3.151), or remaining catalyst by studying the images. Various methods of producing nanotubes have been found and each demonstrates a slightly different profile of homogeneity and purity. These impurities can be carbon coated metal, amorphous carbon, or other allotropes of carbon such as fullerenes and graphite. These facts can be utilized to compare the purity and homogeneity of the samples made from different processes, as well as monitor these characteristics as different steps or reactions are performed on the material. The distance between the tip and the surface has proven itself to be an important parameter in noncontact mode AFM and has shown that if the tip is moved past the threshold distance, approximately 30 μm, it can move or damage the nanotubes. If this occurs, a useful characterization cannot be performed due to these distortions of the image.

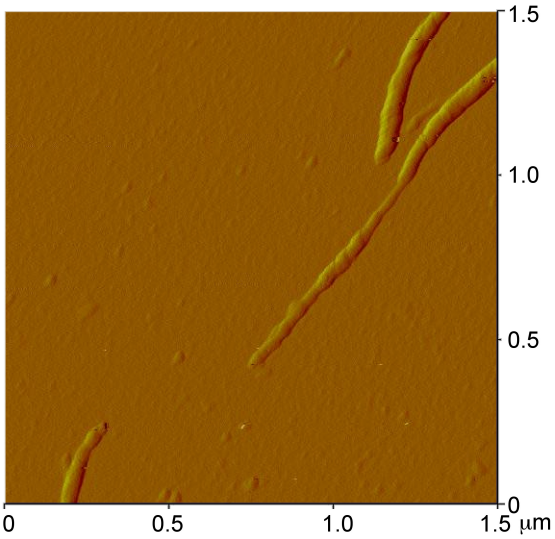

Figure 3.151: AFM image of a polyethyleneimine-functionalized single walled carbon nanotube (PEI-SWNT) showing the presence of PEI "globules" on the SWNT. Adapted from E. P. Dillon, C. A. Crouse, and A. R. Barron, *ACS Nano*, 2008, **2**, 156.

3.3.4.5.2 AFM of fullerenes

Atomic force microscopy is best applied to aggregates of fullerenes rather than individual ones. While the AFM can accurately perform height analysis of individual fullerene molecules, it has poor lateral resolution and it is difficult to accurately depict the width of an individual molecule. Another common issue that arises with contact AFM and fullerene deposited films is that the tip shifts clusters of fullerenes which can lead to discontinuities in sample images.

3.3.4.6 Bibliography

- R. Anderson and A. R. Barron, *J. Am. Chem. Soc.*, 2005, **127**, 10458.
- M. Bellucci, G. Gaggiotti, M. Marchetti, F. Micciulla, R. Mucciato, and M. Regi, *J. Physics: Conference Series*, 2007, **61**, 99.
- I. I. Bobrinetskii, V. N. Kukin, V. K. Nevolin, and M. M. Simunin. *Semiconductor*, 2008, **42**, 1496.
- S. H. Cohen and M. L. Lightbody. *Atomic Force Microscopy/Scanning Tunneling Microscopy 2*. Plenum, New York (1997).
- E. P. Dillon, C. A. Crouse, and A. R. Barron, *ACS Nano*, 2008, **2**, 156.
- C. Gu, C. Ray, S. Guo, and B. B. Akhremitchev, *J. Phys. Chem.*, 2007, **111**, 12898.
- G. Kaupp, *Atomic Force Microscopy, Scanning Nearfield Optical Microscopy and Nanoscratching: Application to Rough and Natural Surfaces*. Springer-Verlag, Berlin (2006).
- S. Morita, R. Wiesendanger, E. Meyer, and F. J. Giessibl. *Noncontact Atomic Force Microscopy*. Springer, Berlin (2002).

3.3.5 Scanning Tunneling Microscopy of Nanomaterials[34]

3.3.5.1 Introduction

Scanning tunneling microscopy (STM) is a powerful instrument that allows one to image the sample surface at the atomic level. As the first generation of scanning probe microscopy (SPM), STM paves the way for the study of nano-science and nano-materials. For the first time, researchers could obtain atom-resolution images of electrically conductive surfaces as well as their local electric structures. Because of this milestone invention, Gerd Binnig (Figure 3.152) and Heinrich Rohrer (Figure 3.153) won the Nobel Prize in Physics in 1986.

Figure 3.152: German physicist Gerd Binnig (1947 -).

[34] This content is available online at <http://cnx.org/content/m38335/1.2/>.

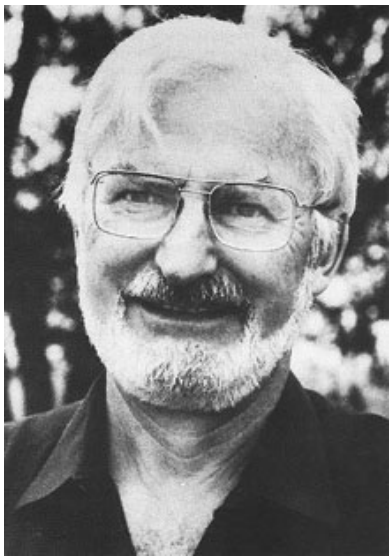

Figure 3.153: Swiss physicist Heinrich Rohrer (1933 -)

3.3.5.2 Principles of scanning tunneling microscopy

The key physical principle behind STM is the *tunneling effect*. In terms of their wave nature, the electrons in the surface atoms actually are not as tightly bonded to the nucleons as the electrons in the atoms of the bulk. More specifically, the electron density is not zero in the space outside the surface, though it will decrease exponentially as the distance between the electron and the surface increases (Figure 3.154a). So, when a metal tip approaches to a conductive surface within a very short distance, normally just a few Å, their perspective electron clouds will starting to overlap, and generate tunneling current if a small voltage is applied between them, as shown in Figure 3.154b.

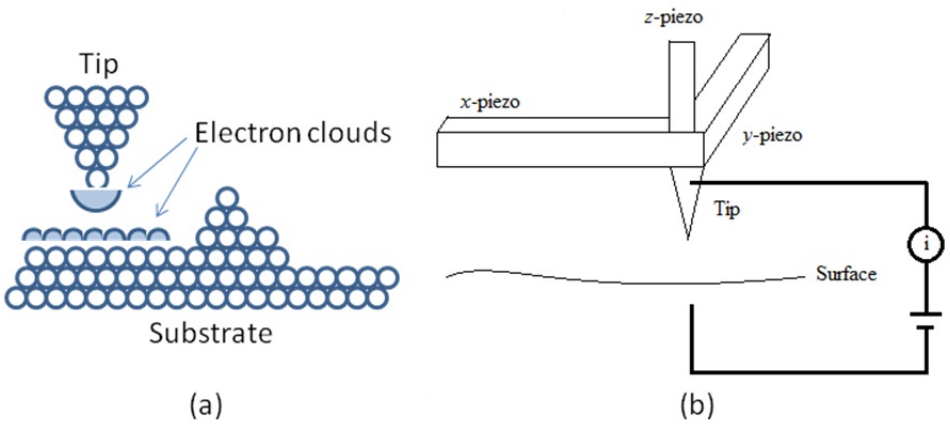

Figure 3.154: Schematic diagram of the principles of AFM showing (a) the interactions between tip and surface and (b) the tunneling current generated from tip and surface is measured and used as feedback to control the movement of the tip.

When we consider the separation between the tip and the surface as an ideal one-dimensional tunneling barrier, the tunneling probability, or the tunneling current I, will depend largely on s, the distance between the tip and surface, (3.76), where m is the electron mass, e the electron charge, h the Plank constant, *[U+03D5]* the averaged work function of the tip and the sample, and V the bias voltage.

$$I \propto \exp(-2s\,[2m/h^2\,(\langle\phi\rangle - e|V|/2)]^{1/2} \tag{3.76}$$

A simple calculation will show us how strongly the tunneling current is affected by the distance (s). If s is increased by $\Delta s = 1$ Å, (3.77) and (3.78).

$$\Delta I = \exp(-2k_0\,\Delta s) \tag{3.77}$$

$$k_0 = [2m/h^2\,(\langle\phi\rangle - e|V|/2)]^{1/2} \tag{3.78}$$

Usually ($<$[U+03D5]$>$ -e$|$V$|/2$) is about 5 eV, which k_0 about 1 Å^{-1}, then $\Delta I/I = {}^1/_8$. That means, if s changes by 1 Å, the current will change by one order of the magnitude. That's the reason why we can get atom-level image by measuring the tunneling current between the tip and the sample.

In a typical STM operation process, the tip is scanning across the surface of sample in x-y plain, the instrument records the x-y position of the tip, measures the tunneling current, and control the height of the tip via a feedback circuit. The movements of the tip in x, y and z directions are all controlled by piezo ceramics, which can be elongated or shortened according to the voltage applied on them.

Normally, there are two modes of operation for STM, *constant height mode* and *constant current mode*. In constant height mode, the tip stays at a constant height when it scans through the sample, and the tunneling current is measured at different (x, y) position (Figure 3.154b). This mode can be applied when the surface of sample is very smooth. But, if the sample is rough, or has some large particles on the surface, the tip may contact with the sample and damage the surface. In this case, the constant current mode is applied. During this scanning process, the tunneling current, namely the distance between the tip and the sample, is settled to an unchanged target value. If the tunneling current is higher than that target value, that

means the height of the sample surface is increasing, the distance between the tip and sample is decreasing. In this situation, the feedback control system will respond quickly and retract the tip. Conversely, if the tunneling current drops below the target value, the feedback control will have the tip closer to the surface. According to the output signal from feedback control, the surface of the sample can be imaged.

3.3.5.3 Comparison of atomic force microscopy (AFM) and scanning tunneling microscopy (STM)

Both AFM and STM are widely used in nano-science. According to the different working principles though, they have their own advantages and disadvantages when measuring specific properties of sample (Table 3.15). STM requires an electric circuit including the tip and sample to let the tunneling current go through. That means, the sample for STM must be conducting. In case of AFM however, it just measures the deflection of the cantilever caused by the van der Waals forces between the tip and sample. Thus, in general any kind of sample can be used for AFM. But, because of the exponential relation of the tunneling current and distance, STM has a better resolution than AFM. In STM image one can actually "see" an individual atom, while in AFM it's almost impossible, and the quality of AFM image is largely depended on the shape and contact force of the tip. In some cases, the measured signal would be rather complicated to interpret into morphology or other properties of sample. On the other side, STM can give straight forward electric property of the sample surface.

	AFM	**STM**
Sample requirement	-	Conducting
Work environment	Air, liquid	Vacuum
Lateral resolution	∼1 nm	∼0.1 nm
Vertical resolution	∼0.05 nm	∼0.05 nm
Working mode	Tapping, contact	Constant current, constant height

Table 3.15: Comparison of AFM and STM.

3.3.5.4 Applications of scanning tunneling microscopy in nanoscience.

STM provides a powerful method to detect the surface of conducting and semi-conducting materials. Recently STM can also be applied in the imaging of insulators, superlattice assemblies and even the manipulation of molecules on surface. More importantly, STM can provide the surface structure and electric property of surface at atomic resolution, a true breakthrough in the development of nano-science. In this sense, the data collected from STM could reflect the local properties even of single molecule and atom. With these valuable measurement data, one could give a deeper understanding of structure-property relations in nanomaterials.

An excellent example is the STM imaging of graphene on Ru(0001), as shown in Figure 3.155. Clearly seen is the superstructure with a periodicity of ∼30 Å , coming from the lattice mismatch of 12 unit cells of the graphene and 11 unit cells of the underneath Ru(0001) substrate. This so-called moiré structure can also be seen in other systems when the adsorbed layers have strong chemical bonds within the layer and weak interaction with the underlying surface. In this case, the periodic superstructure seen in graphene tells us that the formed graphene is well crystallized and expected to have high quality.

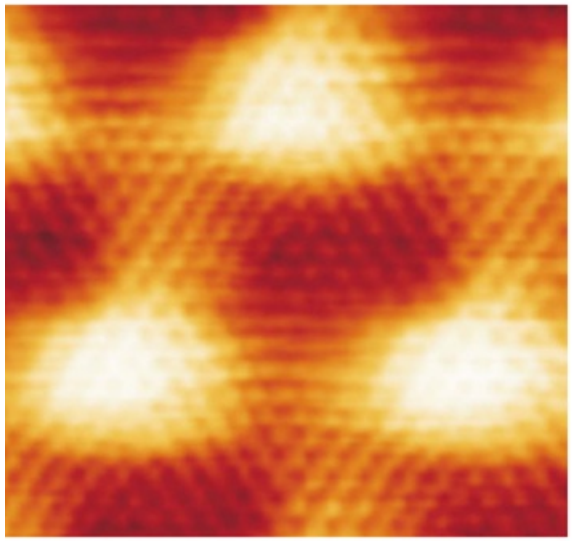

Figure 3.155: Atomically resolved image of the graphene overlayer. The scanning area is 40 x 40 Å, the operation mode is constant current mode, I_t is 1 nA, V_{Bias} is -0.05 V. Adapted with permission from S. Marchini, S. Gunther, and J. Wintterlin, *Phys. Rev. B*, 2007, **76**, 075429. Copyrighted by the American Physical Society.

Another good example is shown to see that the measurement from STM could tell us the bonding information in single-molecular level. In thiol- and thiophene-functionalization of single-wall carbon nanotubes (SWNTs) (Figure 3.156), the use of Au nanoparticles as chemical markers for AFM gives misleading results, while STM imaging could give correct information of substituent location. From AFM image, Au-thiol-SWNT (Figure 3.157a) shows that most of the sidewalls are unfunctionalized, while Au-thiophene-SWNT (Figure 3.157c) shows long bands of continuous functionalized regions on SWNT. This could lead to the estimation that thiophene is better functionalized to SWNT than thiol. Yet, if we look up to the STM image (Figure 3.157b and d), in thiol-SWNTs the multiple functional groups are tightly bonded in about 5 - 25 nm, while in thiophene-SWNTs the functionalization is spread out uniformly along the whole length of SWNT. This information indicates that actually the functionalization levels of thiol- and thiophene-SWNTs are comparable. The difference is that, in thiol-SWNTs, functional groups are grouped together and each group is bonded to a single gold nanoparticle, while in thiophene-SWNTs, every individual functional group is bonded to a nanoparticle.

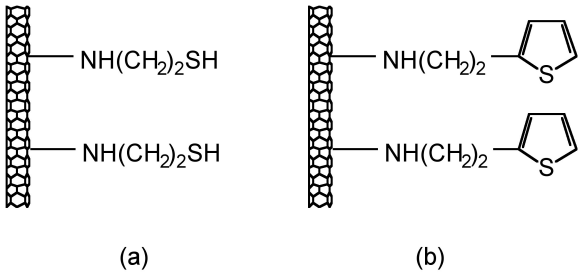

Figure 3.156: Structure of (a) thiol-functionalized SWNTs and thiophene-functionalized SWNTs.

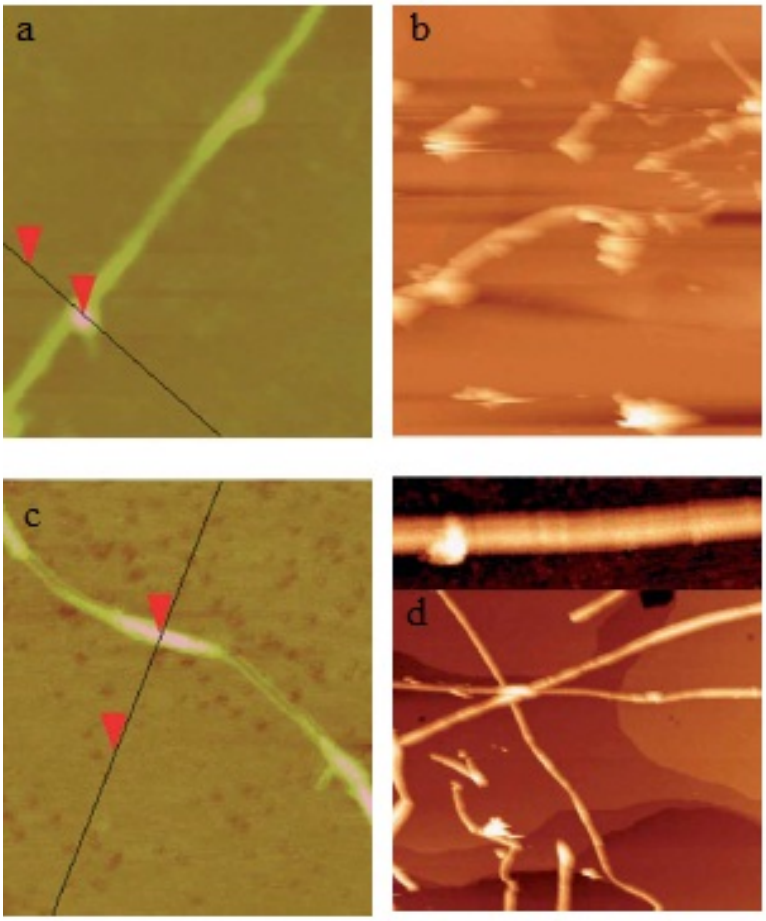

Figure 3.157: Difference between AFM and STM images of functionalized SWNTs. (a) and (c) are tapping mode AFM images and height profiles of thiol- and thiophene-SWNTs. (b) and (d) are STM images of thiol-SWNTs (scanning area is 4560 x 4000 Å, the operation mode is constant current mode, I_t is 3.25 pA, V_{Bias} is -0.5 V) and thiophene-SWNTs (scanning area is 4560 x 4000 Å, the operation mode is constant current mode, I_t is 5.66 pA, V_{Bias} is -0.8 V). Inset in (d) is a higher resolution image of the local defects on thiophene-SWNT (500 x 140 Å, the operation mode is constant current mode, I_t is 25.5 pA, V_{Bias} is -0.8 V). Adapted from L. Zhang, J. Zhang, N. Schmandt, J. Cratty, V. N. Khabashesku, K. F. Kelly, and A. R. Barron, *Chem. Commun.*, 2005, 5429 (http://dx.doi.org/10.1039/b509257d[35]). Reproduced by permission of The Royal Society of Chemistry.

3.3.5.5 Bibliography

- G. Binnig and H. Rohrer. *Surf. Sci.*, 1983, **126**, 236.
- G. Binnig and H. Rohrer, *Surf. Sci.*, 1985, **152/153**, 17.
- J. Griffith, *Annu. Rev. Mater. Sci.*, 1990, **20**, 219.

[35] http://dx.doi.org/10.1039/b509257d

- M. Poggi, L. Bottomley, and P. Lillehei, *Anal. Chem.*, 2002, **74**, 2851.
- P. Samori. *J. Mater. Chem.*, 2005, **14**, 1353.
- S. Marchini, S. Gunther, and J. Wintterlin, *Phys. Rev. B*, 2007, **76**, 075429.
- L. Zhang, J. Zhang, N. Schmandt, J. Cratty, V. N. Khabashesku, K. F. Kelly, and A. R. Barron, *Chem. Commun.,* 2005, 5429.

3.3.6 Rolling Molecules on Surfaces Under STM Imaging[36]

3.3.6.1 Introduction to surface motions at the molecular level

As single molecule imaging methods such as scanning tunneling microscope (STM), atomic force microscope (AFM), and transmission electron microscope (TEM) developed in the past decades, scientists have gained powerful tools to explore molecular structures and behaviors in previously unknown areas. Among these imaging methods, STM is probably the most suitable one to observe detail at molecular level. STM can operate in a wide range of conditions, provides very high resolution, and able to manipulate molecular motions with the tip. An interesting early example came from IBM in 1990, in which the STM was used to position individual atoms for the first time, spelling out "I-B-M" in Xenon atoms. This work revealed that observation and control of single atoms and molecular motions on surfaces were possible.

The IBM work, and subsequent experiments, relied on the fact that STM tip always exerts a finite force toward an adsorbate atom that contains both van der Waals and electrostatic forces was utilized for manipulation purpose. By adjusting the position and the voltage of the tip, the interactions between the tip and the target molecule were changed. Therefore, applying/releasing force to a single atom and make it move was possible Figure 3.158.

[36] This content is available online at <http://cnx.org/content/m22965/1.3/>.

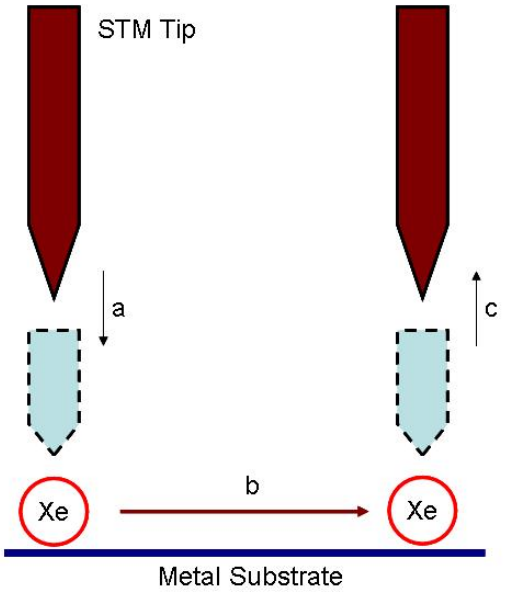

Figure 3.158: Manipulation of STM tip toward a xenon atom. a) STM tip move onto a target atom then change the voltage and current of the tip to apply a stronger interaction. b) Move the atom to a desire position. c) After reaching the desire position, the tip released by switching back to the scanning voltage and current.

The actual positioning experiment was carried out in the following process. The nickel metal substrate was prepared by cycles of argon-ion sputtering, followed by annealing in a partial pressure of oxygen to remove surface carbon and other impurities. After the cleaning process, the sample was cooled to 4 K, and imaged with the STM to ensure the quality of surface. The nickel sample was then doped with xenon. An image of the doped sample was taken at constant-current scanning conditions. Each xenon atom appears as a located randomly 1.6 Å high bump on the surface (Figure 3.159a). Under the imaging conditions (tip bias = 0.010 V with tunneling current 10^{-9} A) the interaction of the xenon with the tip is too weak to cause the position of the xenon atom to be perturbed. To move an atom, the STM tip was placed on top of the atom performing the procedure depicted in Figure 3.158 to move it to its target. Repeating this process again and again led the researcher to build of the structure they desired Figure 3.159b and c.

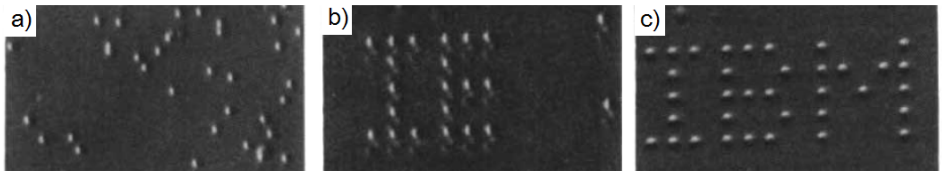

Figure 3.159: Manipulation of STM tip starting with a) randomly dosed xenon sample, b) under construction - move xenon atom to desire position, and c) accomplishment of the manipulation. Adapted from D. M. Eigler and E. K. Schweizer, *Nature*, 1990, **344**, 524.

All motions on surfaces at the single molecule level can be described as by the following (or combination of the following) modes:

i. Sliding.
ii. Hopping.
iii. Rolling.
iv. Pivoting.

Although the power of STM imaging has been demonstrated, imaging of molecules themselves is still often a difficult task. The successful imaging of the IBM work was attributed to selection of a heavy atom. Other synthetic organic molecules without heavy atoms are much more difficult to be imaged under STM. Determinations of the mechanism of molecular motion is another. Besides imaging methods themselves, other auxiliary methods such as DFT calculations and imaging of properly designed molecules are required to determine the mechanism by which a particular molecule moves across a surface.

Herein, we are particularly interested in surface-rolling molecules, i.e., those that are designed to roll on a surface. It is straightforward to imagine that if we want to construct (and image) surface-rolling molecules, we must think of making highly symmetrical structures. In addition, the magnitudes of interactions between the molecules and the surfaces have to be adequate; otherwise the molecules will be more susceptible to slide/hop or stick on the surfaces, instead of rolling. As a result, only very few molecules are known can roll and be detected on surfaces.

3.3.6.2 Surface rolling of molecules under the manipulation of STM tips

As described above, rolling motions are most likely to be observed on molecules having high degree of symmetry and suitable interactions between themselves and the surface. C_{60} is not only a highly symmetrical molecule but also readily imageable under STM due to its size. These properties together make C_{60} and its derivatives highly suitable to study with regards to surface-rolling motion.

The STM imaging of C_{60} was first carried out at At King College, London. Similar to the atom positioning experiment by IBM, STM tip manipulation was also utilized to achieve C_{60} displacement. The tip trajectory suggested that a rolling motion took into account the displacement on the surface of C_{60}. In order to confirm the hypothesis, the researchers also employed *ab initio* density function (DFT) calculations with rolling model boundary condition (Figure 3.160). The calculation result has supported their experimental result.

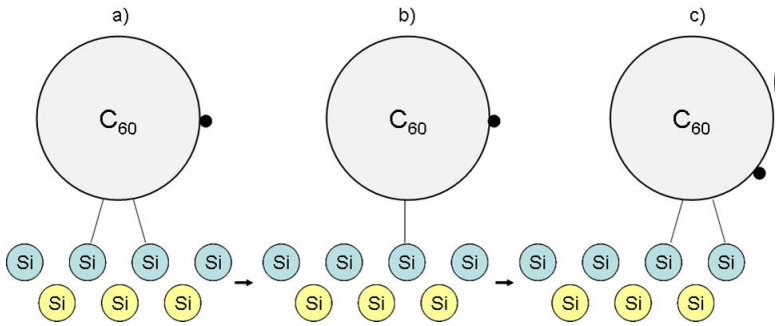

Figure 3.160: Proposed mechanism of C_{60} translation showing the alteration of C_{60}···surface interactions during rolling. a) 2-point interaction. The left point interaction was dissociated during the interaction. b) 1-point interaction. C_{60} can pivot on surface. c) 2-point interaction. A new interaction formed to complete part of the rolling motion. a) - c) The black spot on the C_{60} is moved during the manipulation. The light blue Si balls represent the first layer of molecules the silicon surface, and the yellow balls are the second layer.

The results provided insights into the dynamical response of covalently bound molecules to manipulation. The sequential breaking and reforming of highly directional covalent bonds resulted in a dynamical molecular response in which bond breaking, rotation, and translation are intimately coupled in a rolling motion (Figure 3.161), but not performing sliding or hopping motion.

A triptycene wheeled dimeric molecule Figure 3.161 was also synthesized for studying rolling motion under STM. This "tripod-like" triptycene wheel ulike a ball like C_{60} molecule also demonstrated a rolling motion on the surface. The two triptycene units were connected via a dialkynyl axle, for both desired molecule orientation sitting on surface and directional preference of the rolling motion. STM controlling and imaging was demonstrated, including the mechanism Figure 3.161.

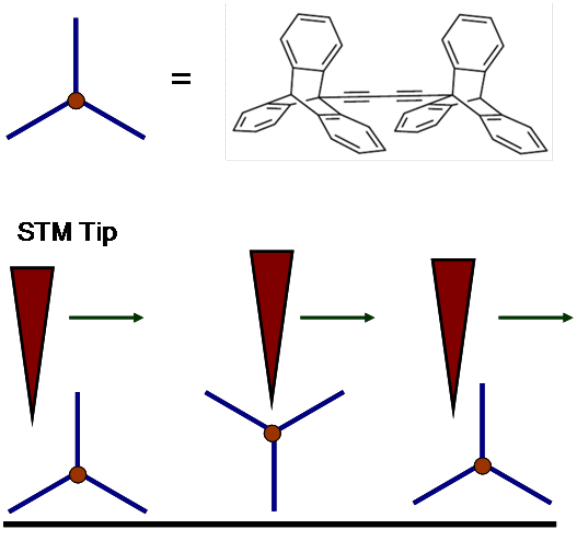

Figure 3.161: Scheme of the rolling mechanism (left to right). Step 1 is the tip approach towards the molecule, step 2 is a 120 degree rotation of a wheel around its molecular axle and in step 3 the tip reaches the other side of the molecule. It shows that, in principle, only one rotation of a wheel can be induced (the direction of movement is marked by arrows).

3.3.6.3 Single molecule nanocar under STM imaging

Another use of STM imaging at single molecule imaging is the single molecule nanocar by the Tour group at Rice University. The concept of a nanocar initially employed the free rotation of a C-C single bond between a spherical C_{60} molecule and an alkyne, Figure 3.162. Based on this concept, an "axle" can be designed into which are mounted C_{60} "wheels" connected with a "chassis" to construct the "nanocar". Nanocars with this design are expected to have a directional movement perpendicular to the axle. Unfortunately, the first generation nanocar (named "nanotruck" Figure 3.163) encountered some difficulties in STM imaging due to its chemical instability and insolubility. Therefore, a new of design of nanocar based on OPE has been synthesized Figure 3.164.

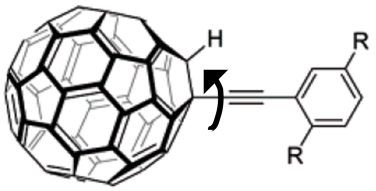

Figure 3.162: Structure of C_{60} wheels connecting to an alkyne. The only possible rolling direction is perpendicular to the C-C single bond between C_{60} and the alkyne. The arrow indicates the rotational motion of C_{60}.

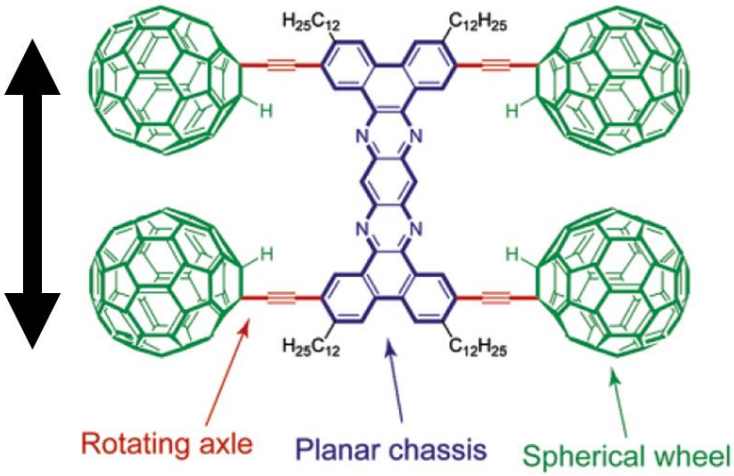

Figure 3.163: Structure of the nanotruck. No rolling motion was observed under STM imaging due to its instability, insolubility and inseparable unreacted C_{60}.The double head arrow indicates the expected direction of nanocar movement. Y. Shirai, A. J. Osgood, Y. Zhao, Y. Yao, L. Saudan, H. Yang, Y.-H. Chiu, L. B. Alemany, T. Sasaki, J.-F. Morin, J. M. Guerrero, K. F. Kelly, and J. M. Tour, *J. Am. Chem. Soc.*, 2006, **128**, 4854. Copyright American Chemical Society (2006).

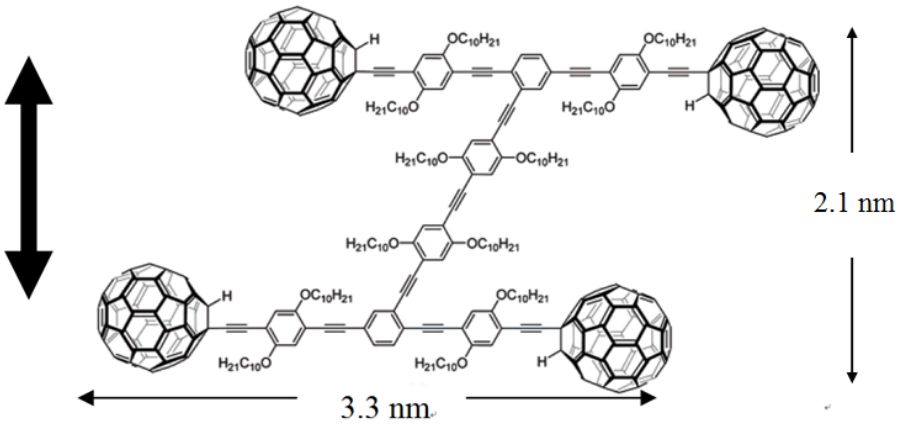

Figure 3.164: Nanocar based on OPE structure. The size of the nanocar is 3.3 nm X 2.1 nm (W x L). Alkoxy chains were attached to improve solubility and stability. OPE moiety is also separable from C_{60}. The bold double head arrow indicates the expected direction of nanocar movement. The dimension of nanocar was 3.3 nm X 2.1 nm which enable direct observation of the orientation under STM imaging. Y. Shirai, A. J. Osgood, Y. Zhao, K. F. Kelly, and J. M. Tour, *Nano Lett.*, 2005, **5**, 2330. Copyright American Chemical Society (2005).

The newly designed nanocar was studied with STM. When the nanocar was heated to ~200 °C, noticeable displacements of the nanocar were observed under selected images from a 10 min STM experiment Figure 3.165. The phenomenon that the nanocar moved only at high temperature was attributed their stability to a relatively strong adhesion force between the fullerene wheels and the underlying gold. The series of images showed both pivotal and translational motions on the surfaces.

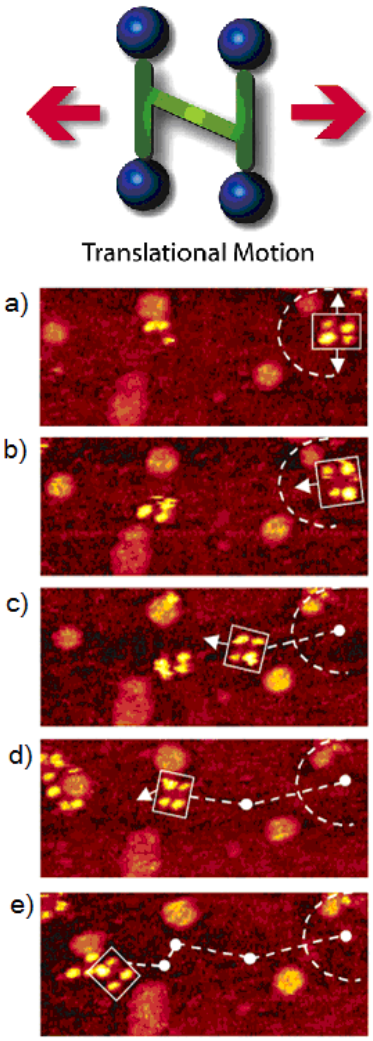

Figure 3.165: Pivotal and translational movement of OPE based nanocar. Acquisition time of one image is approximately 1 min with (a – e) images were selected from a series spanning 10 min. The configuration of the nanocar on surface can be determined by the distances of four wheels. a) – b) indicated the nanocar had made a 80 ° pivotal motion. b) – e) indicated translation interrupted by small-angle pivot perturbations. Y. Shirai, A. J. Osgood, Y. Zhao, K. F. Kelly, and J. M. Tour, *Nano Lett.*, 2005, **5**, 2330. Copyright American Chemical Society (2005).

Although literature studies suggested that the C_{60} molecule rolls on the surface, in the nanocar movement studies it is still not possible to conclusively conclude that the nanocar moves on surface exclusively via a rolling mechanism. Hopping, sliding and other moving modes could also be responsible for the movement of the nanocar since the experiment was carried out at high temperature conditions, making the C_{60} molecules more energetic to overcome interactions between surfaces.

To tackle the question of the mode of translation, a trimeric "nano-tricycle" has been synthesized. If the movement of fullerene-wheeled nanocar was based on a hopping or sliding mechanism, the trimer should give

observable translational motions like the four-wheeled nanocar, however, if rolling is the operable motion then the nano-tricycle should rotate on an axis, but not translate across the surface. The result of the imaging experiment of the trimer at ∼200 °C (Figure 3.166,) yielded very small and insignificant translational displacements in comparison to 4-wheel nanocar (Figure 3.165). The trimeric 3-wheel nanocar showed some pivoting motions in the images. This motion type can be attributed to the directional preferences of the wheels mounted on the trimer causing the car to rotate. All the experimental results suggested that a C_{60}-based nanocar moves via a rolling motion rather than hopping and sliding. In addition, the fact that the thermally driven nanocar only moves in high temperature also suggests that four C_{60} have very strong interactions to the surface.

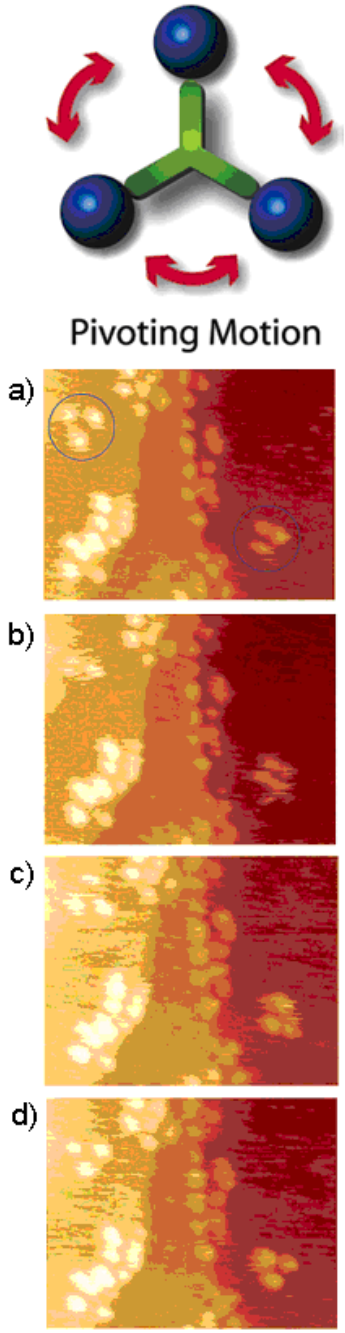

Figure 3.166: Pivot motion of the trimer. a) - d) Pivot motions of circled trimered were shown in the series of images. No significant translation were observed in comparison to the nanocar. Y. Shirai, A. J. Osgood, Y. Zhao, K. F. Kelly, and J. M. Tour, *Nano Lett.*, 2005, **5**, 2330. Copyright American Chemical Society (2005).

3.3.6.4 Bibliography

- D. M. Eigler and E. K. Schweizer, *Nature*, 1990, **344**, 524.
- L. Grill, K. -H. Rieder, F. Moresco, G. Rapenne, S. Stojkovic, X. Bouju, and C. Joachim, *Nat. Nanotechnol.*, 2007, **2**, 95.
- Y. Shirai, A. J. Osgood, Y. Zhao, K. F. Kelly, and J. M. Tour, *Nano Lett.*, 2005, **5**, 2330.
- Y. Shirai, A. J. Osgood, Y. Zhao, Y. Yao, L. Saudan, H. Yang, Y.-H. Chiu, L. B. Alemany, T. Sasaki, J.-F. Morin, J. M. Guerrero, K. F. Kelly, and J. M. Tour, *J. Am. Chem. Soc.*, 2006, **128**, 4854.

3.3.7 The Application of VSI (Vertical Scanning Interferometry) to the Study of Crystal Surface Processes[37]

3.3.7.1 Introduction

The processes which occur at the surfaces of crystals depend on many external and internal factors such as crystal structure and composition, conditions of a medium where the crystal surface exists and others. The appearance of a crystal surface is the result of complexity of interactions between the crystal surface and the environment. The mechanisms of surface processes such as dissolution or growth are studied by the physical chemistry of surfaces. There are a lot of computational techniques which allows us to predict the changing of surface morphology of different minerals which are influenced by different conditions such as temperature, pressure, pH and chemical composition of solution reacting with the surface. For example, Monte Carlo method is widely used to simulate the dissolution or growth of crystals. However, the theoretical models of surface processes need to be verified by natural observations. We can extract a lot of useful information about the surface processes through studying the changing of crystal surface structure under influence of environmental conditions. The changes in surface structure can be studied through the observation of crystal surface topography. The topography can be directly observed macroscopically or by using microscopic techniques. Microscopic observation allows us to study even very small changes and estimate the rate of processes by observing changing the crystal surface topography in time.

Much laboratory worked under the reconstruction of surface changes and interpretation of dissolution and precipitation kinetics of crystals. Invention of AFM made possible to monitor changes of surface structure during dissolution or growth. However, to detect and quantify the results of dissolution processes or growth it is necessary to determine surface area changes over a significantly larger field of view than AFM can provide. More recently, vertical scanning interferometry (VSI) has been developed as new tool to distinguish and trace the reactive parts of crystal surfaces. VSI and AFM are complementary techniques and practically well suited to detect surface changes.

VSI technique provides a method for quantification of surface topography at the angstrom to nanometer level. Time-dependent VSI measurements can be used to study the surface-normal retreat across crystal and other solid surfaces during dissolution process. Therefore, VSI can be used to directly and nondirectly measure mineral dissolution rates with high precision. Analogically, VSI can be used to study kinetics of crystal growth.

3.3.7.2 Physical principles of optical interferometry

Optical interferometry allows us to make extremely accurate measurements and has been used as a laboratory technique for almost a hundred years. Thomas Young observed interference of light and measured the wavelength of light in an experiment, performed around 1801. This experiment gave an evidence of Young's arguments for the wave model for light. The discovery of interference gave a basis to development of interferomertry techniques widely successfully used as in microscopic investigations, as in astronomic investigations.

The physical principles of optical interferometry exploit the wave properties of light. Light can be thought as electromagnetic wave propagating through space. If we assume that we are dealing with a linearly polarized

[37] This content is available online at <http://cnx.org/content/m22326/1.4/>.

wave propagating in a vacuum in z direction, electric field E can be represented by a sinusoidal function of distance and time.

$$E(x,y,z,t) = a\cos[2\pi(\mathrm{vt} - z/\lambda)] \tag{3.79}$$

Where a is the amplitude of the light wave, v is the frequency, and λ is its wavelength. The term within the square brackets is called the phase of the wave. Let's rewrite this equation in more compact form,

$$E(x,y,z,t) = a\cos\lceil\omega\mathrm{t} - \mathrm{kz}\rceil \tag{3.80}$$

where $\omega = 2\pi v$ is the circular frequency, and $k = 2\pi/\lambda$ is the propagation constant. Let's also transform this second equation into a complex exponential form,

$$E(x,y,z,t) = \mathrm{Re}\{a\exp(\mathrm{i}\varphi)\exp(\mathrm{i}\omega\mathrm{t})\} = \mathrm{Re}\{A\exp(\mathrm{i}\omega\mathrm{t})\} \tag{3.81}$$

where $\varphi = 2\pi z/\lambda$ and $A = \exp(-\mathrm{i}\varphi)$ is known as the complex amplitude. If n is a refractive index of a medium where the light propagates, the light wave traverses a distance d in such a medium. The equivalent optical path in this case is

$$p = n \cdot d \tag{3.82}$$

When two light waves are superposed, the result intensity at any point depends on whether reinforce or cancel each other (Figure 3.167). This is well known phenomenon of interference. We will assume that two waves are propagating in the same direction and are polarized with their field vectors in the same plane. We will also assume that they have the same frequency. The complex amplitude at any point in the interference pattern is then the sum of the complex amplitudes of the two waves, so that we can write,

$$A = A_1 + A_2 \tag{3.83}$$

where $A_1 = a_1\exp(-\mathrm{i}\varphi_1)$ and $A_2 = a_2\exp(-\mathrm{i}\varphi_2)$ are the complex amplitudes of two waves. The resultant intensity is, therefore,

$$I = \mid A \mid^2 = I_1 + I_2 + 2(I_1 I_2)^{1/2}\cos\Delta\varphi \tag{3.84}$$

where I_1 and I_2 are the intensities of two waves acting separately, and $\Delta\varphi = \varphi_1 - \varphi_2$ is the phase difference between them. If the two waves are derived from a common source, the phase difference corresponds to an optical path difference,

$$\Delta\mathrm{p} = (\lambda/2\pi)\Delta\varphi \tag{3.85}$$

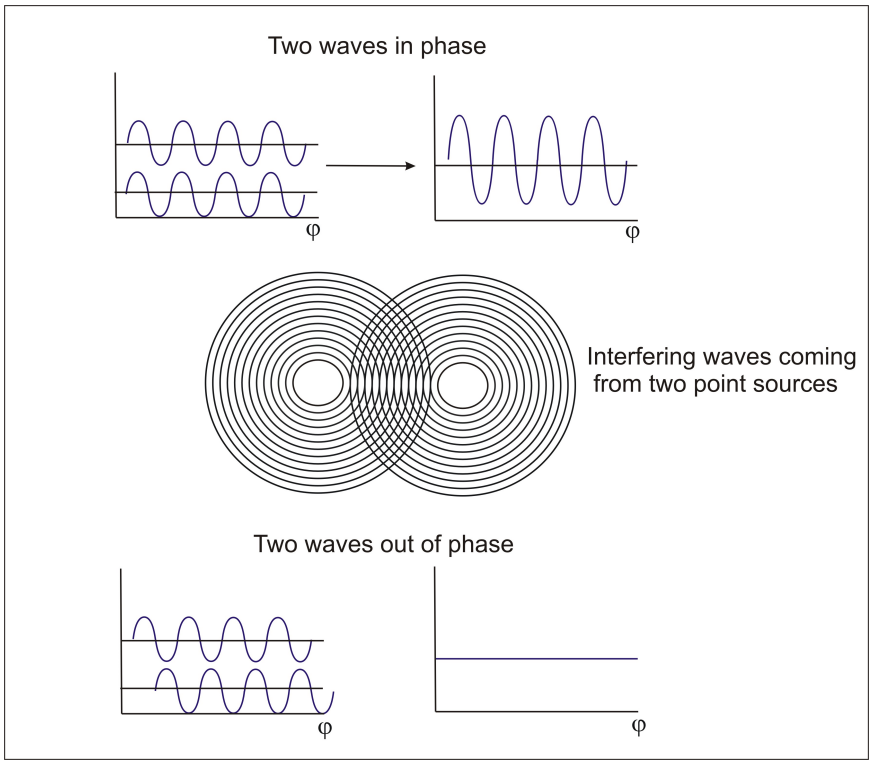

Figure 3.167: The scheme of interferometric wave interaction when two waves interact with each other, the amplitude of resulting wave will increase or decrease. The value of this amplitude depends on phase difference between two original waves.

If $\Delta\varphi$, the phase difference between the beams, varies linearly across the field of view, the intensity varies cosinusoidally, giving rise to alternating light and dark bands or fringes (Figure 3.167). The intensity in an interference pattern has its maximum value

$$I_{\max} = I_1 + I_2 + 2\left(I_1 I_2\right)^{1/2} \tag{3.86}$$

when $\Delta\varphi = 2m\pi$, where m is an integer and its minimum value

$$I_{\min} = I_1 + I_2 - 2\left(I_1 I_2\right)^{1/2} \tag{3.87}$$

when $\Delta\varphi = (2m+1)\,\pi$.

The principle of interferometry is widely used to develop many types of interferometric set ups. One of the earliest set ups is Michelson interferometry. The idea of this interferometry is quite simple: interference fringes are produced by splitting a beam of monochromatic light so that one beam strikes a fixed mirror and the other a movable mirror. An interference pattern results when the reflected beams are brought back together. The Michelson interferometric scheme is shown in Figure 3.168.

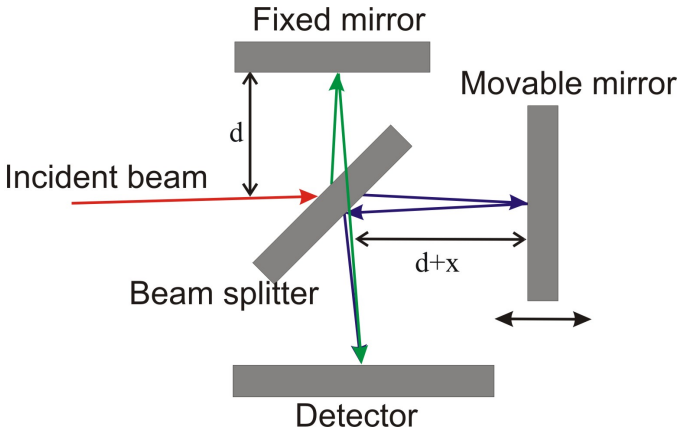

Figure 3.168: Schematic representation of a Michelson interferometry set-up.

The difference of path lengths between two beams is 2x because beams traverse the designated distances twice. The interference occurs when the path difference is equal to integer numbers of wavelengths,

$$\Delta \mathrm{p} = 2x = \mathrm{m}\lambda, m = 0, \pm 1, \pm 2... \tag{3.88}$$

Modern interferometric systems are more complicated. Using special phase-measurement techniques they capable to perform much more accurate height measurements than can be obtained just by directly looking at the interference fringes and measuring how they depart from being straight and equally spaced. Typically interferometric system consist of lights source, beamsplitter, objective system, system of registration of signals and transformation into digital format and computer which process data. Vertical scanning interferometry is contains all these parts. Figure 3.169 shows a configuration of VSI interferometric system.

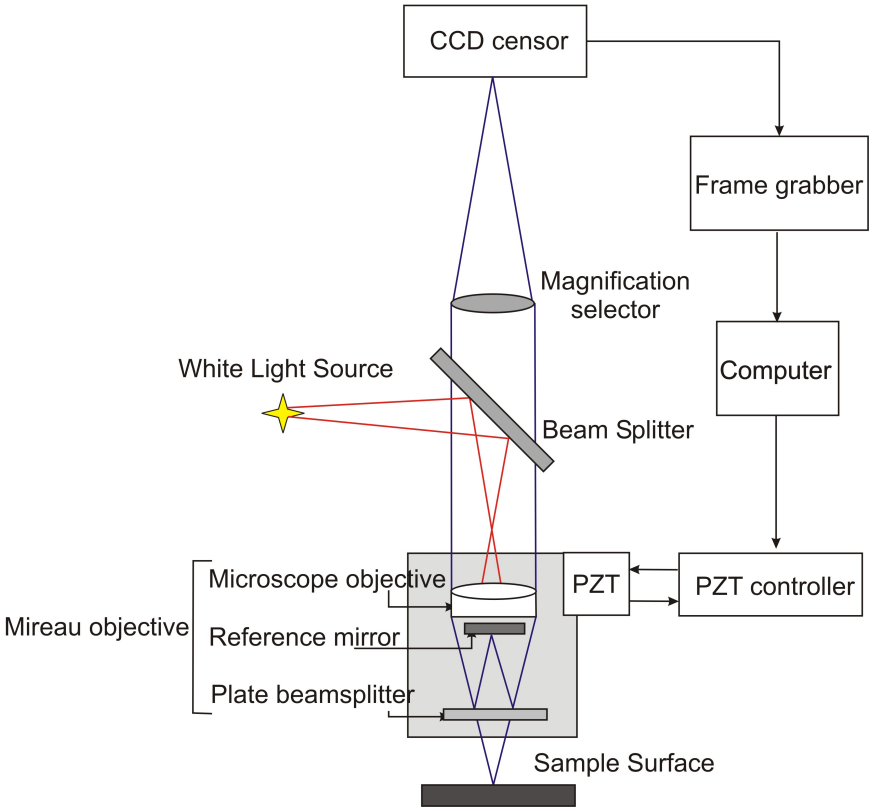

Figure 3.169: Schematic representation of the Vertical scanning interferometry (VSI) system.

Many of modern interferometric systems use Mirau objective in their constructions. Mireau objective is based on a Michelson interferometer. This objective consists of a lens, a reference mirror and a beamsplitter. The idea of getting interfering beams is simple: two beams (red lines) travel along the optical axis. Then they are reflected from the reference surface and the sample surface respectively (blue lines). After this these beams are recombined to interfere with each other. An illumination or light source system is used to direct light onto a sample surface through a cube beam splitter and the Mireau objective. The sample surface within the field of view of the objective is uniformly illuminated by those beams with different incidence angles. Any point on the sample surface can reflect those incident beams in the form of divergent cone. Similarly, the point on the reference symmetrical with that on the sample surface also reflects those illuminated beams in the same form.

The Mireau objective directs the beams reflected of the reference and the sample surface onto a CCD (charge-coupled device) sensor through a tube lens. The CCD sensor is an analog shift register that enables the transportation of analog signals (electric charges) through successive stages (capacitors), controlled by a clock signal. The resulting interference fringe pattern is detected by CCD sensor and the corresponding signal is digitized by a frame grabber for further processing with a computer.

The distance between a minimum and a maximum of the interferogram produced by two beams reflected from the reference and sample surface is known. That is, exactly half the wavelength of the light source. Therefore, with a simple interferogram the vertical resolution of the technique would be also limited to $\lambda/2$. If we will use a laser light as a light source with a wavelength of 300 nm the resolution would be

only 150 nm. This resolution is not good enough for a detailed near-atomic scale investigation of crystal surfaces. Fortunately, the vertical resolution of the technique can be improved significantly by moving either the reference or the sample by a fraction of the wavelength of the light. In this way, several interferograms are produced. Then they are all overlayed, and their phase shifts compared by the computer software Figure 3.170. This method is widely known as phase shift interferometry (PSI).

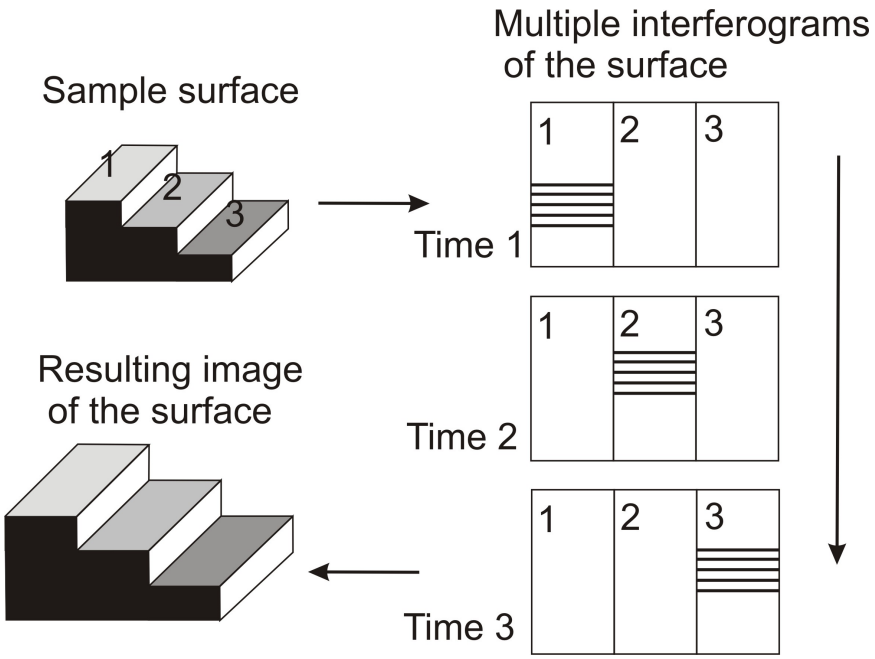

Figure 3.170: Sketch illustrating phase-shift technology. The sample is continuously moved along the vertical axes in order to scan surface topography. All interferograms are automatically overlayed using computer software.

Most optical testing interferometers now use phase-shifting techniques not only because of high resolution but also because phase-shifting is a high accuracy rapid way of getting the interferogram information into the computer. Also usage of this technique makes the inherent noise in the data taking process very low. As the result in a good environment angstrom or sub-angstrom surface height measurements can be performed. As it was said above, in phase-shifting interferometry the phase difference between the interfering beams is changed at a constant rate as the detector is read out. Once the phase is determined across the interference field, the corresponding height distribution on the sample surface can be determined. The phase distribution $\phi(x, y)$ is recorded by using the CCD camera.

Let's assign $A(x, y)$, $B(x, y)$, $C(x, y)$ and $D(x, y)$ to the resulting interference light intensities which are corresponded to phase-shifting steps of 0, $\pi/2$, π and $3\pi/2$. These intensities can be obtained by moving the reference mirror through displacements of $\lambda/8$, $\lambda/4$ and $3\lambda/8$, respectively. The equations for the resulting intensities would be:

$$A(x,y) = I_1(x,y) + I_2(x,y)\cos\alpha(x,y) \tag{3.89}$$

$$B(x,y) = I_1(x,y) - I_2(x,y)\sin\alpha(x,y) \tag{3.90}$$

$$C(x,y) = I_1(x,y) - I_2(x,y)\cos\alpha(x,y) \tag{3.91}$$

$$D(x,y) = I_1(x,y) + I_2(x,y)\sin\alpha(x,y) \tag{3.92}$$

where $I_1(x,y)$and $I_2(x,y)$ are two overlapping beams from two symmetric points on the test surface and the reference respectively. Solving equations (3.89)–(3.92), the phase map $\phi(x, y)$ of a sample surface will be given by the relation:

$$\varphi(x,y) = \frac{B(x,y) - D(x,y)}{A(x,y) - C(x,y)} \tag{3.93}$$

Once the phaseis determined across the interference field pixel by pixel on a two-dimensional CCD array, the local height distribution/contour, $h(x, y)$, on the test surface is given by

$$h(x,y) = \frac{\lambda}{4\pi}\varphi(x,y) \tag{3.94}$$

Normally the resulted fringe can be in the form of a linear fringe pattern by adjusting the relative position between the reference mirror and sample surfaces. Hence any distorted interference fringe would indicate a local profile/contour of the test surface.

It is important to note that the Mireau objective is mounted on a capacitive closed-loop controlled PZT (piezoelectric actuator) as to enable phase shifting to be accurately implemented. The PZT is based on piezoelectric effect referred to the electric potential generated by applying pressure to piezoelectric material. This type of materials is used to convert electrical energy to mechanical energy and vice-versa. The precise motion that results when an electric potential is applied to a piezoelectric material has an importance for nanopositioning. Actuators using the piezo effect have been commercially available for 35 years and in that time have transformed the world of precision positioning and motion control.

Vertical scanning interferometer also has another name; white-light interferometry (WLI) because of using the white light as a source of light. With this type of source a separate fringe system is produced for each wavelength, and the resultant intensity at any point of examined surface is obtained by summing these individual patterns. Due to the broad bandwidth of the source the coherent length L of the source is short:

$$L = \frac{\lambda^2}{\mathrm{n}\Delta\lambda} \tag{3.95}$$

where λ is the center wavelength, n is the refractive index of the medium, $\Delta\lambda$ is the spectral width of the source. In this way good contrast fringes can be obtained only when the lengths of interfering beams pathways are closed to each other. If we will vary the length of a pathway of a beam reflected from sample, the height of a sample can be determined by looking at the position for which a fringe contrast is a maximum. In this case interference pattern exist only over a very shallow depth of the surface. When we vary a pathway of sample-reflected beam we also move the sample in a vertical direction in order to get the phase at which maximum intensity of fringes will be achieved. This phase will be converted in height of a point at the sample surface.

The combination of phase shift technology with white-light source provides a very powerful tool to measure the topography of quite rough surfaces with the amplitude in heights about and the precision up to 1-2 nm. Through a developed software package for quantitatively evaluating the resulting interferogram, the proposed system can retrieve the surface profile and topography of the sample objects Figure 3.171.

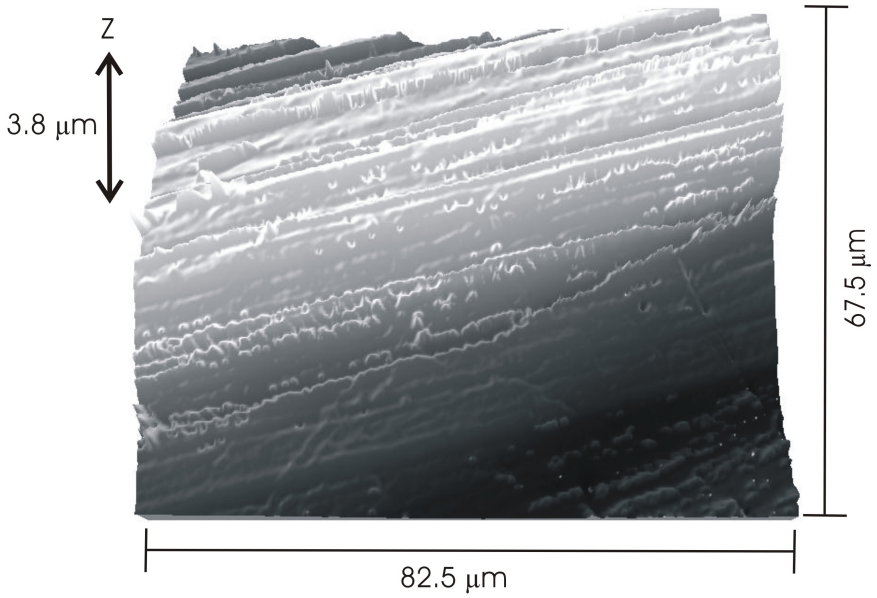

Figure 3.171: Example of muscovite surface topography, obtained by using VSI- 50x objective.

3.3.7.3 A comparison of common methods to determine surface topography: SEM, AFM and VSI

Except the interferometric methods described above, there are a several other microscopic techniques for studying crystal surface topography. The most common are scanning electron microscopy (SEM) and atomic force microscopy (AFM). All these techniques are used to obtain information about the surface structure. However they differ from each other by the physical principles on which they based.

3.3.7.3.1 Scanning electron microscopy

SEM allows us to obtain images of surface topography with the resolution much higher than the conventional light microscopes do. Also it is able to provide information about other surface characteristics such as chemical composition, electrical conductivity etc, see Figure 3.172. All types of data are generated by the reflecting of accelerated electron beams from the sample surface. When electrons strike the sample surface, they lose their energy by repeated random scattering and adsorption within an outer layer into the depth varying from 100 nm to 5 microns.

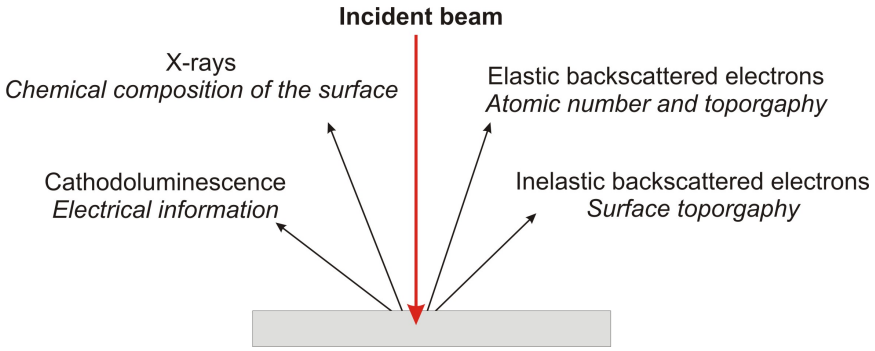

Figure 3.172: Scheme of electron beam-sample interaction at SEM analysis

The thickness of this outer layer also knows as interactive layer depends on energy of electrons in the beam, composition and density of a sample. Result of the interaction between electron beam and the surface provides several types of signals. The main type is secondary or inelastic scattered electrons. They are produced as a result of interaction between the beam of electrons and weakly bound electrons in the conduction band of the sample. Secondary electrons are ejected from the k-orbitals of atoms within the surface layer of thickness about a few nanometers. This is because secondary electrons are low energy electrons (<50 eV), so only those formed within the first few nanometers of the sample surface have enough energy to escape and be detected. Secondary backscattered electrons provide the most common signal to investigate surface topography with lateral resolution up to 0.4 - 0.7 nm.

High energy beam electrons are elastic scattered back from the surface. This type of signal gives information about chemical composition of the surface because the energy of backscattered electrons depends on the weight of atoms within the interaction layer. Also this type of electrons can form secondary electrons and escape from the surface or travel father into the sample than the secondary. The SEM image formed is the result of the intensity of the secondary electron emission from the sample at each x,y data point during the scanning of the surface.

3.3.7.3.2 Atomic force microscopy

AFM is a very popular tool to study surface dissolution. AFM set up consists of scanning a sharp tip on the end of a flexible cantilever which moves across a sample surface. The tips typically have an end radius of 2 to 20 nm, depending on tip type. When the tip touch the surface the forces of these interactions leads to deflection of a cantilever. The interaction between tip and sample surface involve mechanical contact forces, van der Waals forces, capillary forces, chemical bonding, electrostatic forces, magnetic forces etc. The deflection of a cantilever is usually measured by reflecting a laser beam off the back of the cantilever into a split photodiode detector. A schematic drawing of AFM can be seen in Figure 3.173. The two most commonly used modes of operation are contact mode AFM and tapping mode AFM, which are conducted in air or liquid environments.

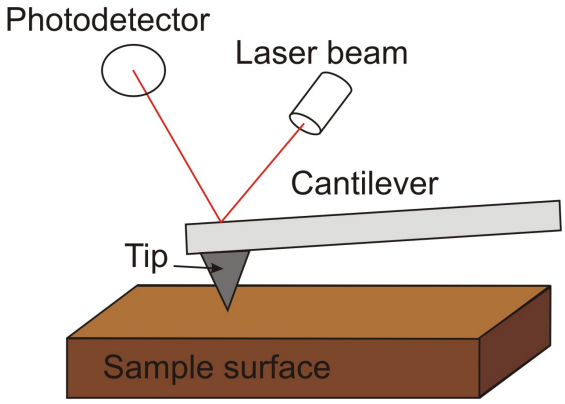

Figure 3.173: Schematic drawing of an AFM apparatus.

Working under the contact mode AFM scans the sample while monitoring the change in cantilever deflection with the split photodiode detector. Loop maintains a constant cantilever reflection by vertically moving the scanner to get a constant signal. The distance which the scanner goes by moving vertically at each x,y data point is stored by the computer to form the topographic image of the sample surface. Working under the tapping mode AFM oscillates the cantilever at its resonance frequency (typically~300 kHz) and lightly "taps" the tip on the surface during scanning. The electrostatic forces increase when tip gets close to the sample surface, therefore the amplitude of the oscillation decreases. The laser deflection method is used to detect the amplitude of cantilever oscillation. Similar to the contact mode, feedback loop maintains a constant oscillation amplitude by moving the scanner vertically at every x,y data point. Recording this movement forms the topographical image. The advantage of tapping mode over contact mode is that it eliminates the lateral, shear forces present in contact mode. This enables tapping mode to image soft, fragile, and adhesive surfaces without damaging them while work under contact mode allows the damage to occur.

3.3.7.3.3 Comparison of techniques

All techniques described above are widely used in studying of surface nano- and micromorphology. However, each method has its own limitations and the proper choice of analytical technique depends on features of analyzed surface and primary goals of research.

All these techniques are capable to obtain an image of a sample surface with quite good resolution. The lateral resolution of VSI is much less, then for other techniques: 150 nm for VSI and 0.5 nm for AFM and SEM. Vertical resolution of AFM (0.5 Å) is better then for VSI (1 - 2 nm), however VSI is capable to measure a high vertical range of heights (1 mm) which makes possible to study even very rough surfaces. On the contrary, AFM allows us to measure only quite smooth surfaces because of its relatively small vertical scan range (7 μm). SEM has less resolution, than AFM because it requires coating of a conductive material with the thickness within several nm.

The significant advantage of VSI is that it can provide a large field of view (845 $\times$ 630 μm for 10x objective) of tested surfaces. Recent studies of surface roughness characteristics showed that the surface roughness parameters increase with the increasing field of view until a critical size of 250,000 μm is reached. This value is larger then the maximum field of view produced by AFM (100 $\times$ 100 μm) but can be easily obtained by VSI. SEM is also capable to produce images with large field of view. However, SEM is able to provide only 2D images from one scan while AFM and VSI let us to obtain 3D images. It makes quantitative

analysis of surface topography more complicated, for example, topography of membranes is studied by cross section and top view images.

	VSI	**AFM**	**SEM**
Lateral resolution	0.5-1.2 μm	0.5 nm	0.5-1 nm
Vertical resolution	2 nm	0.5 Å	Only 2D images
Field of view	845 $\times$ 630 μm (10x objective)	100 $\times$ 100 μm	1-2 mm
Vertical range of scan	1 mm	10 μm	-
Preparation of a sample	-	-	Required coating of a conducted material
Required environment	Air	Air, liquid	Vacuum

Table 3.16: A comparison of VSI sample and resolution with AFM and SEM.

3.3.7.4 The experimental studying of surface processes using microscopic techniques

The limitations of each technique described above are critically important to choose appropriate technique for studying surface processes. Let's explore application of these techniques to study dissolution of crystals.

When crystalline matter dissolves the changes of the crystal surface topography can be observed by using microscopic techniques. If we will apply an unreactive mask (silicon for example) on crystal surface and place a crystalline sample into the experiment reactor then we get two types of surfaces: dissolving and remaining the same or unreacted. After some period of time the crystal surface starts to dissolve and change its z-level. In order to study these changes *ex situ* we can pull out a sample from the reaction cell then remove a mask and measure the average height difference $\Delta \overset{\Psi}{h}$between the unreacted and dissolved areas. The average heights of dissolved and unreacted areas are obtained through digital processing of data obtained by microscopes. The velocity of normal surface retreat v_{SNR} during the time interval Δt is defined as

$v_{\mathrm{SNR}} = \frac{\Delta \overline{h}}{\Delta \mathrm{t}}$

Dividing this velocity by the molar volume $\overline{V}(\mathrm{cm}^3/\mathrm{mol})$ gives a global dissolution rate in the familiar units of moles per unit area per unit time:

$$R = \frac{v_{\mathrm{SNR}}}{\overline{V}} \tag{3.96}$$

This method allows us to obtain experimental values of dissolution rates just by precise measuring of average surface heights. Moreover, using this method we can measure local dissolution rates at etch pits by monitoring changes in the volume and density of etch pits across the surface over time. VSI technique is capable to perform these measurements because of large vertical range of scanning. In order to get precise values of rates which are not depend on observing place of crystal surface we need to measure enough large areas. VSI technique provides data from areas which are large enough to study surfaces with heterogeneous dissolution dynamics and obtain average dissolution rates. Therefore, VSI makes possible to measure rates of normal surface retreat during the dissolution and observe formation, growth and distribution of etch pits on the surface.

However, if the mechanism of dissolution is controlled by dynamics of atomic steps and kink sites within a smooth atomic surface area, the observation of the dissolution process need to use a more precise technique. AFM is capable to provide information about changes in step morphology *in situ* when the dissolution occurs. For example, immediate response of the dissolved surface to the changing of environmental conditions (concentrations of ions in the solution, pH etc.) can be studied by using AFM.

SEM is also used to examine micro and nanotexture of solid surfaces and study dissolution processes. This method allows us to observe large areas of crystal surface with high resolution which makes possible to measure a high variety of surfaces. The significant disadvantage of this method is the requirement to cover examine sample by conductive substance which limits the resolution of SEM. The other disadvantage of SEM is that the analysis is conducted in vacuum. Recent technique, environmental SEM or ESEM overcomes these requirements and makes possible even examine liquids and biological materials. The third disadvantage of this technique is that it produces only 2D images. This creates some difficulties to measure $\Delta\overline{h}$ within the dissolving area. One of advantages of this technique is that it is able to measure not only surface topography but also chemical composition and other surface characteristics of the surface. This fact is used to monitor changing in chemical composition during the dissolution.

3.3.7.5 Bibliography

- A. C. Lasaga, *Kinetic Theory in the Earth Sciences*. Princeton Univ. Press, Princeton, NJ (1998).
- A. Luttge, E. V. Bolton, and A. C. Lasaga A.C., *Am. J. Sci.*, 1999, **299**, 652.
- D. Kaczmarek, *Vacuum*, 2001, **62**, 303.
- P. Hariharan. *Optical interferometry*, Second edition, Academic press (2003) ISBN 0-12-311630-9.
- A. Luttge and P. G. Conrad, *Appl. Environ. Microbiol.*, 2004, **70**, 1627.
- A. C. Lasaga and A. Luttge, *American Mineralogist*, 2004, **89**, 527.
- K. J. Davis and A. Luttge, *Am. J. Sci.*, 2005, **305**, 727.
- S. H. Wang and Tay, *Meas. Sci. Technol.*, 2006, **17**, 617.
- A. Luttge and R. S. Arvidson, in *Kinetics of water-rock interaction*, Ed. S. Brantley, J. Kubicki, and A. White, Springer (2007).
- L. Zhang and A. Luttge, *American Mineralogist*, 2007, **92**, 1316.
- C. Fischer A. and Luttge, *Am. J. Sci.*, 2007, **307**, 955.
- Y. Wyart, G. Georges, C. Deumie, C. Amra, and P. Moulina, *J. Membrane Sci.*, 2008, **315**, 82.
- T. C. Vaimakis, E. D. Economou, and C. C. Trapalis, *J. Therm. Anal. Cal.*, 2008, **92**, 783.